UNIVERSITÀ
DEGLI STUDI
FIRENZE

DOTTORATO DI RICERCA IN

SCIENZE CHIMICHE

CICLO XXXV

COORDINATORE Prof. Anna Maria Papini

Advanced computational modelling of structural and dynamic properties of complex systems.

Settore Scientifico Disciplinare CHIM/02

Dottorando

Dott. Lorenzo Briccolani Bandini

Tutore

Prof. Gianni Cardini

Coordinatore

Prof. Anna Maria Papini

Anni 2019/2023

Advanced computational modelling of structural and dynamic properties of complex systems.

by

Lorenzo Briccolani Bandini

Abstract

This doctoral dissertation focuses on the theoretical and computational modeling of the electronic structure of complex systems. The study of chemical systems with several degrees of freedom requires the proper selection of the contributions to simplify the system and develop a physical-chemical model. In this context, the characterization of the electronic structure is fundamental. Depending on the experimental framework, two approaches were applied: *ab initio* calculations and simulations of *ab initio* Molecular Dynamics (AIMD). On the basis of these premises, a variety of experimental systems have been investigated.

The Brandi-Guarna reaction has been investigated to interpret the lack of regioselectivity in the cycloaddition reaction which takes to the formation of the 5-isoxazolidine compound and the syntesis of the piridone and enaminone side product by the thermal rearrangement of the isoxazolidine.

The theoretical investigation of the tautomerization of [2,2'-bipyridyl]-3,3'-diol allowed us to evaluate the accuracy of the exchange-correlation functional at a chosen level of theory. The tautomerization involves a double proton transfer and is substantially correlated with both the energy of the first transition state and the delocalization error of the adopted functional. The computational results show that the step-by-step mechanism of tautomerism can only be found in xc-functionals with high levels of either terms.

The computational study on Posner-like clusters has been carried out in collaboration with an experimental research group, allowing to obtain a useful method for the interpretation of the experimental results. The *ab initio* optimization of Posner-like clusters show that the addition of Mg^{2+} to Amorphous Calcium Phosphate (ACP) samples stabilizes the amorphous phase against heating. This simplified computational model contributed to define a strategy to synthetize ACP nanoparticles with a customized elemental composition.

The *ab initio* modeling of the adenine adsorption on the (111) gold surface shows that the two selected tautomeric forms (N9 and N7) have substantially distinct behaviors. The steric hindrance given by the different protonated nitrogens is a decisive factor in the adsorption process. The presence of a tautomerization process between the two tautomeric forms of adenine would explain the sometimes contradicting conclusions found in the scientific literature. These results suggest further investigations into the mechanism of water-mediated tautomerization of adenine when adsorbed on the metal surface.

THIS PAGE INTENTIONALLY LEFT BLANK

Contents

Chapter 1

Introduction

The purpose of this thesis is to investigate complex systems of chemical interest through the use of computational methodologies, to clarify the accuracy of the adopted level of theory and to provide a useful computational protocol for the interpretation of the experimental data.

The main aim of computational chemistry is to understand properties of matter, to rationalise experimental data and to predict real materials properties and experimental observable and to relate them to a microscopic description. According to the theory adopted to describe the interaction of particles, the numerical methodologies can be classified as *ab initio* and semi-empirical methods. The resulting *ab initio* or semi-empirical models can be adopted to characterize a complex system at the atomic level.

Based on quantum chemistry, the *ab initio* methods are either wave function or density based. The semiempirical methods, which are significantly faster than *ab initio*, are based on parametrizations derived from *ab initio* results or experimental data. Generally, these are less accurate than ab initio methods but they can be applied to relatively large systems. The choice between these approaches is determined by the number of degrees of freedom of the system and by the requested accuracy.

In this thesis the electronic structure has been investigated using a combination of computational methods and theoretical approaches to characterize their accuracy and to evaluate the most appropriate one to support the experimental research. Electronic structure and its effects on determining the interactions of matter are a

huge topics of study. Moreover, all the results here reported refer to the properties that arise from the electronic ground state.

Most of the calculations were carried out within the Kohn-Sham Density Functional Theory, which is one of the most used tools in theoretical and computational chemistry and physics. Indeed, DFT is the best method for performing quantum mechanical calculations on the electronic structure of many electrons and many atoms systems, as well as performing *ab initio* molecular dynamics. This is due to the fact that density functional theory is the most cost-effective way to obtain reasonably reliable and useful results on such problems. The application of post-Hartree-Fock methods such as Møller-Plesset and Coupled Cluster, here, was limited to a comparison with DFT results.

The characterization of the properties deriving from the electronic ground state was also carried out by the *ab initio* Molecular Dynamics (AIMD) method. The forces are described at the level of the many-body problem of interacting electrons and nuclei that form atoms and molecules using the framework of quantum mechanics, whereas nuclear dynamics follow classical mechanics. Due to its inherent virtues, *ab initio* molecular dynamics is a popular and overly expanding computational tool employed to study physical, chemical, and biological phenomena in a very broad sense. In particular, it is the basis of what could be called a "virtual laboratory approach" used to study complex processes at the atomic level.

The investigation of reaction mechanisms in organic synthesis through the determination of electron structure has been the major topic of this thesis. In the framework of DFT calculations, we explored processes for which atomistic level characterisation of the reaction mechanism could not be elucidated via organic synthesis. The computational investigation has been conducted through the characterization of the geometry of the stationary points, vibrational frequency calculation, the distribution of electron density, and estimation of the energy differences within the limits of the experimental accuracy. From the calculation of the electron density distribution, it was possible to estimate the dipole moment, charge distribution, bond orders, and various molecular orbital shapes.

The study of electronic structure in the field of solid state physics has led to the

resolution of different challenges; in particular, the study of crystalline and amorphous systems has significantly contributed to an experimental research in the fields of nanoparticle characterization and synthesis. The purpose of this study was to determine the influence of varying ion ratios relative to total cation concentration on the characteristics of precipitated amorphous phases. The structure of the amorphous was obtained by substitution of the atomic species in the crystal lattice. The computational and experimental results have provided a simple but effective strategy to tune the composition and thermal stability of nanoparticles for researchers working on inorganic colloids and in particular on amorphous phosphates.

During my time in Paris, the collaboration with a theoretical research group made possible to study how the exchange and correlation functionals affect the characterization of the electronic structure. The KS-DFT implies that the density of the original interacting system's ground state is equivalent to that of a set of non-interacting systems. All of the troublesome many-body variables are incorporated into an exchange-correlation functional of the density, resulting in independent particle equations for non-interacting systems that are regarded as exactly solvable. However, the exchange correlation in terms of density is unknown, so approximations, such as the use of semi-empirical parameters, are required. The purpose of this study was to investigate the effect of the parameterization of the exchange and correlation functional on the determination of the mechanism of a model tautomerization reaction. This reaction has been investigated in the ground state using both static and dynamic approaches, detailing the reaction process and estimating the free energy surface to highlight any potential differences between functionals that, according to the methodology, ought to be equivalent. The computational results show that the characterization of the reaction mechanism is dependent on the delocalization error of the xc-functional adopted.

Analysis of the potential energy surface in the tautomerization reaction has inspired a more ambitious research: characterization of the interaction between a biomolecule and a metal substrate through *ab initio* molecular dynamic simulations. Our primary focus has been the identification of stationary points, whose determination necessitates a computationally intensive investigation of the phase

space. Utilizing accelerated phase space sampling techniques, such as metadynamics, has proven to be advantageous because it has enabled the identification of local minima given by the various possible orientations and distances of the biomolecules with respect to the metal surface within reasonable simulation times.

Thesis outline

In this Ph.D. dissertation, the electron structure of complex systems has been explored using a combination of computational and theoretical methods in order to characterize the capabilities of the adopted methods and to provide explanations to challenges in experimental research. The structure of this thesis is as follows:

1. In Chapter 2 definitions and discussions of theoretical methodologies employed are given;

2. In Chapter 3 a computational investigation of the Brandi-Guarna reaction and the "cyclopropilidene effect" was carried out in order to gain important information and provide an accurate interpretation of the apparent remote influence of the stereochemical environment on favoring the distinct pathways;

3. In Chapter 4 the effect of the parameterization of the exchange and correlation functional on the determination of the mechanism of tautomerization of [2,2'-bipyridyl]-3,3'-diol have been investigated;

4. In Chapter 5 computational methods were utilized to provide atomic-level insight into the effect of Mg^{2+} concentration on the structure and stability of Amorphous Calcium Phosphate clusters, revealing new knowledge regarding the function of Mg^{2+} substitution in ACP. A comprehensive analysis was undertaken by optimizing a series of model clusters with varying Mg^{2+}/Ca^{2+} ratios, beginning with Posner's cluster and ending with the fully Mg-substituted cluster;

5. In Chapter 6 The adsorption of tutomeric forms of adenine molecule on (111) gold surfaces is investigated by means of DFT approach. The complexity of

the potential energy surface, given by the several possible orientations and distances of the adenine with respect to the surface, has required accelerated sampling techniques to recognize the different relative minima with affordable computational cost.

6. In Chapter 7 a brief conclusion regarding these three years of Ph.D. research is provided.

All the explicit calculations have been done by the present author.

Chapter 2

Theoretical background

This chapter presents the theoretical foundations of electronic structure theory and an overview of solving the equations of motion for classical and ab-initio for molecular dynamic simulations. While many of the methodologies discussed may well be found in traditional quantum chemistry[1–5] and MD simulation[6–8] textbooks, this is an occasion to provide a concise and cohesive framework that contextualizes the computational approaches employed in this dissertation.

The next sections describe the fundamentals of wavefunction theory and density functional theory. After introducing the potential energy surface, certain fundamental concepts regarding the resolution of the equations of motion and accelerated sampling techniques, such as metadynamics and umbrella sampling, are presented.

The molecular Hamiltonian To understand the fundamental notions of chemical bond theory, it is required to examine the motion and energy of the molecule's constituent particles. If the total energy of the nuclei and electrons in the molecule is less than the sum of the energies of the individual atoms, then the molecule is stable. The spatial arrangement (bond lengths and bond angles) with the lowest energy will determine the molecule's structure. Quantum mechanics is the fundamental theory of physics that can explain the system's energy, and thus the motion of nuclei and electrons The starting point is the Schrödinger equation in the position rapprentation is

$$\hat{\mathcal{H}} \left|\Psi(\mathbf{r},t)\right\rangle = i\hbar \frac{\partial}{\partial t} \left|\Psi(\mathbf{r},t)\right\rangle , \tag{2.1}$$

where $\hbar = \frac{h}{2\pi}$, with h Planck's constant, $\hat{\mathcal{H}}$ the Hamiltonian operator and $|\Psi\rangle$ the wavefunction which fully describes a state of the system. This linear partial differential equation describes the time evolution of a N particle system, with coordinates $\mathbf{r} = \{\mathbf{r}_i\}$, $i = 1, \ldots, N$.

The wavefunction itself has no physical meaning, but $|\Psi(\mathbf{r}, t)|^2$ is the probability density of finding each particle at a given point and at a given time. Other physical properties can also be obtained from the wavefunction by applying operators, since $|\Psi\rangle$ contains all the information of the system. In the framework of quantum mechanics, any measurable property has an associated linear operator $\hat{A}$ i.e. $\hat{A}^\dagger = \hat{A}$. For example, in the case of N charged particles, $\hat{\mathcal{H}}$ becomes

$$\hat{\mathcal{H}} = -\sum_{i=1}^{N} \frac{\hbar^2}{2m_i}\nabla_i^2 + \sum_{i=1}^{N-1}\sum_{j>i}^{N} \frac{q_i q_j}{4\pi\varepsilon_0 |\mathbf{r}_i - \mathbf{r}_j|}, \tag{2.2}$$

where the first term is the kinetic energy $\hat{T}$, with m_i being the mass of the i-th particle and ∇^2 being the Laplacian operator acting on the coordinates of the i-th particle, and the second one is the potential energy $\hat{V}$, including the sum of two-particle Coulomb's interactions.

Since Eq.2.2 has no explicit dependence on time, the wavefunction can be factorized as a product of spatial and temporal terms

$$|\Psi(\mathbf{x}_i, t)\rangle = |\Psi(t)\rangle\, |\Psi(\{\mathbf{x}_i\})\rangle \tag{2.3}$$

where $|\Psi_t(t)\rangle = A\exp(-iEt)$, i.e. it is a phase and therefore it carries no information on the physics of the system. Therefore, one can keep only the space-dependent part, reaching the time-independent (non-relativistic) Schrödinger equation:

$$\hat{\mathcal{H}}\, |\Psi(\{\mathbf{x}_i\})\rangle = E\, |\Psi(\{\mathbf{x}_i\})\rangle\,, \tag{2.4}$$

from which, being the Hamiltonian operator hermitian, the energy can be calculated as $E = \langle\Psi|\hat{\mathcal{H}}|\Psi\rangle$. Electrons and nuclei are the two types of particles found in chemical systems. The kinetic energy contributions of a system containing n electrons and N nuclei can be split into the electronic and nuclear parts, $\hat{T}_e$ and $\hat{T}_n$.

There are three terms in the potential energy: electron-electron, nucleus-nucleus, and electron-nucleus ($\hat{V}_{ee}$, $\hat{V}_{nn}$, $\hat{V}_{en}$, respectively). The last term couples electrons and nuclei, making it impossible to separate the system into wavefunctions that depend on electrons and nuclear coordinates. Therefore, the molecular Hamiltonian (in atomic units) is as follows

$$\hat{\mathcal{H}} = -\sum_{i=1}^{n}\frac{1}{2}\nabla_i^2 - \sum_{k=1}^{N}\frac{1}{2M_k}\nabla_k^2 - \sum_{i=1}^{n}\sum_{k=1}^{N}\frac{Z_k}{|\mathbf{r}_i - \mathbf{R}_k|} + \sum_{i<j}^{n}\frac{1}{|\mathbf{r}_i - \mathbf{r}_j|} + \sum_{k<l}^{N}\frac{Z_k Z_l}{|\mathbf{R}_k - \mathbf{R}_l|}. \tag{2.5}$$

where Z_k are the atomic numbers and $\mathbf{r}$ and $\mathbf{R}$ are the electronic and nuclear coordinates, respectively. The non-separability of the wavefunction into an electronic and a nuclear part limits the analythycal solution of Eq. 2.5, to only biatomic molecules with only one electron assuming nuclear position fixed. However, molecules are multielectronic systems and some additional approximations have to be introduced.

The Born-Oppenheimer approximation The Born-Oppenheimer approximation, also known as the adiabatic approximation, consists of treating the motion of electrons to be independent from that of nuclei due to the mass difference between the particles (about 1800 times more). The Schrödinger equation for a molecule made by N atoms and n electrons is:

$$\hat{\mathcal{H}}\,|\psi(\mathbf{r};\mathbf{R})\rangle = E\,|\psi(\mathbf{r};\mathbf{R})\rangle\,. \tag{2.6}$$

with the form of the Hamiltonian operation described in Eq. 2.5. The wavefunction is therefore rewritten as:

$$\psi(\mathbf{r};\mathbf{R}) = \psi_e(\mathbf{r};\bar{\mathbf{R}})\psi_n(\mathbf{R}) \tag{2.7}$$

where $\bar{\mathbf{R}}$ is a fixed nuclei configuration.

The kinetic energy of the nuclei can be neglected, and the nuclei-nuclei repulsion term is considered to be a constant. The remaining terms form the so-called electronic Hamiltonian, which describes the motion of n electron for a fixed configuration

of N nuclei

$$\hat{\mathcal{H}}_e \left|\psi_e(\mathbf{r};\bar{\mathbf{R}})\right\rangle = E_e \left|\psi_e(\mathbf{r};\bar{\mathbf{R}})\right\rangle, \tag{2.8}$$

$$\hat{\mathcal{H}}_e = -\sum_{i=1}^{n} \frac{1}{2}\nabla_i^2 - \sum_{i=1}^{n}\sum_{k=1}^{N} \frac{Z_k}{r_{ik}} + \sum_{i<j}^{n} \frac{1}{r_{ij}}, \tag{2.9}$$

where $r_{ik} = |\mathbf{r}_i - \mathbf{R}_k|$ and $r_{ij} = |\mathbf{r}_i - \mathbf{r}_j|$. Within this approximation, the electronic dynamics can be considered separated from the nuclear one. The $|\psi(\mathbf{r};\mathbf{R})\rangle$ are eigenfunctions of $\hat{\mathcal{H}}_e$ and therefore they form an orthonormal basis set in the Hilbert space

$$\langle\psi_q(\mathbf{r};\mathbf{R})|\psi_s(\mathbf{r};\mathbf{R})\rangle = \delta_{qs}.$$

Assuming to be able to solve Eq. 2.8 for each nuclear configuration $\{\mathbf{R}\}$, the total molecular wavefunction $|\Psi(\mathbf{r};\mathbf{R})\rangle$ can be expanded on the basis of $|\psi_q(\mathbf{r};\mathbf{R})\rangle$

$$\left|\Psi(\mathbf{r};\mathbf{R})\right\rangle = \sum_q \chi_q(\mathbf{R}) \left|\psi_q(\mathbf{r};\mathbf{R})\right\rangle. \tag{2.10}$$

Inserting Eq. 2.10 into Eq. 2.8 and projecting onto the ψ_q basis set (integrating only on electronic coordinates), we can evaluate how the different terms of $\hat{\mathcal{H}}$ act on $\chi_q(\mathbf{R})$ and $\psi_q(\mathbf{r};\mathbf{R})$. In particular the kinetic energy operator of nuclei $-\sum_k \frac{\hbar^2}{2M_k}\nabla_k^2$ is not diagonal on the $|\psi_q(\mathbf{r};\mathbf{R})\rangle$ basis. The Born-Oppenheimer approximation decouples the electronic dynamics from the nuclear dynamics by neglecting the off-diagonal components of this operator. This presumption is extremely mild and totally justifiable in the great majority of situations.

Pauli exclusion principle In Newtonian physics, two particles can be identified based on their trajectories, but this is not possible in quantum mechanics due to the Uncertainty Principle. Electrons are non-distinguishable particles. That is, any observable derived from the wavefunction, like their probability density, must be invariant given any permutation of the electronic coordinates

$$|\Psi(\mathbf{r}_1,\ldots,\mathbf{r}_i,\mathbf{r}_j,\ldots,\mathbf{r}_n)|^2 = |\Psi(\mathbf{r}_1,\ldots,\mathbf{r}_j,\mathbf{r}_i,\ldots,\mathbf{r}_n)|^2$$

Introducing the permutation operator $\hat{P}$ of parity p, which permutes two electrons in the wavefunction, we can formalize the following: $\hat{P}\,|\Psi\rangle = (-1)^p\,|\Psi\rangle$. This is the Pauli exclusion principle, which states that the wavefunction of n electrons must be antisymmetric relative to the exchange of any two electrons. Consequently, if two electrons had identical spatial and spin coordinates, we would obtain

$$\hat{P}\,|\Psi(\mathbf{r}_1,\ldots,\mathbf{r}_i,\mathbf{r}_j,\ldots,\mathbf{r}_n)\rangle = (-1)\,|\Psi(\mathbf{r}_1,\ldots,\mathbf{r}_i,\mathbf{r},\ldots,\mathbf{r}_n)\rangle$$
$$2\Psi(\mathbf{r}) = 0 \rightarrow \Psi(\mathbf{r}) = 0$$

Therefore, two electrons cannot be found with the same spatial and spin coordinates. This concept must be observed for every electronic (and, more generally, fermionic) wavefunction.

Approximate methods There are few quantum mechanical systems with the exact resolution characterized to be single particle systems or that can be transformed in single particle problems between these systems are not, therefore, included systems of chemical interest like multi electron molecules. The reason for this is the electron-electron interaction term. If electrons did not interact, a polyelectron system's Hamiltonian could be expressed as a sum of monoelecttronic Hamiltonians, each of which could be solved independently. Due to the electrostatic interaction between electrons, the Hamiltonians cannot be separated, and the Scroedinger equation cannot be resolved exactly. Consequently, for a polyelectronic system, approximation methods are required.

Variational theorem and Hartree-Fock method

Theorem. *given a generic test function Φ and the ground state energy E_0 of a Hamiltonian system $\mathcal{H}$, the hypothesis that the test function is normalized yields the following*

$$\langle\Phi|\hat{\mathcal{H}}|\Phi\rangle \geq E_0 \tag{2.11}$$

In quantum chemistry, the variational principle (Eq. 2.11) is a fundamental theorem on which many computational approaches are based. Given a normalized

trial wavefunction $|\Phi\rangle$ that satisfies the proper boundary conditions (often that the wavefunction goes to zero at infinity), the expectation value of the Hamiltonian is an upper bound on the exact ground state energy.

The polyelectronic wave function must satisfy two conditions: the electrons' indistinguishability and the Pauli exclusion principle. Consequently, it is insufficient to construct the wavefunction as product of non-interacting single electron spin-orbitals $|\chi(\mathbf{x})\rangle = |\Psi(\mathbf{r})\rangle\,|\omega(\sigma)\rangle$ (where the spin function $|\omega(\sigma)\rangle$ can assume two values, $|\alpha\rangle$ or $|\beta\rangle$). A better choice is provided by the so-called Slater determinant, which for a system of N electrons results

$$\Psi_{SD}(\mathbf{x}_1, \mathbf{x}_2, \ldots, \mathbf{x}_N) = \frac{1}{\sqrt{N!}} \begin{vmatrix} \chi_1(\mathbf{x}_1) & \chi_2(\mathbf{x}_1) & \cdots & \chi_N(\mathbf{x}_1) \\ \chi_1(\mathbf{x}_2) & \chi_2(\mathbf{x}_2) & \cdots & \chi_N(\mathbf{x}_2) \\ \vdots & \vdots & & \vdots \\ \chi_1(\mathbf{x}_N) & \chi_2(\mathbf{x}_N) & \cdots & \chi_N(\mathbf{x}_N) \end{vmatrix} = |\chi_1\chi_2\ldots\chi_N|. \tag{2.12}$$

This is the starting point of the Hartree-Fock method (HF). Therefore if we consider the one-electron term (h_i) referred to the electron 1, the two-electrons terms (K_{ij} and J_{ij}) referred to electrons 1 and 2 and the index i and j to the spin-orbits, the energy results $E = \langle\Psi_{SD}|\hat{\mathcal{H}}|\Psi_{SD}\rangle$, that is for a constant nuclear potential V_{NN}:

$$E = \sum_{i=1}^{N} h_i + \sum_{i=1}^{N}\sum_{j=1}^{N}(J_{ij} - K_{ij}), \tag{2.13}$$

These terms are the one-electron energy, the Coulomb and the Exchange integral respectively and they are defined as

$$h_i = \langle\chi_i|\hat{T}_e + \hat{V}_{en}|\chi_i\rangle\,, \tag{2.14}$$

$$J_{ij} = \langle\chi_i\chi_j|\frac{e^2}{r_{12}}|\chi_i\chi_j\rangle\,, \tag{2.15}$$

$$K_{ij} = \langle\chi_i\chi_j|\frac{e^2}{r_{12}}|\chi_j\chi_i\rangle\,. \tag{2.16}$$

The Hartree-Fock theory is a mean-field theory, i.e. each electron feels the averaged effect of the rest by means of Fock operators. The two latter terms come from

$\hat{V}_{ee}$ acting on the wavefunction, where r_{ij} is the distance between the i-th and j-th electrons. The Coulomb integral (J_{ij}) represents the electrostatic interaction between two charge densities $|\chi_i|^2$ and $|\chi_j|^2$ while the exchange integral (K_{ij}) arises from the antisymmetric nature of the Slater determinant. Both J_{ij} and K_{ij} are positive, and therefore, if $i = j$ they vanish, preventing any self-interaction spurious effect which would come from J_{ii}. The core of the Hartree-Fock theory is to apply the variational method to this independent particle model. By proceeding this way, J_{ij} and K_{ij} integrals can be expressed as single-electron operators, defined by the spin-orbitals themselves

$$J_j\chi_i(\mathbf{x}) = \chi_i(\mathbf{x}) \int \frac{|\chi_j(\mathbf{x}')|^2}{|\mathbf{x} - \mathbf{x}'|} d\mathbf{x}', \tag{2.17}$$

$$K_j\chi_i(\mathbf{x}) = \chi_j(\mathbf{x}) \int \frac{\chi_j^*(\mathbf{x}')\chi_i(\mathbf{x}')}{|\mathbf{x} - \mathbf{x}'|} d\mathbf{x}'. \tag{2.18}$$

Collecting these two terms plus h_i, one obtains the Fock operator, which may be defined for a given spin direction σ, either up or down (α, β), as:

$$\hat{F}^\sigma |\chi_i^\sigma\rangle = \left[\hat{h} + \sum_{j,\sigma'} (\hat{J}_j^{\sigma'} - \delta_{\sigma\sigma'} K_j^\sigma)\right] |\chi_i^\sigma\rangle = \varepsilon_i^\sigma |\chi_i^\sigma\rangle \tag{2.19}$$

where ε_i^σ are the energies associated with the i-th spin-orbtial with spin σ. These are the unrestricted HF (UHF) equations, in which each electron is allowed to occupy a distinct spatial orbital due to the spin's separation. Despite this, the two sets of orbitals continue to be connected by Coulomb's term. For a molecule with a closed shell, the previous equation becomes

$$\hat{F} |\phi_i\rangle = \left[\hat{h} + \sum_j (2\hat{J}_j - \hat{K}_j)\right] |\phi_i\rangle = \varepsilon_i |\phi_i\rangle , \tag{2.20}$$

in which each spin-orbital is filled by two electrons (α, β). This gives rise to the restricted HF (RHF) theory. One could also take a midway by forcing orbitals to behave as RHF as far as possible and the remaining ones as UHF, which is the restricted open-shell HF (ROHF) method. The total RHF and ROFH wave

functions are also eigen functions of the total squared spin operator $\hat{S}^2$, while the UHF ones are not.

Electron correlation In the Hartree-Fock method, each electron feels the averaged effect of the $n-1$ electrons. This implies that it is far from giving the exact values of energy because the electronic correlation energy is completely missed. The electronic correlation energy is the energy required to reach the exact value

$$E_{corr} = E_{exact} - E_{HF}. \tag{2.21}$$

Electron correlation can be categorized as either Coulomb's and Fermi's correlation or static and dynamic correlation. The first classification describes the interaction between electrons with parallel (Fermi correlation) and anti-parallel (Coulomb correlation) spins. Due to the Pauli principle, a given spin-orbital in RHF theory can only contain two electrons with anti-parallel spins. Therefore, Coulomb correlation can occur between electrons in both the same and different spatial orbitals. Fermi correlation, on the other hand, may only occur between electrons in distinct orbitals; consequently, it is weaker. The second classification (into dynamic and static correlation) is similar to the first but conceptually distinct. Static correlation is connected with near-degenerate states, whereas dynamic correlation takes instantaneous electron correlation into account (spin-orbitals of similar energy). The dynamic correlation between electrons in the same orbital is more significant than the static correlation between electrons in different orbitals. UHF can extract more static correlation than RHF in this regard.

Post Hartree-Fock methods Post-Hartree–Fock methods are a collection of methodologies designed to enhance the Hartree–Fock (HF) or self-consistent field (SCF) method. These methods have been developed to evaluate the electronic correlation, giving a more accurate evaluation of the electron repulsions than in the Hartree–Fock method, where electron repulsions are just averaged.

Møller-Plesset perturbation theory The Møller-Plesset theory describes a ground state consisting of doubly occupied spin-orbitals (RHF) through orthonormal spin-orbitals u_i. The Fock operator results for the electron n

$$\hat{f}(n) = -\frac{1}{2}\nabla_n^2 - \sum_\alpha \frac{Z_\alpha}{r_{n\alpha}} + \sum_{i=1}^{N} \left[\hat{J}_i(n) - \hat{K}_i(n)\right] \tag{2.22}$$

$$\hat{J}_i(n) = \int d\mathbf{x}_2 \Psi_j^*(2) \frac{1}{r_{nj}} \Psi_j^*(2) \tag{2.23}$$

$$\hat{K}_i(n) u_i(n) = \left[\int d\mathbf{x}_2 \Psi_j^*(2) \frac{1}{r_{nj}} u_i(2) \Psi_j^*(2)\right] \Psi_j(n) \tag{2.24}$$

The spin-orbits u_i are eigen functions of the Fock operator

$$\hat{f}(n) u_i(n) = \epsilon_i(n) u_i(n) \tag{2.25}$$

The unperturbed Hamiltonian in the MP method is defined as the sum of the Fock operators

$$\hat{\mathcal{H}}^0 = \sum_{n=i}^{N} \hat{f}_i(n) \tag{2.26}$$

and the wave function of the ground state Ψ_0 is the Slater determinant of the spin-orbitals

$$\hat{\mathcal{H}}^0 \Psi_0 = \left(\sum_{n=1}^{N} \epsilon_n\right) \Psi_0 \tag{2.27}$$

The Hamiltonian $\hat{\mathcal{H}}$ describes the perturbed system, the difference between the two Hamiltonians is the perturbation $\hat{\mathcal{H}}'$

$$\hat{\mathcal{H}}' = \hat{\mathcal{H}} - \hat{\mathcal{H}}^0 \tag{2.28}$$

For a poly electronic system $\hat{\mathcal{H}}^0 = \sum_i \hat{f}_i$ and the perturbed Schrödinger equation to solve is then

$$(\hat{\mathcal{H}}^0 + \hat{\mathcal{H}}') \left|\Psi_0\right\rangle = E \left|\Psi_0\right\rangle . \tag{2.29}$$

The energy at zero order $E_0^{(0)}$ and first order $E_0^{(1)}$ of perturbation are respectively

$$E_0^{(0)} = \langle\Psi|\,\hat{\mathcal{H}}^0\,|\Psi_0\rangle \tag{2.30}$$

$$E_0^{(1)} = \langle\Psi|\,\hat{\mathcal{H}}'\,|\Psi_0\rangle \tag{2.31}$$

$$E_0^{(0)} + E_0^{(1)} = \langle\Psi|\,\hat{\mathcal{H}}^0\,|\Psi_0\rangle + \langle\Psi|\,\hat{\mathcal{H}}'\,|\Psi_0\rangle \tag{2.32}$$

$$= \langle\Psi|\,\hat{\mathcal{H}}^0 + \hat{\mathcal{H}}'\,|\Psi_0\rangle \tag{2.33}$$

$$= \langle\Psi|\,\hat{\mathcal{H}}^0 + \hat{\mathcal{H}} - \hat{\mathcal{H}}^0\,|\Psi_0\rangle \tag{2.34}$$

$$= \langle\Psi|\,\hat{\mathcal{H}}\,|\Psi_0\rangle = E_{HF} \tag{2.35}$$

and their sum gives the variational Hartree-Fock integral. The energy in the second order is

$$E_0^{(2)} = \sum_{s\neq 0}^{\infty} \frac{\langle\Psi_0|\,\hat{\mathcal{H}}'\,|\Phi_s^0\rangle\,\langle\Phi_s^0|\,\hat{\mathcal{H}}'\,|\Psi_0\rangle}{E_0^{(0)} + E_s^{(0)}} \tag{2.36}$$

where Φ_s^0 represents each possible Slater determinant generated by N distinct spin orbitals. To calculate the second order correction, integrals of type $\langle\Psi_0|\,\hat{\mathcal{H}}'\,|\Phi\rangle_s^0$ must be calculated, in which the function Φ_s^0 must diverge from the Slater determinant of the ground state Ψ_0 for one or more spin orbitals. The indices i,j,k,k describe the occupied orbitals of the eigenfunction Ψ_0 and a,b,c,d denote the unoccupied spin-obritals. The possible combination is

- Φ_s^0 differs from Ψ_0 by only one orbital spin Φ_i^a

$$\langle\Psi_0|\,\hat{\mathcal{H}}'\,|\Phi_i^a\rangle = \langle\Psi|\,\hat{\mathcal{H}} - \hat{\mathcal{H}}^0\,|\Phi_i^a\rangle \tag{2.37}$$

$$= \langle\Psi_0|\,\hat{\mathcal{H}}\,|\Phi\rangle_i^a - \langle\Psi_0|\,\hat{\mathcal{H}}^0\,|\Phi_i^a\rangle = 0 \tag{2.38}$$

  the first integral is zero for the Brullion theorem, the second integral is zero because the unperturbed Hamiltonian is $\hat{H} = \sum_n \hat{f}$

- Φ_s^0 is distinct from Ψ_0 by at least three spin orbitals. Since the perturbation term is bi-electronic, the integrals of type $\langle\Psi_0|\,\hat{\mathcal{H}}'\,|\Phi_{ijk}^{abc}\rangle$ are zero according to the Slater-Condon criteria.

- the only admissible determinants are those of double excitationΦ_{ij}^{ab}, which

results in a second-order correction

$$E_0^{(2)} = \sum_{i<j,a<b} \frac{|\langle\Psi_0|\,\hat{\mathcal{H}}'\,|\Phi_{ij}^{ab}\rangle|^2}{(\epsilon_i + \epsilon_j - \epsilon_a - \epsilon_b)} \tag{2.39}$$

The first corrective term in MP perturbation theory is the second order, which only comprises double excitation determinants.

$$E_{MP2} = E_{HF} + E_{MP}^{(2)} \tag{2.40}$$

In order to compute the successive corrections one may use the knowledge of the previous ones by using the energy of the unperturbed (zeroth order) equation. In the MP formalism, it is just the sum of the energies of the occupied spin-orbitals (which counts the electron-electron twice). It can be shown that the n-th correction to the energy is $E^{(n)} = \langle\Psi_0|\hat{\mathcal{H}}'|\Psi^{(n-1)}\rangle$. The first-order correction removes the electron-electron interaction once, and therefore the sum of zeroth and first order is just the HF energy. Hence, MP does not recover any electron correlation until second-order. Møller-Plesset methods are labeled as MPn where n is the order of the correction where the expansion is truncated. The usual ones are MP2, MP3, and MP4. Since this family of methods is not variational, energy is not an upper bound to the real one, and therefore, it may actually be lower than the true one.

Coupled cluster theory Coupled cluster (CC) theory was initially developed for the quantum-chemical study of nuclear matter. After its inclusion into electronic structure theory, it became one of the most efficient schemes in quantum chemistry for high-precision calculations of electron correlations.

The fundamental equation in CC theory is

$$|\Psi\rangle = \exp(\hat{T})\,|\Phi_{HF}\rangle \tag{2.41}$$

where Ψ_{CC} is the exact non-relativistic ground-state molecular wavefunction, Φ_{HF} the normalized ground-state Hartree-Fock function and $\exp(\hat{T})$ is defined by Taylor-

series expansion

$$\exp(\hat{T}) \equiv 1 + \hat{T} + \frac{\hat{T}^2}{2!} + \frac{\hat{T}^3}{3!} + \cdots = \sum_{k=0}^{\infty} \frac{\hat{T}^k}{k!} \tag{2.42}$$

and the cluster operator $\hat{T}$ is

$$\hat{T} \equiv \hat{T}_1 + \hat{T}_2 + \ldots \hat{T}_{N_e}. \tag{2.43}$$

the one-particle ($\hat{T}_1$) and two-particles ($\hat{T}_2$) operators are defined

$$\hat{T}_1 \Phi_{HF} = \sum_{a=n+1}^{\infty} \sum_{i=1}^{n} t_i^a \Phi_i^a \tag{2.44}$$

$$\hat{T}_2 \Phi_{HF} = \sum_{b=a+1}^{\infty} \sum_{a=n+1}^{\infty} \sum_{j=i+1}^{n} \sum_{i=1}^{n} t_{ij}^{ab} \Phi_{ij}^{ab} \tag{2.45}$$

$$\tag{2.46}$$

where Φ_i^a is a singly excited Slater determinant with the occupied spin-orbital u_i replaced by the virtual spin-orbit u_a and t_i^a, called amplitude, is a numerical coefficient whose value is determined by requiring that Eq. 2.41 be satisfied.

The operator $\hat{T}_1$ converts the Slater determinant Φ_{HF} into a linear combination of all possible singly excited Slater determinants. Similarly Φ_{ij}^{ab} is the Slater determinant with the occupied spin-orbitals u_i, u_j replaced with the virtual spin-orbitals u_a, u_b. No operators of a higher order than $\hat{T}_n$ are examined, as only n electrons may be excited by the n-electron wavefunction Φ_{HF}. By definition, when $\hat{T}_i$ operates on a determinant containing both occupied and virtual spin-orbitals, the resulting excitation contains only determinants from the occupied orbitals ($\hat{T}_1^2 \equiv \hat{T}_1(\hat{T}_1 \Phi_{HF})$, whereas $\hat{T}_1$ returns zero when operating on a determinant containing only virtual spin orbitals. The mixing into the wavefunctions of Slater determinants with electrons excited from occupied to virtual spin-orbitals allows electrons to keep away from one another and thereby provides for electron correlation.

The effect of the $\exp(\hat{T})$ operator is to express Ψ as a linear combination of Slater determinants that include Φ_{HF} and all possible excitations of electrons from

occupied to virtual spin-orbitals. This functional form (Eq. 2.41) ensures size-consistency and size-extensivity of the electron-correlation treatment even within a truncated scheme that omits a full CI calculation and expresses Ψ as a linear combination including all possible excitations. Coupled Cluster theory, therefore, is, by construction, a size-extensive approach.

Definition. *The size consistency of a method indicates that the energy of two molecules separated by an infinite distance is equal to the sum of the energies calculated separately for each molecule, in formula* $E_{AB} = E_A + E_B$ *for* $r \longrightarrow \infty$. *Size extensivity means that correlation energy scales correctly (linearly) with the size of the system.*

The CC wave function is often not determined by the variational principle due to the exponential ansatz. The CC wave function is instead placed into the Schrodinger equation, which is then multiplied from the left with $\exp(-\hat{T})$, and a formula for the energy is derived by projecting onto the reference determinant

$$E = \langle \Psi_{HF} | \exp(-\hat{T}) \hat{\mathcal{H}} \exp(\hat{T}) | \Psi_{HF} \rangle \tag{2.47}$$

and nonlinear equations for the amplitudes are obtained by projection onto the excited determinants $|\Psi_Q\rangle$

$$0 = \langle \Psi_Q | \exp(-\hat{T}) \hat{\mathcal{H}} \exp(\hat{T}) | \Psi_{HF} \rangle \,, \tag{2.48}$$

which has to be solved for every possible $|\Psi_Q\rangle$. CC theory shows its advantages only when used with a truncated cluster operator. The usual choices are $\hat{T} = \hat{T}_1 + \hat{T}_2$ (CC singles and doubles (CCSD)), $\hat{T} = \hat{T}_1 + \hat{T}_2 + \hat{T}_3$ (CC singles, doubles, triples (CCSDT)), and $\hat{T} = \hat{T}_1 + \hat{T}_2 + \hat{T}_3 + \hat{T}_4$ (CC singles, doubles, triples, quadruples (CCSDTQ)), etc.

However, third-order excitations is usually implemented perturbationally, resulting in the CCSD(T) approach, commonly referred to as the "gold standard" in quantum chemistry. In fact, the triple contribution is computed separately using perturbation theory of the fourth order and added to the CCSD results. In addition,

a term originating from a perturbation of the fifth order that describes the coupling between singles and triples is also provided.

Explicitly correlated methods In general, electron correlation methods suffer from the issue of slow convergence of the basis set, and very large basis sets are frequently required to produce converged results. The basis set problem results from the fact that the expansion in products of limited 1-electron functions (orbitals) does not adequately describe the shape of the wave function at small to intermediate values of electron distance r_{12}, which must satisfy the electronic wave function cusp condition

$$\left.\frac{\partial \Psi}{\partial r_{12}}\right|_{r_{12}=0} = \frac{1}{2}\Psi(r_{12}=0). \tag{2.49}$$

This problem can be avoided by incorporating terms into the wave function that depend directly on r_{12} and so accurately characterize the cusp. Early implementations employed a linear R_{12} correlation factor, and several so-called R_{12}-methods were created. Later, it was observed that a Slater-type function $F_{12} \sim \exp(-\gamma r_{12})$ produces significantly superior convergence of the basis set and numerical stability. This group of procedures is referred to as the F12 methods. The γ exponent is often specified in the input files as a parameter. Numerous investigations have demonstrated that the best value for γ is highly dependent on the size of the basis set and typically ranges from 0.80 to 1.40. In the majority of instances, the value 1 has been proven to be an appropriate choice. In general, larger γ values are more advantageous for larger basis sets.[9] The general expression of the wavefunctions, that holds both for standard CCSD, is

$$\Psi_{\mathrm{CCSD(-F12)}} = e^{\hat{T}_1+\hat{T}_2}\Psi_{\mathrm{HF}} \tag{2.50}$$

For explicitly correlated methods the double excitation operator $\hat{T}_2$ is extended by an additional term with the explicitly correlated amplitudes $\mathcal{T}^{ij}_{\alpha\beta}$. The single excitations, only present in Eq. 2.50, are not expanded because the explicit correlation acts on

electron pairs:

$$\hat{T}_1 = \sum_{ia} t_a^i \hat{E}_i^a$$

$$\hat{T}_2 = \frac{1}{2}\left(\sum_{ijab} \mathcal{T}_{ab}^{ij} \hat{E}_{ij}^{ab} + \sum_{ij\alpha\beta} \mathcal{T}_{\alpha\beta}^{ij} \hat{E}_{ij}^{\alpha\beta}\right)$$

where the explicitly correlated amplitudes are build by the projector $\hat{Q}_{12}$ and the correlation factor F_{12} as

$$\mathcal{T}_{\alpha\beta}^{ij} = \sum_{mn} T_{mn}^{ij} \langle mn|F_{12}\hat{Q}_{12}|\alpha\beta\rangle \,.$$

The indexes $i, j, k, l, \ldots$ identify occupied orbitals, a and b the virtual orbitals, while α and β the complete virtual orbital basis. The $\hat{Q}_{12}$ operator ensures orthogonality between the explicitly correlated part and the reference one. In order not to overburden the mathematical notation, we refer readers to an elegant and clear review by Liguo and coworkers for the derivation of the F12 equations.[10]

To calculate some blocks of the Fock matrix and exchange operators it is usual practice to rely on density fitting (DF), which reduces the associated computing cost. The DF method requires the use of a complementary auxiliary basis set (CABS), which is designed to span the orthogonal complement of the space occupied by the orbital basis. As a result, the CABS is created by combining the orbital and auxiliary bases. Auxiliary basis sets for DF and RI have the same functional form as orbital basis sets, but different exponents, and are often uncontracted. Similarly to the orbital basis sets, they are derived from basis set libraries.

The CCSD(T)-F12 methods contain many ansatz and approximations. The error generated by these approximations is dependent on the system and the estimated property but is typically quite minor. There are two primary estimates for CCSD-F12, namely F12a and F12b. Practically speaking, CCSD-F12a tends to overstate the correlation energy, but CCSD-F12b always falls within the base set limit.

Density functional theory All the previous methods are wave function-based methods, which rely on a very complex entity (Ψ) that depends (N electron system) on 4N variables (3N coordinates and N spins). Density functional theory (DFT), on

the other hand, relies on a much simpler quantity: the electron density, which just depends on three spatial variables and it can be obtained from the wave function:

$$\rho(\mathbf{r}) = N \int \dots \int d\mathbf{x}_2 \dots \mathbf{x}_N \Psi^*(\mathbf{x}_1, \dots, \mathbf{x}_N)\Psi(\mathbf{x}_1, \dots, \mathbf{x}_N). \tag{2.51}$$

The electron density $\rho(\mathbf{r})$ contains the same information as the N-electron wave function Ψ, but it is independent of the phase. DFT formalizes the electronic energy of a molecular system as a functional of the density

$$E[\rho] = V_{NN} + E_e[\rho] = V_{NN} + V_{eN}[\rho] + J_e[\rho] + T[\rho] + E_{xc}[\rho], \tag{2.52}$$

$$V_{eN}[\rho] = -\sum_{k=0}^{N} Z_k \int \rho(\mathbf{r}) r_k^{-1} d\mathbf{r}, \tag{2.53}$$

$$J_e[\rho] = \frac{1}{2} \int \int \rho(\mathbf{r}_1)\rho(\mathbf{r}_2) r_{12}^{-1} d\mathbf{r}_1 d\mathbf{r}_2. \tag{2.54}$$

where $V_{eN}[\rho]$ is the functional that describes the electron-nucleus interaction and $J_e[\rho]$ the functional related to the Coulomb's terms. It may seem somewhat unnatural that the molecular Hamiltonian can be fully specified from a quantity that does not describe two-particle distributions but only one-particle ones. However, it can be intuitively shown that the system can be completely defined by the electron density in its ground state. The Hamiltonian is completely determined by the number of electrons and the potential V_{Ne}, usually called "external" potential. Both quantities can be derived from the electron density: its integral over the whole volume is the number of electrons, the cusps of the density are the positions of nuclei, and their heights define the nuclear charges, these two, in turn, define V_{Ne}. Finally, the Hamiltonian determines the energy, the wave function, and the associated properties. Therefore, there must be a one-to-one correspondence between the electron density and the energy of the system. This was mathematically proved by the first Hohenberg and Kohn theorem, which ensures the existence of a universal energy functional of the electronic density. Additionally, they showed in their second theorem that the ground state energy can be obtained by means of the variational principle, starting with a trial density, $\tilde{\rho}$, so that $E[\tilde{\rho}] \geq E[\rho]$, where ρ

is the exact dendity.[11] Furthermore, the unrestricted scheme can be introduced in DFT by simply splitting the total electron density into the electron density for α and β electrons ($\rho = \rho_\alpha + \rho_\beta$). The only problem is that, although $E[\rho]$ is proved to exist and to be universal, it is unknown. The reason lies in the $T[\rho]$ and $J_e[\rho]$ functionals that cannot be directly written in terms of $\rho(\mathbf{r})$. If they were known, DFT would return the exact ground-state energy. To overcome this, Kohn and Sham ingeniously considered a fictitious system, of non-interacting electrons moving within an "external" potential (V_{eN}).[12] Such a system can be exactly described by a Slater determinant made up by auxiliary Kohn-Sham (KS) spin-orbitals. As a constraint, it is then required that the electron density derived from these auxiliary functions is the same as the one of DFT i.e., $\rho_{KS}(\mathbf{r}) = \sum_i \int |\chi_i(\mathbf{x})|^2 d\sigma = \rho(\mathbf{r})$. The (small) difference in kinetic energy between the real and the fictitious ($T_s[\rho]$) system is added to the exchange-correlation term, which becomes $E_{xc}[\rho] = E'_{xc}[\rho] + T[\rho] - T_s[\rho]$. This $E_{xc}[\rho]$ is now the only unknown term. However, it is possible to deduce some exact xc-functional's properties:

- absence of self-interaction;

- linear scale property , given $\rho_\lambda[\lambda x, \lambda y, \lambda z]$ and $\rho[x, y, z]$ the the exchange term results:

  $$E_x[\rho_\lambda] = \lambda E_x[\rho]$$

  while for the correlation term the scale property has been demonstrated only for low densities ($\lambda > 1$)

  $$-E_c[\rho_\lambda] = \lambda E_c[\rho]$$

  for $\lambda \to \infty$ the correlation energy for a finite system is constant and has a negative value;

- the Lieb-Oxford condition that sets a maximum on the exchange and correlation energies

- the exchange potential should have an asymptotic trend ($-r^{-1}$) for $r \to \infty$ instead it is exponential; while the correlation potential should have an asymp-

totic trend ($-\frac{1}{2}\alpha r^{-4}$) where α is the polarizability of the system with minus an electron;

- the xc-potential as a function of the number of electrons is discontinuous, the value of the discontinuity should be the difference between the electron affinity and the ionization energy.

The formulation of different $E_{xc}[\rho]$ functionals has resulted in the emergence of several hundreds of approximated xc-functionals that make DFT realizable; and this is the reason why DFT frequently contains semi-empirical parameters. Simple approximations work exceptionally well for a wide variety of chemistry and physics problems, especially when predicting the structure and thermodynamic properties of molecules and solids. This is the secret to density functional theory's success.

According to the fundamental ingredients in each method, Perdew and Schmidt proposed a classification into five families.[13] The resulting Jacob's ladder of DFT is a classification that connects the "hell" of non-interacting electrons to the "heaven" of chemical accuracy. The farther up the ladder one goes, the more accurate the results are, but at the cost of additional computational effort. The ladder's steps are as follows, in order of increasing difficulty: (i) the local spin density approximation (LSDA) assumes that the electronic density is a slowly changing function of $\mathbf{r}$, so that the uniform electron gas model is able to describe the non-uniform density system locally, (ii) the generalized gradient approximation (GGA), in which corrections accounting for the non uniformity of ρ through the gradient of the electron density are introduced, (iii) the meta-GGA family, which adds higher order corrections based on higher order derivatives of the electronic density (and in some cases the kinetic energy from the auxiliary orbitals), (iv) the hybrid DFT methods, which improve the highly local nature of the previous families (they care about the electronic density at specific points and their close vicinity) by mixing some "exact" exchange energy (computed following the HF method with the KS auxiliary spin-orbitals), which is non local, to the GGA and meta-GGA rungs, and finally (v) one can also include some (dynamical) correlation estimated by perturbative methods like MP2, with this leading to double-hybrid methods, at the expenses of a higher computational

cost.

A final remark is deserved regarding dispersion corrections. It is well known that LDA and GGA approximations predict exponential falloffs of the interatomic interactions instead of the expected asymptotic r^{-6} behavior. Hybrids do not improve this picture, as the inclusion of HF-like exact exchange may end up in repulsive forces. Double-hybrids instead do improve the picture by the addition of correlation from the perturbative correction. However, usually, DFT functionals are corrected in order to properly describe London dispersion forces. The most popular strategy is due to Grimme, and relies on its simplicity and negligible additional computational cost. Indeed, the so-called D3[14,15] and D3(BJ)[16] corrections, improve the descriptions of medium-range interactions with respect to previous generation corrections, are less empirical and incorporate dependence on the chemical environment of each atom by accounting for the number of directly bonded atoms. The D3(BJ) version includes the Becke-Johnson damping function, which controls the overlap between short and long-range interactions, as the former is described by DFT. The equation for D3 correction is given by

$$\Delta E_{\text{disp}}^{\text{D3}} = -\frac{1}{2}\sum_{n=6,8}\sum_{A\neq B} s_n \frac{C_n^{AB}}{R_{AB}^n} f_{\text{damp}}(R_{AB}),$$

where s_n is a scaling factor which depends on the chosen functional, C_n^{AB} are the nth order dispersion parameters for each AB atom pair, R_{AB} are the AB inter-nuclear distances and

$$f_{\text{damp}}(R_{AB}) = \frac{1}{1+\exp\left(-\gamma_n\left(\frac{R_{AB}}{s_{r,n}R_0^{AB}}-1\right)\right)}.$$

are damping functions where R_{AB} are cut-off radii, $s_{r,6}$ are DFT functional dependent scaling factors, $s_{r,8}$ is set to 1 for all functionals and γ_n are constants, set to 14 for $n = 6$ and 16 for $n = 8$. Regarding D3(BJ) correction, the equation becomes

$$\Delta E_{\text{disp}}^{\text{D3(BJ)}} = -\frac{1}{2}\sum_{n=6,8}\sum_{A\neq B} s_n \frac{C_n^{AB}}{R_{AB}^n + f_{\text{damp}}^n(R_{AB}^0)}.$$

Here, $f(R_{AB}^0) = a_1 R_{AB}^0 + a_2$ where a_i are fit parameters (the BJ parameters)

and $R_{AB}^{0} = \sqrt{\frac{C_8^{AB}}{C_6^{AB}}}$. For either D3 and D3(BJ), the fit parameters ($s_{r,6}$ and s_8 for the former, a_1 , s_8 and a_2 for the latter) are determined by a least-squares fit on a set of 130 dispersion interaction energies.

Delocalization Error Despite the general adoption and performance of DFT, its application can still be afflicted by widespread inaccuracies that lead to qualitative failures in the characterization of physical properties.[17] These failures are not attributable to weaknesses in the theory itself, but rather to deficiencies in the approximate adopeted exchange-correlation functionals. A systematic method for developing universally applicable functionals is a problem that has remained unsolved till now. The principal defects in DFT calculations are the underestimating of the barriers of chemical reactions, the band gaps of materials, the energy of dissociating molecular ions, and the excitation energies in charge transfer. In addition, they overestimate the binding energies of charge transfer complexes and the response of molecules and materials to an electric field. Surprisingly, all of these distinct issues are related to the same source: the delocalization error of approximate functionals, which is generated by the dominant Coulomb factor that pushes electrons away. This inaccuracy is explicable from the perspective of fractional charges.[17] These violations appear in incredibly simple model molecules, such as H_2^+. Functionals accurately describe the chemical bond but fail significantly when the molecule is stretched. At the dissociation limit, two H atoms with half an electron each are produced, and the energy is underestimated. Due to the discrete nature of electrons, the energy of an atom as a function of its charge is a straight-line of interpolation between the integers. However, approximate functionals are erroneously convex between integers and predict energy that is too low for fractional charges. The energy is too low for the stretched H_2^+ if the electron is delocalized over the two centers. This is a result of the delocalization error, which relates to the propensity of approximated functionals to artificially spread the electron density. This phenomenon is related to the self-interaction error[18,19] well defined only for one electron systems, with analogy made for many electron systems[20,21]. However, the erroneous convex behavior of the energy as a function of the fractional charge is better described as

the delocalization error, as it encapsulates the physical basis of the issue[22].

Transition state theory For a single-step reaction A + B $\longrightarrow$ P, the rate of change of the abundances of either reactants and products is called the reaction rate law, and it's given by

$$\text{rate} = \frac{d[P]}{dt} = k[A][B], \tag{2.55}$$

where [...] are the abundances of species involved in the reaction and k is the reaction rate constant. The experimental relation for k is given by the Arrhenius equation:

$$k = A \exp\left(-\frac{E_a}{k_B T}\right) \tag{2.56}$$

where E_a is the activation energy and A is the pre-exponential or frequency component (which may have a small temperature dependence). If a reaction obeys the Arrhenius equation, then the Arrhenius plot ($\ln k$ vs $\frac{1}{T}$) should be a straight line with $-\frac{E_a}{R}$ and $\ln A$ as the slope and intercept, respectively. The activation energy is the least energy that reactants must possess in order to produce products, while the pre-exponential factor is a measure of the collision rate. Tolman[23,24] offered a more accurate interpretation of E_a proving that the Arrhenius energy of activation is the average total energy (relative translation + internal) of all reacting pairs of reactants minus the average total energy of all reacting pairs, including non-reactive pairs.

TST provides an expression of k in terms of statistical mechanics quantities that can be calculated for every molecular species. The main result of TST is the following expression for the thermal rate coefficient:

$$k = \frac{k_B T}{h} \frac{Z^{\ddagger}}{Z_R} \exp\left(-\frac{E_a}{k_B T}\right) \tag{2.57}$$

where $Z^{\ddagger}$ and Z_R are the partition functions of the transition state and reactants, respectively. TST is based on some key assumptions:

1. there is chemical equilibrium between reactants and the "activated complex" (the high energy species formed corresponding to the saddle point, the TS)

2. once a molecule has reached the TS it may either come back to reactants or evolve into products

3. if it crosses the TS, the system can only evolve into products.

The canonical transition state theory can be applied also to reactions that present a loose transition state. In this case, as the molecular configuration of the transition state cannot be univocally identified, it is necessary to apply the variational principle to the computation of the rate coefficient. Indeed, the transition state corresponds in terms of reactive flux to the minimum flux of reactive molecules that pass from reactants to products per unit of time. This principle allows us to locate the transition state, choosing the position along the reaction coordinate that minimizes the canonical rate coefficient. This procedure requires only a little more effort than the standard TST, as one repeats the calculation of k for a number of different transition states until the position giving the minimum value for k is determined.

Molecular Dynamics In the classical limit, molecular dynamics is a substantially an exact technique. The correctness of the interaction model used to represent the system has a big impact on how well its conclusions match the results of experiments: the more realistic is the model, the more accurate are the results. The most common simulated statistical sets in MD consist of:

- NVE, a statistical ensemble in which the total energy (E) of the system , the volume (V) and the number of particles (N) in the system are fixed. In order for the system to maintain statistical equilibrium, the microcanonical ensemble must be completely isolated (unable to exchange energy or particles with its surroundings);

- NVT, is a statistical ensemble in which the energy is not conserved, but the number of particles (N), the volume (V) and the temperature (T) are constant. The canonical ensemble can be used to describe a closed system that was in weak thermal contact with a heat bath. To be in statistical equilibrium, a system must be completely closed and may come into weak thermal contact with other systems characterized by ensembles at the same temperature;

- NPT is a statistical ensemble in which the energy is not conserved, but the number of particles (N), the pressure (P) and the temperature (T) are constant. This ensemble is utilized extensively in chemistry, as chemical reactions are often done at constant pressure settings. The NPT ensemble is also useful for calculating the equation of state for model systems whose virial expansion for pressure cannot be approximated.[8]

Equation of motion for atomic systems The classical equation of motion for a system of N molecules interacting via a potential V is defined by the Lagrangian equation of motion as a function of the generalized coordinates q_k and velocities $\dot{q}_k$:

$$\frac{d}{dt}\left(\frac{\partial \mathcal{L}}{\partial \dot{q}_k}\right) - \left(\frac{\partial \mathcal{L}}{\partial q_k}\right) = 0 \tag{2.58a}$$

$$\mathcal{L} = K - V \tag{2.58b}$$

$$K(\dot{q}) = \frac{1}{2}\sum_{i=1}^{N} m_i \dot{q}_i^2 \tag{2.58c}$$

$$V(q) = \sum_i v_1(q_i) + \sum_i \sum_{j>i} v_2(q_i, q_j) + \sum_i \sum_{j>i} \sum_{k>j} v_3(q_i, q_j, q_k) + \dots \tag{2.58d}$$

where K represents the kinetic term (2.58c) and V potential (2.58d), divided into terms depending on the coordinates of individual atoms, pairs, triplets, and so on.

The equation of motion for a system of atoms of mass m_i with Cartesian coordinates $\mathbf{r}_i$ becomes:

$$f_i = m_i \ddot{\mathbf{r}}_i \tag{2.59}$$

$$f_i = \nabla_{\mathbf{r}_i} \mathcal{L} = -\nabla_{\mathbf{r}_i} V \tag{2.60}$$

where f_i is the force applied on the ith atom, or in the case of the center of mass, represents the total force on molecule i. This system of differential equations (Eq.2.60) can be numerically solved at time intervals Δt small enough to conserve the thermodynamic quantity in the selected simulation ensemble when the interaction potentials are continuous with a continuous first derivative. The value of the integration in-

terval depends on the interaction potential employed and the mass of the particles. When the resultant of the forces acting on the particles is greater, it is obvious that the integration interval Δt must be smaller, as particles with a smaller mass will move faster. The generalized momentum p_k conjugate with q_k is defined as

$$p_k = \frac{\partial \mathcal{L}}{\partial \dot{q}_k} \tag{2.61}$$

The momenta feature in the Hamiltonian form of the equations of motion

$$\dot{q}_k = \frac{\partial \mathcal{H}}{\partial p_k} \tag{2.62}$$

$$\dot{p}_k = -\frac{\partial \mathcal{H}}{\partial q_k} \tag{2.63}$$

The Hamiltonian is strictly defined by the equation:

$$\mathcal{H}(\mathbf{p}, \mathbf{q}) = \sum_k \dot{q}_k p_k - \mathcal{L}(q, \dot{q}) \tag{2.64}$$

where the velocities $\dot{q}_k$ are written as a function of the momenta $\mathbf{p}$. Being the potential V independent from the velocities, $\mathcal{H}$ is equal to the energy, for Cartesian coordinates, the Hamilton's equations become:

$$\dot{\mathbf{r}}_i = \frac{\mathbf{p}_i}{m_i} \tag{2.65}$$

$$\dot{\mathbf{p}}_i = -\nabla_{\mathbf{r}_i} V = \mathbf{f}_i \tag{2.66}$$

For any set of particles, it is possible to choose six generalized coordinates, changes that correspond to translation and rotation of the center of mass, and, for the system as a whole, changes in the remaining $3N-6$ coordinates involving the motion of the particles relative to one another. If the potential V depends only on the magnitude of particle separations and there aren't applied external fields, then V, $\mathcal{L}$, and $\mathcal{H}$ are manifestly independent of these six generalized coordinates. The corresponding conjugate momenta, in Cartesian coordinates, are the total linear $\mathbf{P}$ and angular $\mathbf{L}$

momentum:

$$\mathbf{P} = \sum_i \mathbf{p}_i \tag{2.67}$$

$$\mathbf{L} = \sum_i \mathbf{r}_i \times \mathbf{p}_i = \sum_i m_i \mathbf{r}_i \times \dot{\mathbf{r}}_i \tag{2.68}$$

where the origin of the Cartesian axes corresponds with the center of mass of the systems. For completely isolated molecules, these quantities are conserved, but this situation is difficult to find in a real simulation. A more general criterion for the conservation of these laws is provided by symmetry considerations: if the system is invariant for translation, the corresponding momentum component is conserved, if the system is invariant for rotation about an axis, the corresponding angular momentum is conserved. The translation invariance is preserved in the case of periodic boundary conditions (PBC), and thus the total linear momentum $\mathbf{P}$ is conserved. Assuming that the Hamiltonian is stationary the total derivative $\dot{\mathcal{H}}$ results:

$$\frac{d}{dt}\mathcal{H} = \sum_k \left(\frac{\partial \mathcal{H}}{\partial q_k} \dot{q}_k + \frac{\partial \mathcal{H}}{\partial p_k} \dot{p}_k \right) \tag{2.69}$$

Hence the Hamiltonian constitutes a constant of the motion. This energy conservation law applies whether or not an external potential exists; the essential condition is that no explicit time-dependent or velocity-dependent forces act on the system. The second point concerning the equation of motion is that time-reversible; changing the signs of all momenta makes it possible to retrace the molecular trajectory.

The system of differential equations(2.60) can be numerically solved at time intervals Δt if the interaction potentials are of class C1. The value of Δt, as mention before, is determined by the interaction potential and the mass of the particles. For the numerical resolution of equations of motion, there are two major categories of algorithms: predictor-corrector and Verlet-type methods. Predictor-corrector algorithms are expensive because they need to calculate up to the fourth derivative with respect to time. However, they integrate the equations of motion with great precision but some times they show instability. Algorithms of the Verlet type utilize only the second derivative, resulting in less precision but greater stability. To be

clear, accuracy refers to the conservation of energy between two successive steps of integration, whereas stability refers to the capacity of an algorithm to integrate without drifts in the propagation of motion invariants. Verlet algorithms, except for the velocity Verlet formulation, are not self-starting hence it is necessary to initialize the velocities using a Taylor series expansion. According to the ergodic theorem, for sufficiently long intervals of time, the averages calculated on time sequences and those calculated in phase space coincide.

$$< x >_{NVE} = < x >_t = \lim_{t\to\infty} \frac{1}{T_s} \int_0^{T_s} dt x(t) \tag{2.70}$$

where T_s is the time of simulation. For the ergodic hypothesis to be satisfied, the system must explore the whole phase space; hence, it is desirable to employ the largest time step compatible with the forces acting on the particles.

The Born-Oppenheimer Molecular Dynamics In order to introduce the electronic structure into simulations of classical molecular dynamics, the electronic Hamiltonian must be solved for each nuclear configuration whose temporal evolution is defined by the equations of motion. This method, known as Born-Oppenheimer molecular dynamics, is only one of several ways to incorporate electronic structure into MD simulations.

The trajectory is obtained by solving the electronic problem for a given nuclear configuration, the forces acting on the nuclei are determined, and the nuclei move according to the equation $\mathbf{F} = M\ddot{\mathbf{R}}$, resulting in a new nuclear configuration for which the electronic problem must be solved in a self-consistent way. This implies that the time dependency is a consequence of the nuclear motion and not an intrinsic property.

The Born-Oppenheimer MD is fully described by the following system of equations

$$M_J \ddot{\mathbf{R}}_J(t) = -\nabla_J \min_{\Psi_0} \langle \Psi_0 | \mathcal{H}_e | \Psi_0 \rangle , \tag{2.71}$$

$$E_0 \Psi_0 = \mathcal{H}_e \Psi_0 \tag{2.72}$$

minimum $\langle H \rangle_e$ must be achieved in each step of a Born-Oppenheimer molecular dynamics propagation, resulting in an increase in computational cost.

Car-Parinello molecular dynamics The "Best of all Worlds Methods" [8] should: (i)integrate the equation of motion on the long time scale set by nuclear motion, (ii) intrinsically take advantage of the smooth time evolution of the dynamically evolving electronic subsystem as much as possible. The second point permits avoiding explicit diagonalization or minimization in order to tackle the electronic structure problem iteratively before the next stage in molecular dynamics.

Car-Parinello molecular dynamics is an effective solution that automatically satisfies condition (ii) and provides an acceptable time step length compromise (i). The Car-Parinello approach takes direct advantage of the quantum-mechanical adiabatic time scale separation between fast electronic (quantum) and slow nuclear (classical) motion. In order to transfer the two-component quantum/classical problem onto a two-component classical problem with two distinct energy scales, the physical time information of the quantum subsystem dynamics must be sacrificed. The energy of the electronic system $\langle \Psi_0 | \mathcal{H}_e | \Psi_0 \rangle$ is clearly a function of the nuclear position $\mathbf{R}$, but it "may" also be considered a function of the wave function Ψ_0 and, by extension, of the orbitals u_i employed to construct this wave function (i.e. a Slater determinant). In classical mechanics, the force on the nuclei is derived from the Lagrangian derivative relative to the nuclear locations. This suggests that, given an appropriately determined Lagrangian, a functional derivative with respect to the orbitals, which are regarded as classical fields, might deliver the correct force on the orbitals. Under these fundamental observations Car and Parrinello introduce the following class of extended Lagrangians

$$\mathcal{L}_{CP} = \underbrace{\sum_I \frac{1}{2} M_I \dot{\mathbf{R}}_I^2 + \sum_i \mu \langle \dot{u}_i | \dot{u}_i \rangle}_{\text{Kinetic energy}} - \underbrace{\langle \Psi_0 | \mathcal{H}_e | \Psi_0 \rangle}_{\text{potential energy}} + \underbrace{\text{constraints}}_{\text{orthonormality}} \tag{2.73}$$

The corresponding Newtonian equations of motion are obtained from the associated

Euler-Lagrange equations

$$\frac{d}{dt}\frac{\partial \mathcal{L}}{\partial \dot{\mathbf{R}}_I} = \frac{\partial \mathcal{L}}{\partial \mathbf{R}_I} \tag{2.74}$$

$$\frac{d}{dt}\frac{\delta \mathcal{L}}{\delta \dot{u}_i} = \frac{\delta \mathcal{L}}{\delta u_i} \tag{2.75}$$

similar to classical mechanics, but applied to nuclear position and orbitals. The general Car-Parinello equations of motion have been discovered to be

$$M_I \ddot{\mathbf{R}}_I(t) = -\frac{\partial}{\partial \mathbf{R}_I} \langle \Psi_0 | \, \mathcal{H}_e \, | \Psi_0 \rangle + \frac{\partial}{\partial \mathbf{R}_I} \text{ constraints } (u_i, \mathbf{R}_I) \tag{2.76}$$

$$\mu \ddot{u}_i(t) = -\frac{\delta}{\delta u_i} \langle \Psi_0 | \, \mathcal{H}_e \, | \Psi_0 \rangle + \frac{\delta}{\delta u_i} \text{ constraints } (u_i, \mathbf{R}_I) \tag{2.77}$$

where μ represents the fictitious mass. In general, these constraints are a function of the set of orbitals u_i and of the nuclear positions $\mathbf{R}_I$.Both of these dependencies must be correctly considered while obtaining the Car-Parinello equations in order to produce an energy-conserving dynamical evolution. For the specific case of one-particle Hamiltonians, such as those coming from Kohn-Sham theory in conjunction with position-independent constraints, the Lagrangian $\mathcal{L}_{CP}$ is simplified, and the corresponding equations of motion result

$$M_I \ddot{\mathbf{R}}_I(t) = -\nabla_I \langle \Psi_0 | \, H_e^{KS} \, | \Psi_0 \rangle \tag{2.78}$$

$$\mu \ddot{u}_i(t) = -H_e^{KS} u_i + \sum_j \Lambda_{ij} u_j \tag{2.79}$$

where the proper orbital orthonormality ($\delta_{ij} = \langle \phi_i | \phi_j \rangle$) must be imposed by Lagrange multipliers Λ_{ij} All constraints inherent in a generic Lagrangian (Eq.2.73) lead to associated constraint forces in the equation of motion due to their derivatives, such as the term $\sum_j \Lambda_{ij} u_j$.

The CP method is essentially an extended Lagrangian MD scheme in which the electronic degrees of freedom are treated as fictitious dynamical variables and propagated along the nuclear degrees of freedom; CP calculations are often performed in a plane wave basis set. The ADMP method[25–27] is an alternative to the original

Car-Parinello method in which atom-center Gaussian orbitals are propagated along nuclear degrees of freedom. Compared to the plane wave basis, fewer Gaussians are required to achieve the desired precision since they are localized in regions of higher electron density and move with the nuclei. On an orthonormal basis, the extended Lagrangian for the system is

$$\mathcal{L} = \frac{1}{2}Tr\left(\mathbf{V}^T\mathbf{M}\mathbf{V}\right) + \frac{1}{2}Tr(\mathbf{W}\mathbf{W}) - E(\mathbf{R},\mathbf{P}) - Tr[\mathbf{\Lambda}(\mathbf{P}\mathbf{P}-\mathbf{P})] \tag{2.80}$$

where $\mathbf{M}$, $\mathbf{R}$ and $\mathbf{V}$ are the nuclear masses, positions and velocities respectively. The density matrix and density matrix of velocities are $\mathbf{P}$ and $\mathbf{W}$ respectively. Constraints on the total number of electrons (N_e) and on the idempotent of the density matrix are imposed using the Lagrangian multiplier matrix Λ. The ADMP method is implemented in the Gaussian suite of programs[28].

Metadynamics The findings of an MD simulation are only useful if the simulation run is long enough for the system to visit all energetically relevant configurations, or if the system is ergodic in the simulation period. This is not always the case in practical circumstances. High free-energy barriers may separate relevant configurations, which is a common source of difficulty. In such a circumstance, the transition from one metastable state to another is only possible if triggered by those infrequent fluctuations that take the system beyond its free energy barriers. Another possibility is that the system diffuses in configuration space incredibly slowly. Under these circumstances, obtaining appropriate statistics demands an excessive amount of computer time. Metadynamics[29] refers to a set of techniques in which sampling is facilitated by the introduction of an additional bias potential (or force) that acts on a chosen number of degrees of freedom, sometimes known as collective variables (CVs).

In metadynamics, an external, CV-dependent, history-dependent bias potential is added to the Hamiltonian of the system. This potential can be expressed as the sum of Gaussians deposited along the route of the system in the CVs space to dissuade the system from returning previously sampled configurations. During an MD simulation, the bias was continually applied using an extended Lagrangian

formalism or by operating directly on the microscopic coordinates of the system. Let S be a collection of d functions of the system's microscopic coordinates R:

$$S(R) = S_1(R) \dots S_d(R) \tag{2.81}$$

At time t, the metadynamics bias potential can be written as:

$$V_G(S,t) = \int dt' \omega \exp\left(-\frac{\sum_{i=1}^{d} (S_i(R) - S_i(R(t')))^2}{2\sigma_i^2} \right) \tag{2.82}$$

where ω is an energy rate and σ_i is the width of the Gaussian for the i-th CV. The energy rate $\omega = \frac{W}{\tau_G}$ is constant and usually expressed in terms of a Gaussian height W and a deposition stride τ_G. Frequently, interesting free-energy landscapes have multiple local minima. If the free-energy differences between these minima are of the order of a few $k_B T$, they may all be relevant. However, if they are separated by a high saddle point in the free-energy landscape (i.e. a low probability region), then the transition between them will take a long period, and these minima will correspond to metastable states. In simulations at finite temperature, it is typically of interest to analyze both the absolute minimum and the local minima that are separated by barriers of varying amplitudes. Instead, as time passes, Gaussians are deposited in the metadynamics simulation, forcing the underlying bias potential to develop until the system is driven out of the initial basin and into a new local minimum. Passing the lowest barrier and falling into the left basin is the simplest and most natural escape path. Here, the Gaussian accumulation begins once more. The system diffuses in the region between the first two minima at this time. When all of the basins are compensated by the bias potential, the system evolves according to a random walk on the flattened FES. The bias potential V_G offers an unbiased estimate of the underlying free energy

$$V_G(S, t_\infty) = -F(S) + C \tag{2.83}$$

$$F(S) = -\frac{1}{\beta} \ln \left(\int dR \delta(S - S(R)) \exp(-\beta U(R)) \right) \tag{2.84}$$

where C is an additive constant and F(S) is the free energy. In contrast to umbrella sampling, metadynamics naturally investigates low free-energy regions first.

Ubrella Sampling The umbrella sampling is another approach for transitioning from one minimum to another that may require an unrealistic timescale for MD. If the shape of the potential energy surface $P(s)$ is a function of one or more collective variables (CV) that were known beforehand, it would be possible to explore all possible metastable states using MD simulation by simply applying an external potential. The biased surface will be flat and barrier-free, this potential functions act as an "umbrella" that allows overcoming the barriers.

However, it is almost impossible to predict the potential energy surface beforehand. Due to this, umbrella sampling is frequently employed in a slightly different manner. Considering a generic reaction as an example, it is impossible to know the position of the barriers in advance. However, through chemical intuition, one can estimate the reaction coordinate and the energy involved (in terms of k_BT). To promote the sampling of the surface nearby to the transition state, it would suffice to add a harmonic constraint to the CV of the type

$$V(s) = \frac{1}{2}k(s - s_0)^2 \tag{2.85}$$

where s_0 is the reference value of the collective variable and the value of the constant is generally set as $k \approx \frac{k_BT}{\sigma^2_{CV}}$. The sampled distribution will be

$$P'(q) \propto P(Q) \exp\left(-\frac{k(s - s_0)^2}{2k_BT}\right) \tag{2.86}$$

For large values of k, only sites near s_0 will be investigated. Adding such a restriction makes it obvious how one might limit the system to explore only a predefined region of space. By combining simulations performed with different values of s_0, one could generate a continuous series of simulations covering the transition state from one minimum to the next.

THIS PAGE INTENTIONALLY LEFT BLANK

Chapter 3

The Brandi Guarna reaction

The Brandi-Guarna rearrangement[30,31] of 5-spirocyclopropane isoxazolidines (**A**) has been widely applied in the synthesis of polycyclic heterocycles and natural products (Scheme 3.20).[32–35] It consists of a thermal induced ring opening of isoxazolidines (**A**) leading to the formation of tetrahydropyridones (**B**) (Scheme 3.1). This type of skeleton, i.e. a piperidine ring-containing framework, is widely diffuse in alkaloids and bioactive molecules,[36–41] for recent applications of the Brandi-Guarna rearrangement see ref.[42–47]. Despite the Brandi-Guarna rearrangement is quite selective, in a few cases the main product (**B**) is accompanied by a side product, i.e. an open chain isomer (**C**) featuring an enaminone moiety. The process is believed to occur through a homolytic cleavage of the N-O bond of isoxazolidines (**A**) followed by the cleavage of one of the cyclopropane vicinal bonds and intramolecular coupling of diradical intermediate. Furthermore, the formation of the side product (**C**) is generally explained by a [1,5]-H shift, from the CHR′ carbon leading to imine that in turn tautomerizes to enamine (**C**).[48]

Recent experimental results showed that the thermal rearrangement of two epimeric 5-spirocyclopropane isoxazolidine derivatives affords the piperidinone and enaminone products in different ratio.[47] How the diastereomeric environment influences the competitive formation of the cyclic and the open chain product is not easy to be rationalized. A computational investigation of both competitive avenues of the rearrangement process has been conducted in order to gain important information and provide a correct interpretation of the apparent remote influence of the stereo-

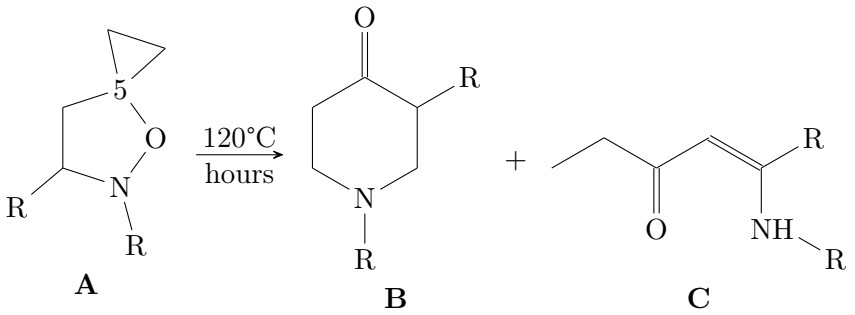

Scheme 3.1: Thermal rearrangement of 5-spirocyclopropane isoxazolidines (**a**) leading to tetrahydropyridones (**B**) and enaminones (**C**)

chemical environment on favoring the distinct pathways.

The second aspect that must be examined is the reaction that leads to the formation of of the isoxazolidines (**A**). Indeed, the BG rearrangement is made possible by the presence in the isoxazolidines (**A**) of a strained oxyspirocyclopropane moiety where the oxygen is linked to a nitrogen with a bond that is easily cleaved under thermal activation[49,50]. Isoxazolidines (**A**) find their origin in a 1,3-dipolar cycloaddition (1,3-DC) of nitrones with methylenecyclopropane (MCP, Scheme 3.2).[51–53] MCP is a rather volatile alkene, commercially available, that, despite its strained

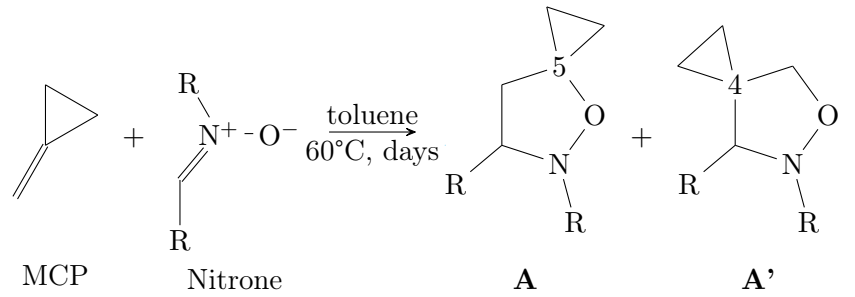

Scheme 3.2: 1,3 DC between MethilenCycloPropane and nitrone, leading to the formation of 5-spirocyclopropane isoxazolidines (**a**) and 4-pirocyclopropane isoxazolidines(**A'**)

nature, results rather sluggish in its reactivity with nitrones. The cycloaddition process requires heating above 60 °C, the length of the reaction takes several days according to the substituent groups of the nitrone, . The same occurs in the cycloaddition of nitrones with 1-alkyl- or 1,1-dialkyl substituted alkenes that results even more slow.[54] This fact should not surprise knowing the nature of nitrones as electron neutral dipoles (Sustmann's classification)[55] and of dipolarophiles missing any activating electron-withdrawing group. However, the similarities of MCP with

these alkenes ends at this point, because as regards as regioselectivity the behavior of MCP is rather different from a normal 1-alkyl- or 1,1-dialkyl substituted alkene. Indeed, whereas a dipolarophile like isobutene (Scheme 3.3), which is the alkene with the highest similarity to MCP, reacts with nitrone to give exclusively one adduct, i.e. the 5,5-disubstituted isoxazolidine (**F**)[56] MCP generally affords a mixture of regioisomers where the 5-spirocyclopropane isoxazolidine (**A**) is the major (the ratio is approximately 2:1), but not the exclusive cycloadduct, as shown in the examples of Scheme 3.2.[57,58]

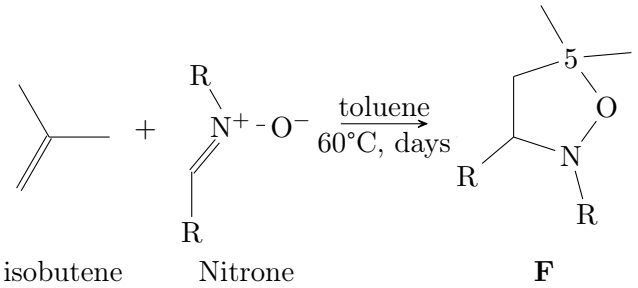

Scheme 3.3: 1,3 DC between isobutene and nitrone, leading to the formation of 5,5-dimethylisoxazolidine(**F**)

It is rather evident the awkwardness of this result as regard to the application of this process in function of the successive thermal rearrangement or β-lactam synthesis. In fact, regioisomeric 4-spirocyclopropane isoxazolidines(**A'**, Scheme 3.2), lacking the oxyspirocyclopropane moiety, are not able to undergo any useful rearrangement. However, the unexpected lack of regioselectivity in 1,3-DC of MCP rises several questions about the nature of its double bond and its resemblance with a simple alkene. More concerns are added if we consider the cycloaddition to another similar alkene, methylenecyclobutane (MCB, Scheme 3.4), where a cyclobutane replaces the cyclopropane ring[59]. If we assume that the strain energy of the ring has a role in the regioselectivity of the cycloaddition a similar result for MCP and MCB should be expected. Indeed, the cycloaddition with MCB affords exclusively regioisomer substitued with the cyclobutane on 5 (**G**), analogously to the regioselectivity obtained with isobutene . This data makes clear that there must be a "cyclopropylidene effect" in the 1,3-DC with nitrones to justify the observed lack of high regioselectivity. The 1,3-DC reaction mechanism has been computationally

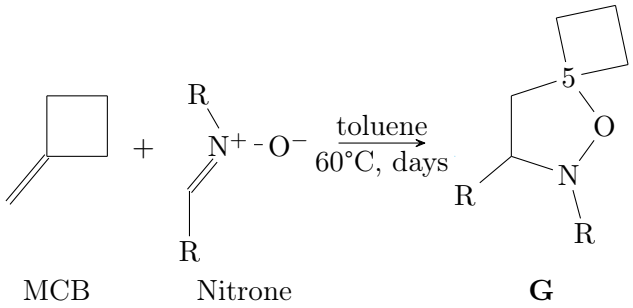

MCB Nitrone **G**

Scheme 3.4: 1,3 DC between MethilenCycloButane and nitrone, leading to the formation of 5-spirocyclobutane isoxazolidines (**G**)

investigated with DFT and post-HF methods; it consists of a concerted, frequently asynchronous, pericyclic cycloaddition mechanism.[60]

The Brandi-Gaurna reaction is therefore investigated computationally on two levels. The first purpose is to explore the lack of regioselectivity in the synthesis of 5-spirocyclopropane isoxazolidines (Scheme 3.2) and the possibility of a cyclopropylidene effect. The second objective is to characterize the reaction mechanism of the thermally induced ring opening of isoxazolidines (**A**, Scheme 3.1) and to explain the differing yields in the synthesis of piridone and enamminone.

The results that led to the full characterization of the molecular mechanisms underlying the Brandi-Guarna reaction are discussed in great detail in the following paragraphs. In anticipation of the conclusions, this study has shown, with regard to the first point, that the "cyclopropylidene effect" is produced by the electronic influence of the alkene substituents, which determines a polarization of the alkene double bond that favors the relative orientation of the reactants, thereby producing the observed regioselectivity of the cycloadditions.

The main result of the computational investigation of the Brandi-Guarna reaction is that two distinct routes involving the homolitic cleavage of each of the two CC bonds of the spiroclycopropyl moiety branch off from the first intermediate. These two CC bonds are not equivalent: one path involves the cleavage of the α cyclopropane bond and leads to the synthesis of enaminone (**B**), while the other involves the cleavage of the β bond and results in the formation of indolizidinone (**A**).This study indicates that the outcome of the rearrangement does not depend on a late step, such as the propensity to close the six-membered ring, but rather on

the second step, i.e. the competitive cleavage of the diastereotopic α and β bonds of the cyclopropane ring.

3.1 Computational Details

The reaction mechanisms of the 1,3DC have been characterized by performing DFT calculations at PBE0/6-311++G(d,p)[61–64] level of theory including the Grimme's empirical dispersion1 (GD3) with the Gaussian suite of programs.[65,66] Due to the di-radical nature of the Brandi Guarna reaction, all the calculations have been performed using the unrestricted B3LYP exchange-correlation functional[67,68] along with the 6-31G(d,p) or the 6-311++G(d,p) basis sets. The choice of this level of theory is justified by the fact that we started with Ochoa's work, which utilized the functional UB3LYP in conjunction with a 6-31G* basis set.[69] In addition, the correspondence between stationary points obtained at the UPBE0 and UB3LYP levels of theory was verified. In both reactions, Transition States (TS), pre-reactive minima, and products have been located through geometry optimization calculations with very tight convergence criteria. The QST2[70] or QST3[71] algorithms have been adopted to determine the transition states. All the Hessian eigenvalues are positive for the pre-reactive minima and products, while only one negative eigenvalue has been obtained for the TS. The eigenvector, corresponding to the negative eigenvalue, describes the displacements along the formed C-C and C-O bonds, providing insights on the concerted reaction mechanism. The transition states have been adopted as starting points for a series of IRC (intrinsic reaction coordinates) calculations[72] using either the Hessian based predictor-corrector integrator (HPC)[73,74] or the local quadratic approximation (LQA).[75,76] Different analyses have been carried out to describe the behavior of alkenes with nitrone and to understand the "cyclopropylidene effect". The characterization of the stationary points allows determining the energy gaps between the TS and reagents or products, to assess any possible kinetic control of the reaction and the balance between the products. The electronic effects of the alkyl substituent on the alkenes have been investigated by the value and the orientation of the dipole moment on the reagents and through the determination of

the ESP atomic charges.[77] To further support the electronic structure analysis, a comparison between the ESP atomic charges and those obtained through the CM5[78] and NPA[79,80] methods has been reported in the Appendix A (Table A.1-Table A.7). The kinetic constants of the reactions have been calculated using the Eyring transition state theory.[81–83] The results allowed a comparison of the kinetic parameters for the two different orientations of the alkenes and to explain the different experimental yields. In the characterization of the BG reaction the solvent effect has been taken into account computing its contribution to the energy of the stationary points by Polarizable Continuum Model calculations[84] adopting as solvent toluene. To characterize the electronic structure rearrangement during the reaction mechanism, the electronic localization has been computed using the electron localization scheme proposed by Boys[85] at the B3LYP/sdall level of theory.

For the studied systems, the expression of the kinetic constant $k(T)$ in the Eyring approximation is simplified, treating the reagents in the pre-reactive minimum as single molecular complex, and the results

$$k(t) = \frac{k_B T}{h} \frac{Q^{\neq}_{TS}}{Q_{GS}} e^{-\frac{\Delta E}{k_B T}} \tag{3.1}$$

where k_B is the Boltzmann constant, T the temperature, h the Planck constant and ΔE is the energy gap (zero-point energy included). The two functions are the product of vibrational and rotational partition functions for the transition state $Q^{\neq}_{TS}$ and ground state Q_{GS}. The kinetic constants have been calculated for the experimental reaction temperature range between 300 K and 400 K. All calculations were performed using the Gaussian suite of programs (G16, G09).[60,86]

3.2 The cyclopropylidene effect

The 1,3-DC between nitrones and alkenes is a well-known transformation leading to isoxazolidines (Scheme 3.5). The reaction mechanism is affected by the electrostatic interaction between the nitrone and the alkenes. Alkyl substituents are electron-donating groups (EDG) and increase the electron density of the double bond trough

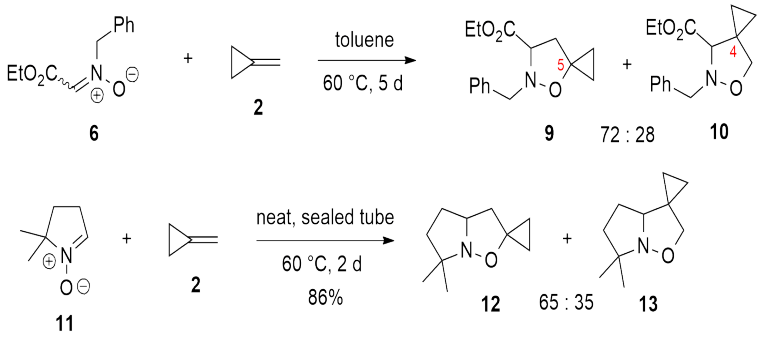

Scheme 3.5: 1,3-DC of nitrones **6** and **11** with MCP (**2**)

an inductive donating effect. To gain a further insight, we have also considered an electron-attractor group (EWG) as a substituent: an ester group. His effect is to increase the negative charge on carbon C_α depleting the electron density over the double bond. Another possible effect is the polarization of the alkene double bond given by the high dipole moment on the nitrone. The regioselectivity of the 1,3-DCs,

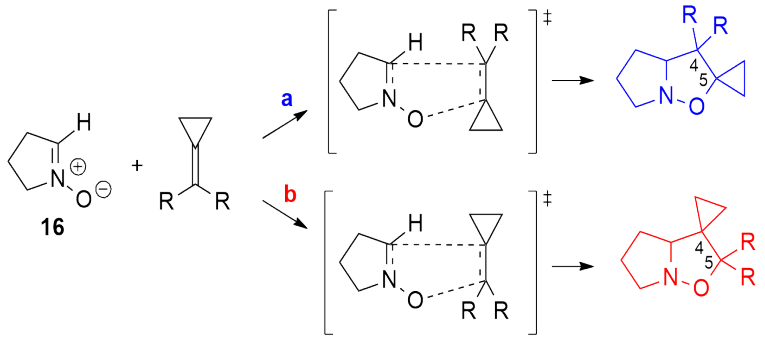

Scheme 3.6: Transition states originated from different paths a and b leading to regioisomeric cycloadducts.

i.e. the relative orientation of the substituted alkene to the nitrone in the TS, is influenced by the effect of the substituents on the dipolarophile. For this reason, we have considered two alkene orientations to explain the different selectivities for the studied reactions: the orientation labelled **a** leads to the product with the cyclopropane (or the cycloalkane) in position 5; label **b** refers to the orientation of the alkenes leading to the regioisomer spirofused in 4 (Scheme 3.6).

The choice of a five-membered cyclic nitrone (**16**) for the study is justified by the copious literature available for the cycloadditions of cyclopropylidene dipolarophiles with this class of nitrones.[58,87] In addition, nitrone featuring a defined configuration

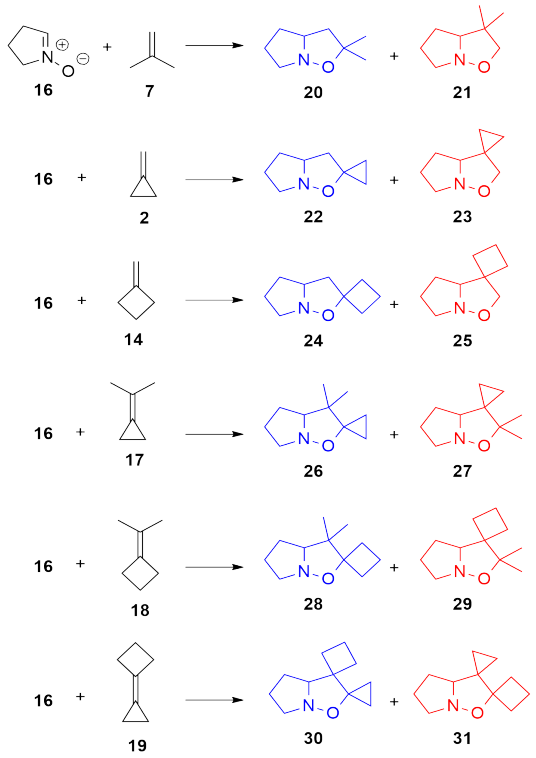

Scheme 3.7: Reactions studied trought DFT calculations of PBE0/6-311G(d,p)-GD3 level of theory.

eliminates the E,Z-configuration variable that should be considered in the case of acyclic nitrones. Seven substituted dipolarophiles have been analysed to investigate the electronic effect of the substituents (Scheme 3.7): isobutene (**7**), methylenecyclopropane (MCP, **2**), methylenecyclobutane (MCB, **14**), isopropylidenecyclopropane (ICP, **17**), isopropylidenecyclobutane (ICB, **18**), ciclobutylideneciclopropane (CPCB, **19**).

3.2.1 Isobutene

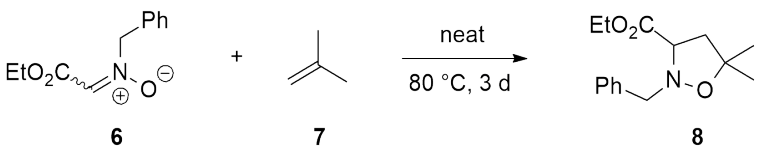

Scheme 3.8: 1,3-DC of nitrone **6** with isobutene (**7**)

The 1,3-DC of a nitrone with isobutene (**7**) experimentally gives one single regioisomer, **9** i.e. the 5,5-dimethyl substituted isoxazolidine (see, structure 8 in

Scheme 3.8).

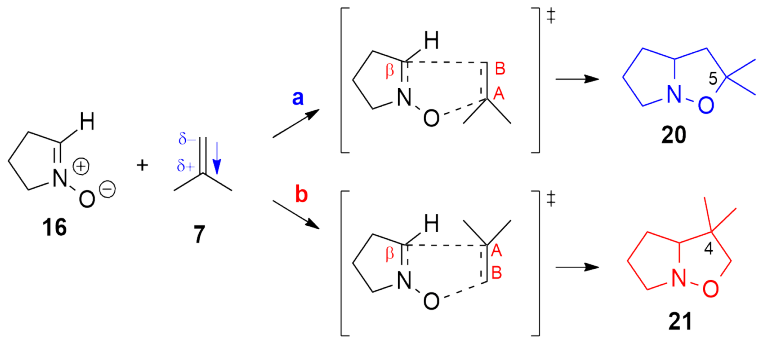

Scheme 3.9: 1,3-DC between isobutene **7** and nitrone **16**, the orientation **a** leads to the 5,5-dimethylisoxazolidine **20**, and orientation **b** leads to the 4,4-dimethylisoxazolidine **21**. The dipole moment on **7** is oriented toward the dimethyl group.

The reaction paths obtained by the computational analysis on regioisomers **20** and **21** (Scheme 3.9) suggest an explanation for such regioselectivity. The path a of the 1,3-DC with the isobutene **7** leads to the formation of isoxazolidine **20** substituted with two methyl groups on position 5. This arrangement of the reagents has a lower activation energy ($\Delta E_{TS}(\mathbf{a}-\mathbf{b}) = -18.0\text{kJ/mol}$) and the product **20** results more stable than isoxazolidine **21** (path **b**) (Table A.8).

The analysis of the ESP charges has evidenced that the two methyl groups determine a positive charge on the C_A carbon (0.469) and a charge transfer toward the C_B (-0.737) of the isobutene (Scheme 3.9, Table A.9). This charge distribution on the isobutene corresponds to the dipole moment of 0.59 D, which lies on the $C_A - -C_B$ bond and is oriented toward the EDG groups. In the pre-reactive minimum, the nitrone dipole further increases the polarization of isobutene, as evidenced by the charges of the carbons C_A and C_B reported in Table A.16. The reaction mechanism is favoured by the **a**-arrangement of the reactants because the carbon C_A involved into the attack of the nitrone oxygen is positive (0.506). The polarization effect given by the nitrone in the **b**-orientation determines instead a negative charge on C_B (-0.748) that makes the attack of nitrone oxygen less favoured (Scheme 3.9). Therefore, the charge distribution and orientation of the alkene's dipole moment justify the kinetic ratio calculated at the experimental temperature with the Eyring's equation ($k_{\mathbf{a/b}} = 114.4$ at 350 K) and indicate the 5,5-disubstituted isoxazolidine 20 as the favourite

product of the 1,3-DC.

3.2.2 Methylenecyclopropane and Methylenecyclobutane

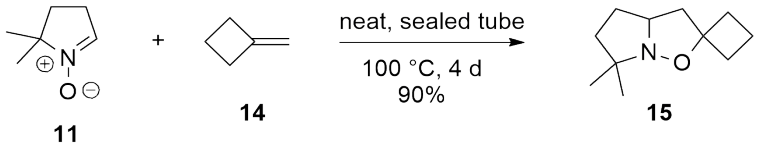

Scheme 3.10: 1,3-DC of nitrone **11** with MCB (**14**)

The comparison of cycloaddition of nitrone 11 with methylenecyclopropane (**2**, MCP) and methylenecyclobutane (**14**, MCB) is rather interesting as the first leads experimentally to the formation of a mixture of regioisomers roughly 65:35, where the major is the 5-spiro fused isoxazolidine **12**, whereas MCB affords exclusively the 5-spiro fused isoxazolidine **15** (Scheme 3.5 and Scheme 3.10).

At a first glance, this difference is surprising since it contrasts with the apparent similarity of the two dipolarophiles. The computational analysis, indeed, infers an explanation for this different reactivity.

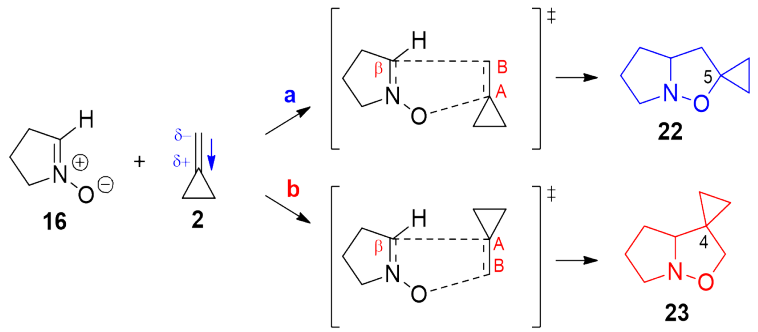

Scheme 3.11: 1,3 DC between MCP (2) and nitrone 16. Orientation **a** leads to isoxazolidine 22, and orientation **b** leads to isoxazolidine 23. The dipole moment on 2 is oriented toward the cyclopropane.

The difference in activation energy between the TS of the two chosen orientations (**a**, **b**) of the MCP is moderate ($\Delta E_{TS}(\mathbf{a}-\mathbf{b}) = -7.7$ kJ/mol, Table A.10). The orientation **a** (Scheme 3.11) is favoured and leads to 5-spirocyclopropane isoxazolidine **22**, which is also more stable than the isomeric 4-spirocyclopropane **23** obtained with the b-oriented MCP ($\Delta E(\mathbf{a}-\mathbf{b}) = -10.4$kJ/mol).

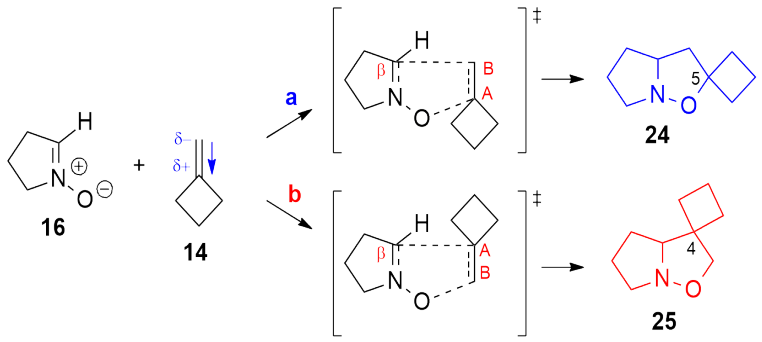

Scheme 3.12: 1,3-DC between MCB 14 and nitrone 16. Orientation a leads to isoxazolidine 24, and orientation **b** leads to isoxazolidine 25. The dipole moment on the alkene is oriented toward the cyclobutane.

The difference in activation energy for the two chosen orientations of MCB is higher than in the previous case ($\Delta E_{TS}(\mathbf{a}-\mathbf{b}) = -15.7$ kJ/mol, Table A.10). Indeed, the orientation **a** results favoured, and leads to the more stable product with the spirocyclobutane in position 5 (**24**) ($\Delta E(\mathbf{a}-\mathbf{b}) = -23.6$kJ/mol) (Scheme 3.12). The inductive effect on the cyclopropane determines a carbon with a positive charge (C_A) and one with a negative charge (C_B, Table A.11). As a proof of this charge distribution on the double bond, the dipole moment on the MCP (0.455 D) is oriented toward the cyclopropane.

In the pre-reactive minima, the polarization of the MCP is increased by the nitrone dipole according to the orientation (Table A.11). The two sp2 carbons (C_A, C_β), as acceptors of electron density, are involved in the bonding at the Transition State (Scheme 3.11). Therefore, the positive charge on C_A (0.147) and the less negative charge on C_β (-0.101) in the a-arrangement favour the reaction outcome (Table A.11).

The inductive effect of the cyclobutane on the double bond of the MCB is greater if compared to the cyclopropane one. Indeed, the dipole moment of the double bond in MCB (0.612 D) lies on the double bond axis and is oriented toward the cyclobutane substituent. The dipole moment of the nitrone increases the polarization of the dipolarophile. The arrangement of the reagents in orientation **a** determines a positive charge on alkene carbon C_A (0.237) and a less negative charge on the nitrone carbon C_β (-0.143), favouring the cycloaddition mechanism (Table A.11, see also Scheme 3.12). Therefore, the computational results for the

1,3-DC of MCP explain the experimental regioselectivity i.e. the obtainment of two regioisomers with a prevalence of the product deriving from orientation **a**. Indeed, the two orientations do not differ greatly in term of activation energy, neither on product stability. The ratio between rate constants obtained for the two orientations ($k_{\mathbf{a/b}} = 5$) (Table A.12) suggests a reduction of the kinetic control of the regioselectivity in this cycloaddition. However, the orientation **a** provides a relatively minor activation energy ($\Delta E_{TS}(\mathbf{a} - \mathbf{b}) = -7.7$ kJ/mol) and the most stable isoxazolidine ($\Delta E(\mathbf{a} - \mathbf{b}) = -10.4$ kJ/mol). Also, the charge distribution on the alkene **2** in the **a**-arrangement suggests that the isoxazolidine **22** with the spirocyclopropane substituent in 5 is the favoured product (Table A.11). In the reaction with MCB instead the ratio between rate constants obtained for the two orientations ($k_{\mathbf{a/b}} = 117$) and the different stability of the two isoxazolidines indicate a kinetic control of the reaction. The analysis of the charge distribution on the double bond of the MCB confirms that the 5-spirocyclobutane isoxazolidine **24**, obtained with the a-arrangement, is the highly favoured product (Table A.12). The different reactivity of MCP and MCB can be therefore explained by the kinetic and electrostatic behaviours in the two reactions. In the 1,3-DC with MCP the lack of regioselectivity is due to a lower EDG effect of the substituent, that leads to the formation of both **22** and **23** products according to the experimental ratio ($\mathbf{a} > \mathbf{b}$).[57,58] Instead, the electronic effect of the cyclobutane determinates a charge distribution over the alkene that is conducive to the formation of the isoxazolidine **24** substituted with the spirocyclobutane on position 5.

3.2.3 Isopropylidenecyclopropane and Isopropylidenecyclobutane

The 1,3-DC between ICP and nitrones experimentally gives one single regioisomer featuring the methyl groups on C-5 of the isoxazolidine ring (Scheme 3.13). This complete regioselectivity can be explained by the different reactivity of the ICP (**17**) in the two studied orientations. Indeed, the computed cycloaddition between the ICP and nitrone **16** shows two reaction paths rather different, according to the ori-

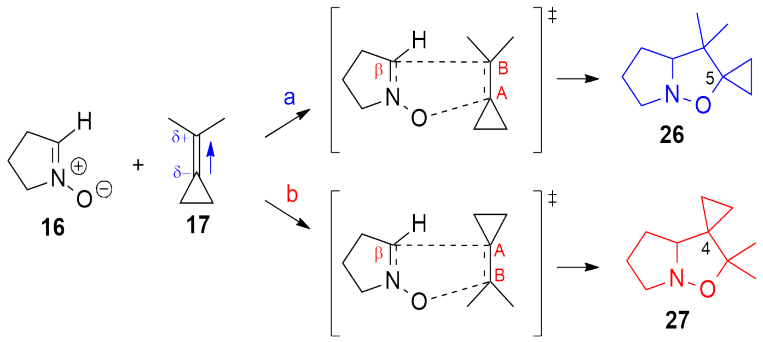

Scheme 3.13: 1,3-DC between ICP and nitrone **16**. Orientation **a** leads to isomer **26**, and orientation **b** leads to isomer **27**. The dipole moment on the alkene is oriented toward the dimethyl group.

entation chosen: the proposed orientation **a** (Scheme 3.13) leads to the isoxazolidine **26** spirofused at C-5 and orientation **b** leads to the isomer **27**.

The arrangement of ICP proposed in orientation **a** has the highest activation energy of the studied reactions (99 kJ/mol v.s. 40-50 kJ/mol). The arrangement of the **b**-oriented ICP determines a sensibly lower activation energy ($\Delta E_{TS}(\mathbf{a}-\mathbf{b}) = 61.5$ kJ/mol) and leads to the more stable isoxazolidine **27**, 12.540 kJ/mol) (Table A.13). This difference in activation energy and the kinetic ratio ($k_{\mathbf{a/b}} = 4.610^{-11}$) indicates a kinetic control of the reaction leading to the formation of one product i.e isomer 27 (Table A.15). All substituents of ICP are EDG groups, the dipole moment of the molecule is quite small (0.167 D) compared to the values of the other alkenes. The dipole lies on the double bond axis and is oriented toward the dimethyl group, which means that the dimethyl provides the bigger EDG contribution to the alkene favouring the formation of **27**. Indeed, in orientation **b** the ICP carbon involved in the intermolecular O-C bond formation, has a small positive charge (0.009) whereas, in the other orientation **a**, the carbon belonging to the cyclopropane ring (C_A) experiences a negative charge (-0.020) (Table A.14).

From these data, it can be concluded that the cycloaddition between nitrone **16** and ICP **17** proceeds through the **b**-oriented TS, which is favoured from a kinetic point of view, and leads to the formation of the more stable product **27**. The ratio of kinetic constants between the orientation **a** and **b** ($k_{\mathbf{a/b}} = 10^{-10}$) (Table A.15) is much lower than 1, confirming that orientation **b** is kinetically much more favoured. These results therefore explain the formation of isoxazolidine **27** as the exclusive

product. Experimental data for the reaction of nitrones with the ICB (**18**) are not available, but this dipolarophile has been studied to evaluate the electronic effect of the two different cycloalkanes in the presence of the dimethyl group.

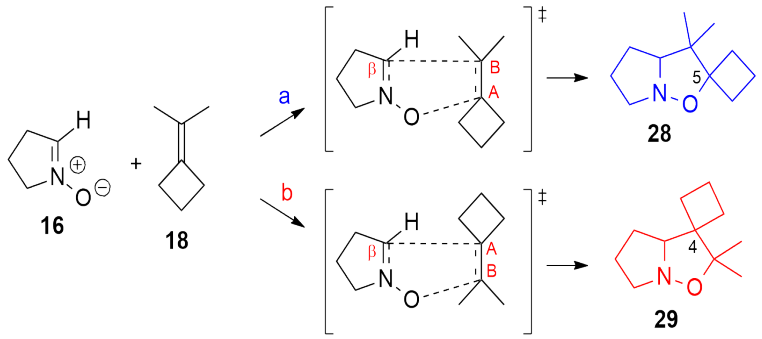

Scheme 3.14: 1,3-DC between ICB and nitrone 16. Orientation **a** leads to isoxazolidine 28, and orientation **b** leads to isomer 29. The dipole moment of 18 is close to zero.

The reaction shows lower differences according to the chosen orientation of the alkene. The difference in activation energy for the two orientations of ICB with nitrone 16 is much lower ($\Delta E_{TS}(\mathbf{a}-\mathbf{b}) = 3.8$ kJ/mol) than the previous case: the orientation **a** (Scheme 3.14) leads to the 5-spirocyclobutane-4,4-dimethyl isoxazolidine 28, while the orientation **b** leads to the more stable 5,5-dimethyl-4-spirocyclobutane isoxazolidine **29** ($\Delta E(\mathbf{a}-\mathbf{b}) = 15.8$ kJ/mol) (Table A.13). As seen in the previous case all substituents of the alkene are EDG groups: the value of the dipole moment (0.011 D) is near to the accuracy of the method, so no consideration can be made about the dipole orientation. However, the polarization induced by nitrone dipole and the EDG effect of the substituents promotes a positive charge on carbon C_B promoting the formation of isomer **29** (Table A.14). Indeed, the kinetic ratio of the reaction ($k_{\mathbf{a/b}} = 610^{-2}$) suggests that the path b is slightly kinetically favoured due to a better charge distribution over the reagents. All together these data indicate that isoxazolidine **29** is only slightly favoured (Table A.15). The compared assessment of reactions of ICP and ICB with nitrone **16** and their full computational analysis has brought about a sharp difference of behaviour of a cyclopropylidene compared to a cyclobutylidene group. Indeed, for the ICB the electronic effect of the dimethyl and cyclobutane are similar, as shown by the dipole moment value.

Instead, the charges on the sp2 carbons (C_A, C_B) on the alkene **17** are de-

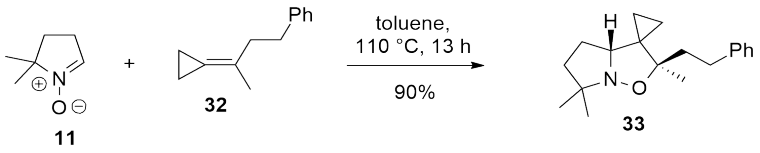

Scheme 3.15: 1,3-DC of nitrone 11 with 32.

termined by the stronger EDG effect of the two methyl groups compared to the cyclopropane, therefore the path b results in a more favourable charge distribution leading to isoxazolidine **27** ($k_{\mathbf{a/b}} = 610^{-10}$). Indeed, cycloaddition of nitrone **11** with **32**, a dipolarophile analogous to ICB, experimentally gives only regioisomer **33**, originating from the **b**-orientation like **27**, in excellent yield (Scheme 3.15).[88]

3.2.4 Cyclobutylidenecyclopropane

The computational study of the reaction of nitrone 16 with CBCP gives a further confirmation of the existence of this "cyclopropylidene effect" experimentally observed.

Scheme 3.16: 1,3-DC of nitrone 34 with CBCP (19).

Experimentally, 1,3-DC of nitrone **34** with CBCP gave exclusively isoxazolidine **35** featuring the cyclopropane ring on position 4 of the isoxazolidine ring (Scheme 3.16).[89]

The difference in activation energy ($\Delta E_{TS}(\mathbf{a}-\mathbf{b}) = -6.9$ kJ/mol) is in favour of the b-oriented alkene, which leads to the isoxazolidine substituted with the cyclobutane on position 5 (isomer **31**) that is also thermodynamically more stable (-9.0 kJ/mol) than the other possible product (isomer **30**) deriving from orientation **a** (Table A.16).

The alkene dipole moment is quite small (0.168 D), since all substituents are EDG groups, and is oriented toward the cyclobutane, due to its greater inductive effect on the molecule. In the a-arrangement the carbon C_A is involved into the formation

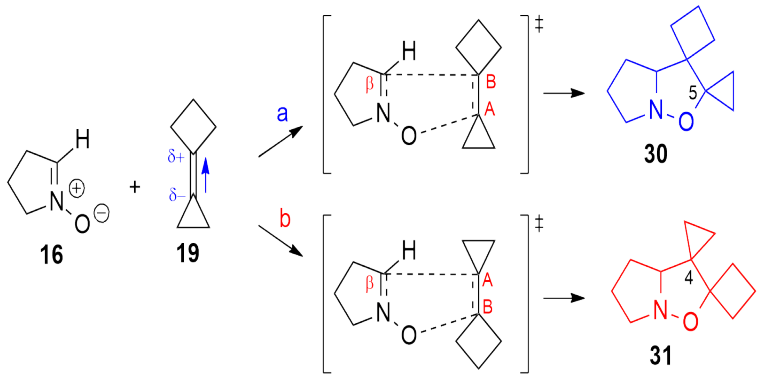

Scheme 3.17: 1,3-DC of **19** with nitrone **16**. Orientation **a** leads to isoxazolidine 30, and orientation **b** leads to isomer **31**. The dipole moment on the alkene is oriented toward the cyclobutane.

of C-O bond, while in the orientation **b** the carbon involved is C_B. As the previous cases, the nitrone dipole polarizes the alkene double bond, increasing the partial charges on the sp2 carbon atoms. The reaction mechanism is therefore favoured in orientation **b** by the positive charge on carbon C_B (0.125, Table A.17). These results and the kinetic ratio of the reaction ($k_{\mathbf{a/b}} = 0.1$) indicate that isoxazolidine **31** is the favoured product in complete agreement with the experimental data (Scheme 3.16).

3.2.5 Cyclopropylideneacetate

We have also investigated the effect of an electron attractor group (EWG), i.e. an ester group, combined with the cyclopropane.

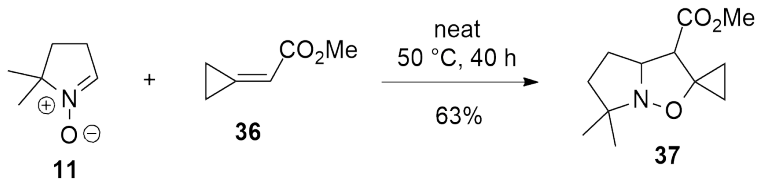

Scheme 3.18: 1,3-DC of cyclopropylideneacetate 36 with nitrone 11.

1,3-DC of nitrones with **36** gives experimentally only isoxazolidines substituted with the spirocyclopropane on position 5, as shown in the example of Scheme 3.18. The outcome of the cycloaddition is therefore inverted respect to the results shown previously. This depends on the electron withdrawing character of the CO_2Me substituent.

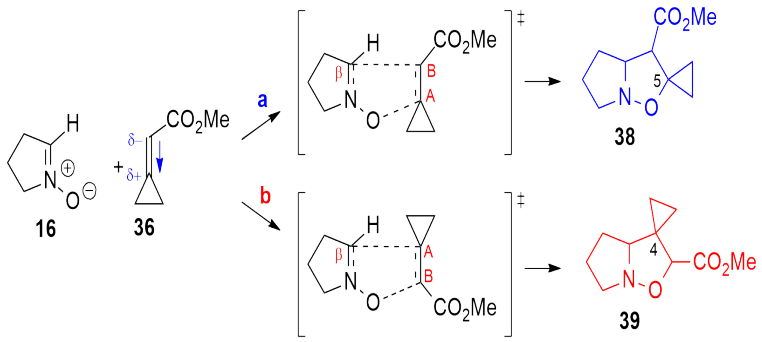

Scheme 3.19: 1,3-DC between cyclopropylideneacetate **36** and nitrone **16**. Orientation a leads to isoxazolidine **38**, and orientation **b** leads to isoxazolidine **39**. The dipole moment on the alkene is oriented toward the cyclopropane.

The alkene is substituted on C_A with the cyclopropane, and on C_B with the carboxymethyl group, therefore the carbon C_A is the β carbon compared to the carbonyl acetate (Scheme 3.19). Both the ester and alkyl group contribute to polarize the double bond increasing the negative charge on C_B (-0.807) and consequently the positive charge on C_A (0.447, Table A.19). Indeed, the resulting dipole moment (3.064 D) is oriented toward the cyclopropane group and his value is higher compared to the previous cases due to the methyl carboxylate effect. In orientation **a**, the positive charge on carbon C_A enhances the attack on the nitrone oxygen (Scheme 3.19). Indeed, this arrangement of the reagents determines the lowest activation energy ($\Delta E(\mathbf{a}-\mathbf{b}) = -14.1$ kJ/mol, Table A.18) and leads to the formation of 5-spirocyclopropane isoxazolidine **38**. The polarization of the double bond and the resultant negative charge on carbon CB make the **b** orientation less favourited. Also, the nitrone dipole moment increases the polarization of the alkene double bond, favouring the charge distribution adopted in orientation **a**. Indeed, the kinetic constant rates ($k_{\mathbf{a/b}} = 123$) obtained with the Eyring equation shows that the isoxazolidine **38** is the kinetic product of the 1,3-DC, in agreement with the experimental data.

3.3 The Brandi-Guarna reaction

The Brandi-Guarna rearrangement (Scheme 3.20) involves the thermally induced ring opening of isoxazolidines, which leads to the synthesis of tetrahydropyridones.

Even though the reaction is quite selective, in a few instances the main product (**2**) is accompanied by a side product, a chain-opening isomer (**3**) containing an enaminone moiety. As mentioned before, it is hypothesized that the process involves the homolytic cleavage of the N-O bond of isoxazolidines (**1**), followed by the cleavage of one of the cyclopropane vicinal bonds and intramolecular coupling of the diradical intermediate (**5**). Moreover, the synthesis of the enaminone (**3**) is commonly explained by a [1,5]-H shift from the CHR′ carbon to the terminal C radical in intermediate (**5**), resulting in imine (**6**), which then tautomerizes to enamine(**3**).[48] In the previous section , the cyclopropilidene effect that leads to the synthesis of

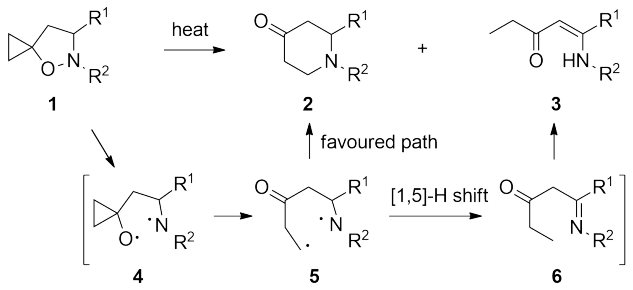

Scheme 3.20: Thermal rearrangement of spirocyclopropane isoxazolidines **1** leading to tetrahydropyridones **2** and enaminones **3**.

4- and 5-spirocyclopropane isoxazolidine was examined in detail. However, it is essential to recall that only the 5-substituted isoxazolidine (**1**) is responsible for the BG reaction. Recent research discovered that thermal activation of the two 5-spiro-cyclo-pro-pane isoxazolidine derivatives results in different yields of piperidinone and enaminone.[47] It is difficult to quantify how the diastereomeric environment influences the competitive growth of cyclic and open-chain products. In fact, the open chain diradical intermediate **5** has lost the majority of its stereochemical constraint; hence, the stereochemical memory at this level is predicted to be lowered. A computational study of both competitive pathways of the rearrangement mechanism was carried out to collect significant information and to provide an accurate evaluation of the apparent remote influence of the stereochemical environment in favoring the distinct pathways.

The rate determining step of the Brandi-Guarna reaction was thorougly analyzed, a few years ago by Ochoa *et al.*[69], using Unrestricted Density Functional

Theory (UDFT) on a series of model spiro-fused isoxazolidines. They analyzed three alternative reaction paths for the cleavage of the N-O e C-C bonds, one concerted and two step-wise. The most energetically favourable was the step-wise mechanism consisting in the homolitic cleavage of two bonds: first the isoxazolidine N-O followed by the cyclopropane C-CH_2. Both intermediates and transition states are radicals, therefore the computational approach which has to be applied in studying these systems is a critical aspect.[90] Performing a comparison with correlated wavefunctions based methods such as QCISD and CCSD(T) on the stationary points, Ochoa et al.[69] showed that UDFT is an adequate computational method to analyze the Brandi-Guarna rearrangment. This computational method has been applied with success in computational studies of organic systems containing radicals and in particular of ring opening reactions.[91,92] Several authors[93–98] have shown that UDFT allows to qualitatively describe chemical reaction mechanisms involving intermediate radical systems, in agreement with both experimental data and calculations at higher level of theory. This allows us to confidently use the same approach of Ochoa et al.[69] in the present study, aimed to the identification of the different reaction paths leading to tetrahydropyridone and enaminone.

3.3.1 Results and Discussion

In the course of studies on the synthesis of bioactive 1,2-dihydroxiindolizidines, the thermal rearrangement of diastereomeric 5-spirocyclopropane isoxazolidines **7a** and **7b** was carried out as an entry to the corresponding indolizidinones **8a** and **8b** (Scheme 3.21).[47] The thermal rearrangement of the two optically pure epimeric isoxazolidines **7a** and **7b** was carried out under the same reaction conditions (toluene, 170° C, sealed vial, in a microwave apparatus, therefore the reaction occurs at constant volume) and led to the expected indolizidinones **8a** and **8b**, in 71% and 25% yields, respectively, along with minor amounts of enaminone **9** in 4% and 18% yields, respectively.[99] A similar trend is observed for analogous isoxazolidines featuring a 3'-ethoxycarbonyl- in place of the 3'-hydroxymethyl group. However in these cases the thermal isomerization of several stereocentres does not allow a clear-cut analysis.[100] It is worth noting that enaminones are compounds much more fragile than the

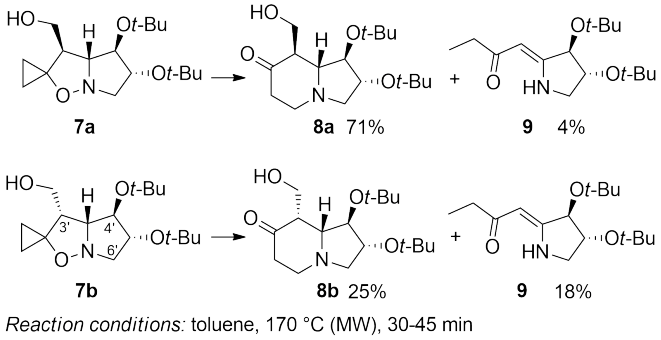

Scheme 3.21: Rearrangement of isoxazolidines **7a** and **7b** to indolizidinones **8a** and **8b** and enaminone **9**.

corresponding indolizidinones, and hence their yields could be affected by major loss either during the thermal process or during the chromatographic purification. The results show that the substituent at C-3' on the concave face in **7b** hampers the formation of indolizidinone **8b** compared with **7a**, which features the 3'-hydroxymethyl group on the convex face of the molecule and is converted into indolizidinone **8a** in better yield (71% vs 25%). The other way around happens for the formation of enaminone **9**. In fact the enaminone is more abundant when formation of the indolizidinone is disadvantaged. Interestingly, when a substituent is lacking on the isoxazolidine C-3' carbon as in **10**, the formation of an almost 1:1 mixture of the two isomeric rearrangement products, indolizidinone **11** and enaminone **12** is observed (Scheme 3.22).[101]

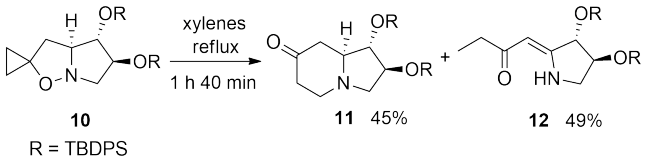

Scheme 3.22: Thermal rearrangement of isoxazolidine **10** to indolizidinone **11** and enaminone **12**.

On the other hand, when C-3' is a quaternary carbon, like in **13** (Scheme 3.23), the exclusive formation of indolizidinone **16** is observed.[102] It cannot be excluded, however, that this result is due to the buttressing effect of the two C-3' substituents that coerces the intramolecular radical coupling in intermediate **15** (Scheme 3.23).

The different behavior of the two diastereomers **7a** and **7b** suggests to perform a computational study to verify the origin of this different reactivity, to answer

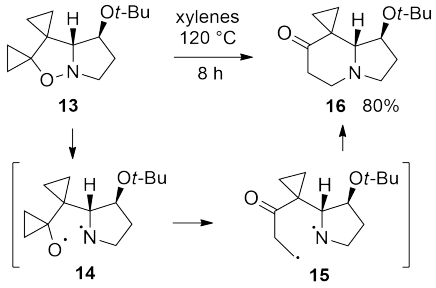

Scheme 3.23: Thermal rearrangement of isoxazolidine **13** to indolizidinone **16**.

the question: is the stereochemical arrangement of the substituent on the isoxazolidine ring of **7a** and **7b** able to drive the rearrangement outcome? The thermal rearrangement of 5-spirocyclopropane isoxazolidines has been then computationally investigated through the study of model compounds, to elucidate the different paths leading to cycled products and enaminones. Starting from the results of Ref. 69, it was chosen to extend the calculations to other model molecules, trying to characterize the reaction path from the reactant to the first transition state and, in many cases, till the final products that can be formed. A series of model compounds that differ for the substituent on the isoxazolidine ring have been analyzed in the previous paragraph (Par.3.2).

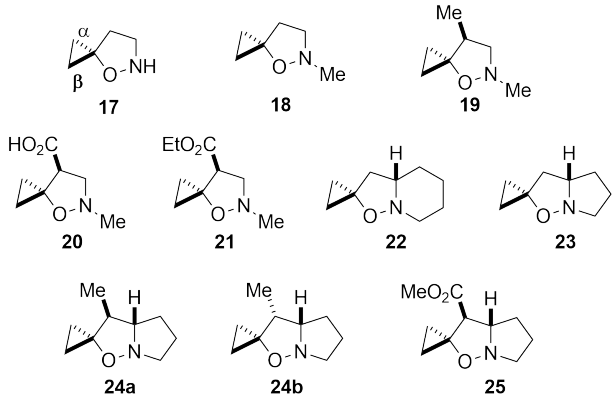

Scheme 3.24: Molecular structures of the studied models.

Our results, reported in the Appendix A confirmed those obtained by Ochoa *et al.*.[69] Indeed, the Brandi-Guarna reaction is thermally activated and proceeds, in the first step, via a homolytic cleavage of the N-O bond that is followed by the homolytic cleavage of a C-CH_2 bond of the spiro-fused cyclopropane ring. These two C-CH_2 bonds seem to be equivalent because, on one side, their cleavage ener-

gies result of the same order of magnitude[103], and on the other side they have a similar spatial environment. However, their cleavage can give rise, at least, to two different minimum energy reaction paths. That is, by labeling as α and β the two cyclopropane C-CH_2 bonds oriented, respectively, below and above the plane of the molecule as shown in Scheme 3.24,[104] the cleavage of the α and β bonds triggers two different reaction paths. It is interesting to note that the cleavage of the β bond triggers more easily to the formation of a cyclic compound independently from the kind of substituents on the adjacent C atom (C-4 in monocyclic derivatives **17**-21, C-3' in bicyclic isoxazolidines **2**2-25, see Scheme 3.24, R= H, Me, CO_2H, CO_2Et, CO_2Me) and this made us confident on the choice of the model systems reported in Scheme 3.25.

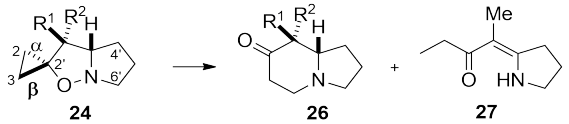

Scheme 3.25: Rearrangement products of model isoxazolidines **24a** and **24b**.

In more details, diastereomers **24a** and **24b** were used as model systems of compounds **7a** and **7b** and the two minimum energy reaction paths arising from the cleavage of the two diastereotopic cyclopropane bonds α and β, were examined. The stationary points have been initially determined at the UB3LYP/6-31G(d,p) level of theory and their energies are reported Appendix A (Table A.20) of the SI. These stationary points have been re-optimized also with the basis set 6-311++G(d,p) as reported in Table A.21). As observed by Ochoa et al.[69] all the intermediates and transition states are characterized by a spin contamination and the eigenvalues of $\langle S^2 \rangle$ are as large as 1 (see Table A.24) suggesting a strong mixture with the triplet state, after the purification the value is reduced by an order of magnitude. The calculations here reported are therefore of a broken symmetry type[105–107] and this allows to take partially into account static correlation other than the dynamical one. Moreover, the adeguacy of this approach for a qualitative, if not semiquantitave, description has been shown for this kind of reaction by Ochoa et al.[69] that have compared the DFT results with post HF methods.

The energy of the optimized structures of both **24a** and **24b** at the UB3LYP/6-311++G(d,p) level of theory are reported in Apeendix A (Table A.20, Table A.21). The difference in energy between the two diastereomers is only 7.3 kJ/mol with **24a** being slightly more stable than **24b**. The results of an electronic structure analysis have been collected in Figure 3-1, where HOMO, LUMO and centroids of the Boys orbitals are reported. While the HOMO is essentially localized on the nitrogen atom, the LUMO is characterized by a high density on the oxygen and nitrogen atoms and practically no probability at the center of the N-O bond is observed suggesting a dissociative state. This information, along with the Boys centroids, provides a first insight into the chemical reactivity of the two molecules.

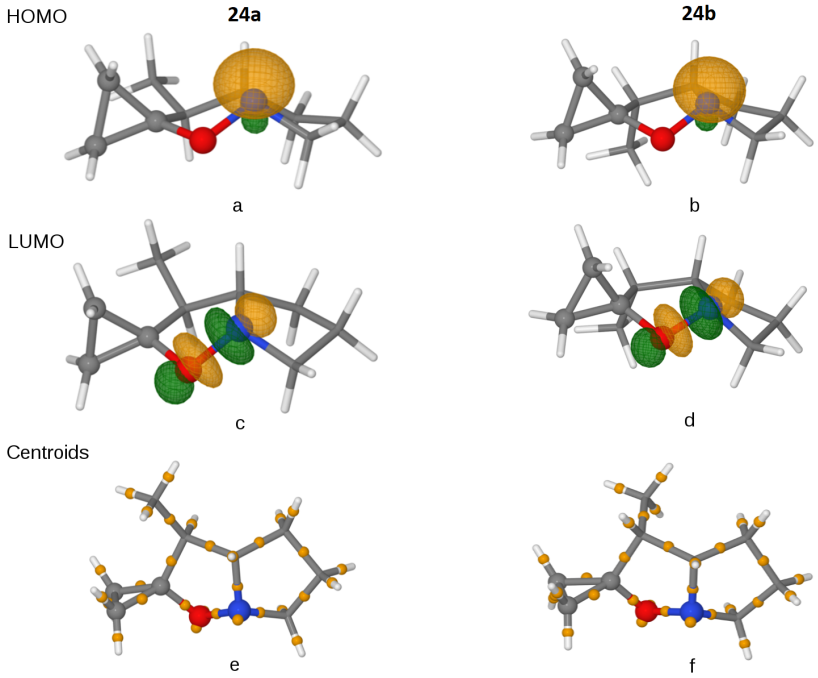

Figure 3-1: **a** and **b** display the HOMO, and **c** and **d** the LUMO of **24a** and **24b** respectively; **e** and **f** show, with small spheres, the centroids of the Boys orbitals.

Reaction mechanism: formation of indolizidinones 26

The reaction mechanism of the rearrangement is characterized by a first step, common to all reagents, which involves the homolytic cleavage of the N-O bond and the formation of TS_1 and TS_2. The electronic structure of TS_1 is characterized by the non-coincidence of the centroids related to α e β electrons along the N-O bond and

on the cyclopropane moiety, as shown in Figure 3-2. This result is consistent with an initial homolytic cleavage of the N-O bond.[69] This is particularly evident in Figure 3-2, where the electronic rearrangement for the intermediate Int_1 is depicted. Moreover, while the other electrons on the molecule form pairs on the β bond of the cyclopropane, the two centroids are separated by ∼0.4 Å along the bond, one inside the cycle and the other outside. A strong separation is also observed on the α bond, where only one electron lies on the line connecting the two carbon atoms and the other is moved very close to C-2'. The electronic structure characterization of Int_1 is important, because the reaction path can now proceed along two different paths with the opening of the cyclopropane ring. Two different minimum reaction paths can be obtained, depending on the cleavage of the β or α bond for both **24a** and **24b**. The mechanism of formation of the tetrahydropyridones **2** is the same for both spirofused bicyclic isoxazolidines **24**. This result is confirmed by the electronic structure and vibrational properties of the equilibrium geometries and transition states obtained from the calculations and summarized in Figure 3-3. Starting from the molecular structure of the transition state, it has been verified that the nearest minima on the reaction path are reached by an IRC calculation. Although both the energy and the imaginary frequencies of the first transition state are slightly different in the reactions involving compounds **24a** and **24b**, as shown in Table 3.1, the electronic distribution is almost the same as confirmed by the Boys-centroids analysis.

The stationary point TS_2 is reached from Int_1. It can be noted from Figure 3-2 that the CO bond is oriented on the opposite side respect to the nitrogen, while the three centroids on nitrogen are very similar to those of Int_1. More interesting is the electronic rearrangement occurring in the cyclopropane and CO moieties. Only one centroid, closer to C-2 (∼ 0.7 Å), is present along the β bond. The other centroid is moved on the CO bond that now has 3 centroids, a pair and an isolated one that is slightly closer to C-2'. A pair and three centroids on the opposite side equispaced are located on the oxygen. The system evolves along the minimum reaction path towards the final product, which is characterized by all paired electrons, as shown in Figure 3-2. The reaction of **24b** follows the same mechanism as confirmed by

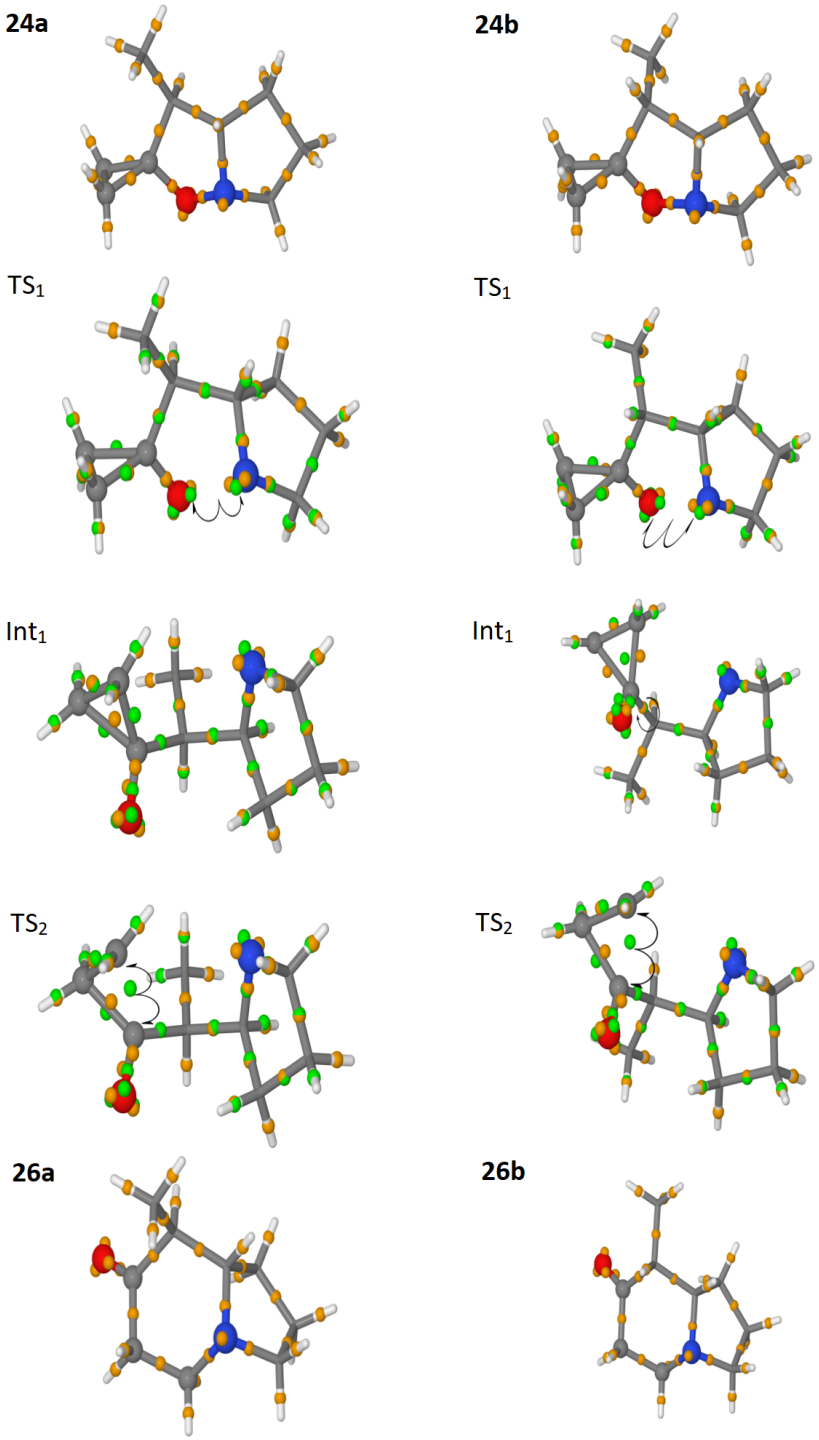

Figure 3-2: Minima and transition states of the **24a** and **24b** reactions leading to the formation of indolizidinones **26a** and **26b**. Green and orange centroids refer to β and α spins.

Table 3.1: Difference in Energy in kJ mol^{-1} with and without the solvent effect (ΔE_{PCM}) of the statiorary points along the reaction path from **24** to **26**. The imaginary frequencies of the transition states are reported in cm^{-1}.

	Stationary points	ΔE_{PCM}	ΔE	ΔE_{disp}	Freq
24a	**24a**	0.0	0.0	0.0	
	TS_1	117.4	119.5	117.1	-209.2
	Int_1	102.8	105.2	100.0	
	TS_2	104.2	106.7	101.3	-338.2
	26a	-236.0	-224.1	-239.4	
24b	**24b**	0.0	0.0	0.0	
	TS_1	113.2	115.4	113.5	-266.4
	Int_1	85.7	88.4	85.4	
	TS_2	87.6	90.4	87.2	-343.0
	26b	-247.0	-244.3	-250.1	

the electronic structure rearrangement in Figure 3-2. As reported in Table 3.1 the effect of the solvent, computed by PCM,[108] on the stationary points is less than 3 kJ mol^{-1} except for the final product **26a** that show a difference of 12 kJ mol^{-1}, therefore the qualitative description of the formation mechanism of the indolizidones is not affected by the presence of toluene as solvent. A few calculations have been performed to evaluate the contribution of the dispersion interactions and are reported in the Appendix A (Table A.25) and their effect is similar, as order of magnitude, to the solvent contribution computed with the PCM method.

Reaction mechanism: formation of enaminone 27

The reaction path involving the α bond cleavage in Int_1 and leading to the formation of the enaminone requires a different description for the **24a** and **24b** reactants as reported in Figure 3-4 and Table 3.2.

In fact, while the first two steps of the reactions are similar, the TS_3 energy is different due to a different reaction path. The shift of a proton occurs in the third step (TS_3) of the rearrangement of isomer **24a** and in the fourth step (TS_4) in the case of **24b** as shown in Figure 3-5 and Figure 3-6.

Regarding the reaction of **24a** leading to the enaminone **27**, the second step is characterized by the homolytic cleavage of the α bond in the cyclopropane moiety.

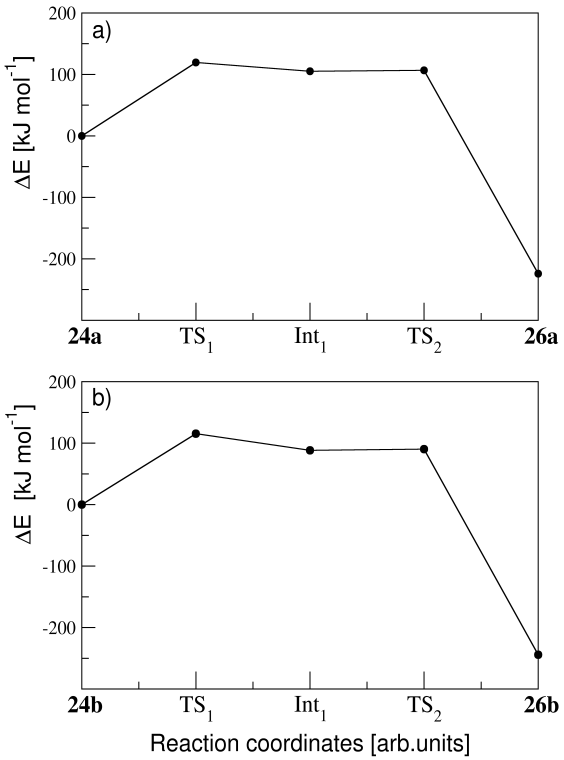

Figure 3-3: Reaction energy profiles related to the indolizidinone formation, from: a) **24a** and b) **24b**.

Table 3.2: Difference in Energy in kJ mol^{-1} with and without the solvent effect (ΔE_{PCM}) of the statiorary points along the reaction path from **24** to **27**. The imaginary frequencies of the transition states are reported in cm^{-1}.

	Stationary points	ΔE_{PCM}	ΔE	ΔE_{disp}	Freq
24a	**24a**	0.0	0.0	0.0	
	TS_1	117.4	119.5	117.1	-209.2
	Int_1	102.8	105.2	100.0	
	TS_2	103.6	106.8	101.8	-344.1
	Int_2	48.9	51.1	46.5	
	TS_3	59.1	62.7	61.4	-54.0
	Int_3	48.4	53.2	48.0	
	TS_4	51.1	54.9	54.5	-167.7
	Int_4	-241.7	-238.9	-240.2	
	TS_5	-22.2	-13.3	-10.4	-1781.5
	27	-265.7	-259.7	-256.3	
24b	**24b**	0.0	0.0	0.0	
	TS_1	113.2	115.4	113.5	-266.4
	Int_1	85.7	88.4	85.4	
	TS_2	86.0	89.3	86.4	-316.7
	Int_2	35.6	37.7	35.6	
	TS_3	118.7	121.0	121.0	-1739.8
	Int_3	-24.2	-19.1	-19.1	
	TS_4	38.4	44.8	47.7	-1642.0
	27	-266.3	-259.3	-257.0	

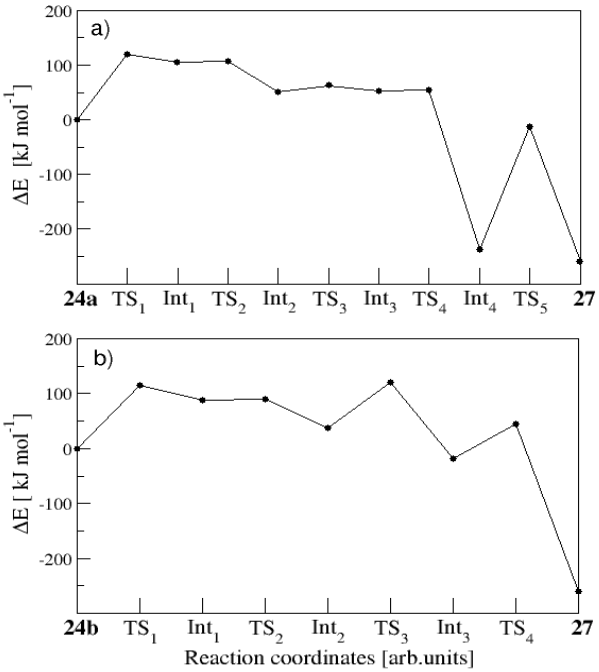

Figure 3-4: Reaction energy profiles related to the enaminone formation, from a)**24a** and b)**24b**, respectively.

The reaction evolves toward Int_2 through a structural rearrangement with the nitrogen and oxygen atoms at longer distance and subsequently through a rotation in TS_3, as shown in Figure 3-5. The terminal CH_2 group obtained by the cleavage of α bond interacts with the hydrogen atom initially bonded to C-**3a'** to obtain a terminal methyl group. Finally, the enaminone is obtained through isomerization of the imine to enamine. As in the case of the **24a**, the epimeric **24b** is converted into enamine **27** through the homolysis of cyclopropane α bond. However, the reaction occurs through a different sequence with respect to those discussed in the previous section as shown in Figure 5. As observed in the case of the reaction of **24a**, the second transition state and third stationary point (TS_2 and Int_2) are, in sequence, the α bond breaking and a structural rearrangement of the CH_2-$CH_2^{\bullet}$ moiety, as shown in Figure 3-5. The main difference with the rearrangement of **24a** stems in the transition state TS_3, which is characterized by a hydrogen atom shift, leading to the formation of the CH_2-CH_3 group. The nitrogen atom interacts with the hydrogen atom of C-**3a'** giving rise to the formation of an imine intermediate (Int_3) that

isomerizes to enaminone **27**. It is to be noted that for **24a** TS_1 is not the highest barrier along the reaction path. At this level of theory the highest barrier is TS_3 as reported in Table 3.2. Considering toluene as implicit solvent, also in the case of enaminone formation, the overall energy profile is not modified appreciably, as shown in Table 3.2. However, the role of the solvent can be relevant on the dynamics of the reaction in the experimental conditions. In fact, the trasformation is characterized by many statiorary points and involves a much more complex structural rearrangent to reach the elongated enaminone structure than to obtain the pyridone.

3.4 Conclusion

Extensive analysis of the Brandi-Guarna reaction has helped us to understand the critical points that the experiments brought up: the lack of regioselectivity in the cycloaddition reaction that makes the 5-soxazolidine compound and the fact that enaminone is made when isoxazolidine rearranges itself when heated. The conclusions that follow examine the 1,3-DC reaction and heat rearrangement in depth.

3.4.1 The Cyclopropilidene Effect

The lack of regioselectivity in 1,3-DC of methylenecyclopropane (MCP, **2**), compared to the high regioselectivity of other 1,1-disubstituted alkenes, has been computationally investigated through DFT calculations, to rationalize the experimental finding. The computational analysis has been extended to tetrasubstituted alkenes and to cyclopropylideneacetate to substantiate the results. It has been observed that the electrostatic interactions play a fundamental role into the regioselectivity of these 1,3-DC reactions. In fact, the electronic structure of the substituents (EDG and EWG) causes a polarization of the alkene double bond, which in turn favours a proper structural arrangement between the reactants and consequently controls the regioselectivity. The comparison of the reactions between nitrone 16 and 1,1-disubstituted alkenes isobutene (**7**) and MCB (**14**) shows that for similar substituents (dimethyl, cyclobutyl) the reaction outcome is essentially due to the electrostatic interaction (atomic charges and dipole moment), with a preferential

formation of the 5,5-disubstituted isoxazolidine. In the case of MCP, where the electrostatic interaction is less marked, the differences in 5- and 4-spirofused isoxazolidine formation is lower and consequently the kinetic constants of the two paths are similar (the kinetic constant ratio is only $k_{\mathbf{a/b}} = 5$). The electronic structure analysis of 1,3-DC with the tetrasubstituted alkenes ICP (**17**), ICB (**18**), and CPCB (**19**) reveals a smaller value of the dipole moment, because all the substituents are alkyl groups, and the partial charges on the double bond are given by the subtraction of the substituent EDG effects. The alkenes ICP and CPCB feature both a cyclopropyl group on one end of the double bond, and on the other end: a geminal dimethyl group and a cyclobutyl ring, respectively. The comparison of these two dipolarophiles allow to understand how the cycloaddition reaction is influenced by the alkene substituents with the largest EDG effect. In ICP the EDG effect of the geminal dimethyl is stronger than the one of cyclopropyl: the $k_{\mathbf{a/b}}$ ratio shows that the reaction is completely shifted toward the formation of isomer **27** with methyl groups on C-5 ($k_{\mathbf{a/b}} = 610^{-10}$). A similar behaviour, although with a lower weight, occurs in CPCB. In the case of 1,3-DC with ICB, the electrostatic contributes of the substituents are similar, thus the polarization of the double bond is small but still enough to favour the formation of the isoxazolidine with methyl groups on C-5 ($k_{\mathbf{a/b}} = 610^{-2}$). The cyclopropylideneacetate **36** is the only example studied featuring a cyclopropyl ring and an EWG. In this case the two electronic effects sum, as shown by the value and orientation of the alkene dipole moment. The contribute given by the EWG is dominant and leads exclusively to the formation of product **39** ($k_{\mathbf{a/b}} = 123$). Summing up, the electronic effect of the alkene substituents measured in this study determines a polarization of the alkene double bond favouring the relative orientation between the reactants leading to the observed regioselectivity of the cycloadditions. The study has allowed to explain the role of a cyclopropylidene group (the "cyclopropylidene effect") in inducing the regioselectivity in nitrone 1,3-dipolar cycloadditions.

3.4.2 The Brandi-Guarna reaction

The stationary points for the Brandi-Guarna rearrangement of the spiro-fused bicyclic isoxazolidines **24** into indolizidinones **26** and enaminone **27** have been characterized at the UB3LYP/6-311++G(d,p) level of theory. The rearrangement occurs throught an initial homolysis of the isoxazolidine N-O bond followed by the cleavage of a cyclopropane C-CH_2 bond. The main result of the present study is that two different pathways branch off from the first intermediate Int_1 in both **24a** and **24b**. One path involves the cleavage of the α cyclopropane bond and leads to enaminone **27**, while the other, which features the cleavage of the β bond, ends up with indolizidinone **26** formation. This finding proves that the outcome of the rearrangement does not depend on a late step, such as a higher or lower propensity to close the six membered ring, but on the second step, i.e. on the competitive cleavage of the diastereotopic α and β bonds of the cyclopropane ring. It is interesting to note that the pathways leading to enaminones requires a larger number of steps with an increase of the spanned space. This can be important in condensed phase under the experimental conditions. We can therefore hypothesize that, at constant volume conditions and in the presence of the solvent, the yield of enaminones is lower than that of indolizidinones, due to more complex reaction paths involving large rearrangements that can be made less probable by the presence of the solvent molecules. It is to be noted that the calculations predict a strong decrease in energy from the last transition state to the product for all the reaction paths reported. This energy can be dissipated by interaction with the solvent but it can be also accumulated initially in vibrational degree of freedom and this can reduce the percentage of enaminone that can be obtained experimentally since it is a more fragile compound. We can also notice that the curvature of the energy profile at the transition state involving the H-shift is very high and nuclear quantum effects can be important in this reaction step.[109] Despite the differences among the energy barriers of the four calculated pathways are negligible, the study gives a clear description of the reaction mechanism. The sterical effect exerted by the substituent is involved in the selective cleavage of one of the two cyclopropane bonds with the cleavage of the β bond leading to the formation of the pyridone product.

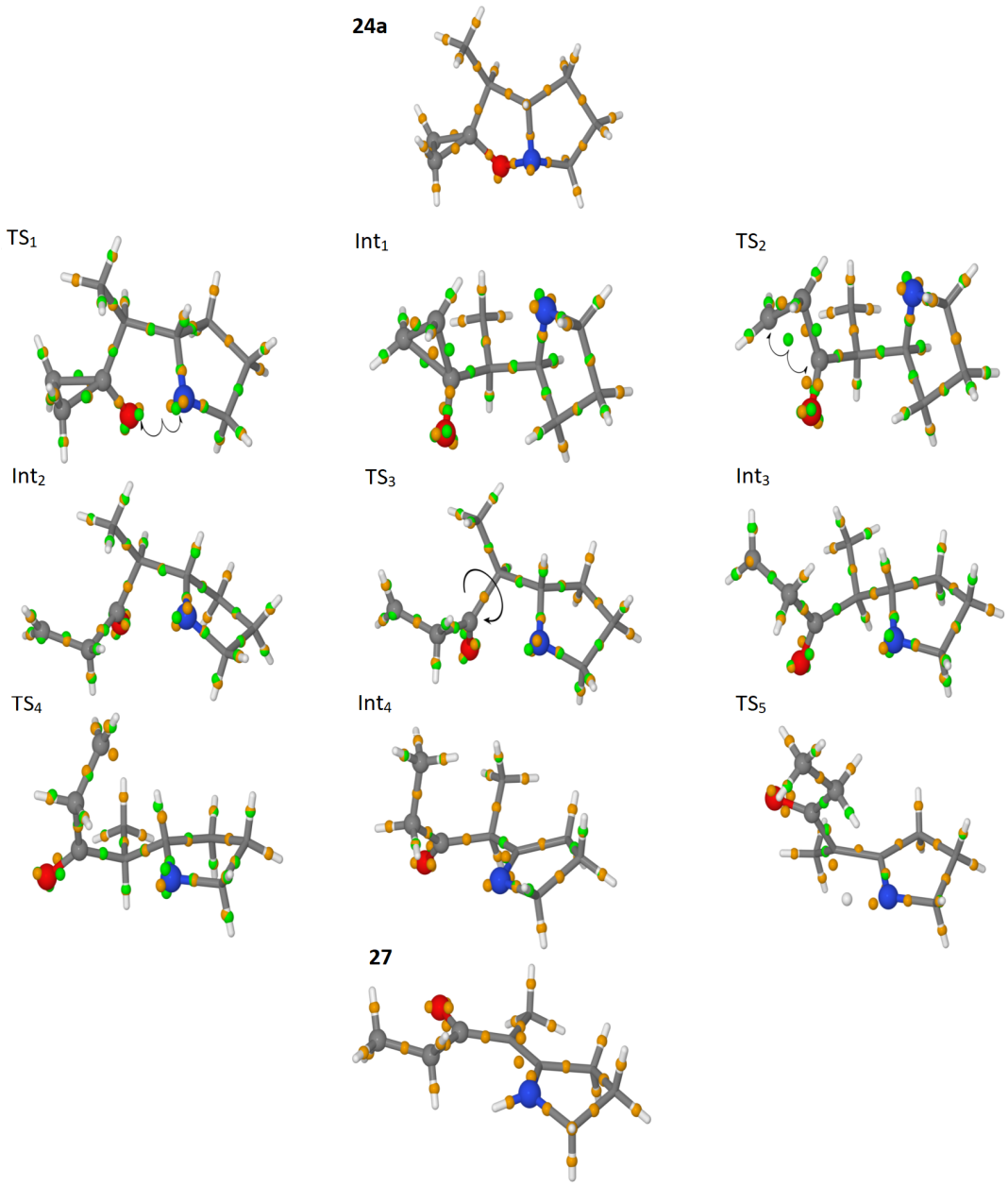

Figure 3-5: Minima and transition states of the reaction of **24a** leading to the formation of the enaminone.

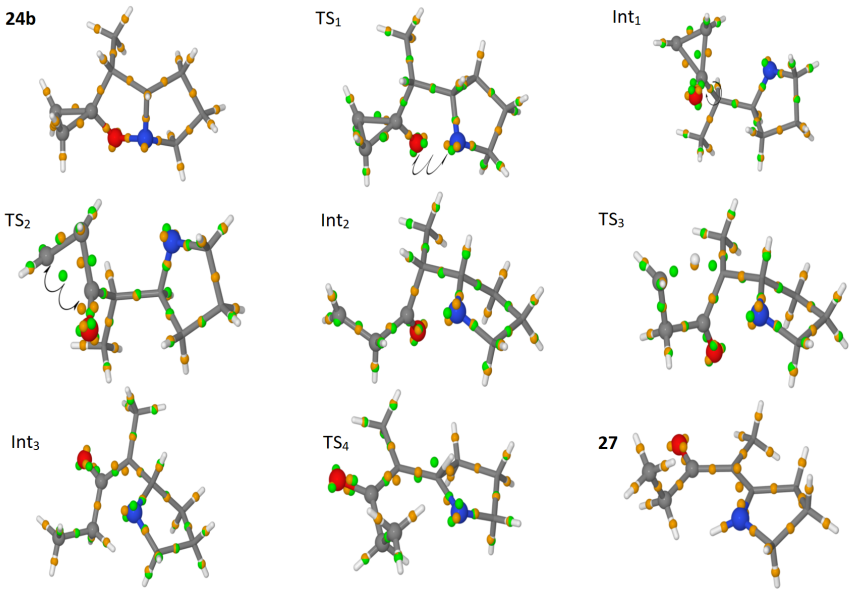

Figure 3-6: Minima and transition states of the reaction of **24b** leading to the formation of enaminone **27**.

Chapter 4

Analysis of a tautomerization reaction path: why does it depend on the adopted exchange correlation functional?

In theoretical and computational chemistry, Koh-Sham density functional theory has become one of the most extensively utilized tools for describing the electronic structure. KS-DFT assumes that the ground state density of the original interacting system is equal to that of a set of non-interacting systems. This leads to independent particle equations for non-interacting systems that are considered as exactly soluble with all of the problematic many-body terms included into an exchange-correlation functional of the density. Exchange arises from anti-symmetry due to the Pauli exclusion principle and correlation accounts for the remaining many-body effects, however the exchange correlation in terms of density is unknown and it is necessary to use approximations, such as the use of semi-empirical parameters. The purpose of this study is to contribute to the topic of the arbitrariness of xc-functional choice within a given theoretical framework. To highlight any potential differences between the adopted xc-functionals, a model reaction involving proton transfer between highly conjugated systems in which electron density plays a substantial role was required. All these requirement are satisfied by the tautomerization of [2,2'-

bipyridyl]-3,3'-diol which involves a double proton transfer between a nitrogen and carbonyl moiety on conjugated bipyridyl rings. The determination of the detailed reaction mechanism is currently a subject of discussion,[110–112] and the tautomerization has been investigated both in terms of excited state intramolecular proton transfer (ESIPT)[113,114] and ground state analyses.[115,116] The reaction has been investigated in the ground state using both static and dynamic approaches, detailing the reaction process and estimating the free energy surface to highlight any potential differences between functionals that, according to the methodology, ought to be equivalent. Contrary to expectations, both static and dynamic simulations show that the characterization of the reaction mechanism is dependent on the delocalization error of the xc-functional adopted: functionals with a high delocalization error define a step-wise reaction mechanism, whereas xc-functionals with a lower delocalization error define a concerted reaction mechanism with different degrees of synchronicity.

4.1 Computational details

Geometry optimization methods with very tight convergence criteria have been used to locate transition states (TS), pre-reactive minima, and products for each of the functionals reported in Table 4.1. The Hessian matrix for the TS is characterized by only one negative eigenvalue, and the associated eigenvector reflects the displacements along the two newly created O–H bonds, providing insight into the concerted or step wise reaction process.

The 6-311+G(d,p) basis set was utilized for all geometry optimizations. The reference structures were computed at the B2PLYP//M06/6-311+G(d,p)[134,135] level of theory, single point energy calculations at the CCSD(T)-F12/ cc-pVTZ-F12-CABS[136,137] level of theory have been performed for a more accurate energy reference. This method requires a near-complete auxiliary basis (CABS) in addition to the orbital basis set. The F12 correction strongly improves the basis set convergence of correlation and reaction energies. Errors of the Hartree-Fock contributions are effectively removed by including MP2 single excitations into the auxiliary basis

Table 4.1: List of exchange-correlation functionals and methods considered in this work, ordered by the proportion of HF-exact exchange EXX (min/max for range separated hybrids).

Type	Functional	Ref	E_{XC}	%EXX
HF	HF	117	E_X^{HF}	100
ρ	Xα	118	ρ	0
	SVWN5	118,119		
GGA	BLYP	120,121	$\rho, \nabla\rho$	0
	PBE	122		
	M06L	123		
Global Hybrids	B3LYP	124,125	$\rho, \nabla\rho, \nabla^2\rho,$ E_X^{HF}	20
	PBE0	61		25
	BH&HLYP	126		50
	M06	127		27
	M062X	123		54
	M06HF	128		100
Range Separated Hybrids	Cam-B3LYP	129	$\rho, \nabla\rho, \nabla^2\rho,$ E_X^{HF}, ω	19/65
	ωB97XD	62		22/100
	M11	130		42.8/100
Double Hybrids	B2-PLYP	131	$\rho, \nabla\rho, \nabla^2\rho,$ $E_X^{HF}, E_C^{MP2_{corr}}$	53
	DSDPBEP86	132		69
PT	MP2	133	E_C^{MP2}	

set. Using aug-cc-pVTZ basis sets the CCSD(T)-F12 calculations are more accurate and two orders of magnitude faster than standard CCSD(T)/aug-cc-pV5Z calculations[138]. Through the determination of the electrostatic potential (ESP), the electronic effects have been investigated.[139,140] In Appendix B comparisons between the ESP atomic charges and those derived by the CM5 method[78] are provided to further enhance the electronic structure analysis. To characterize the electronic structure rearrangement during the reaction mechanism, the electron localization has been computed for specific stationary points using the electron localization scheme proposed by Boys[141] with the sddall basis set.

Due to the fact that both tautomers belong to the C_{2h} point group symmetry, we have also investigated the entirely synchronous double proton transfer, which implies symmetry conservation along the reaction path. In this specific instance, the saddle point along the transformation path is characterized by two imaginary frequencies corresponding to the symmetric and anti-symmetric stretching of the double proton

transfer. In this case the number of functionals examined has been reduced to the B2PLYP, ωB97XD, B3LYP, and BLYP all adopting the 6-31+G(d,p)[134,142] basis set.

Biased dynamics were performed using the ADMP method, which is an extended Lagrangian method where the density matrix is propagated rather than the wavefunction.[25–27] All static and dynamic calculations were performed using the Gaussian suite of programs (G16).[86] The only exception are the coupled cluster calculations and MP2 that were performed with the ORCA program.[143]

The characterization of the reaction mechanism at the MP2/6-311+G(d, p) level has once again showed the limitations of this approach for characterizing aromatic systems.[144–146] Although the structures of the tautomer forms adhered to thigh convergence criteria and characterized by the absence of imaginary frequencies, C_{2h} symmetry and planarity were lost. Performing optimizations with the same level of theory and criteria using the ORCA software does not resolve the issue. The MP2 analysis was therefore omitted; the results are presented in the Appendix B.

The umbrella sampling along the potential energy surface of the tautomerization was carried out using the PLUMED library[147] (version 1.3.[148]) interfaced with a locally customized version of the Gaussian suite of programs (G16).

The exploration of the potential energy surface is the outcome of a harmonic potential acting as a bias (4.1a) expressed as a function of the collective variables (CV), where k (4.1b) is the harmonic force constant and s_0 is the reference value. Since intramolecular proton transfer could be synchronous or step wise, the tautomerization must be modeled using two collective variables, one for each proton (4.1c),(4.1d). (refer to Figure Figure 4-1 for atom labeling)

$$V(CV) = \frac{k}{2}\left(CV - s_0\right)^2 \tag{4.1a}$$

$$k \approx \frac{k_B T}{\sigma_{CV}^2} \tag{4.1b}$$

$$CV_1 = |R(N_3) - R(H_1)| - |R(O_5) - R(H_1)| \tag{4.1c}$$

$$CV_2 = |R(N_4) - R(H_2)| - |R(O_6) - R(H_2)| \tag{4.1d}$$

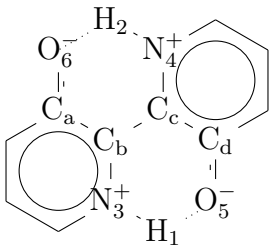

Figure 4-1: CV_i refers to the collective variable i; $R(X)$ indicate the position of the X atom, reported in the figure;

Ten IRC (Intrinsic Reaction Coordinate) configurations were collected along the proton transfer pathway with a collective variable step value of 0.5 Bhor, based on the stationary points and intermediate geometries for each proton transfer. Each of these structures provides the input for the biased NVE dynamics conducted at room temperature with an integration time step of 0.2 fs for 3 ps. This simulations are preceded by an equilibration run of 1.5 ps utilizing a nuclear kinetic energy thermostat[26] implemented in Gaussian with a temperature check every 500 fs for the first picosecond. Except for the double hybrids functionals, the MP2, for which the ADPM algorithm is not implemented, and the M11 the dynamics were performed for each of the functionals listed in Table Table 4.1.

Due to the computational cost, it was not practical to use the same basis set adopted for static calculations in the ADMP simulations. The modified 6-31+G(d,p) basis set with the diffuse function on nitrogen and oxygen was found to represent the optimal balance between accuracy and computational cost savings, as determined by an estimation of the barriers with alternative basis sets .To verify that the exploration of phase space was compatible with the sampling of the IRC, special care was taken to confirm that the reaction pathways given with the 6-31+G(d,p) modified basis produced the same results as those predicted using the 6-311+G(d,p) basis set.

The sampling of the phase space is determined by the value of the force constant (k): for large values of k only points near to s_0 are investigated (4.1a). Therefore a small k (4.1b)value would be ideal for investigating as much surface area as possible, but since the dynamic is NVE, energy conservation must be guaranteed. In addition, the two collective variables must be separated during the analysis of the potential

surface close to the transition states in order to evaluate the reaction mechanism (4.1c)(4.1d). For these reasons we chose different values of k (4.1b) along the reaction path: 0.005 for minimum configurations, 0.10 for intermediate structures and 0.20 for TS geometries.

The weighted histogram analysis method (WHAM)[149] is applied to each acquired trajectory to reconstruct the potential energy surface at room temperature with a convergence criteria of $1 \cdot 10^{-5}$ (a.u.).

The minimum energy path (mep) was computed by considering the minimum energy value relative to a linear combination of the two collective variables (CV_1, CV_2). The resulting two-dimensional energy profile was calculated using a fifth-order polynomial (the values and the polynomial expression are reported in the B).

4.2 Results and discussion

Chemical intuition and previous works[114,116] suggests that the tautomerism can proceed in two different ways (Figure 4-2): through a concerted mechanism with variable synchronicity involving a double proton transfer, or by a step-wise approach that involves the formation of the keto-eno intermediate (**2**).

The diketo (**1**, Figure 4-2) tautomer is characterized by a loss of aromaticity along the two cycles, a negative partial charge on the oxygen atoms and a positive one on the nitrogen atoms, and partial conjugation between the two beta carbons and the two carbonyl moieties.The dienol form (**3**) is expected to reconstruct the aromaticity on the cycles, resulting in a more stable structure. As a result, we selected the diketo (**1**) as the starting form and the dieno tautomer (**3**) as the product.

4.2.1 Static Calculations

The diketo (**1**) and dieno (**3**) tautomers are characterized by the C_{2h} symmetry. Under the assumption that C_{2h} symmetry is conserved throughout the reaction, the synchronous double proton transfer mechanism has been investigated.

The saddle point geometry of the double proton transfer (Figure 4-3) is characterized by two negative eigenvalues with eigenvectors corresponding to antisym-

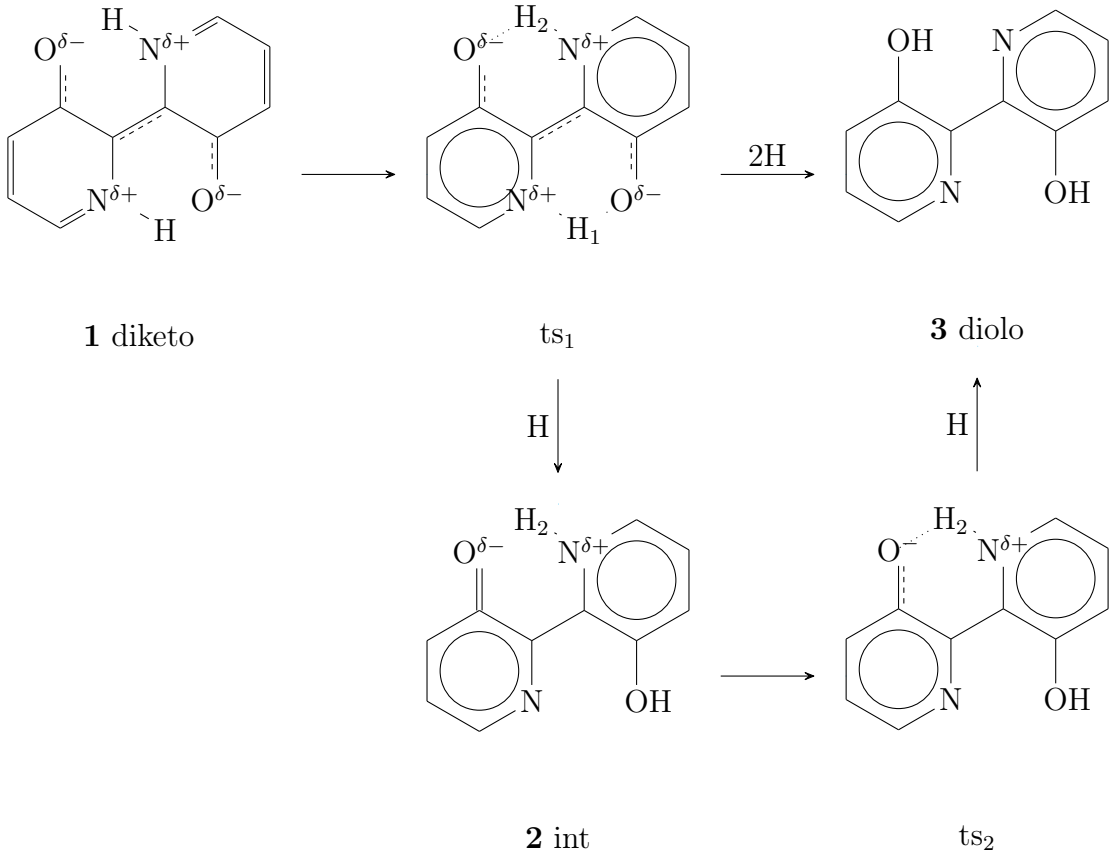

Figure 4-2: The two proposed reaction mechanism for the tautomerization of [2,2'-bipyridyl]-3,3'-diol.

metric (Fig.4-3a) and symmetric (Fig.4-3b) stretching. The symmetric describe the syncronous formation of the dieno while the second brakes the symmetry.

The stationary points have been optimized using very tight convergence criteria with the 6-311+G(d,p) basis set. Due o the computational cost less functionals have been used. The estimated activation energies are approximately 35 kcal/mol for the DSDPBEP86, wB97XD, and B3LYP and significantly lower at 21 kcal/mol for the BLYP (exact values reported in Appendix B). The magnitude of the activation energies for the tautomerism and the occurrence of two negative eigenvalues in the stationary point suggest that a distinct reaction path, which describes an asyncronous or stepwise reaction mechanism, involving a reduction of the C_{2h} symmetry is more plausible.

The reference energies for the two proposed mechanisms involving a loss of symmetry, concerted and stepwise, were calculated at the CCSD(T)-F12/cc-pVTZ-F12-CABS level of theory using the geometries obtained at the B2PLYP/6-311G(d,p)

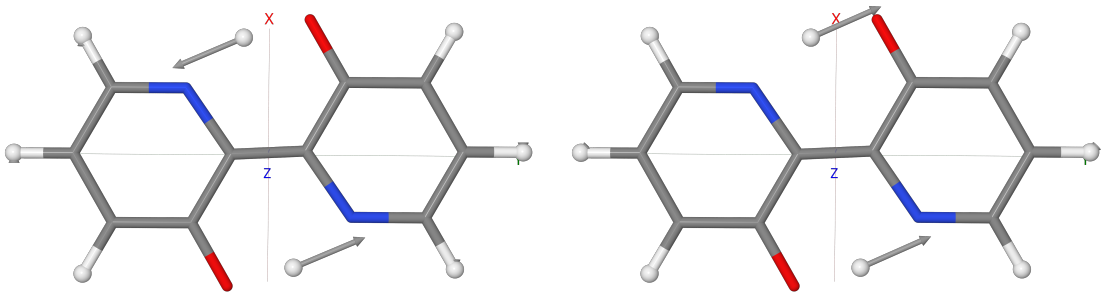

(a) -1611.3 cm^{-1} (b) -1532.9 cm^{-1}

Figure 4-3: Imaginary frequencies at B2PLYP/6-311+G(d,p) level of theory

and M06/6-311+G(d,p) levels, respectively.

The B2PLYP functional describes a tautomerization characterized by a concerted asyncronous reaction mechanism[150] in which the first proton transfer is the rate-determining step (1.6 kcal/mol) and the system evolves into the dieno tautomer with C_{2h} symmetry (**3**, -16.6 kcal/mol) without encountering any other energy barriers (Table 4.2). The CCSD(T)-F12/cc-pVTZ-F12-CABS single point calculations on the optimized structures decrease the activation energy for the initial proton transfer (0.6 kcal/mol) and increase the dieno tautomer energy (**3**, -14.6 kcal/mol).

The M06 identifies a step wise mechanism; the activation energy is comparable to the ΔE obtained with the B2PLYP functional (1.6 kcal/mol). The chemical process is characterized by a keto-eno intermediate (**2**, -3.5 kcal/mol) connected to the dieno tautomer (**3**, -12.0 kcal/mol) by a second proton transfer (0.3 kcal/mol). Single point coupled cluster calculations on the optimized M06 geometries reveal that the barrier for the first TS and the stabilization of the dienol form are identical to B2PLYP (0.6 and -12.0 kcal/mol, respectively), while the TS2 (-5.4 kcal/mol) energy is lower than the keto-eno intermediate (-4.3 kcal/mol).

At this level of theory, the reaction process is asynchronous, with the dienol form (**3**) being more stable than the diketonic form (**1**), with tautomerization proceeding

Table 4.2: Functional/6-311+G(d.p), Δ E (kcal/mol), ν (cm^{-1}).

LoT	ts_1	int_1	ts_2	di-eno	$\nu_1(ts_1)$	$\nu_2(ts_2)$
B2PLYP// CCSD(T)-F12/ cc-pVTZ-F12-CABS	0.597			-14.622		
M06// CCSD(T)-F12/ cc-pVTZ-F12-CABS	0.568	-4.536	-5.347	-14.622		
B2-PLYP	1.649			-16.610	-1021.3	
DSDPBEP86	1.467			-19.683	-968.6	
wB97XD	0.970			-12.740	-995.4	
Cam-B3LYP	0.587			-13.072	-905.3	
M11	0.341			-12.541	-753.8	
B3LYP	1.264			-9.690	-1037.8	
PBE0	0.396			-10.50	-787.5	
BHandHLYP	1.322			-15.917	-1139.4	
M06	1.654	-3.519	-3.244	-11.992	-1495.6	-1017.9
M062X	0.039			-16.388	-389.1	
PBE	0.455			-5.616	-744.1	
BLYP	1.438	-0.943	-0.927	-5.648	-978.0	-330.2
M06L	2.626	-1.465	-0.631	-7.778	-1400.8	-1407.9
HF	2.230	-11.051	-10.253	-26.535	-1355.7	-1013.72

by a single TS corresponding to the first proton transfer and resulting in a loss of symmetry in the C_{2h} molecule. The second proton transfer is barrierless. According to the energy profile along the IRC reaction coordinate, the surface of energy between the first and second proton transfers is flat. This work shows that a local minimum relating to the keto-eno intermediate (**2**) and a second maximum (ts2) corresponding to the second proton transfer are detectable in this region of phase space, depending on the chosen xc-functional.

Proceeding from the lowest to the highest level of theory employed. The HF analysis of the reaction processes establishes a step wise mechanism that involves the formation of the keto-eno intermediate. The barrier for the first transition state at HF is 2.2 kcal/mol. The intermediate (**2**) is 10 kcal/mol more stable than the ground state (**1**, C_{2h}), whereas the activation energy required for the second proton transfer is 1 kcal/mol. This behavior suggests that the characterization of the response mechanism may be reliant on the xc-functional. Following the Jacob's ladder, the investigation is expanded to two completely local functionals (Xα and SVWN5). In this case, neither functional recognizes the diketo form (**1**, C_{2h}) as a

local minimum: starting with an optimized HF geometry of the diketo (**1**, C_{2h}), the geometry optimization directly leads to the dieno product (**3**, C_{2h}).

As we move to the GGA functionals, the situation becomes more complicated. The reaction mechanism is step wise for M06L and BLYP while concerted for PBE. The investigation of the structures, the charge distribution (ESP) and the dipole's value are useful tools for explaining such behavior. In particular the analysis of the partial charges on the atoms in the diketo tautomer (**1**), which describe the conjugation of the two cycles, and the initial transition state which represents the dividing point between two reaction mechanisms. The comparison of the evolution of partial charge (Table B.22) on the atoms between the transition state and the diketo form (**1**) reveals that the functionals M06L and BLYP are subject to a smaller variation of the charge distribution between the transition state and the pre-reactive minimum (**1**) compared to PBE, which defines a concerted process and has a lower activation energy (activation energies for M06L, BLYP and PBE are 2.6, 1.4 and 0.4 kcal/mol respectively Table 4.2). The low magnitude of the dipole moment for the PBE transition state (0.7 Debye, Table B.17) offers a measure of the mechanism's synchronization.

The analysis of the keto-eno intermediate (**2**) obtainated with the M06L and BLYP indicates a balanced distribution of charges (Table B.20), which explains the stability of the keto form. There are no significant differences in the description of the charge distribution, and the energy gain is comparable (1.4 kcal/mol for M06 and 0.9 kcal/mol for BLYP). However, the keto-eno intermediate (**2**) is characterized by a loss of symmetry, and the activation energy for the second proton transfer is low for both functionals (0.8 kcal/mol for M06L and 0.4 kcal/mol for BLYP). The system evolves to dieno tautomers (**3**) with C_{2h} symmetry, with the BLYP and PBE providing the same stabilization (-5.6 kcal/mol), while the M06L provides a more stable form for the dieno (-7.8 kcal/mol).

In the case of global hybrid functionals, the characterization of the reaction mechanism is also dependent on the xc-functional. Both tauotomers (**1**, **3**) show C_{2h} symmetry for the functionals under examination. A concerted reaction mechanism is found by the BH&HLYP, B3LYP, and PBE0. The activation energy for the first

two functionals is the same (1.3 kcal/mol, Table 4.2), and the immaginary mode frequency of the two TS is similar (-1139 and -1038 cm^{-1}, respectively). The PBE0 is characterized by a lower activation energy (0.4 kcal/mol). The evolution of the ESP charge from the diketo tautomer to the first transition state is comparable to that of the other two functional groups, whereas the dipole momentum in the TS is smaller (0.8 Debye for PBE and 1.1 Debye for B3LYP and BH&HLYP Table B.17), showing a greater degree of synchronicity in the double proton transfer.

The analysed Minnesota functionals (M06, M062X and M06HF) display a different behavior. The M06 detects a step-wise mechanism and, as mention before, the activation energy is the highest for this family of functionals (1.6 kcal/mol).The investigation of the charge distribution and, more specifically, the evolution of the charges between the first transition state and the diketo form (**1**, Table B.19) reveals a charge distribution closer to the diketo minimum configuration distribution, consistent with the trend observed in the GGA functionals. Due to the step wise nature of the reaction mechanism, symmetry considerations cannot be made through the analysis of the dipole momentum (0.9 Debye Table B.17) in this instance. In order to exclude any potential basis set effects on the characterisation of the reaction mechanism, the keto-eno intermediate (**2**) has once again been optimized at the M06/pvqz[151] level, providing the same structure.

The M062X, that involves a double HF exchange contribution (54%), defines a syncronus reaction mechanism with a low activation barrier (0.04 kcal/mol). In the functionals examined so far, despite being concerted, the mechanism appears to be highly asynchronous, as evidenced by the imaginary frequencies in the first transition state that describe the transfer of a single proton (the value varies between -900 and -1000 cm^{-1} depending on the functional, Table 4.2). For the M062x, however, the TS has an imaginary frequency of 300 cm^{-1}, which is the lowest observed value. This behavior is due to the fact that the normal mode partially involves the transfer of the second hydrogen. The resulting reaction mechanism is more synchronized than in previous examples. The TS structure analysis reveals that the NH distance for both hydrogens is comparable (1.13 and 1.09 Å) and that the value of the dipole is low (0.3 Debye, compared to the average value of 1 Debye for the other functionals

Table B.17), indicating that the geometry of the transition state is close to the C_{2h} symmetry of the two minima (**1**, **3**).

The M06HF, which has the 100% of HF exchange, does not optimize the diketo tautomer (**1**). Examining the acquired data, it appears that for Minnesota functionals, the increase in the non-local exchange contribution of HF results in the identification of a step wise (M06L 0% HF, M06 27% HF), to concerted (M062X 54% HF), to absent reaction mechanism (M06HF % 100HF).

The range separated functionals (Cam-B3LYP, ωB97XD, M11) identify a concerted reaction mechanism with the diketo(**3**) and dieno(**2**) tautomers characterized by a C_{2h} symmetry. The M11 functional stabilizes the initial TS more than Cam-B3LYP and ωB97XD, resulting in a slightly lower activation energy for the first proton transfer (0.4, 0.6 and 1 kcal/mol, respectively Table 4.2); this trend is reflected by the value of the dipole moment (0.8, 0.9 and 1.1 Debye). The relative energy values obtained with the Cam-B3LYP are the closest to the B2PLYP//CCSD(T)-F12 reference values.

The reaction mechanism for the investigated double hybrid functionals (DSDP-BEP86 and B2PLYP) is concerted, both the diketo (**3**) and dieno (**3**) form have C_{2h} symmetry and they are connected by a single TS (the activation energy is 1.5 and 1.6 kcal/mol respectively). Double hybrids provide the best stabilization for the dienol form (**3**, -16.6 and -19.7 kcal/mol respectively) among the functionals tested. The reference energies at CCSD(T)/cc-pVTZ-F12-CABS level of theory were determined using the B2PLYP stationary point structures as input (see Appendix B Table B.2).

It is not possible to differentiate the two reaction mechanisms according only to the optimized structures with the studied functionals . Indeed, regardless of the reaction mechanism the stationary points are characterized by a zero average value of the dihedral angle (NCCO) computed along the IRC path (Fig Figure 4-2, $\theta = -1.83 \cdot 10^{-3} \pm 1.39 \cdot 10^{-5}$) and by the absence of a z component in the TS dipole (Table B.18). The symmetry of the diketo and dieno tautomers is C_{2h} while the simmetry of the transition states and keto-eno intermediate is C_S (Table B.4). These results confirm that the two cycles maintain their planarity along the reaction pathway. Hydrogen

is coordinated by both nitrogen and oxygen during the proton transfer, resulting in two six-point cycles intermediate that locks pinolo to be planar. The diketo form (**1**) imposes the loss of aromaticity in the two cycles, the average value of the C-C bond between them during the mechanism is 1.39Å(± 0.09). Suggesting that the steric hindrance created by the interaction between the nitrogen and oxygen moieties is sufficiently strong that an alpha-beta delocalization along the CC moiety is partially inhibited. In the diketo form (**1**), the oxygen-carbon interatomic distance specifies a carbonilic moiety with a full double bond (1.2 Å). Whereas in the product (**3**), the interatomic distance is shorter (1.3 Å) than it would be for a single carbon-oxygen bond (1.4 Å), suggesting a partially conjugated double bond. All information regarding dihedral angles and bond distances is provided in appendix B . These observations apply to each of the investigated functionals.

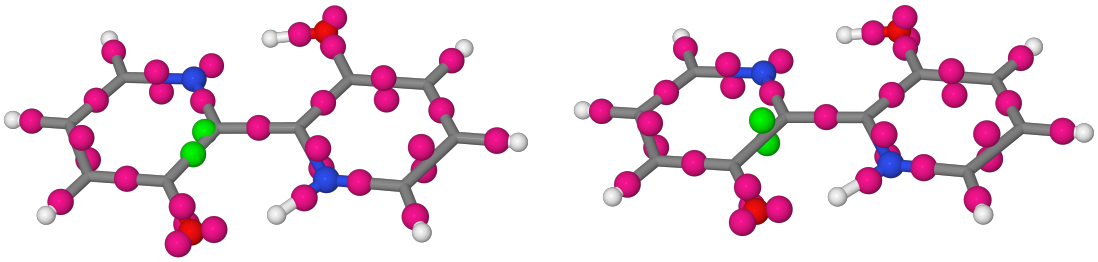

(a) Keto-eno intermediate (**2**) Cs (b) Ts2, Cs

Figure 4-4: Boys localized molecular orbitals at M06/sdall level of theory

The peculiar behavior of certain functionals (BLYP, M06L, M06) in the characterization of the reaction mechanism is to be searched in their long-term exchange and correlation balance. The characterization of the Boys type centroids in the keto-eno intermediate (**2**) allows to graphically describe the position of the localized molecular orbitals (LMO, Figure 4-4). The three functionals under examination (M06, BLYP and M06L) define C_s symmetry for the keto-eno intermediate (**2**) and for the second TS.

The aromaticity of the two rings is reconstructed during the tautomerization of keto-enol to dienol. This process is observable via the characterization of Localized Molecule Orbitals in the TS and, in the case of a step wise mechanism, in the keto-

enol intermediate. The LMOs for M06 functional are reported in Figure 4-4. In the ket-enol intermediate (Fig. 4-4a) the ring with the protonated oxygen is aromatic while the ketone substituted ring has two double bonds and two doublets (green) localized one on the beta carbon (0.23 Å) and the other one on the inter-nuclear axes (0.76 Å). Going from the minimum to the second ts (ΔE=0.28 kcal/mol), the aromaticity is rebuilded: the position of the two centroids changes, both placing themselves at the same distance to the beta carbon (0.56 Å, Fig. 4-4b) but outside the inter-nuclear axis, just above and below of the molecular plane.

The functionals M06, BLYP and M06L describe a saddle point for structures that the other functionals recognise as decreasing in energy. Indeed, the single point energies calculated for all the other studied functionals shows how the energy of the structure relative to the ts2 is lower than the energy of the keto-eno intermediate (**2**, Table B.3).

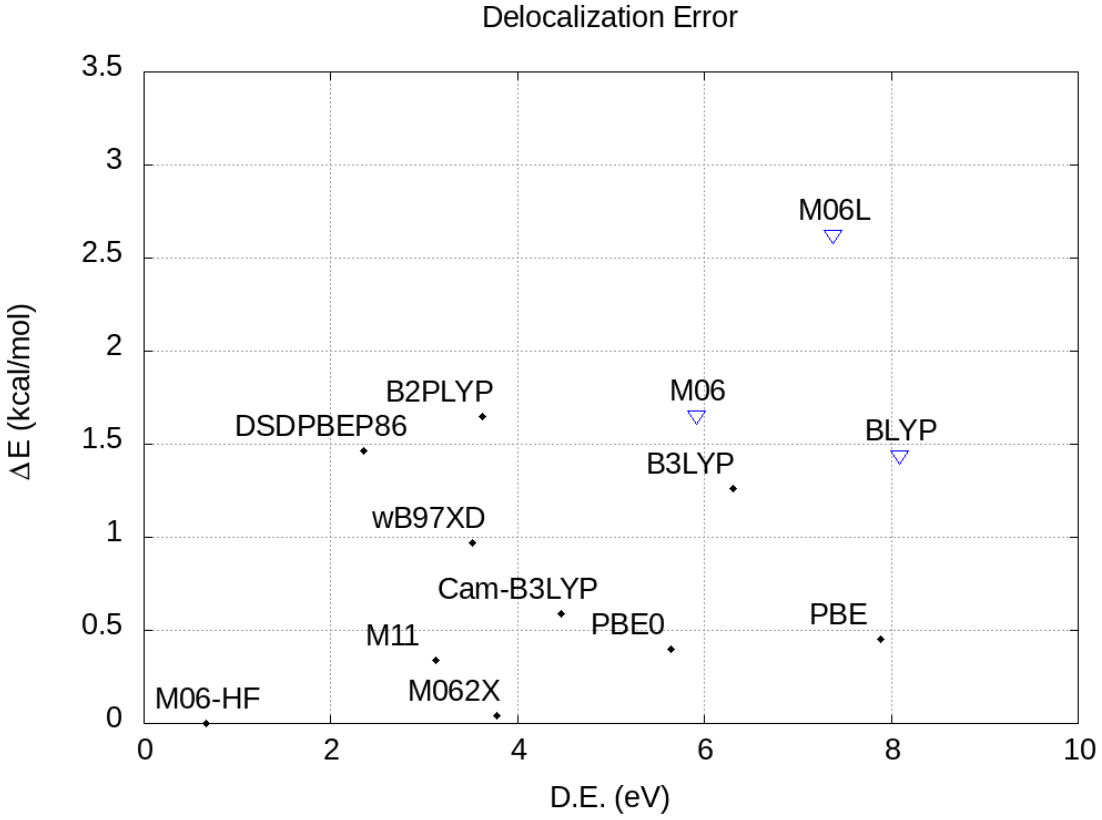

Figure 4-5: Activation energy (kcal/mol) as a function of the delocalization error (eV.) for the investigated functionals: concerted reaction mechanism ($\cdot$); step wise reaction mechanism (∇)

The evolution of energy and the determination of the reaction mechanism cannot be directly attributed only to the percentage of exact HF exchange in the functional. Therefore, it was chosen to characterize the activation energies of each functional (expressed in kcal/mol) as a function of their own delocalization error (eV) (Fig. Figure 4-5). The delocalization energy is determined by comparing the ionization energies of a cluster of non-interacting He atoms to those of a single He atom. This difference is related to a delocalization error[19,152,153].

The comparison between the activation energy relative to the initial transition state and the delocalization error (Figure 4-5) reveals that functionals that identify a stepwise reaction mechanism have a high activation energy (above 1.3 kcal/mol) and a large delocalization error (around 6 eV). Significant delocalization error in functionals results in an erroneous description of the electronic density, leading to the definition of a minimum (**2**, 4-4a). The keto-eno intermediate has an asymmetrical electronic structure between an aromatic ring and a cycle with an electron doublet located on the beta carbon of the ketone. This behavior can also be observed in the variation of partial charges between the diketo tautomer (**1**) and the first transition state, as mentioned previously. Compared to their corresponding functionals that describe a concerted reaction mechanism, the ESP charges of functionals that describe a step-by-step process exhibit a small degree of variation. This tendency not to delocalize the charges on the entire ring, as with the keto-enol intermediate (**2**), results in the stabilization of localized electronic densities on the atoms.

4.2.2 ADMP

Static calculations prove how the xc-functional's long-term balance of exchange and correlation determines the reaction mechanism. The free energy surface (FES) investigation aims to confirm that these variations in determining the reaction mechanism persist even in simulations at finite temperature. Particularly since the tautomerization reaction has low activation energies that are easily overcome at room temperature, especially the second TS. Admp simulations[26] are performed with xc-functionals of type GGA (BLYP, M06L), Global Hybrids (M06, BH&HLYP, PBE0, B3LYP, M062X), and Range Separted Hybrids (Cam-B3LYP, ωB97XD) using a 6-

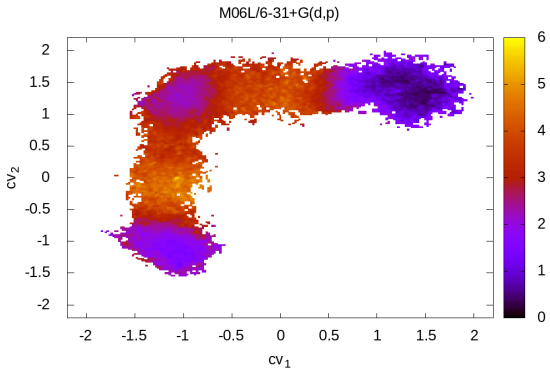

Figure 4-6: M06L fes ΔE(kcal/mol)

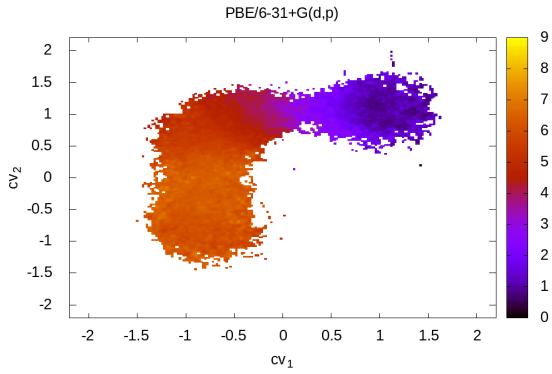

Figure 4-7: PBE fes ΔE(kcal/mol)

31+G(d,p) basis with the diffused component only on oxygen and nitrogen. The reaction mechanisms for the xc-functionals under investigation were validated using the 6-31+G(d,p) basis set, with the exception of the functional BLYP, which produced results that were inconsistent with those obtained using the 6-311+G(d,p) basis set. As a result, the characterization of the FES with this xc-functional has not been computed.

The surface generated with the xc-functional M06L (Fig.Figure 4-6) is characterised by the presence of three minima, one for the diketonic form, one for the keto-enol intermediate, and one for the dienol tautomer. The minima are connected by two transition states representing the transfer of the two protons associated with each of the two collective variables. The energy color gradient shows that the kinetic determining step is the first, as predicted by the static calculations (TS_1=2.6 kcal/mol; TS_2=0.8 kcal/mol Table 4.2).

The static calculations done with the PBE functional identify a concerted reaction mechanism. The free energy surface (Fig.Figure 4-7) is defined by the presence of only one TS. The comparison of the surfaces shows how, due to the step wise character of the process, the collective coordinates that describe the two proton transfers are completely decoupled for the M06.

The study of the free energy surfaces computed for the Global Hybrid functionals reveals that the minimum associated with the keto-enol intermediate can be identified exclusively for the M06 functional (Figure 4-8), consistent with the results of the static calculations. The remaining functionals describe a synchronized reaction

Figure 4-8: M06

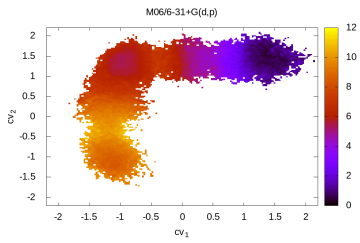

Figure 4-9: M062X

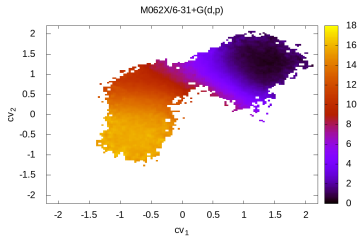

Figure 4-10: BH&HLYP

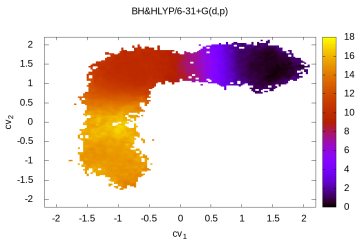

Figure 4-11: B3LYP

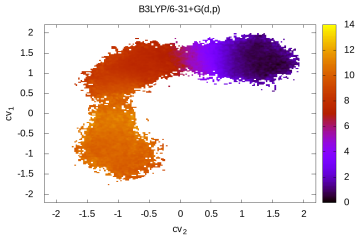

Figure 4-12: PBE0

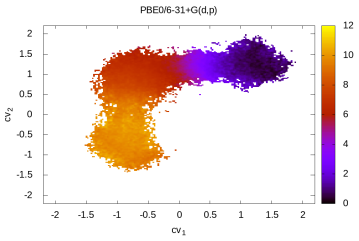

mechanism with different degrees of coordination. The M062X reaction mechanism is characterized by a low activation energy and small TS dipole value (0.04 kcal/mol and 0.35 Debye respectively). Involving a coupling between the two proton transfers, the computed FES (Figure 4-9) reveals a wider surface for the values between the zeros of the two collective variables. The two proton transfers appear graphically uncoupled for the B3LYP and BH&HLYP functionals (Figure 4-10, Figure 4-11). Consistent with the results of the static calculations, the comparison of the two free energy surfaces reveals that BH&HLYP is characterized by a minimum of the dienol form that is more stable than B3LYP (-15.9 and -9.7 kcal/mol respectively). The PBE0 (Figure 4-12) describes a concerted reaction mechanism with a lower activation energy and partial coupling between the two proton transfers, as described by the shape of the surface shared by the two collective variables.

Analyzed range-separated functionals (Cam-B3LYP and ωB97XD) show comparable behavior. Both the free energy surfaces (Figure 4-14 and Figure 4-13) are characterized by the presence of two minima connected by a single transition state; the coupling between the two proton transfers is comparable such as the dieno tautomer's stability.

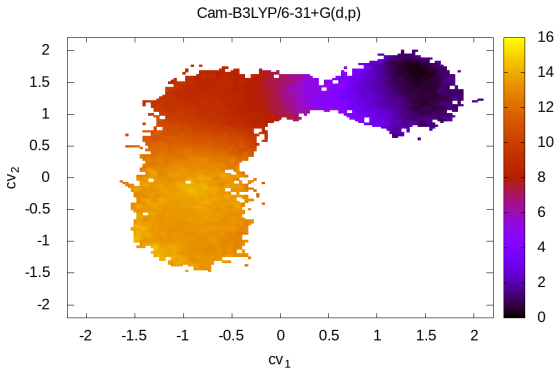

Figure 4-13: Cam-B3LYP fes- ΔE(kcal/mol)

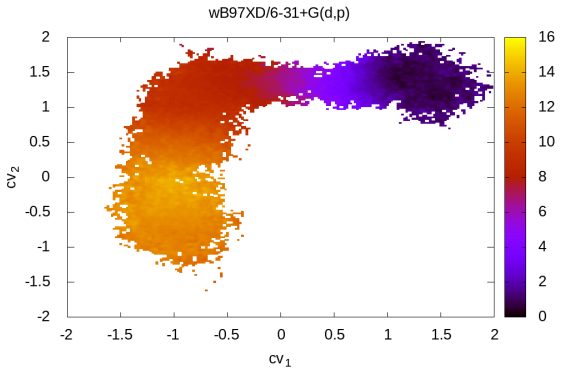

Figure 4-14: ωB97XD fes ΔE(kcal/mol)

The computed free energy surfaces show a correspondence in the determination of the reaction mechanism between the static calculations and the finite temperature simulations. The minimum energy paths (mep) of the computed Free Energy Surfaces provide a more accurate comparison of the various trends (Figure 4-15). The Global Hybrid and Range Separated functionals, with the exception of the M06, depict a concerted reaction mechanism with varying degrees of synchrony. The slope of the surface in the region between the first TS and the second barrier-free proton transfer is what distinguishes the various functionals. The M062X and BH&HLYP functionals provided less stability of the diketo tautomers, resulting in a greater energy difference between their two tautomeric forms, which defines a steeper surface slope between the two proton transfers. Functionals that stabilize the diketonic form and lower the energy difference between the two tautomeric forms define a gradually sloping line with a minimum slope of M06, which describes a step wise mechanism (Fig. 4-15a). Both analyzed GGA functionals stabilize the diketonic form in the same manner. This provides a better understanding of the contribution made by the delocalization error, which, in the case of M06L, stabilizes the intermediate keto enol and results in the identification of two TS, one for each proton (Fig. 4-15b).

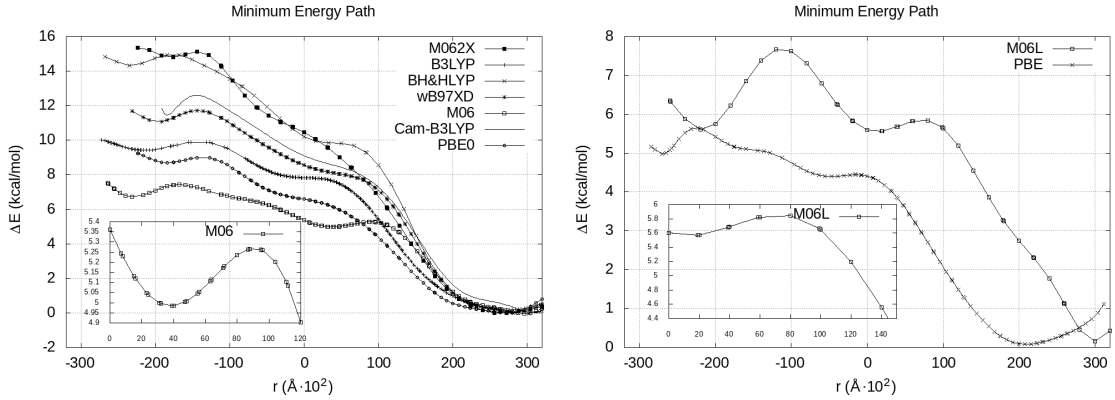

(a) Global Hybrids and Range-Separated (b) GGA

Figure 4-15: The minimum energy path was established by fitting the computed fes with a fifth order polynomial. ($E = \sum_{j=0}^{k} |p(x_j) - y_j|^2$) and r is defined as a linear combination of the two collective variables;

4.3 Conclusions

This study shows that the choice of exchange-correlation functional at a given level of theory can provides ambiguous results when the nature of the chemical reaction is able to reveal the deficiencies of the adopted xc-functionals. It is essential to distinguish between theoretical model defects and a discrepancy in the obtained results related to approximations. In the first instance, as illustrated by the MP2 method for aromatic systems that lose planarity[144–146] (see also the results reported in Appedix B), a molecule that is incompatible with the chemical nature of the process is obtained and this contradicts the experimental evidence. In the second instance (see, for instance, the results with BLYP, M06L, and M06), the xc-functional describes structures that are compatible with the chemical nature of the process but incompatible with the results reached at a higher level of theory. The obvious solution is to use more theoretically accurate xc-functionals where the adoption of functionals extending from range-separated to double hybrids uniquely establishes a concerted mechanism for the reaction. However, the computational cost and the lack of availability might hinder the use of this strategy.

The results obtained in the characterization of the reaction mechanism and the free energy surface with the xc-functionals BLYP, M06L, and M06 are attributable to an imprecise description of the electron density, quantified by the delocalization

error, in correspondence with some reactive centers of the reaction (C_β). The computed reaction mechanism is substantially correlated with both the first transition state energy and the delocalization error of the chosen functional. The mechanism of the stepwise reaction is predicted by xc-functionals with high levels of both attributes.

Another potential source of error is the use of a too-small basis set, which can be easily verified by increasing the size of the basis set at the expense of increased computing costs. In the reaction under investigation, we have shown that the functional M06 optimizes the keto-enol intermediate (suggesting a stepwise mechanism) despite the presence of a pvqz basis set[151] and very tight convergence criteria as with the smaller basis set.

This issue cannot be handled with a single solution. Once the framework of the theory has been established, it is advisable to compare more functionals; discordant results imply that the system requires a higher level of theory to achieve the required consistency in the results.

Chapter 5

The effect of Mg^{2+} substitution on Posner's clusters.

This chapter summarizes the computational study of an extensive research covering the synthesis and experimental characterization of Mg-substituted Amorphous Calcium Phosphate nanoparticles (ACP). The ACP is particularly important among the numerous forms of calcium phosphate (CaP) found in nature and in living organisms.[154] Given its chemical and structural diversity, ACP plays an important biological role as a transient intermediate in the formation of the apatitic inorganic matrix of bones and teeth, as well as in the formation of functional structures such as casein micelles, calciprotein particles, and amorphous nanoparticles in the small intestine.[155] ACP has a short-range order that corresponds to the so-called "Posner's Cluster" $Ca_9(PO_4)_6$[156], which is thermodynamically unstable and spontaneously evolves into crystalline forms of CaP, such as hydroxyapatite (HA, $Ca_{10}(PO_4)_6(OH)_2$) and brushite ($CaHPO_4{\cdot}2H_2O$). The ion Mg^{2+} can be integrated into the amorphous cluster to generate Amorphous Magnesium Calcium Phosphate (AMCP) particles, which is significant not only for the crystallization pathway of ACP but also for the structural properties of the amorphous phase itself. It has been shown that a variation in the Mg/Ca ratio from 0 to 0.04 increases the lifetime of the amorphous phase during the conversion kinetic of ACP to HA by a factor of 4 to 9 depending on the temperature.[157] Other works indicate that the creation of Mg-phosphate complexes is responsible for the improvement of the amor-

phous' lifespan.[158] Different interpretations of this behaviour have been proposed in numerous published works throughout the years, some of which are reported in the following. Abbona and Baronnet theorized that the first Mg^{2+} substitution for Ca^{2+} in Posner's clusters generates mechanical stresses and inhibits HA nucleation, in addition to the effect of Mg^{2+} adsorption onto the surfaces of ACP and apatite crystallites.[159] Yang *et al.* hypothesized that the formation of Mg-phosphate ion pairs decreases the thermodynamic driving force for ACP nucleation and subsequent crystallization to HA,[160] while other hypothesized that Mg^{2+} may also have an influence on improving HA's solubility.[161] Ding et al. investigated the effect of Mg^{2+} ions on the various stages of HA precipitation from ACP precursor particles, which can be either adsorbed or absorbed.[162]

The regulation of AMCP particles with a fitted Ca/Mg ratio and the knowledge of their structural characteristics are crucial to the manufacture of particles with a predefined stability. The purpose of this study is to investigate how the Ca/Mg ratio and total cation concentration influence the characteristics of precipitated amorphous phases.

The experimental study consisted of a systematic analysis of 15 different syntheses in which the reagent solution concentrations were adjusted to test five different Ca/Mg ratios (0.4, 0.7, 1, 2, and 3) at three different Mg^{2+} concentrations for each ratio (10, 50 and 100 mM). The resulting particles were investigated for crystallinity, shape, elemental content, and thermal stability in order to produce AMCP nanoparticles with a customized elemental composition. The Appendix C contains all information regarding the preparation of samples and the list of measurements performed. Regarding the discussion of the experimental results, reference is made to the published article.[163]

Computational methods were utilized to provide atomic-level insight into the effect of Mg^{2+} concentration on the structure and stability of ACP clusters, revealing new knowledge regarding the function of Mg^{2+} substitution in ACP. A comprehensive analysis was undertaken by optimizing a series of model clusters with varying Mg^{2+}/Ca^{2+} ratios, beginning with Posner's cluster and ending with the fully Mg-substituted cluster.

The results prove that AMCP particles with configurable crystallinity and composition can be produced. The computational analysis and the investigation of the heat-induced crystallization of AMCP reveal that the stability of the particles depends on the degree of Mg^{2+} substitution in the cluster. The reported results shed light on the effect of Mg^{2+} on ACP characteristics at various structural levels and may provide useful suggestions for the creation and design of AMCP particles with a particular Ca/Mg ratio.

5.1 Computational Details

The cluster structures have been obtained starting from the experimental structure of the Brushite crystal (box 5.8x15.1x6.9 Å, $\alpha = \gamma$=90°, β =116.4°, Ia)[164]. The atomic positions have been optimized with the Quick Step module of CP2K employing the LDA exchange and correlation functional within the Padé approximation.[165,166] The wave functions for each atomic species have been described through a DZVP-MOLOPT basis set[167], whereas the electron density has been represented with a plane wave expansion with a 340 Ry cutoff. The super-cell is made up by 3x1x3 unit cells. The calculations show a complete agreement between the computed and experimental structure.[164]

The optimized brushite crystal formed the basis for sampling a Posner cluster with nine metal-occupied sites and six phosphate groups, two of which have been hydrogenated according to the experimental results.[163] This Posner-like cluster constitutes the starting structure for the optimization of structures with different Ca/Mg ratios, whose values are reported in the Table 5.1 . For each ratio, 4 structures were generated and optimized which differ only in the position of the Mg atoms. In the Table 5.1 the simulated clusters are identified as An', where the presence of the apex indicates a chemical composition of the cluster close to that obtained in the synthesized samples An (Table C.1 in the Appendix C). The "N_{Ca}" or "N_{Mg}" label indicates the number of Ca or Mg ions present in the simulated cluster, respectively.

To investigate the structural properties of selected magnesium and calcium phosphate clusters, DFT calculations at the B3LYP/6-31G(d) level of theory with tight

Table 5.1: are reported the different ratio Ca/Mg, Ca/P and Mg/P for the analysed Posner's clusters. Four different arrangement have been chosen for each sample.

	Ca/Mg	Ca/P	Mg/P	n_{Ca}	n_{Mg}
A'_0	0.12	0.16	1.33	1	8
A'_3	0.5	0.5	1	3	6
A'_6	0.8	0.66	.83	4	5
A'_1	2	1	0.5	6	3
A'_7	3.5	1.16	0.33	7	2

convergence criteria were performed using the Gaussian suite of programs (G16,[28]). The distances between oxygen atoms and metal ions were later determined by analyzing the optimized structures. The interaction energy between a particular Mg^{2+} ion and the remaining cluster has been estimated using the counterpoise correction method.[168,169]

5.2 Results and discussion

This study shows that the different crystallization temperatures observed in AMCP samples do not correspond to a phase transition. The plot of the crystallization temperature (maximum of the first peak) versus the Ca/Mg ratio of the particles shown in Figure 5-1 (left y axis) indicates that the crystallization temperature increases as the Ca/Mg ratio of the particles decreases. This assumption is valid until a Ca/Mg ratio of about 2. Incorporating Mg2+ into the lattice of the particles stabilizes the amorphous phase against heating, in addition to its known stabilizing effect in the conversion of amorphous to crystalline calcium/magnesium phosphates in solution.[170]

The computational analyses further support these results. The computed interaction energies between the inner site of the Mg^{2+} ion and the remaining Posner's cluster for various Ca/Mg ratios are shown in Fig.Figure 5-1 (right y axis). For the homogeneous system Ca_0 (consisting of exclusively magnesium cations), the inner site's interaction energy with the cluster is roughly -357 kcal/mol. In contrast, the counterpoise correction energy for the cluster with two Mg^{2+} and seven Ca^{2+} (A7', Table 5.1) is -552 kcal/mol. The observed trend validates the stabilizing effect of

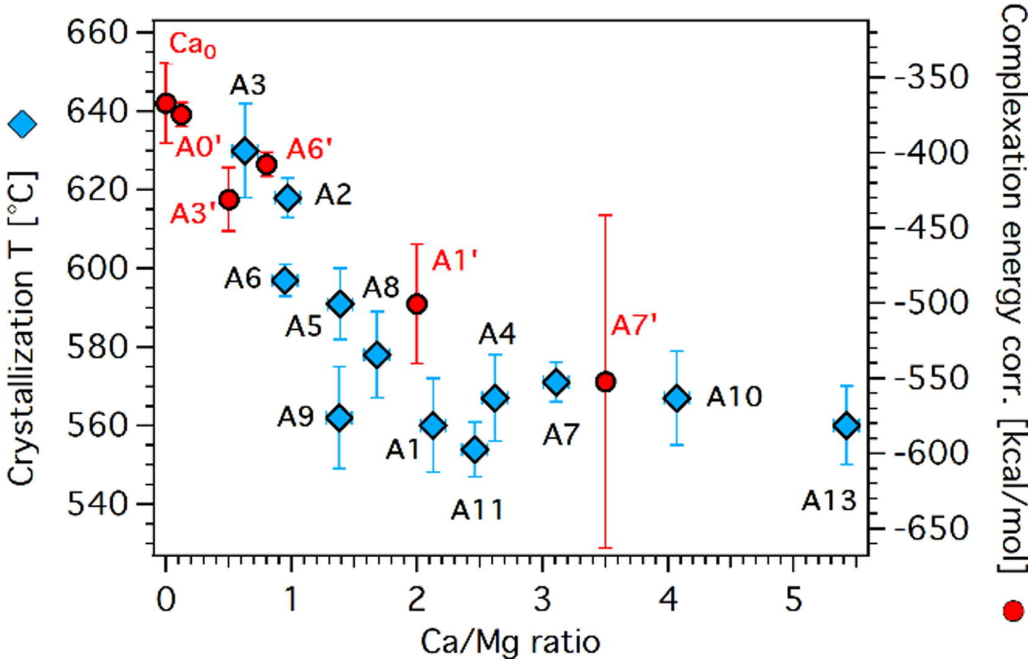

Figure 5-1: Plot of the crystallization T (1st peak maximum) vs the Ca/Mg ratio (left y axis). The blue diamond markers represent the average values ± standard deviations (see the materials and methods section). The plot also shows the counterpoise correction energy (red dots) as a function of Ca/Mg ratio. The error bars in calculations progressively enlarge due to the limit in configuration sampling.

the Mg^{2+} cation as calcium concentration increases. In fact, the binding energy of Posner's cluster increases (absolute value) with increasing calcium content. This trend can be explained qualitatively by the larger coordination effect due to the increased hardness of magnesium compared to calcium. This determines a decrease in intermolecular distances, including those involving Mg^{2+} ions. In this sense, clusters with a higher magnesium concentration have a greater electrostatic repulsion, and hence, lower binding energy.

The analysis of the Mg-O distances of the clusters in which Ca^{2+} ions are replaced by Mg^{2+} ions supports these findings (Table 5.1). As shown in Figure 5-2a, an increase in the magnesium concentration of the cluster causes a progressive stabilization of the contacts at Mg-O distances higher than 4.0 *AA*. In contrast, starting with a completely magnesium-substituted Posner cluster and increasing the quantity of Ca^{2+} leads to the loss of structure for Ca-O distances higher than 4.0 Å. (Figure 5-2b). As expected, this behavior can be explained by the increased hardness of Mg^{2+} ion compared to Ca^{2+} ion.

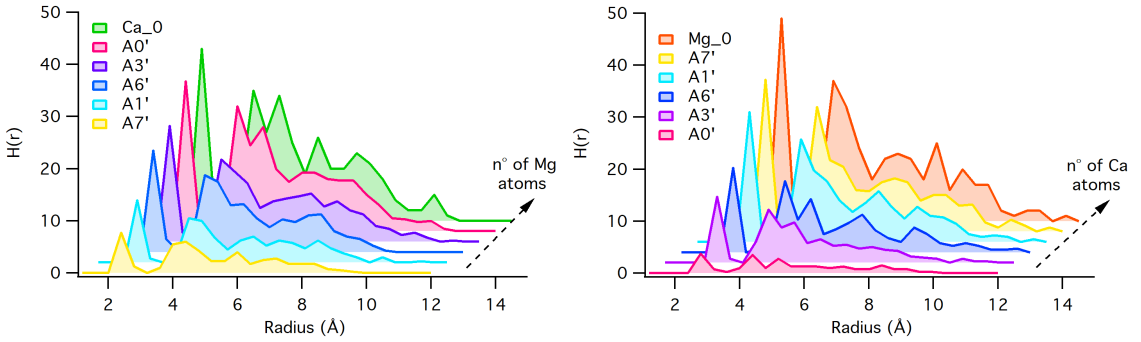

(a) Mg-O (b) Ca-O

Figure 5-2: Distribution of the M^{2+}-O interactions

Keeping the cell parameters constant, the comparison of atomic locations in the two optimized crystals validates these results, as shown in Table 5.2 and Figure 5-3. All inter-molecular lengths between the Mg^{2+} ion and its initial neighbors are less than their counterparts in the calcium crystal. The reduction in distances is consistent with the optimization calculations performed on Posner's clusters.

The structural properties of the precipitated AMCP nanoparticles were also investigated using a multi-technique approach. To prevent the formation of crystalline brushite, the synthetic conditions necessary to produce totally amorphous particles were identified. Despite the fact that XRD, FT-IR, and SEM analyses did not disclose any significant differences between the prepared particles, the elemental composition research indicated a variable Ca/Mg ratio in the particles, which was associated with the synthesis conditions. The presence of Mg^{2+} in the particles retards the crystallization heat of AMCP, demonstrating that this ion has a stabilizing function when incorporated into the ACP structure. These findings are supported by simulations of Posner-like clusters with increasing quantities of magnesium. Simulations of the Mg-O and Ca-O distances in the clusters, as well as the interaction energies, reveal that the addition of Mg atoms stabilizes the cluster. The submitted results contribute to the clarification of the effect of Mg^{2+} substitution in ACP-based systems and the establishment of guidelines for easy synthetic techniques to manufacture AMCP nanoparticles with a tailored elemental composition.

Mg^{2+}	Brushite-Mg	Brushite
O_1(O)	2.03	2.37
O_2(OH)	2.08	2.38
O_3(O)	2.04	2.51
O_4(OH)	2.14	2.51
O'(O)	2.36	2.45
O"(OH)	2.57	2.67
Mg^{2+}"	3.91	4.04

Table 5.2: Distances (Å) between metal cation and first neighbors in optimized Brushite-Mg and Brushite crystal structures.

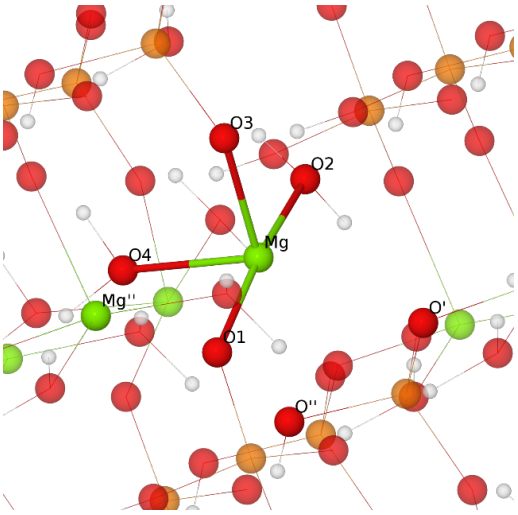

Figure 5-3: Identification of atoms in Brushite-Mg structure

THIS PAGE INTENTIONALLY LEFT BLANK

Chapter 6

What is the structure of adenine adsorbed on a gold (111) surface? A computational investigation

The adsorption of biological molecules on the nanostructured surfaces of noble metals is crucial for diagnostic applications in the medical, biological, and technological areas.[171,172] A proper knowledge of the interactions between adsorbate and metal surfaces is required for the correct development of systems based on molecular interactions with surfaces. Adenine, a crucial component of nucleic acids, is one of the most extensively studied biomolecules, and it can be utilized to validate a computational methodology.[173–177] The orientation of adenine on the metal surface is a controversial topic, as the interaction can take place with multiple nitrogen atoms. Indeed, contradictory articles continue to be produced on this apparently simple subject.[173,178–180]

The adsorption of adenine on gold surfaces has been investigated by means of the density functional theory (DFT). Absorption of adenine can occur via physisorption and chemisorption. Through the characterization of the electronic structure, it is possible to characterize the two processes and then calculate observables for comparison with the experimental data, such as the vibrational spectrum.[181] In the present work, to characterize the adsorption mechanism, we consider the explicit surface, and this represents a significant improvement compared to the previous

works reported in the literature, which consider the metal surface made of a single atom or small clusters.[182,183]

6.1 Computational Details

The gold surface was modelled starting from the fcc crystal's coordinates reported in the American Mineralogist Crystal Structure Database[184](Fm3m, 4.078 Å). The primitive cut (111) of the cell was therefore obtained and converted into orthorhombic to reduce the computational cost of the simulation. On the resulting Au(111) surface (108 atoms for 17.35x15.03x7.02 Å, 3 layers), an adenine molecule was positioned at 4 Å with its center of mass aligned with the geometric center of the surface.

The potential energy surface is characterized by several minima characterized by different orientations and distances of the adenine with respect to the gold surface, to explore this complex phase space it is necessary an accelerated simulation technique, in this work, we opted for the metadynamics method.[29,185] To characterize the various local minima, two collective variables (CV) have been defined.

The first CV describes the interaction between the nitrogen atoms, that may interact with the gold surface when adsorption might occur, and the atoms of the gold surface. The CV_1 is chosen to be approximately zero when the molecules are far from the layer and to become larger than zero, but always smaller than one, when one or more nitrogen atoms get closer to the layer. With the given parameter the coordination number of the CV_1 start being larger than zero for distances below 4 Å.

$$CV_1 = \frac{1}{N_N} \sum_{iN} \sum_{jAu} \frac{1 - \left(\frac{r_{ij}}{R_0}\right)^{nn}}{1 - \left(\frac{r_{ij}}{R_0}\right)^{nd}} \tag{6.1}$$

The parameters of CV_1 are: nn =8, nd =14 , and 1.6 Å for the interaction radius (R_0) (the index iN runs on the nitrogen atoms and the index jAu on the gold atoms). The second collective variable (CV_2) is defined as the distance between the adenine center of mass and the geometric center of the plane defined by the external gold layer.

The metadynamics simulation was carried out at the BLYP/DZVP-MOLOPT level of theory, including the D3 dispersion contribution proposed by Grimme[131] with a cutoff of 350 Ry for the plane wave expansion[186]. The simulation is performed at constant temperature (300 K, $\Delta T = \pm 20$K), during the simulation a Nosé-Hoover chain thermostat implemented in CP2K (version 8.2) was adopted. The Nosé-Hoover chain thermostat parameters are: chain lenght (3), number of multiple timesteps to be used for the Nosé-Hoover chain (2), the Yoshida parameter (3) and the time constant (1 ps). The initial configuration for each dynamic was generated by optimizing, at the same level of theory, a configuration extracted from an NVE dynamics performed to verify the integration time step. The dynamics of the biased NVT have been performed using an integration time step of 1 fs for 10 ps. These simulations are preceded by an equilibration run of 5 ps. The cell size is 17.34x15.03x25 Å in which, the atoms of three layers of gold are fixed and Periodic Boundary Conditions have been adopted. The long range electrostatic interaction has been computed with the smooth particle mesh Ewald using beta-Euler splines.[187] The convergence criteria for the SCF is tight (10^{-7}) and the value for the grid is set to 5.

6.2 Results and discussion

Surface adsorption of adenine is regulated by the interaction of nitrogen functional groups with gold atoms. In addition to physisorption, we wanted to test if adenine could bound to the surface of metal (111). For this purpose, two tautomeric forms of adenine (Figure 6-2) have been chosen: the protonated N9 form (Fig. 6-1a), which is the most common and of most biological relevance, and, the protonated N7 form (Fig. 6-1a), which eliminates the hydrogen steric hindrance in order to invstigate a possible chemisorption. The sum of the covalent and vdW radii of nitrogen (0.75 Å, 1.55 Å) and gold (1.44 Å, 1.66 Å) is respectively 2.19 Å and 3.21 Å. This results suggest that for a N-Au distance less than their van der Waals radius we can consider the absorption with a covalent contribution that increase decreasing the distance and therefore refer to the adsorption as chemical.

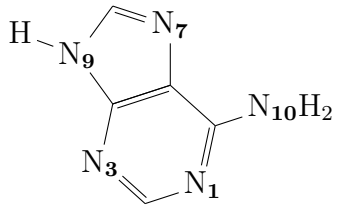

(a) N9 -467.451400335 Hartree

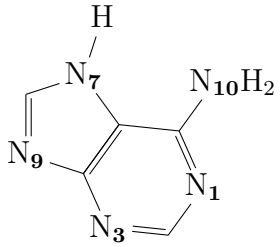

(b) N7 -467.438173105 Hartree

Figure 6-1: Tautomerism in adenine

The two tautomeric forms of adenine show different behaviors. The adenine protonated in N9 (Fig. 6-1a) is the stable form (the difference in energy between the two isolated molecule is $\Delta E = \sim 8$ kcal/mol). This result is in agreement with the experimental evidence which indicates the protonated adenine in N9 as the most widespread tautomeric form. In the scientific literature, the tautomerization N9-N7 has been investigated in the context of DFT[188] showing that the tautomerization process is mediated by three water molecules, and the barrier is approximately 20 kcal/mol.

The optimized structure of the protonated adenine in N9 (Fig.6-2a) displays the out-of-plane interaction between the molecule and the surface. This structure constitutes the input of the thermalization run. The coordination of nitrogen in the NH_2 group is interesting to examine. The distance between the nitrogen atom and the nearest gold atom on the surface is $\sim$ 2.7 Å, meanwhile the $\angle$ HNH angle measures 112°degrees and the $\angle$ AuNH angle is 104.5°. This geometry suggests that nitrogen is coordinated tetrahedrally.

The optimization of the protonated adenine in N7 (Fig.6-2b) clearly shows how the molecule is arranged perpendicular to the surface (the distance is $\sim$ 2.5 Å). The adenine substrate system in this case is overall more stable than the analogous system with the adenine protonated in N9 (the energy difference between two optimized structures is about $\sim$ 12 kcal/mol). The outcomes of the *ab initio* molecular dynamic simulations, for both tautomeric forms of adenine, are consistent with the geometry optimizations. The interaction between N9 adenine and the gold surface happens largely through the out-of-plane electron density of the adenine molecule. The minima identified during the exploration of the phase space (Fig. Figure 6-3)

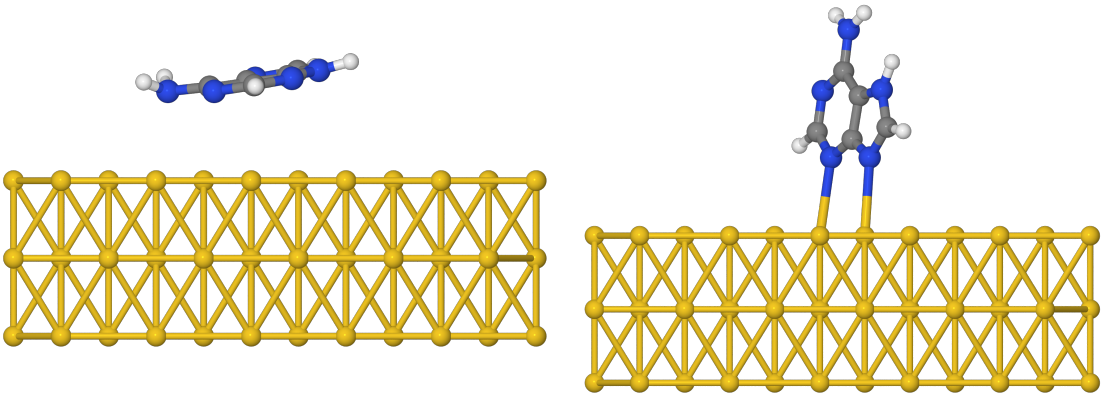

(a) Ade 1 N9 (b) Ade 2 N7

Figure 6-2: Potential Energy Path

differ in the type of out-of-plane contact that occurs between the molecule and the metal surface.

Three main minima have been identified (A, B, and C, Figure 6-3) on the potential energy surface, each of which corresponds to different out-of-plane interactions between adenine and the metal surface. The characterization of the structures associated with these three minima is done by comparing the graph of the potential energy with the values of the two collective variables (Figure 6-4).

Each of the main minima (A, B, C, Figure 6-3) corresponds to a maximum for the variable CV_1 (Fig. 6-4a) and a minimum for the variable CV_2 (Fig. 6-4b).

In the first minimum, marked by the letter A (around 2 ps, Figure 6-3), the adenine N9 is arranged parallel to the surface. At this minimum corresponds a local maximum for the CV_1 ($\sim$ 0.7, Fig. 6-4a) and a deep minimum for the CV_2 ($\sim$ 3Å, Fig. 6-4b). Following the trajectory of the dynamics, the adenine goes away from the surface, rotates on its N3-N10 axis (Figure 6-2), and then returns to it, as indicated by the minimum point B on the graph (Figure 6-3). The orientation of the molecule is always parallel to the surface. The interaction between the nitrogen atoms and the surface is not uniform, resulting in a distribution of peaks around the maximum value (at $\sim$ 4 ps) of the CV_1 (Fig. 6-4a), which corresponds to the

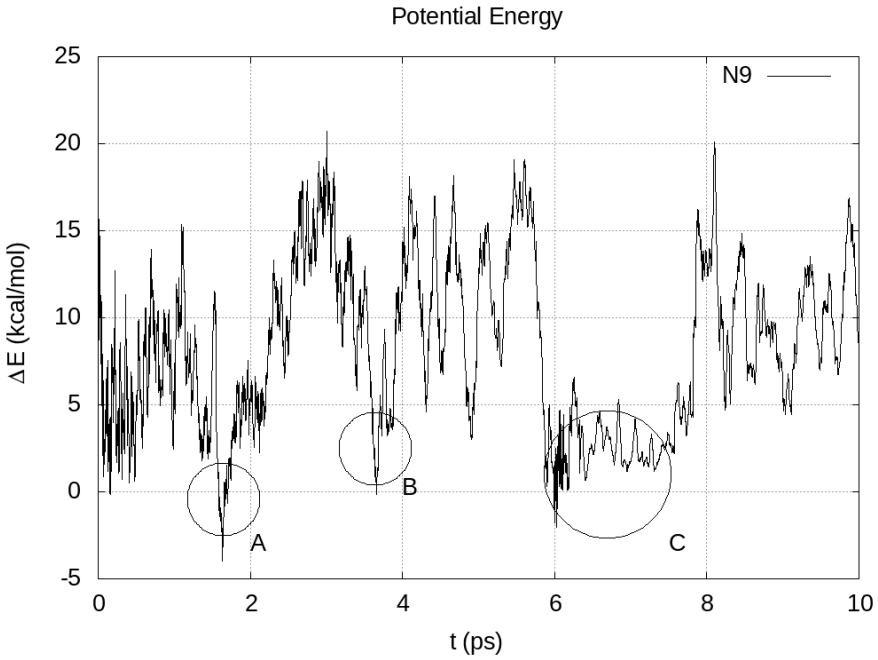

Figure 6-3: Potential Energy of the NVT simulation of adenine N9

minimum of the potential energy and the minimum of the CV_2 ($\sim$ 3Å, Fig. 6-4b). In the interval between 4 and 6 ps, the adenine moves away without rotating on its own axis; the molecule is tilted, and the interaction with the surface is mediated mostly by atoms N1 and N10 (Fig. 6-1a). The minimum of potential energy C constitutes the longest time interval in which the adenine molecule is physisorbed on the gold surface. The molecule is arranged parallel to the surface and all nitrogen atoms contribute uniformly to the physisorption as can be deduced by the distribution of the CV_1 values (Fig. 6-4a). The analysis of the adenine N9 trajectory and the values of the two collective variables show that the molecule is physisorbited and is aligned parallel to the gold surface 111.

The N9 adenine could not undergo chemisorption because the interaction between the N9 and N3 atoms does not form a stable minimum due to the steric hindrance of hydrogen.

The optimization of adenine N7 (Fig.6-2b) shows instead that the molecule is chemisorbed at the surface via nitrogen atoms N3 and N9. By analyzing the trends of the two collective variables (CV_1 Au-N coordination and CV_2 distance between the adenine center of mass and the geometric center of the surface), it is possible to

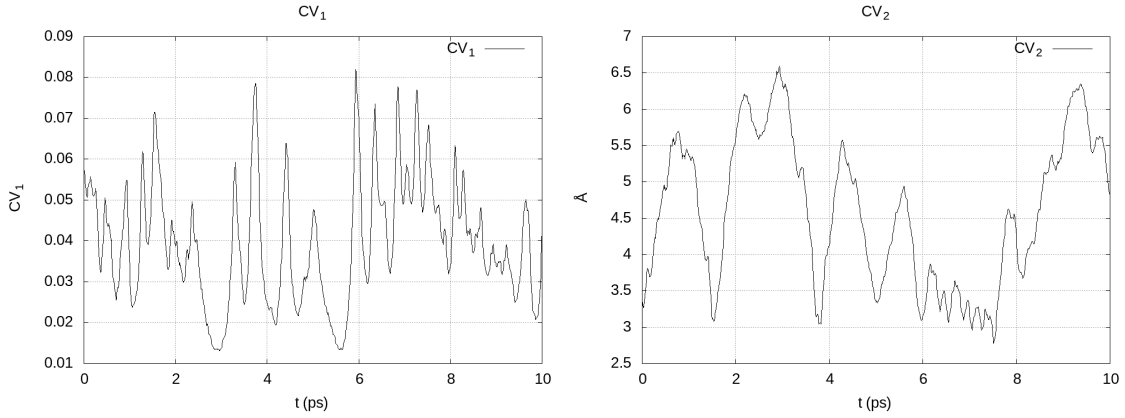

(a) CV1 (b) CV2

Figure 6-4: Collective variables of adenine N9

determine the trend of potential energy in the simulation of the second tautomeric form of adenine N7 (Fig. 6-1b). Between 0 and 4 ps, the molecule is oriented perpendicular to the surface. The interaction occurs because the nitrogen atoms n3 and n9 are not hindered by the presence of a proton and the fluctuations in potential energy are caused by the movement of the molecule over the metal surface. Chemisorption of adenine occurs about 4 ps, which corresponds to the deepest minimum of the potential. This arrangement of adenine corresponds to the maximum value of the variable CV_1 ($\sim$ 0.01) and the minimum value of the coordinate CV_2 ($\sim$ 2.4 Å). Between 4.5 and 6 ps, the molecule moves away from the surface and subsequently returns to it, as indicated by the CV_2 trend. It is fascinating to see that the local minimum at 7 ps in CV_2 corresponds with the local maximum of CV_1. In this instance, only the nitrogen atoms N1 and N10 are the closest to the surface; hence, the molecule is edgewise to the gold surface. Following the trajectory of the dynamics, the adenine returns perpendicular to the surface before desorption.

These results represent a preliminary research and suggest that the two selected tautomeric forms of adenine show a significantly distinct behaviors. Adenine N9 (Fig. 6-2a), the most biologically significant tautomeric form and the most stable (ΔE = 8kcal/mol), is physisorbited on gold surface (111). On the other hand, adenine N7 (Fig. 6-2b) induces chemisorption via nitrogen N3 and N9 (Fig. 6-1b). These results indicate that steric hindrance is a determining element in the adsorption process and suggest the existence of a tautomerization mechanism between the

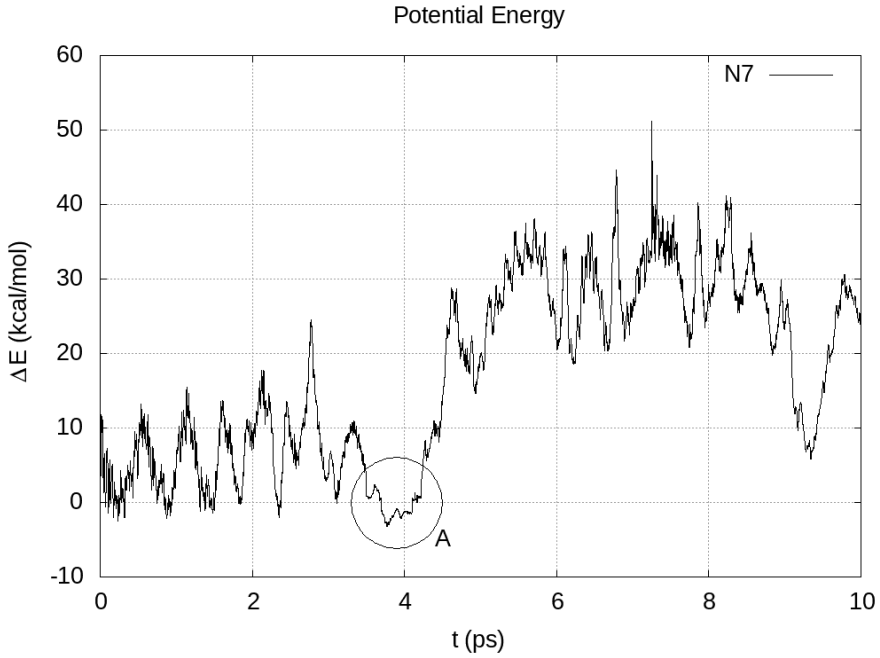

Figure 6-5: Potential Energy of the NVT simulation of adenine N7

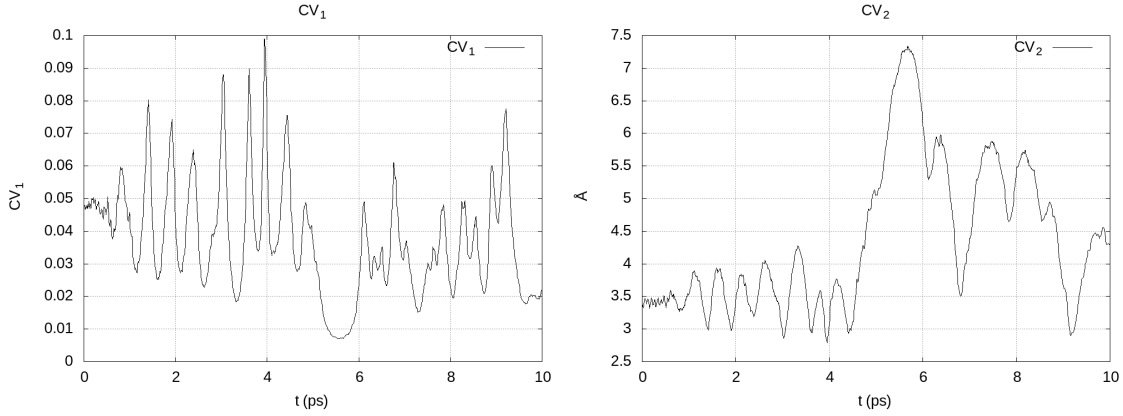

(a) CV1 (b) CV2

Figure 6-6: Collective Variables of adenine N7

two forms of adenine. In fact, the coexistence of the two tauotomeric forms would explain the occasionally contradictory conclusions reported in the literature. [173,178–180] The definition of a model that adequately characterizes the electron density would make it possible to examine the stability of the various tautomeric forms adsorbed on the surface and their relative orientations in order to assign intensities to the experimental spectra and to evaluate if the adsorption on the surface, in presence of water, will decrease the free energy barrier between tautomer N9 and N7.

THIS PAGE INTENTIONALLY LEFT BLANK

Chapter 7

Conclusion

This dissertation represents a significant part of my three-year PhD research. The primary objective was to achieve, through the study of electronic structure, a comprehension of reaction mechanisms and to provide useful information for the proper setup of the experiments. Taking inspiration from experimental research, we also attempted to diversify the nature of the investigated complex systems.

The extensive *ab initio* analysis of the Brandi-Guarna reaction enabled us to interpret the reaction profiles and explain the critical points highlighted by the experiments: the lack of regioselectivity in the cycloaddition reaction that produces the 5-isoxazolidine compound and the syntesis of the piridone and enaminone side product by the thermal rearrangement of the isoxazolidine.

The theoretical investigation of the tautomerization of [2,2'-bipyridyl]-3,3'-diol allowed to evaluate the accuracy of the exchange-correlation functional at a chosen level of theory. The tautomerization involves a double proton transfer between the nitrogen and carbonyl moieties. The computed reaction mechanism is substantially correlated with both the first transition state energy and the delocalization error of the adopted functional. The computational results show that only xc-functionals with high levels of both terms identify the stepwise mechanism of tautomerism.

The computational work, done in collaboration with an experimental research group, has produced a useful tool for the interpretation of the experimental results. The simplified computational model of amorphous nanoparticles proves that the addition of Mg^{2+} to Amorphous Calcium Phosphate samples stabilizes the amorphous

phase against heating. This effect is added to the known stabilizing effect on the conversion of amorphous to crystalline calcium/magnesium phosphates in solution. The *ab initio* optimization of Posner-like clusters with increasing concentrations of magnesium contributes to the elucidation of the effect of Mg^{2+} replacement in ACP-based systems and the formulation of guidelines for simple synthetic approaches to make ACP nanoparticles with a customized elemental composition.

The characterization of biologically relevant molecule adsorption processes on metal surfaces has been made possible thanks to *ab initio* modeling. Simulations show that the two selected tautomeric forms of adenine (N9 and N7) have substantially distinct behaviors. The steric hindrance given by the different protonated nitrogens (7, 9) is a decisive factor in the adsorption process and suggests the presence of a mechanism for tautomerization between the two forms of adenine. In fact, the coexistence of the two tauotomeric forms would explain the sometimes contradicting conclusions found in the scientific literature. The tautomerization reaction mediated by water has already been investigated in the gaseous phase. These results therefore suggest to investigate the water-mediated tautomerization mechanism for the adenine adsorbed on the metal surface. To develop a model that properly reproduces the experimental conditions: an adenine-containing solution on a gold electrode (111). In order to assign intensities to experimental spectra, the construction of a model that appropriately defines the electron density would allow to analyze the stability of the various tautomeric forms adsorbed on the surface and their relative orientations.

Bibliography

[1] T. Helgaker, P. Jørgensen, and J. Olsen. *Molecular electronic-structure theory.* John Wiley & Sons, 2000.

[2] A. Szabo and N. S. Ostlund. *Modern quantum chemistry: introduction to advanced electronic structure theory.* Dover Publications, 1996.

[3] R. G. Parr and W. Yang. *Density-functional theory of atoms and molecules.* Oxford University Press, 1989.

[4] F. Jensen. *Introduction to computational chemistry.* John Wiley & Sons, 2017.

[5] Ira N Levine, Daryle H Busch, and Harrison Shull. *Quantum chemistry*, volume 6. Pearson Prentice Hall Upper Saddle River, NJ, 2009.

[6] Michael P Allen and Dominic J Tildesley. *Computer simulation of liquids.* Oxford university press, 2017.

[7] Mark Tuckerman. *Statistical mechanics: theory and molecular simulation.* Oxford university press, 2010.

[8] Dominik Marx and Jürg Hutter. *Ab initio molecular dynamics: basic theory and advanced methods.* Cambridge University Press, 2009.

[9] O. Marchetti and H.-J. Werner. Accurate calculations of intermolecular interaction energies using explicitly correlated wave functions. *Phys. Chem. Chem. Phys.*, 10:3400–3409, 2008.

[10] L. Kong, F. A. Bischoff, and E. F. Valeev. Explicitly correlated R12/F12 methods for electronic structure. *Chem. Rev.*, 112:75–107, 2012.

[11] P. Hohenberg and W. Kohn. Inhomogeneous electron gas. *Phys. Rev.*, 136: B864–B871, 1964.

[12] W. Kohn and L. J. Sham. Self-consistent equations including exchange and correlation effects. *Phys. Rev.*, 140:A1133–A1138, 1965.

[13] J. P. Perdew and K. Schmidt. Jacob's ladder of density functional approximations for the exchange-correlation energy. *AIP Conf. Proc.*, 577(1):1–20, 2001.

[14] S. Grimme, J. Antony, S. Ehrlich, and H. Krieg. A consistent and accurate ab initio parametrization of density functional dispersion correction (DFT-D) for the 94 elements H-Pu. *J. Chem. Phys.*, 132(15), 2010.

[15] D. G. A. Smith, L. A. Burns, K. Patkowski, and C. D. Sherrill. Revised damping parameters for the D3 dispersion correction to density functional theory. *J. Phys. Chem. Lett.*, 7(12):2197–2203, 2016.

[16] S. Grimme, S. Ehrlich, and L. Goerigk. Effect of the damping function in dispersion corrected density functional theory. *J. Comput. Chem.*, 32(7):1456–1465, 2011.

[17] Aron J Cohen, Paula Mori-Sánchez, and Weitao Yang. Insights into current limitations of density functional theory. *Science*, 321(5890):792–794, 2008.

[18] John P Perdew and Alex Zunger. Self-interaction correction to density-functional approximations for many-electron systems. *Physical Review B*, 23 (10):5048, 1981.

[19] Yingkai Zhang and Weitao Yang. A challenge for density functionals: Self-interaction error increases for systems with a noninteger number of electrons. *The Journal of chemical physics*, 109(7):2604–2608, 1998.

[20] Paula Mori-Sánchez, Aron J Cohen, and Weitao Yang. Many-electron self-interaction error in approximate density functionals. *The Journal of chemical physics*, 125(20):201102, 2006.

[21] Adrienn Ruzsinszky, John P Perdew, Gabor I Csonka, Oleg A Vydrov, and Gustavo E Scuseria. Density functionals that are one-and two-are not always many-electron self-interaction-free, as shown for h 2+, he 2+, li h+, and ne 2+. *The Journal of chemical physics*, 126(10):104102, 2007.

[22] Paula Mori-Sánchez, Aron J Cohen, and Weitao Yang. Localization and delocalization errors in density functional theory and implications for band-gap prediction. *Physical review letters*, 100(14):146401, 2008.

[23] R. C. Tolman. *Statistical mechanics with applications to physics and chemistry*. The Chemical Catalog Company, Inc., 1927.

[24] D. G. Truhlar. Interpretation of the activation energy. *J. Chem. Educ.*, 55(5): 309, 1978.

[25] H Bernhard Schlegel, John M Millam, Srinivasan S Iyengar, Gregory A Voth, Andrew D Daniels, Gustavo E Scuseria, and Michael J Frisch. Ab initio molecular dynamics: Propagating the density matrix with gaussian orbitals. *The Journal of Chemical Physics*, 114(22):9758–9763, 2001.

[26] Srinivasan S Iyengar, H Bernhard Schlegel, John M Millam, Gregory A. Voth, Gustavo E Scuseria, and Michael J Frisch. Ab initio molecular dynamics: Propagating the density matrix with gaussian orbitals. ii. generalizations based

on mass-weighting, idempotency, energy conservation and choice of initial conditions. *The Journal of Chemical Physics*, 115(22):10291–10302, 2001.

[27] H Bernhard Schlegel, Srinivasan S Iyengar, Xiaosong Li, John M Millam, Gregory A Voth, Gustavo E Scuseria, and Michael J Frisch. Ab initio molecular dynamics: Propagating the density matrix with gaussian orbitals. iii. comparison with born–oppenheimer dynamics. *The Journal of chemical physics*, 117 (19):8694–8704, 2002.

[28] M. J. Frisch, W. Trucks, G., B. Schlegel, H., E. Scuseria, G., A. Robb, M., R. Cheeseman, J., G. Scalmani, V. Barone, A. Petersson, G., H. Nakatsuji, X. Li, M. Caricato, A. V. Marenich, J. Bloino, B. G. Janesko, R. Gomperts, B. Mennucci, H. P. Hratchian, J. V. Ortiz, A. F. Izmaylov, J. L. Sonnenberg, D. Williams-Young, F. Ding, F. Lipparini, F. Egidi, J. Goings, B. Peng, A. Petrone, T. Henderson, D. Ranasinghe, V. G. Zakrzewski, J. Gao, N. Rega, G. Zheng, W. Liang, M. Hada, M. Ehara, K. Toyota, R. Fukuda, J. Hasegawa, M. Ishida, T. Nakajima, Y. Honda, O. Kitao, H. Nakai, T. Vreven, K. Throssell, J. A. Montgomery, Jr., J. E. Peralta, F. Ogliaro, M. J. Bearpark, J. J. Heyd, E. N. Brothers, K. N. Kudin, V. N. Staroverov, T. A. Keith, R. Kobayashi, J. Normand, K. Raghavachari, A. P. Rendell, J. C. Burant, S. S. Iyengar, J. Tomasi, M. Cossi, J. M. Millam, M. Klene, C. Adamo, R. Cammi, J. W. Ochterski, R. L. Martin, K. Morokuma, O. Farkas, J. B. Foresman, and D. J. Fox. Gaussian 16 Revision C.01, 2016. Gaussian Inc. Wallingford CT.

[29] Alessandro Barducci, Massimiliano Bonomi, and Michele Parrinello. Metadynamics. *Wiley Interdisciplinary Reviews: Computational Molecular Science*, 1 (5):826–843, 2011.

[30] Alfred Hassner and Irishi Namboothiri. *Organic syntheses based on name reactions: a practical guide to 750 transformations*. Elsevier, 2012.

[31] Hg Wang. *Comprehensive Organic Name Reactions*. Wiley, 2010.

[32] Alberto Brandi, Stefano Cicchi, Franca M Cordero, and Andrea Goti. Heterocycles from alkylidenecyclopropanes. *Chemical reviews*, 103(4):1213–1270, 2003.

[33] Franca M Cordero, Francesco De Sarlo, and Alberto Brandi. 5-spirocyclopropane isoxazolidines as versatile intermediates in organic synthesis. *Monatshefte für Chemie/Chemical Monthly*, 135(6):649–669, 2004.

[34] VA Ostrovskii, GI Koldobskii, and RE Trifonov III. *Comprehensive Heterocyclic Chemistry III. Vol. 6*. Elsevier Oxford, UK:, 2008.

[35] Alberto Brandi, Stefano Cicchi, Franca M Cordero, and Andrea Goti. Progress in the synthesis and transformations of alkylidenecyclopropanes and alkylidenecyclobutanes. *Chemical reviews*, 114(15):7317–7420, 2014.

[36] A substructure search of the piperidine ring using the reaxys® chemistry search engine revealed over 949000 piperidine derivatives associated with any pharmacological data. in the list were included discrete monocyclic piperidines (> 59800), bicyclic indolizidines (> 2000) and quinolizidines (> 1300).

[37] Manfred Hesse. *Alkaloids: nature's curse or blessing?* John Wiley & Sons, 2002.

[38] Kate Prichard, David Campkin, Nicholas O'Brien, Atsushi Kato, George WJ Fleet, and Michela I Simone. Biological activities of 3, 4, 5-trihydroxypiperidines and their n-and o-derivatives. *Chemical biology & drug design*, 2018.

[39] Sara Källström and Reko Leino. Synthesis of pharmaceutically active compounds containing a disubstituted piperidine framework. *Bioorganic & medicinal chemistry*, 16(2):601–635, 2008.

[40] Steven WM Crossley and Ryan A Shenvi. A longitudinal study of alkaloid synthesis reveals functional group interconversions as bad actors. *Chemical Reviews*, 115(17):9465–9531, 2015.

[41] Nishanth Kandepedu, Isabelle Abrunhosa-Thomas, and Yves Troin. Stereoselective strategies for the construction of polysubstituted piperidinic compounds and their applications in natural products' synthesis. *Organic Chemistry Frontiers*, 4(8):1655–1704, 2017.

[42] Si-Yi Wu, Wei-Li Chen, Xiao-Pan Ma, Cui Liang, Gui-Fa Su, and Dong-Liang Mo. Copper-catalyzed [3+ 2] cycloaddition and interrupted fischer indolization to prepare polycyclic furo [2, 3-b] indolines from n-aryl isatin nitrones and methylenecyclopropanes. *Advanced Synthesis & Catalysis*, 361(5):965–970, 2019.

[43] Xiao-Pan Ma, Jie-Feng Zhu, Si-Yi Wu, Chun-Hua Chen, Ning Zou, Cui Liang, Gui-Fa Su, and Dong-Liang Mo. Cycloaddition of fluorenone n-aryl nitrones with methylenecyclopropanes and sequential 1, 3-rearrangement: An entry to synthesis of spirofluorenylpiperidin-4-ones. *The Journal of Organic Chemistry*, 82(1):502–511, 2017.

[44] AP Molchanov, TQ Tran, AV Stepakov, GL Starova, and RR Kostikov. Regioselective cycloaddition of c-carbamoylnitrones to methyl (e)-2-(2-phenylcyclopropylidene) acetate and methyl (e)-2-methylidene-3-phenylcyclopropane-1-carboxylate. *Russian Journal of Organic Chemistry*, 50(1):78–82, 2014.

[45] FM Cordero, C Vurchio, C Faggi, and A Brandi. Configuration-guided reactions: the case of highly decorated spiro [cyclopropane-1, $2'(3'$ h)-pyrrolo [1, 2-b] isoxazole] derivatives en route to polyhydroxyindolizidines. *Organic Chemistry Frontiers*, 3(12):1651–1660, 2016.

[46] Julia Malinina, Tung Q Tran, Alexander V Stepakov, Vladislav V Gurzhiy, Galina L Starova, Rafael R Kostikov, and Alexander P Molchanov. [3+ 2] cycloaddition reactions of arylallenes with c-(n-arylcarbamoyl)-and c, c-bis (methoxycarbonyl) nitrones and subsequent rearrangements. *Tetrahedron Letters*, 55(27):3663–3666, 2014.

[47] FM Cordero, C Vurchio, C Faggi, and A Brandi. Configuration-guided reactions: the case of highly decorated spiro [cyclopropane-1, $2'(3'$ h)-pyrrolo [1, 2-b] isoxazole] derivatives en route to polyhydroxyindolizidines. *Organic Chemistry Frontiers*, 3(12):1651–1660, 2016.

[48] In one case, likely because of steric hindrance, the h extraction occurred from the methylene α to ketone moiety leading to an α, β-unsaturated ketone (see ref. 14).

[49] Estael Ochoa, Matthias Mann, Dirk Sperling, and Jürgen Fabian. A combined density functional and ab initio quantum chemical study of the brandi reaction. *European Journal of Organic Chemistry*, 2001(22):4223–4231, 2001.

[50] Lorenzo Briccolani-Bandini, Alberto Brandi, Gianni Cardini, Riccardo Chelli, Franca M Cordero, Cristina Gellini, and Marco Pagliai. Computational investigation of the selective cleavage of diastereotopic cyclopropane bonds in 5-spirocyclopropane isoxazolidines rearrangement. *The Journal of Organic Chemistry*, 84(11):6757–6764, 2019.

[51] Alberto Brandi, Stefano Cicchi, Franca M Cordero, and Andrea Goti. Progress in the synthesis and transformations of alkylidenecyclopropanes and alkylidenecyclobutanes. *Chemical Reviews*, 114(15):7317–7420, 2014.

[52] Andrea Goti, Franca M Cordero, and Alberto Brandi. Cycloadditions onto methylene and alkylidenecyclopropane derivatives. *Small Ring Compounds in Organic Synthesis V*, pages 1–97, 1996.

[53] Alberto Brandi, Stefano Cicchi, Franca M Cordero, and Andrea Goti. Heterocycles from alkylidenecyclopropanes. *Chemical Reviews*, 103(4):1213–1270, 2003.

[54] Alberto Brandi, Yasar Durust, Franca M Cordero, and Francesco De Sarlo. Rearrangement of isoxazoline-5-spiro derivatives. 8. selective formation of tetrahydropyridones from c, c-disubstituted nitrones. *The Journal of Organic Chemistry*, 57(21):5666–5670, 1992.

[55] Reiner Sustmann. A simple model for substituent effects in cycloaddition reactions. i. 1, 3-dipolar cycloadditions. *Tetrahedron Letters*, 12(29):2717–2720, 1971.

[56] Yoshinobu Inouye, Yuko Watanabe, Satoru Takahashi, and Hiroshi Kakisawa. The preparation of n-benzyl-. alpha.-ethoxycarbonylnitrone and its reactions with some olefins. *Bulletin of the Chemical Society of Japan*, 52(12):3763–3764, 1979.

[57] Franca M Cordero, Maria Salvati, Federica Pisaneschi, and Alberto Brandi. Novel prospects of the acidic thermal rearrangement of spiro [cyclopropane-1,5′-isoxazolidines] to β-lactams. *European Journal of Organic Chemistry*, 2004(10):2205–2213, 2004.

[58] A Brandi, A Guarna, A Goti, and F De Sarlo. Rearrangement of nitrone cycloadducts to methylene cyclopropane. synthesis of indolizidine and quinolizidine derivatives. *Tetrahedron Letters*, 27(15):1727–1730, 1986.

[59] Andrea Goti, Alberto Brandi, Francesco De Sarlo, and Antonio Guarna. New synthesis of azepin-4-ones by flash vacuum thermolysis of dihydro and tetrahydroisoxazole-5-spirocyclobutane derivatives. *Tetrahedron Letters*, 27 (43):5271–5274, 1986.

[60] Cristiana Di Valentin, Mauro Freccero, Remo Gandolfi, and Augusto Rastelli. Concerted vs stepwise mechanism in 1, 3-dipolar cycloaddition of nitrone to ethene, cyclobutadiene, and benzocyclobutadiene. a computational study. *The Journal of Organic Chemistry*, 65(19):6112–6120, 2000.

[61] Carlo Adamo and Vincenzo Barone. Toward reliable density functional methods without adjustable parameters: The pbe0 model. *The Journal of chemical physics*, 110(13):6158–6170, 1999.

[62] Matthias Ernzerhof and Gustavo E Scuseria. Assessment of the perdew–burke–ernzerhof exchange-correlation functional. *The Journal of chemical physics*, 110(11):5029–5036, 1999.

[63] AD McLean and GS Chandler. Contracted gaussian basis sets for molecular calculations. i. second row atoms, z= 11–18. *The Journal of Chemical Physics*, 72(10):5639–5648, 1980.

[64] RBJS Krishnan, J Stephen Binkley, Rolf Seeger, and John A Pople. Self-consistent molecular orbital methods. xx. a basis set for correlated wave functions. *The Journal of Chemical Physics*, 72(1):650–654, 1980.

[65] Stefan Grimme. Semiempirical gga-type density functional constructed with a long-range dispersion correction. *Journal of Computational Chemistry*, 27 (15):1787–1799, 2006.

[66] M. J. Frisch, G. W. Trucks, H. B. Schlegel, G. E. Scuseria, M. A. Robb, J. R. Cheeseman, G. Scalmani, V. Barone, G. A. Petersson, H. Nakatsuji, X. Li, M. Caricato, A. V. Marenich, J. Bloino, B. G. Janesko, R. Gomperts, B. Mennucci, H. P. Hratchian, J. V. Ortiz, A. F. Izmaylov, J. L. Sonnenberg, D. Williams-Young, F. Ding, F. Lipparini, F. Egidi, J. Goings, B. Peng, A. Petrone, T. Henderson, D. Ranasinghe, V. G. Zakrzewski, J. Gao, N. Rega, G. Zheng, W. Liang, M. Hada, M. Ehara, K. Toyota, R. Fukuda, J. Hasegawa, M. Ishida, T. Nakajima, Y. Honda, O. Kitao, H. Nakai, T. Vreven, K. Throssell, J. A. Montgomery, Jr., J. E. Peralta, F. Ogliaro, M. J. Bearpark, J. J. Heyd, E. N. Brothers, K. N. Kudin, V. N.

Staroverov, T. A. Keith, R. Kobayashi, J. Normand, K. Raghavachari, A. P. Rendell, J. C. Burant, S. S. Iyengar, J. Tomasi, M. Cossi, J. M. Millam, M. Klene, C. Adamo, R. Cammi, J. W. Ochterski, R. L. Martin, K. Morokuma, O. Farkas, J. B. Foresman, and D. J. Fox. Gaussian˜16 Revision C.01, 2016. Gaussian Inc. Wallingford CT.

[67] A.D. Becke. Density functional thermochemistry. iii: The role of exact exchange. *J. Chem. Phys.*, 97:9173–77, 1992.

[68] C Lee, W Yang, and RG Parr. Lyp gradient-corrected functional. *Physical Review B*, 37(2):785–789, 1988.

[69] Estael Ochoa, Matthias Mann, Dirk Sperling, and Jürgen Fabian. A combined density functional and ab initio quantum chemical study of the brandi reaction. *European Journal of Organic Chemistry*, 2001(22):4223–4231, 2001.

[70] Chunyang Peng and H Bernhard Schlegel. Combining synchronous transit and quasi-newton methods to find t transition states. *Israel Journal of Chemistry*, 33(4):449–454, 1993.

[71] Chunyang Peng, Philippe Y Ayala, H Bernhard Schlegel, and Michael J Frisch. Using redundant internal coordinates to optimize equilibrium geometries and transition states. *Journal of Computational Chemistry*, 17(1):49–56, 1996.

[72] Michael Page, Charles Doubleday, and James W McIver Jr. Following steepest descent reaction paths. the use of higher energy derivatives with abinitio electronic structure methods. *The Journal of Chemical Physics*, 93(8):5634–5642, 1990.

[73] HP Hratchian and HB Schlegel. Using hessian updating to increase the efficiency of a hessian based predictor-corrector reaction path following method. *Journal of chemical theory and computation*, 1(1):61–69, 2005.

[74] Hrant P Hratchian and H Bernhard Schlegel. Accurate reaction paths using a hessian based predictor–corrector integrator. *The Journal of chemical physics*, 120(21):9918–9924, 2004.

[75] Michael Page and James W McIver Jr. On evaluating the reaction path hamiltonian. *The Journal of chemical physics*, 88(2):922–935, 1988.

[76] Michael Page, Charles Doubleday, and James W McIver Jr. Following steepest descent reaction paths. the use of higher energy derivatives with abinitio electronic structure methods. *The Journal of Chemical Physics*, 93(8):5634–5642, 1990.

[77] Brent H Besler, Kenneth M Merz Jr, and Peter A Kollman. Atomic charges derived from semiempirical methods. *Journal of Computational Chemistry*, 11 (4):431–439, 1990.

[78] Aleksandr V Marenich, Steven V Jerome, Christopher J Cramer, and Donald G Truhlar. Charge model 5: An extension of hirshfeld population analysis for the accurate description of molecular interactions in gaseous and condensed phases. *Journal of chemical theory and computation*, 8(2):527–541, 2012.

[79] a) JP Foster and F Weinhold. Natural hybrid orbitals. *Journal of the American Chemical Society*, 102(24):7211–7218, 1980.

[80] Alan E Reed, Robert B Weinstock, and Frank Weinhold. Natural population analysis. *The Journal of Chemical Physics*, 83(2):735–746, 1985.

[81] Samuel Glasstone, Keith James Laidler, and Henry Eyring. The theory of rate processes; the kinetics of chemical reactions, viscosity, diffusion and electrochemical phenomena. Technical report, McGraw-Hill Book Company,, 1941.

[82] Eric V Anslyn and Dennis A Dougherty. *Modern Physical Organic Chemistry*. University science books, 2006.

[83] Terrell L Hill. *An introduction to statistical thermodynamics*. Courier Corporation, 1986.

[84] Jacopo Tomasi, Benedetta Mennucci, and Roberto Cammi. Quantum mechanical continuum solvation models. *Chem. Rev.*, 105(8):2999–3094, 2005.

[85] S Francis Boys. Construction of some molecular orbitals to be approximately invariant for changes from one molecule to another. *Reviews of Modern Physics*, 32(2):296, 1960.

[86] MJ ea Frisch, GW Trucks, HB Schlegel, GE Scuseria, MA Robb, JR Cheeseman, G Scalmani, VPGA Barone, GA Petersson, HJRA Nakatsuji, et al. Gaussian 16, 2016.

[87] Alberto Brandi, Francesca Cardona, Stefano Cicchi, Franca M Cordero, and Andrea Goti. [3+ 2] dipolar cycloadditions of cyclic nitrones with alkenes. *Organic Reactions*, pages 1–321, 2004.

[88] Andrea Goti, Alberto Brandi, Francesco De Sarlo, and Antonio Guarna. Rearrangement of isoxazoline-5-spiro derivatives. part 7. thermal rearrangement of 4, 5-dihydro and tetrahydroisoxazole-5-spirocyclobutanes to azepin-4-one derivatives. *Tetrahedron*, 48(25):5283–5300, 1992.

[89] Armin de Meijere, Malte Von Seebach, Sergei I Kozhushkov, Roland Boese, Dieter Blaser, Stefano Cicchi, Tula Dimoulas, and Alberto Brandi. Cyclopropyl building blocks for organic synthesis, 72. cyclobutylidenecyclopropane: new synthesis and use in 1, 3-dipolar cycloadditions-a direct route to spirocyclopropane-annulated azepinone derivatives. *European Journal of Organic Chemistry*, 49(20):3789–3795, 2001.

[90] T. Bally and W. T. Borden. *Calculations on Open-shell Molecules: A Beginner's Guide*, volume 13 of *Reviews in Computational Chemistry*. Wiley-VCH, John Wiley and Sons,INC, New York, 1999.

[91] JD Goddard and G Orlova. Density functional theory with fractionally occupied frontier orbitals and the instabilities of the Kohn-Sham solutions for defining diradical transition states: Ring-opening reactions. *J. Chem. Phys.*, 111(17):7705–7712, NOV 1 1999. doi:10.1063/1.480108.

[92] G Orlova and JD Goddard. Singularities in the behavior of density functionals in predictions of singlet biradicals: The 1,2-dichalcogenins. *J. Chem. Phys.*, 112(23):10085–10094, JUN 15 2000. doi:10.1063/1.481650.

[93] Ryohei Kishi, Yusuke Murata, Michika Saito, Keisuke Morita, Manabu Abe, and Masayoshi Nakano. Theoretical study on diradical characters and nonlinear optical properties of 1,3-diradical compounds. *The Journal of Physical Chemistry A*, 118(45):10837–10848, 2014. doi:10.1021/jp508657s. URL https://doi.org/10.1021/jp508657s.

[94] Daniel J. Marell, Lawrence R. Furan, Brian P. Woods, Xiangyun Lei, Andrew J. Bendelsmith, Christopher J. Cramer, Thomas R. Hoye, and Keith T. Kuwata. Mechanism of the intramolecular hexadehydro-diels–alder reaction. *The Journal of Organic Chemistry*, 80(23):11744–11754, 2015. doi:10.1021/acs.joc.5b01356. URL https://doi.org/10.1021/acs.joc.5b01356.

[95] Hang Zhang, Guojiao Wu, Heng Yi, Tong Sun, Bo Wang, Yan Zhang, Guangbin Dong, and Jianbo Wang. Copper(i)-catalyzed chemoselective coupling of cyclopropanols with diazoesters: Ring-opening c-c bond formations. *Angewandte Chemie*, 129(14):4003–4008, 2017. doi:10.1002/ange.201612138. URL https://onlinelibrary.wiley.com/doi/abs/10.1002/ange.201612138.

[96] Weiming Wan, Glen R. Jenness, Ke Xiong, Dionisios G. Vlachos, and Jingguang G. Chen. Ring-opening reaction of furfural and tetrahydrofurfuryl alcohol on hydrogen-predosed iridium (111) and cobalt/iridium (111) surfaces. *ChemCatChem*, 9(9):1701–1707, 2017. doi:10.1002/cctc.201601646. URL https://onlinelibrary.wiley.com/doi/abs/10.1002/cctc.201601646.

[97] Rui-Ping Huo, Li-hui Guo, Fu-qiang Zhang, and Xiang Zhang. Multiple electronic state mechanism for carboryne reaction with benzene: A dft study. *International Journal of Quantum Chemistry*, 117(12):e25372, 2017. doi:10.1002/qua.25372. URL https://onlinelibrary.wiley.com/doi/abs/10.1002/qua.25372.

[98] Margot Alves, Raphaël Méreau, Bruno Grignard, Christophe Detrembleur, Christine Jérôme, and Thierry Tassaing. Dft investigation of the reaction mechanism for the guanidine catalysed ring-opening of cyclic carbonates by aromatic and alkyl-amines. *RSC Advances*, 7(31):18993–19001, 2017.

[99] The enaminone product, in this particular case, derives from the primary enaminone by ch_2o moiety extrusion (see ref. 14).

[100] F. m. cordero, c. vurchio, a. brandi, a. unpublished results.

[101] Alberto Brandi, Stefano Cicchi, Franca M Cordero, Roberta Frignoli, Andrea Goti, Sylviane Picasso, and Pierre Vogel. Assignment of the absolute configuration of natural lentiginosine by synthesis and enzymic assays of optically pure (+) and (-)-enantiomers. *The Journal of Organic Chemistry*, 60(21): 6806–6812, 1995.

[102] Chiara Zorn, Beatrice Anichini, Andrea Goti, Alberto Brandi, Sergei I Kozhushkov, Armin de Meijere, and Lorenzo Citti. Studies on the synthesis of aza analogues of illudins by cycloadditions to highly strained methylenecyclopropanes. *The Journal of Organic Chemistry*, 64(21):7846–7855, 1999.

[103] L. Briccolani-Bandini. Brandi reaction, a computational study. Master's thesis, Università di Firenze (IT), 2016.

[104] In bicyclic isoxazolidines **22-25** the cyclopropane bond is on the same side as the bridgehead c-h bond.

[105] JP Perdew, A Savin, and K Burke. Escaping the Symmetry Dilemma through a Pair-Density Interpretation of Spin-Density Functional Theory. *Phys. Rev. A*, 51(6):4531–4541, JUN 1995. doi:10.1103/PhysRevA.51.4531.

[106] Christoph R. Jacob and Markus Reiher. Spin in density-functional theory. *International Journal of Quantum Chemistry*, 112(23):3661–3684, 2012. doi:10.1002/qua.24309. URL https://onlinelibrary.wiley.com/doi/abs/10.1002/qua.24309.

[107] Elfi Kraka and Dieter Cremer. Enediynes, enyne-allenes, their reactions, and beyond. *Wiley Interdisciplinary Reviews: Computational Molecular Science*, 4(4):285–324, 2014. doi:10.1002/wcms.1174. URL https://onlinelibrary.wiley.com/doi/abs/10.1002/wcms.1174.

[108] Roberto Cammi, Benedetta Mennucci, and Jacopo Tomasi. Computational modelling of the solvent effects on molecular properties: an overview of the polarizable continuum model (pcm) approach. *Computational chemistry: reviews of current trends*, pages 1–79, 2003.

[109] Eugene Wigner. Über das überschreiten von potentialschwellen bei chemischen reaktionen. *Zeitschrift für Physikalische Chemie*, 19(1):203–216, 1932.

[110] Sourav Nandi and Nilmoni Sarkar. A review on recent application of proton transfer photophysics of bipyridine-3, 3'-diol in organized assemblies. *Journal of Chemical Sciences*, 134(4):1–13, 2022.

[111] Hao Dong, Huan Yang, Jinfeng Zhao, Xiaoyan Liu, and Yujun Zheng. Modulation of excited state proton transfer. *Journal of Luminescence*, 231:117840, 2021.

[112] Niloy Kundu, Pavel Banerjee, Rupam Dutta, Sangita Kundu, Rajesh Kumar Saini, Mintu Halder, and Nilmoni Sarkar. Proton transfer pathways of

2, 2'-bipyridine-3, 3'-diol in ph responsive fatty acid self-assemblies: multi-wavelength fluorescence lifetime imaging in a single vesicle. *Langmuir*, 32(49): 13284–13295, 2016.

[113] Osama K Abou-Zied. Steady-state and time-resolved spectroscopy of 2, 2'-bipyridine-3, 3'-diol in solvents and cyclodextrins: Polarity and nanoconfinement effects on tautomerization. *The Journal of Physical Chemistry B*, 114 (2):1069–1076, 2010.

[114] V Barone, A Palma, and Nico Sanna. Toward a reliable computational support to the spectroscopic characterization of excited state intramolecular proton transfer:[2, 2'-bipyridine]-3, 3'-diol as a test case. *Chemical physics letters*, 381(3-4):451–457, 2003.

[115] Andrzej L Sobolewski and Ludwik Adamowicz. Double-proton-transfer in [2, 2'-bipyridine]-3, 3'-diol: an ab initio study. *Chemical physics letters*, 252(1-2): 33–41, 1996.

[116] Vincenzo Barone and Carlo Adamo. A theoretical study of proton transfer in [2, 2'-bipyridyl]-3, 3'-diol. *Chemical physics letters*, 241(1-2):1–6, 1995.

[117] C. C. J. Roothaan. New developments in molecular orbital theory. *Rev. Mod. Phys.*, 23:69–89, Apr 1951. doi:10.1103/RevModPhys.23.69. URL `https://link.aps.org/doi/10.1103/RevModPhys.23.69`.

[118] Lu Jeu Sham and Walter Kohn. One-particle properties of an inhomogeneous interacting electron gas. *Physical Review*, 145(2):561, 1966.

[119] S. H. Vosko, L. Wilk, and M. Nusair. Accurate spin-dependent electron liquid correlation energies for local spin density calculations: a critical analysis. *Canadian Journal of Physics*, 58(8):1200–1211, 1980. doi:10.1139/p80-159.

[120] Axel D Becke. Density-functional exchange-energy approximation with correct asymptotic behavior. *Physical review A*, 38(6):3098, 1988.

[121] Chengteh Lee, Weitao Yang, and Robert G Parr. Development of the colle-salvetti correlation-energy formula into a functional of the electron density. *Physical review B*, 37(2):785, 1988.

[122] John P Perdew, Kieron Burke, and Matthias Ernzerhof. Generalized gradient approximation made simple. *Physical review letters*, 77(18):3865, 1996.

[123] Yan Zhao and Donald G Truhlar. A new local density functional for main-group thermochemistry, transition metal bonding, thermochemical kinetics, and noncovalent interactions. *The Journal of chemical physics*, 125(19): 194101, 2006.

[124] Philip J Stephens, Frank J Devlin, Cary F Chabalowski, and Michael J Frisch. Ab initio calculation of vibrational absorption and circular dichroism spectra using density functional force fields. *The Journal of physical chemistry*, 98 (45):11623–11627, 1994.

[125] AD Becke. Density-functional thermochemistry. iii the role of exact exchange j chem phys 98: 5648–5652, 1993.

[126] Axel D Becke. A new mixing of hartree–fock and local density-functional theories. *The Journal of chemical physics*, 98(2):1372–1377, 1993.

[127] Yan Zhao and Donald G Truhlar. The m06 suite of density functionals for main group thermochemistry, thermochemical kinetics, noncovalent interactions, excited states, and transition elements: two new functionals and systematic testing of four m06-class functionals and 12 other functionals. *Theoretical chemistry accounts*, 120(1):215–241, 2008.

[128] Yan Zhao and Donald G Truhlar. Density functional for spectroscopy: no long-range self-interaction error, good performance for rydberg and charge-transfer states, and better performance on average than b3lyp for ground states. *The Journal of Physical Chemistry A*, 110(49):13126–13130, 2006.

[129] Takeshi Yanai, David P Tew, and Nicholas C Handy. A new hybrid exchange–correlation functional using the coulomb-attenuating method (cam-b3lyp). *Chemical physics letters*, 393(1-3):51–57, 2004.

[130] Roberto Peverati and Donald G Truhlar. Improving the accuracy of hybrid meta-gga density functionals by range separation. *The Journal of Physical Chemistry Letters*, 2(21):2810–2817, 2011.

[131] Stefan Grimme. Semiempirical hybrid density functional with perturbative second-order correlation. *The Journal of chemical physics*, 124(3):034108, 2006.

[132] Sebastian Kozuch and Jan ML Martin. Dsd-pbep86: in search of the best double-hybrid dft with spin-component scaled mp2 and dispersion corrections. *Physical Chemistry Chemical Physics*, 13(45):20104–20107, 2011.

[133] Michael J Frisch, Martin Head-Gordon, and John A Pople. A direct mp2 gradient method. *Chemical Physics Letters*, 166(3):275–280, 1990.

[134] Michael J Frisch, John A Pople, and J Stephen Binkley. Self-consistent molecular orbital methods 25. supplementary functions for gaussian basis sets. *The Journal of chemical physics*, 80(7):3265–3269, 1984.

[135] R Krishnan and JS Binkley. Seeger r and pople ja. *J. Chem. Phys.*, 1980:72, 1980.

[136] G. Knizia, B. Adler, Th., and J. Werner, H. Simplified CCSD(T)-F12 methods: theory and benchmarks. *J. Chem. Phys.*, 130:054104, 2009.

[137] G. Knizia, T. B. Adler, and H.-J. Werner. Simplified CCSD(T)-F12 methods: theory and benchmarks. *J. Chem. Phys.*, 130:054104, 2009.

[138] Thomas B Adler, Gerald Knizia, and Hans-Joachim Werner. A simple and efficient ccsd (t)-f12 approximation. *The Journal of chemical physics*, 127 (22):221106, 2007.

[139] U Chandra Singh and Peter A Kollman. An approach to computing electrostatic charges for molecules. *Journal of computational chemistry*, 5(2):129–145, 1984.

[140] Brent H Besler, Kenneth M Merz Jr, and Peter A Kollman. Atomic charges derived from semiempirical methods. *Journal of computational chemistry*, 11 (4):431–439, 1990.

[141] S Francis Boys. Construction of some molecular orbitals to be approximately invariant for changes from one molecule to another. *Reviews of Modern Physics*, 32(2):296, 1960.

[142] Joseph W Ochterski, George A Petersson, and John A Montgomery Jr. A complete basis set model chemistry. v. extensions to six or more heavy atoms. *The Journal of chemical physics*, 104(7):2598–2619, 1996.

[143] Frank Neese, Frank Wennmohs, Ute Becker, and Christoph Riplinger. The orca quantum chemistry program package. *The Journal of chemical physics*, 152(22):224108, 2020.

[144] Damian Moran, Andrew C Simmonett, Franklin E Leach, Wesley D Allen, Paul v R Schleyer, and Henry F Schaefer. Popular theoretical methods predict benzene and arenes to be nonplanar. *Journal of the American Chemical Society*, 128(29):9342–9343, 2006.

[145] David Asturiol, Miquel Duran, and Pedro Salvador. Intramolecular basis set superposition error effects on the planarity of benzene and other aromatic molecules: A solution to the problem. *The Journal of chemical physics*, 128 (14):144108, 2008.

[146] Nagaprasad Reddy Samala and Kenneth D Jordan. Comment on a spurious prediction of a non-planar geometry for benzene at the mp2 level of theory. *Chemical Physics Letters*, 669:230–232, 2017.

[147] The PLUMED consortium. Promoting transparency and reproducibility in enhanced molecular simulations. *Nature methods*, 16(8):670–673, 2019.

[148] Massimiliano Bonomi, Davide Branduardi, Giovanni Bussi, Carlo Camilloni, Davide Provasi, Paolo Raiteri, Davide Donadio, Fabrizio Marinelli, Fabio Pietrucci, Ricardo A Broglia, et al. Plumed: A portable plugin for free-energy calculations with molecular dynamics. *Computer Physics Communications*, 180(10):1961–1972, 2009.

[149] Alan Grossfield. Wham: the weighted histogram analysis method, version 2.0. 9. *Available at membrane. urmc. rochester. edu/content/wham. Accessed November*, 15:2013, 2013.

[150] Vanessa Labet, Christophe Morell, Alejandro Toro-Labbé, and André Grand. Is an elementary reaction step really elementary? theoretical decomposition of asynchronous concerted mechanisms. *Physical Chemistry Chemical Physics*, 12(16):4142–4151, 2010.

[151] David E Woon and Thom H Dunning Jr. Gaussian basis sets for use in correlated molecular calculations. III. the atoms aluminum through argon. *J. Chem. Phys.*, 98:1358–1371, 1993.

[152] Junwei Lucas Bao, Ying Wang, Xiao He, Laura Gagliardi, and Donald G Truhlar. Multiconfiguration pair-density functional theory is free from delocalization error. *The Journal of Physical Chemistry Letters*, 8(22):5616–5620, 2017.

[153] Weitao Yang, Yingkai Zhang, and Paul W Ayers. Degenerate ground states and a fractional number of electrons in density and reduced density matrix functional theory. *Physical Review Letters*, 84(22):5172, 2000.

[154] Sergey V Dorozhkin. Calcium orthophosphates (capo4): occurrence and properties. *Progress in biomaterials*, 5(1):9–70, 2016.

[155] Rita Gelli, Francesca Ridi, and Piero Baglioni. The importance of being amorphous: calcium and magnesium phosphates in the human body. *Advances in colloid and interface science*, 269:219–235, 2019.

[156] F Betts and AS Posner. An x-ray radial distribution study of amorphous calcium phosphate. *Materials Research Bulletin*, 9(3):353–360, 1974.

[157] AL Boskey and AS Posner. Magnesium stabilization of amorphous calcium phosphate: a kinetic study. *Materials Research Bulletin*, 9(7):907–916, 1974.

[158] BN Bachra and HRA Fischer. The effect of some inhibitors on the nucleation and crystal growth of apatite. *Calcified Tissue Research*, 3(1):348–357, 1969.

[159] Francesco Abbona and Alain Baronnet. A xrd and tem study on the transformation of amorphous calcium phosphate in the presence of magnesium. *Journal of Crystal Growth*, 165(1-2):98–105, 1996.

[160] Xiudong Yang, Baoquan Xie, Lijun Wang, Yueling Qin, Zachary J Henneman, and George H Nancollas. Influence of magnesium ions and amino acids on the nucleation and growth of hydroxyapatite. *CrystEngComm*, 13(4):1153–1158, 2011.

[161] Juewen Liu. Adsorption of dna onto gold nanoparticles and graphene oxide: surface science and applications. *Physical chemistry chemical physics*, 14(30): 10485–10496, 2012.

[162] Huachao Ding, Haihua Pan, Xurong Xu, and Ruikang Tang. Toward a detailed understanding of magnesium ions on hydroxyapatite crystallization inhibition. *Crystal growth & design*, 14(2):763–769, 2014.

[163] Rita Gelli, Lorenzo Briccolani-Bandini, Marco Pagliai, Gianni Cardini, Francesca Ridi, and Piero Baglioni. Exploring the effect of mg2+ substitution on amorphous calcium phosphate nanoparticles. *Journal of Colloid and Interface Science*, 606:444–453, 2022.

[164] PF Schofield, KS Knight, JAM Van der Houwen, and E Valsami-Jones. The role of hydrogen bonding in the thermal expansion and dehydration of brushite, di-calcium phosphate dihydrate. *Physics and Chemistry of Minerals*, 31(9):606–624, 2004.

[165] Thomas D Kühne, Marcella Iannuzzi, Mauro Del Ben, Vladimir V Rybkin, Patrick Seewald, Frederick Stein, Teodoro Laino, Rustam Z Khaliullin, Ole Schütt, Florian Schiffmann, et al. Cp2k: An electronic structure and molecular dynamics software package-quickstep: Efficient and accurate electronic structure calculations. *The Journal of Chemical Physics*, 152(19):194103, 2020.

[166] Stefan Goedecker, Michael Teter, and Jürg Hutter. Separable dual-space gaussian pseudopotentials. *Physical Review B*, 54(3):1703, 1996.

[167] Joost VandeVondele and Jürg Hutter. An efficient orbital transformation method for electronic structure calculations. *The Journal of chemical physics*, 118(10):4365–4369, 2003.

[168] S F_ Boys and FJMP Bernardi. The calculation of small molecular interactions by the differences of separate total energies. some procedures with reduced errors. *Mol. Phys.*, 19(4):553–566, 1970.

[169] Sílvia Simon, Miquel Duran, and JJ Dannenberg. How does basis set superposition error change the potential surfaces for hydrogen-bonded dimers? *The Journal of chemical physics*, 105(24):11024–11031, 1996.

[170] Rita Gelli, Martino Scudero, Lucia Gigli, Mirko Severi, Massimo Bonini, Francesca Ridi, and Piero Baglioni. Effect of ph and mg2+ on amorphous magnesium-calcium phosphate (amcp) stability. *Journal of colloid and interface science*, 531:681–692, 2018.

[171] Sebastian Schlücker. Surface-enhanced raman spectroscopy: Concepts and chemical applications. *Angewandte Chemie International Edition*, 53(19): 4756–4795, 2014.

[172] Nathaniel L Rosi and Chad A Mirkin. Nanostructures in biodiagnostics. *Chemical reviews*, 105(4):1547–1562, 2005.

[173] Maurizio Muniz-Miranda, Cristina Gellini, Marco Pagliai, Massimo Innocenti, Pier Remigio Salvi, and Vincenzo Schettino. Sers and computational studies on microrna chains adsorbed on silver surfaces. *The Journal of Physical Chemistry C*, 114(32):13730–13735, 2010.

[174] J Kundu, O Neumann, BG Janesko, D Zhang, S Lal, A Barhoumi, GE Scuseria, and NJ Halas. Adenine- and adenosine monophosphate (amp)- gold

binding interactions studied by surface-enhanced raman and infrared spectroscopies. *The Journal of Physical Chemistry C*, 113(32):14390–14397, 2009.

[175] Evanthia Papadopoulou and Steven EJ Bell. Structure of adenine on metal nanoparticles: ph equilibria and formation of ag+ complexes detected by surface-enhanced raman spectroscopy. *The Journal of Physical Chemistry C*, 114(51):22644–22651, 2010.

[176] Xiu-Feng Lang, Peng-Gang Yin, Ting-Ting You, Li Jiang, and Lin Guo. A dft investigation of surface-enhanced raman scattering of adenine and 2'-deoxyadenosine 5'-monophosphate on ag20 nanoclusters. *ChemPhysChem*, 12 (13):2468–2475, 2011.

[177] Evanthia Papadopoulou and Steven EJ Bell. Surface-enhanced raman evidence of protonation, reorientation, and ag+ complexation of deoxyadenosine and deoxyadenosine-5'-monophosphate (damp) on ag and au surfaces. *The Journal of Physical Chemistry C*, 115(29):14228–14235, 2011.

[178] A. Rodes, M. Rueda, F. Prieto, C. Prado, J. M. Feliu, and A. Aldaz. Adenine adsorption at single crystal and thin-film gold electrodes: An in situ infrared spectroscopy study. *Journal of Physical Chemistry C*, 113(43):18784–18794, 2009. URL www.scopus.com. Cited By :28.

[179] Stefano Piana and Ante Bilic. The nature of the adsorption of nucleobases on the gold [111] surface. *The Journal of Physical Chemistry B*, 110(46): 23467–23471, 2006.

[180] Guohua Yao, Zhimin Zhai, Jie Zhong, and Qing Huang. Dft and sers study of 15n full-labeled adenine adsorption on silver and gold surfaces. *The Journal of Physical Chemistry C*, 121(18):9869–9878, 2017.

[181] Ricardo Aroca. *Surface-enhanced vibrational spectroscopy*. John Wiley & Sons, 2006.

[182] Baris Akbali, Mehmet Yagmurcukardes, FM Peeters, Hsing-Ying Lin, Ting-Yi Lin, Wen-Hao Chen, Simon Maher, Tsan-Yao Chen, and Chen-Han Huang. Determining the molecular orientation on the metal nanoparticle surface through surface-enhanced raman spectroscopy and density functional theory simulations. *The Journal of Physical Chemistry C*, 125(29):16289–16295, 2021.

[183] Guohua Yao and Qing Huang. Dft and sers study of l-cysteine adsorption on the surface of gold nanoparticles. *The Journal of Physical Chemistry C*, 122 (27):15241–15251, 2018.

[184] Ralph WG Wyckoff. Cubic closest packed, ccp, structure. *Crystal structures*, 1:7–83, 1963.

[185] Giovanni Bussi, Alessandro Laio, and Michele Parrinello. Equilibrium free energies from nonequilibrium metadynamics. *Phys. Rev. Lett.*, 96:090601, Mar 2006. doi:10.1103/PhysRevLett.96.090601. URL https://link.aps.org/doi/10.1103/PhysRevLett.96.090601.

[186] Gopalan Rajaraman, Andrea Caneschi, Dante Gatteschi, and Federico Totti. A periodic mixed gaussians–plane waves dft study on simple thiols on au (111): adsorbate species, surface reconstruction, and thiols functionalization. *Physical Chemistry Chemical Physics*, 13(9):3886–3895, 2011.

[187] Ulrich Essmann, Lalith Perera, Max L Berkowitz, Tom Darden, Hsing Lee, and Lee G Pedersen. A smooth particle mesh ewald method. *The Journal of chemical physics*, 103(19):8577–8593, 1995.

[188] Ho-Sung Kim, Doo-Sik Ahn, Sang-Yoon Chung, Sang Kyu Kim, and Sungyul Lee. Tautomerization of adenine facilitated by water: computational study of microsolvation. *The Journal of Physical Chemistry A*, 111(32):8007–8012, 2007.

THIS PAGE INTENTIONALLY LEFT BLANK

Appendix A

Supporting data for Chapter 1

Table A.1: The ESP, CM5, NPA charges have been reported for the sp2 carbons of the isobutene **7** (C_A, C_B) and for the interacting atoms of the nitrone **16** (C_β, N, O). The charge have been calculated for the isolated reactants (nitrone and isobutene).

	ESP	CM5	NPA
$C_{A(\mathbf{7})}$	0.469217	-0.021094	-0.00836
$C_{B(\mathbf{7})}$	-0.736784	-0.214182	-0.41187
$O_{A(\mathbf{16})}$	-0.566773	-0.302139	-0.53059
$N_{A(\mathbf{16})}$	0.441358	-0.115015	0.08629
$C_{\beta(\mathbf{16})}$	-0.230350	0.020439	-0.00385

Table A.2: The ESP, CM5, NPA charges have been reported for the sp2 carbons of the isobutene **2** (C_A, C_B) and for the interacting atoms of the nitrone **16** (C_β, N, O). The charge have been calculated for the isolated reactants (nitrone and isobutene).

	ESP	CM5	NPA
$C_{A(\mathbf{2})}$	0.281712	-0.037240	-0.02053
$C_{B(\mathbf{2})}$	-0.620743	-0.197492	-0.39213
$O_{A(\mathbf{16})}$	-0.566773	-0.302139	-0.53059
$N_{A(\mathbf{16})}$	0.441358	-0.115015	0.08629
$C_{\beta(\mathbf{16})}$	-0.230350	0.020439	-0.00385

Table A.3: The ESP, CM5, NPA charges have been reported for the sp2 carbons of the isobutene **14** (C_A, C_B) and for the interacting atoms of the nitrone **16** (C_β, N, O). The charge have been calculated for the isolated reactants (nitrone and isobutene).

	ESP	CM5	NPA
$C_{A(\mathbf{14})}$	0.271190	-0.022674	0.00339
$C_{B(\mathbf{14})}$	-0.698235	-0.214625	-0.41875
$O_{A(\mathbf{16})}$	-0.566773	-0.302139	-0.53059
$N_{A(\mathbf{16})}$	0.441358	-0.115015	0.08629
$C_{\beta(\mathbf{16})}$	-0.230350	0.020439	-0.00385

Table A.4: The ESP, CM5, NPA charges have been reported for the sp2 carbons of the isobutene **17** (C_A, C_B) and for the interacting atoms of the nitrone **16** (C_β, N, O). The charge have been calculated for the isolated reactants (nitrone and isobutene).

	ESP	CM5	NPA
$C_{A(\mathbf{17})}$	0.100976	-0.04619	-0.04619
$C_{B(\mathbf{17})}$	0.159697	-0.02542	-0.02542
$O_{A(\mathbf{16})}$	-0.566773	-0.302139	-0.53059
$N_{A(\mathbf{16})}$	0.441358	-0.115015	0.08629
$C_{\beta(\mathbf{16})}$	-0.230350	0.020439	-0.00385

Table A.5: The ESP, CM5, NPA charges have been reported for the sp2 carbons of the isobutene **18** (C_A, C_B) and for the interacting atoms of the nitrone **16** (C_β, N, O). The charge have been calculated for the isolated reactants (nitrone and isobutene).

	ESP	CM5	NPA
$C_{A(\mathbf{18})}$	-0.039164	-0.044737	-0.04368
$C_{B(\mathbf{18})}$	-0.037420	0.103927	-0.02125
$O_{A(\mathbf{16})}$	-0.566773	-0.302139	-0.53059
$N_{A(\mathbf{16})}$	0.441358	-0.115015	0.08629
$C_{\beta(\mathbf{16})}$	-0.230350	0.020439	-0.00385

Table A.6: The ESP, CM5, NPA charges have been reported for the sp2 carbons of the isobutene **19** (C_A, C_B) and for the interacting atoms of the nitrone **16** (C_β, N, O). The charge have been calculated for the isolated reactants (nitrone and isobutene).

	ESP	CM5	NPA
$C_{A(\mathbf{19})}$	0.086844	-0.026871	-0.01267
$C_{B(\mathbf{19})}$	-0.003760	-0.054891	-0.05332
$O_{A(\mathbf{16})}$	-0.566773	-0.302139	-0.53059
$N_{A(\mathbf{16})}$	0.441358	-0.115015	0.08629
$C_{\beta(\mathbf{16})}$	-0.230350	0.020439	-0.00385

Table A.7: The ESP, CM5, NPA charges have been reported for the sp2 carbons of the isobutene **36** (C_A, C_B) and for the interacting atoms of the nitrone **16** (C_β, N, O). The charge have been calculated for the isolated reactants (nitrone and isobutene).

	ESP	CM5	NPA
$C_{A(\mathbf{36})}$	0.447448	-0.005028	0.06265
$C_{B(\mathbf{36})}$	-0.807355	-0.108089	-0.31767
$O_{A(\mathbf{16})}$	-0.566773	-0.302139	-0.53059
$N_{A(\mathbf{16})}$	0.441358	-0.115015	0.08629
$C_{\beta(\mathbf{16})}$	-0.230350	0.020439	-0.00385

Table A.8: The $\delta s.p.$ represents the difference in energy of interacting reactants and the energy of the isolated isobutene **7** and **16** for each stationary point of the reaction ($\delta s.p. = E_{s.p.} - E_{\mathbf{7}} - E_{\mathbf{16}}$). The ΔE represents the difference in energy between the chosen orientation (Path **a** and **b**) of the isobutene. The differences in energy are expressed in kJ/mol.

$\delta s.p.$	$E_{Path\mathbf{a}}$	$E_{Path\mathbf{b}}$	$\Delta E_{\mathbf{a-b}}$
δr	-32.8	-30.5	-2.3
δts	35.4	53.4	-18.0
δp	-143.6	-118.0	-25.6

Table A.9: The ESP charges have been reported for the sp2 carbons of the isobutene **7** (C_A, C_B) and for the interacting atoms of the nitrone **16** (C_β, N, O). The ESP charge have been calculated for the isolated reactants (nitrone and isobutene) and for the interacting species in the pre-reactive minimum for the chosen orientations **a** and **b**.

Atoms	Isolated	Path **a**	Path **b**
$C_{A(\mathbf{7})}$	0.469	0.506	0.542
$C_{B(\mathbf{7})}$	-0.737	-0.940	-0.748
$O_{A(\mathbf{16})}$	-0.567	-0.570	-0.560
$N_{A(\mathbf{16})}$	0.441	0.399	0.382
$C_{\beta(\mathbf{16})}$	-0.230	-0.138	-0.185

Table A.10: The $\delta s.p.$ represents the difference in energy of interacting reactants and the energy of the isolated alkene **2**, **14** and **16** for each stationary point of the reaction ($\delta s.p. = E_{s.p.} - E_{\mathbf{nitr.}} - E_{\mathbf{alk.}}$); while the ΔE represents the difference in energy between the two dipolarophile possible orientations. Difference in energy expressed in kJ/mol.

$\delta s.p.$	$E_{\mathbf{2Patha}}$	$E_{\mathbf{2Pathb}}$	$\Delta E_{\mathbf{a-b}}$	$E_{\mathbf{14Patha}}$	$E_{\mathbf{14Pathb}}$	$\Delta E_{\mathbf{a-b}}$
δr	-27.2	-23.7	-3.5	-33.8	-37.9	4.1
δts	28.7	36.5	-7.8	26.5	42.3	-15.8
δp	-172.7	-162.3	-10.4	-158.6	-135.0	-23.6

Table A.11: ESP charges in the pre-reactive minima for dipolarophiles MCP and MCB (C_A, C_B) and nitrone atoms (O, N, C_β) for the isolated molecules and the chosen orientations **a** and **b**.

Atoms	MCP (**2**)			MCB (**14**)		
	Isolated	Path **a**	Path **b**	Isolated	Path **a**	Path **b**
C_A	0.282	0.147	0.266	0.271	0.237	0.236
C_B	-0.621	-0.512	-0.591	-0.698	-0.675	-0.695
O_{16}	-0.567	-0.533	-0.556	-0.567	-0.553	-0.589
N_{16}	0.441	0.401	0.367	0.441	0.389	0.447
$C_{\beta(16)}$	-0.230	-0.101	-0.151	-0.230	-0.143	-0.265

Table A.12: The transmission coefficient (k) has been calculated using the Eyring transition state theory and describes the changing in the rate of a chemical reaction against the experimental temperature.

Dipolarophile	Texp. (K)	k_{Eyring} Path **a**	k_{Eyring} Path **b**	$k_{\mathbf{a/b}}$
2	330	$1\,e^{11}$	$2\,e^{10}$	4.8
14	370	$1\,e^{12}$	$1\,e^{10}$	$1\,e^{2}$

Table A.13: The $\delta s.p.$ represents the difference in energy of interacting reactants and the energy of the isolated alkene **17**, **18** and **16** for each stationary point of the reaction ($\delta s.p. = E_{s.p.} - E_{\mathbf{nitr.}} - E_{\mathbf{alk.}}$); while the ΔE represents the difference in energy between the two dipolarophile possible orientations. Difference in energy expressed in kJ/mol.

$\delta s.p.$	$E_{\mathbf{17Patha}}$	$E_{\mathbf{17Pathb}}$	$\Delta E_{\mathbf{a-b}}$	$E_{\mathbf{18Patha}}$	$E_{\mathbf{18Pathb}}$	$\Delta E_{\mathbf{a-b}}$
δr	-42.3	-43.6	1.3	-49.9	-52.8	2.9
δts	85.8	24.3	61.5	33.1	29.3	3.8
δp	-164.5	-177.1	12.1	-130.9	-146.7	15.8

Table A.14: ESP charges in the pre-reactive minima for ICP and ICB (CA, CB) and nitrone (O, N, C_β) atoms for the isolated molecules and the chosen orientations **a** and **b**

Atoms	ICP (**17**)			ICB (**18**)		
	Isolated	Path **a**	Path **b**	Isolated	Path **a**	Path **b**
C_A	0.101	-0.020	0.218	-0.045	-0.045	-0.006
C_B	0.160	0.263	0.009	0.104	0.195	0.125
O_{16}	-0.567	-0.533	-0.548	-0.567	-0.552	-0.539
N_{16}	0.441	0.380	0.364	0.441	0.397	0.343
$C_{\beta(16)}$	-0.230	-0.112	-0.221	-0.230	-0.188	-0.222

Table A.15: The transmission coefficient ($k_{Eyring}(1/\mathrm{M\ s})$) has been calculated using the Eyring transition state theory and describes the changing in the rate of a chemical reaction against the experimental temperature.

Dipolarophile	Texp. (K)	k_{Eyring} Path **a**	k_{Eyring} Path **b**	$k_{\mathbf{a/b}}$
17	380	$5\,e^{2}$	$6\,e^{11}$	$6\,e^{-9}$
18	330	$4\,e^{7}$	$7\,e^{8}$	$5\,e^{-2}$

Table A.16: The $\delta s.p.$ represents the difference in energy of interacting reactants and the energy of the isolated alkene **19** and **16** for each stationary point of the reaction ($\delta s.p. = E_{s.p.} - E_{\mathbf{nitr.}} - E_{\mathbf{alk.}}$); while the ΔE represents the difference in energy between the two dipolarophile possible orientations. Difference in energy expressed in kJ/mol.

$\delta s.p.$	$E_{Path\mathbf{a}}$	$E_{Path\mathbf{b}}$	$\Delta E_{\mathbf{a-b}}$
δr	-40.4	-45.2	4.8
δts	19.5	26.4	-6.9
δp	-190.9	-181.9	-9.0

Table A.17: ESP charges in the pre-reactive minima for CBCP(19) (C_A, C_B) and nitrone **16** (C_β, N, O) atoms for the isolated molecules at the chosen orientations **a** and **b**.

Atoms	Isolated	Path **a**	Path **b**
$C_{A(\mathbf{19})}$	-0.004	-0.097	-0.006
$C_{B(\mathbf{19})}$	0.087	0.172	0.125
$O_{(\mathbf{16})}$	-0.567	-0.512	-0.539
$N_{(\mathbf{16})}$	0.441	0.323	0.343
$C_{\beta(\mathbf{16})}$	-0.230	-0.248	-0.222

Table A.18: The $\delta s.p.$ represents the difference in energy of interacting reactants and the energy of the isolated alkene **36** and **16** for each stationary point of the reaction ($\delta s.p. = E_{s.p.} - E_{\mathbf{nitr.}} - E_{\mathbf{alk.}}$); while the ΔE represents the difference in energy between the two dipolarophile possible orientations. Difference in energy expressed in kJ/mol.

$\delta s.p.$	$E_{Path\mathbf{a}}$	$E_{Path\mathbf{b}}$	$\Delta E_{\mathbf{a-b}}$
δr	-40.8	-34.3	-6.5
δts	0.6	14.7	-14.1
δp	-149.6	-146.9	-2.7

Table A.19: The ESP charges in the pre-reactive minima for dipolarophile 36 (C_A, C_B) and nitrone **16** (C_β, N, O) atoms for the isolated molecules at the chosen orientations **a** and **b**.

Atoms	Isolated	Path **a**	Path **b**
$C_{A(\mathbf{36})}$	0.447	0.443	0.472
$C_{B(\mathbf{36})}$	-0.807	-0.818	-0.848
$O_{A(\mathbf{16})}$	-0.567	-0.541	-0.571
$N_{A(\mathbf{16})}$	0.441	0.348	0.418
$C_{\beta(\mathbf{16})}$	-0.230	-0.236	0.225

Table A.20: Stationary points of system **24a** at UB3LYP/6-31G(d,p) level of theory.

P. Stat.	**E (Hartree)**	ΔE **(Hartree)**	ΔE **(kcal/mol)**	ΔE **(kJ/mol)**
		24a		
24a	-481.889571138	0.0	0.0	0.0
TS_1	-481.839612302	0.049959	31.349273	131.167305
INT_1	-481.840745934	0.048825	30.6376	128.189989
		24a-β		
TS_2	-481.838165716	0.051405	32.256637	134.963776
INT_2	-481.861027560	0.028544	17.911360	74.942243
TS_3	-481.858613730	0.030957	19.425517	81.277573
26a	-481.977207845	-0.087637	-54.992218	-230.090856
		24a-α		
TS_2	-481.839520908	0.050050	31.406375	131.406225
INT_2	-481.863854926	0.025716	16.136790	67.517332
TS_3	-481.862947635	0.026624	16.706560	69.901285
INT_3	-481.975259054	-0.085688	-53.769220	-224.973758
TS_4	-481.887799328	0.001772	1.111930	4.652384
27	-481.983376797	-0.093806	-58.863265	-246.287559

Table A.21: Stationary points of system **24a** at UB3LYP/6-311++G(d,p) with PCM level of theory.

P. Stat.	**E (Hartree)**	ΔE **(Hartree)**	ΔE **(kcal/mol)**	ΔE **(kJ/mol)**
		24a		
24a	-482.001882305	0.0	0.0	0.0
TS_1	-481.957169458	0.044713	28.057408	117.371625
INT_1	-481.962709302	0.039173	24.581058	102.829125
		24a-β		
TS_2	-481.962205038	0.039677	24.897317	104.152125
26a	-482.091769723	-0.089887	-56.404092	-235.953375
		24a-α		
TS_2	-481.962405388	0.039477	24.771817	103.627125
INT_2	-481.983239555	0.018643	11.698483	48.937875
TS_3	-481.979353946	0.022528	14.136320	59.136000
INT_3	-481.983444694	0.018438	11.569845	48.399750
TS_4	-481.982429267	0.019453	12.206758	51.064125
INT_4	-482.093947829	-0.092066	-57.771415	-241.673250
TS_5	-482.010357903	-0.008476	-5.318690	-22.249500
27	-482.103098921	-0.101217	-63.513668	-265.694625

Table A.22: Stationary points of system **24a** at UB3LYP/6-311++G(d,p) with the contribute of dispersion.

P. Stat.	**E (Hartree)**	ΔE **(Hartree)**	ΔE **(kcal/mol)**	ΔE **(kJ/mol)**
		24a		
24a	-482.022285999	0.0	0.0	0.0
TS_1	-481.977675724	0.044610	27.992775	117.101250
INT_1	-481.984130818	0.038155	23.942263	100.156875

Table A.23: Stationary points of system **24b** at UB3LYP/6-311++G(d,p) with level of theory.

P. Stat.	**E (Hartree)**	ΔE **(Hartree)**	ΔE **(kcal/mol)**	ΔE **(kJ/mol)**
		24b		
24b	-481.999008766	0.0	0.0	0.0
TS_1	-481.955874901	0.043134	27.066585	113.226750
INT_1	-481.966346392	0.032662	20.495405	85.737750
		24b-β		
TS_2	-481.965633428	0.033375	20.942813	87.609375
26b	-482.093097908	-0.094089	-59.040848	-246.983625
		24b-α		
TS_2	-481.966252200	0.032757	20.555018	85.987125
INT_2	-481.985442678	0.013566	8.512665	35.610750
TS_3	-481.953792121	0.045217	28.373667	118.694625
INT_3	-482.008243717	-0.009235	-5.794963	-24.241875
TS_4	-481.984359852	0.014649	9.192248	38.453625
27	-482.100437857	-0.101429	-63.646698	-266.251125

Table A.24: Spin contamination of system **24a** at UB3LYP/6-311++G(d,p) level of theory.

Stationary points	$< S^2 >_{before}$	$< S^2 >_{after}$
24a	0.0	0.0
TS_1	0.7807	0.0392
Int_1	1.0103	0.0853
$TS_{2\beta}$	1.0094	0.1105
26a	0.0	0.0
$TS_{2\alpha}$	1.0142	0.1139
Int_2	1.0089	0.0742
TS_3	1.0092	0.0739
Int_3	1.0086	0.0715
TS_4	0.8498	0.0455
27	0.0	0.0

Table A.25: Stationary points of system **24a** at UB3LYP/6-311++G(d,p) with PCM level of theory.

P. Stat.	**E (Hartree)**	ΔE **(Hartree)**	ΔE **(kcal/mol)**	ΔE **(kJ/mol)**
		24a		
24a	-482.001882305	0.0	0.0	0.0
TS_1	-481.957169458	0.044713	28.057408	117.371625
INT_1	-481.962709302	0.039173	24.581058	102.829125
		24a-β		
TS_2	-481.962205038	0.039677	24.897317	104.152125
26a	-482.091769723	-0.089887	-56.404092	-235.953375
		24a-α		
TS_2	-481.962405388	0.039477	24.771817	103.627125
INT_2	-481.983239555	0.018643	11.698483	48.937875
TS_3	-481.979353946	0.022528	14.136320	59.136000
INT_3	-481.983444694	0.018438	11.569845	48.399750
TS_4	-481.982429267	0.019453	12.206758	51.064125
INT_4	-482.093947829	-0.092066	-57.771415	-241.673250
TS_5	-482.010357903	-0.008476	-5.318690	-22.249500
27	-482.103098921	-0.101217	-63.513668	-265.694625

THIS PAGE INTENTIONALLY LEFT BLANK

Appendix B

Supporting data for Chapter 2

Table B.1: MP2 energies Hartree; * energies computed with default convergence criteria, ** energies computed with very tight convergence criteria. The geometries related to the minima has are not planar and haven't imaginary frequencies.

	diketo	ts_1	dieno
*$MP2_{g16}$/6-311+G(d,p)	-642.080387481	-642.075604863	-642.121302768
**$MP2_{g16}$/6-6311+G(d,p)			-644.24875170982
**$MP2_{orca}$/6-6311+G(d,p)			-644.24904816441

Table B.2: ccsdt-f12, Hartree

S.P.	B2PLYP	M06
diketo	-644.707305168490	-644.707305168490
ts1	-644.706353094145	-644.706399692284
int1		-644.714533923869
ts2		-644.715825861008
dieno	-644.730607891079	-644.730607891078

Table B.3: Int and Ts2 energies at different LoT starting from M06 optimized geometries

LoT/6-311+G(d,p)	ts1	int	ts_2	dieno
B2PLYP	1.525	-5.739	-5.7713	-16.661
DSDPBEP86	1.352	-7.369	-7.4907	-19.8364
Cam-B3LYP	0.432	-4.471	-5.080	-13.31
B3LYP	1.06	-2.639	-2.848	-9.679

Table B.4: Symmetry

LoT	diketo	ts_1	int	ts_2	dieno
B2PLYP	C_{2h}	C_S			C_{2h}
DSDPBEP86	C_{2h}	C_S			C_{2h}
Cam-B3lYP	C_{2h}	C_S			C_{2h}
ωB97XD	C_{2h}	C_S			C_{2h}
M11	C_{2h}	C_S			C_{2h}
BH&HLYP	C_{2h}	C_S			C_{2h}
B3LYP	C_{2h}	C_S			C_{2h}
PBE0	C_{2h}	C_S			C_{2h}
M06	C_{2h}	C_S	C_S	C_S	C_{2h}
M062X	C_{2h}	C_S			C_{2h}
PBE	C_{2h}	C_S			C_{2h}
BLYP	C_{2h}	C_S	C_S	C_S	C_2
M06L	C_{2h}	C_S	C_S	C_S	C_{2h}

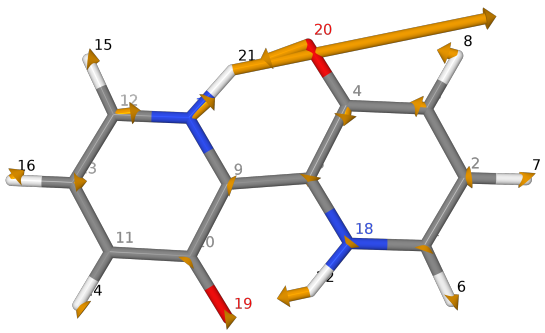

Figure B-1: Freq immaginaria TS1 M062X coinvolge entrambi gli idrogeni

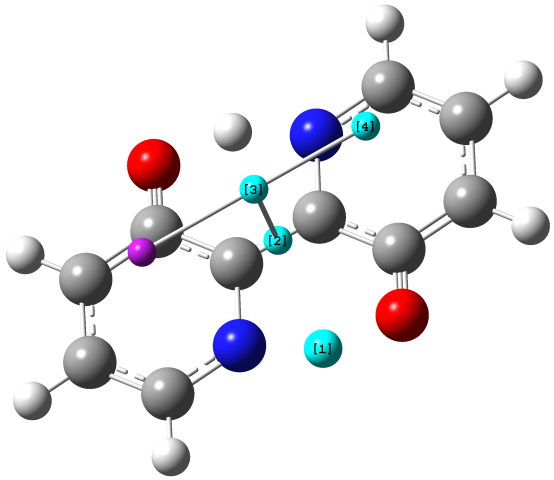

Figure B-2: Scansion of the dihedral angle at XC/6-31+G(d,p). Symm: C_{2h} (E, C_2, i, σ_h)

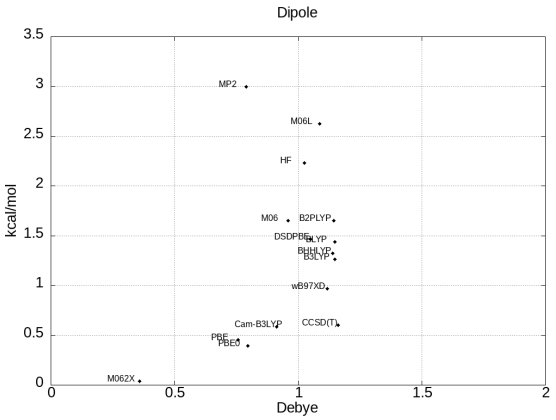

Figure B-3: Comparison between the dipole moment on the TS and the activation energy

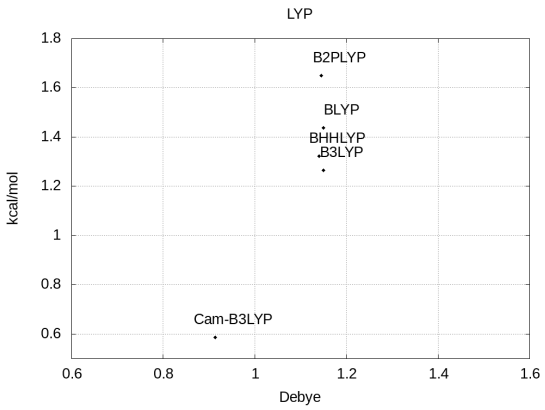

Figure B-4: Comparison between the dipole moment on the TS and the activation energy for the LYP E_{corr} functionals

Table B.5: Diketo stabilization

Lot/6-311+G(d,p)	Hartree	ΔE (Hartree)
CCSD(T)-F12	-644.707305168490	0.000000000
DSDBPBEP86	-643.626703076	1.080602092
B2PLYP	-644.687994552	0.019310616
wB97XD	-645.781779735	-1.074474567
Cam-B3LYP	-645.697632739	-0.990327571
BH&HLYP	-645.619837984	-0.912532816
M062X	-645.747054688	-1.039749520
B3LYP	-646.015569142	-1.308263974
PBE0	-645.277393574	-0.570088406
M06	-645.571990751	-0.864685583
BLYP	-645.829094373	-1.121789205
M06L	-645.930893310	-1.223588142
PBE	-645.930893310	-1.223588142

Table B.6: Cam-B3LYP ESP charges

Atom	Diketo	TS_1	Dieno
1 C	-0.130383	-0.121961	0.015940
2 C	-0.150706	-0.137199	-0.192968
3 C	-0.276622	-0.238791	-0.219726
4 C	0.553458	0.544118	0.398920
5 C	-0.028601	-0.073446	0.091794
6 H	0.170271	0.148001	0.123434
7 H	0.167506	0.147025	0.160427
8 H	0.183664	0.159258	0.189541
18 N	-0.155759	-0.079689	-0.350970
20 O	-0.719621	-0.709458	-0.622145
22 H	0.386180	0.336132	0.403057
9 C	-0.016825	-0.042040	0.111526
10 C	0.532220	0.515937	0.374433
11 C	-0.262173	-0.247375	-0.202591
12 C	-0.138775	-0.169687	-0.000292
13 C	-0.140150	-0.126178	-0.184202
14 H	0.181293	0.171114	0.186958
15 H	0.173620	0.170424	0.128955
16 H	0.162493	0.151177	0.156816
17 N	-0.163863	-0.013868	-0.353808
19 O	-0.715648	-0.689510	-0.618214
21 H	0.388420	0.306017	0.403117

Table B.7: wB97XD ESP charges

Atom	Diketo	TS_1	Dieno
1 C	-0.135212	-0.122646	-0.135212
2 C	-0.156741	-0.145264	-0.156741
3 C	-0.274378	-0.238965	-0.274378
4 C	0.529598	0.532328	0.529598
5 C	-0.025690	-0.089176	-0.025690
6 H	0.175136	0.151706	0.175136
7 H	0.171968	0.151917	0.171968
8 H	0.186333	0.162143	0.186333
18 N	-0.151613	-0.083077	-0.151613
20 O	-0.699183	-0.697340	-0.699183
22 H	0.380960	0.335022	0.380960
9 C	-0.021394	-0.019473	-0.021394
10 C	0.514369	0.488973	0.514369
11 C	-0.262987	-0.243789	-0.262987
12 C	-0.144451	-0.162063	-0.144451
13 C	-0.147736	-0.139554	-0.147736
14 H	0.184561	0.175501	0.184561
15 H	0.178402	0.173419	0.178402
16 H	0.167960	0.157735	0.167960
17 N	-0.152788	-0.036111	-0.152788
19 O	-0.697191	-0.667260	-0.697191
21 H	0.380078	0.315976	0.380078

Table B.8: M06 ESP charges

Atom	Diketo	TS_1	Int	TS_2	Dieno
1 C	-0.146443	-0.112177	0.093147	0.084201	0.099983
2 C	-0.122799	-0.124067	-0.221604	-0.222475	-0.238312
3 C	-0.241738	-0.246572	-0.150643	-0.152104	-0.117576
4 C	0.557529	0.555960	0.402252	0.382857	0.337081
5 C	-0.077517	-0.101998	0.160120	0.178430	0.108519
6 H	0.157733	0.142257	0.079034	0.082958	0.083909
7 H	0.145260	0.140574	0.143527	0.144967	0.149938
8 H	0.153789	0.154227	0.134933	0.139079	0.147317
18 N	-0.070629	-0.100198	-0.407747	-0.401179	-0.359536
20 O	-0.690358	-0.692179	-0.654082	-0.640172	-0.568542
22 H	0.333227	0.344059	0.406924	0.397634	0.374833
9 C	-0.072825	-0.010251	-0.164425	-0.171524	0.069671
10 C	0.558084	0.509081	0.510302	0.507760	0.355769
11 C	-0.255389	-0.241507	-0.219759	-0.220229	-0.127459
12 C	-0.161274	-0.136834	-0.151069	-0.151414	0.081366
13 C	-0.106875	-0.127413	-0.139192	-0.139219	-0.232630
14 H	0.156629	0.162422	0.172274	0.172293	0.150871
15 H	0.160767	0.156383	0.167208	0.165216	0.087313
16 H	0.142406	0.146992	0.150797	0.150565	0.149943
17 N	-0.060943	-0.089487	0.019663	0.026375	-0.321428
19 O	-0.689459	-0.667857	-0.618239	-0.611808	-0.583574
21 H	0.330826	0.338584	0.286579	0.277790	0.352543

Table B.9: B3LYP ESP charges

Atom	Diketo	TS_1	Dieno
1 C	-0.148600	-0.141029	0.084610
2 C	-0.129762	-0.143525	-0.233838
3 C	-0.239787	-0.230358	-0.125263
4 C	0.547124	0.490726	0.338606
5 C	-0.069710	-0.007689	0.110650
6 H	0.161438	0.162801	0.091854
7 H	0.147737	0.151907	0.150830
8 H	0.156985	0.164515	0.150540
20 O	-0.690119	-0.644846	-0.565016
18 N	-0.063104	-0.059604	-0.344353
22 H	0.325656	0.315225	0.361211
9 C	-0.065141	-0.111950	0.066610
10 C	0.548284	0.552842	0.359171
11 C	-0.256000	-0.257246	-0.135904
12 C	-0.167430	-0.159175	0.062399
13 C	-0.110437	-0.108179	-0.227065
14 H	0.160421	0.157947	0.154414
15 H	0.165267	0.153822	0.095963
16 H	0.144431	0.139273	0.150740
17 N	-0.050692	-0.035872	-0.300256
19 O	-0.689288	-0.689379	-0.581655
21 H	0.322727	0.299795	0.335753

Table B.10: BH&HLYP ESP charge

Atom	Diketo	TS_1	Dieno
1 C	-0.122424	-0.109285	0.094359
2 C	-0.166386	-0.144438	-0.256116
3 C	-0.274321	-0.258265	-0.126511
4 C	0.549039	0.579658	0.350980
5 C	-0.019788	-0.098255	0.119410
6 H	0.175020	0.151368	0.097055
7 H	0.174817	0.153354	0.162235
8 H	0.189705	0.168716	0.159906
18 N	-0.173769	-0.112891	-0.366718
20 O	-0.728401	-0.740402	-0.597372
22 H	0.397144	0.358951	0.381531
9 C	-0.012682	0.013842	0.077819
10 C	0.530476	0.521091	0.371353
11 C	-0.261037	-0.245858	-0.136995
12 C	-0.132663	-0.136256	0.075059
13 C	-0.155414	-0.150721	-0.250329
14 H	0.187553	0.176795	0.163568
15 H	0.178707	0.169530	0.100487
16 H	0.169941	0.160775	0.162231
17 N	-0.177579	-0.107581	-0.326578
19 O	-0.725476	-0.708520	-0.613470
21 H	0.397540	0.358391	0.358098

Table B.11: PBE0 ESP charges

Atom	Diketo	TS_1	Dieno
1 C	-0.132222	-0.118549	0.059204
2 C	-0.160828	-0.151458	-0.234764
3 C	-0.275294	-0.238586	-0.142744
4 C	0.519034	0.519561	0.338501
5 C	-0.027771	-0.067087	0.094270
6 H	0.173429	0.153625	0.103196
7 H	0.171694	0.152880	0.158378
8 H	0.186065	0.162374	0.159681
18 N	-0.152869	-0.100052	-0.318839
20 O	-0.678040	-0.674657	-0.552107
22 H	0.377249	0.336496	0.353593
9 C	-0.020733	-0.045615	0.055856
10 C	0.502043	0.506889	0.355424
11 C	-0.262972	-0.259626	-0.150941
12 C	-0.141474	-0.170400	0.039403
13 C	-0.151369	-0.129888	-0.229243
14 H	0.184080	0.175204	0.162855
15 H	0.176812	0.174693	0.107130
16 H	0.167448	0.155518	0.158314
17 N	-0.156492	-0.040048	-0.279055
19 O	-0.675427	-0.656574	-0.567460
21 H	0.377635	0.315298	0.329348

Table B.12: M062X ESP charges

Atom	Diketo	TS_1	Dieno
1 C	-0.131777	-0.152372	0.075902
2 C	-0.162484	-0.147718	-0.248555
3 C	-0.281226	-0.250221	-0.133569
4 C	0.530297	0.516068	0.334156
5 C	-0.030393	-0.046361	0.105047
6 H	0.176685	0.171201	0.103160
7 H	0.175480	0.160827	0.163832
8 H	0.191491	0.174376	0.162845
18 N	-0.159611	-0.051306	-0.343827
20 O	-0.696492	-0.679814	-0.573433
22 H	0.388704	0.325424	0.372487
9 C	-0.023889	-0.092141	0.065800
10 C	0.513121	0.540625	0.352624
11 C	-0.268749	-0.270603	-0.143212
12 C	-0.141230	-0.177437	0.056536
13 C	-0.152687	-0.117989	-0.242716
14 H	0.189511	0.174028	0.166364
15 H	0.180120	0.173737	0.106784
16 H	0.171085	0.153576	0.163780
17 N	-0.162892	-0.032390	-0.304545
19 O	-0.693914	-0.691405	-0.588751
21 H	0.388849	0.319897	0.349292

Table B.13: M06L ESP charges

Atom	Diketo	TS_1	Int	TS_2	Dieno
1 C	-0.125262	-0.105855	0.061296	0.096905	0.024937
2 C	-0.130250	-0.121860	-0.192720	-0.224789	-0.176017
3 C	-0.265157	-0.230678	-0.165016	-0.147622	-0.202845
5 C	-0.027181	-0.074907	0.131331	0.192033	0.087755
6 H	0.156244	0.129792	0.080215	0.075215	0.105808
7 H	0.150173	0.130800	0.131736	0.138980	0.143826
8 H	0.164418	0.141954	0.130396	0.133411	0.170687
18 N	-0.150603	-0.087256	-0.353819	-0.399641	-0.342861
4 C	0.517925	0.517141	0.398760	0.357603	0.363823
20 O	-0.651241	-0.649361	-0.624350	-0.599520	-0.564467
22 H	0.363151	0.322171	0.366971	0.385979	0.387877
9 C	-0.026789	-0.051314	-0.136415	-0.177193	0.103870
11 C	-0.255069	-0.242120	-0.226578	-0.229050	-0.187942
12 C	-0.137515	-0.160815	-0.145745	-0.142886	0.013835
13 C	-0.120205	-0.109635	-0.117542	-0.118739	-0.171911
14 H	0.162859	0.155539	0.162972	0.164827	0.168669
15 H	0.160231	0.155974	0.158360	0.150672	0.109847
16 H	0.146184	0.137116	0.139610	0.137617	0.141706
17 N	-0.146446	-0.019220	0.004641	0.025730	-0.345027
10 C	0.504741	0.488159	0.481158	0.492577	0.344017
19 O	-0.650085	-0.621275	-0.566636	-0.578708	-0.562282
21 H	0.359875	0.295650	0.281373	0.266600	0.386694

Table B.14: BLYP ESP charges

Atom	Diketo	TS_1	Int	TS_2	Dieno
1 C	-0.121889	-0.129058	0.037109	0.041561	0.012400
2 C	-0.139139	-0.102382	-0.185012	-0.190597	-0.173884
3 C	-0.259576	-0.239228	-0.161768	-0.157664	-0.210810
5 C	-0.020558	-0.068859	0.129510	0.135704	0.083891
6 H	0.159591	0.137762	0.091154	0.090746	0.115865
7 H	0.154749	0.127842	0.132914	0.134320	0.147265
8 H	0.168803	0.147344	0.134142	0.135548	0.176252
4 C	0.515322	0.510010	0.388541	0.378526	0.377694
20 O	-0.660448	-0.652805	-0.619464	-0.614334	-0.577204
18 N	-0.161801	-0.063750	-0.320495	-0.324482	-0.335965
22 H	0.364491	0.290758	0.340927	0.340019	0.382374
9 C	-0.018182	-0.044659	-0.131336	-0.122919	0.101492
11 C	-0.245114	-0.239152	-0.230250	-0.225368	-0.195116
12 C	-0.134271	-0.141212	-0.140757	-0.127698	-0.005629
13 C	-0.125440	-0.118335	-0.114282	-0.118046	-0.162533
14 H	0.165564	0.158312	0.166261	0.165293	0.173799
15 H	0.163808	0.153890	0.155068	0.149936	0.121753
16 H	0.149128	0.139204	0.137476	0.136680	0.142919
17 N	-0.167765	-0.039792	0.014318	-0.004261	-0.337533
10 C	0.495854	0.489109	0.475984	0.468774	0.354802
19 O	-0.653768	-0.612494	-0.564633	-0.562551	-0.573817
21 H	0.370642	0.297496	0.264592	0.270813	0.381986

Table B.15: PBE ESP charges

Atom	Diketo	TS_1	Dieno
1 C	-0.112281	-0.162899	-0.003189
2 C	-0.149140	-0.118718	-0.181349
3 C	-0.270630	-0.241861	-0.219266
5 C	-0.024613	-0.056962	0.080140
6 H	0.161403	0.162000	0.124823
7 H	0.160214	0.143678	0.154927
8 H	0.178128	0.162205	0.182198
4 C	0.501728	0.469655	0.366280
20 O	-0.643349	-0.596703	-0.557219
22 H	0.372540	0.288062	0.379549
18 N	-0.173964	-0.017147	-0.323160
9 C	-0.029733	-0.068800	0.083125
11 C	-0.267624	-0.246132	-0.205714
12 C	-0.146339	-0.149405	-0.023808
13 C	-0.138292	-0.110530	-0.170942
14 H	0.175802	0.156012	0.180175
15 H	0.169725	0.149006	0.130740
16 H	0.159412	0.136813	0.151397
17 N	-0.144302	-0.039684	-0.312488
10 C	0.500377	0.485110	0.349354
19 O	-0.643472	-0.627173	-0.557820
21 H	0.364409	0.283472	0.372248

Table B.16: ESP charges TS1 GGA

Moiety	M06L	BLYP	PBE
CO	-0.13222	-0.142795	-0.142063
C	-0.5333	-0.539527	-0.574867
N	-0.087256	-0.063750	-0.039684
H22	0.322171	0.290758	0.283472
CO	-0.133116	-0.123385	-0.127048
C	-0.563884	-0.543358	-0.58044
N	-0.019220	-0.039792	-0.017147
H21	0.295650	0.297496	-0.017147

Table B.17: Dipole moment on the TS, activation energy, imaginary frequency for the first TS

Functional	D_{TS}(Debye)	Δ E (kcal/mol)	ν cm$^{-}-1$
CCSD(T)	1.161	0.6	
MP2	0.789	2.999	-787.6
DSDPBE	1.0487	1.467	-968.6
B2PLYP	1.1446	1.649	-1021.3
Cam-B3LYP	0.9134	0.587	-905.3
wB97XD	1.1186	0.970	-995.4
M062X	0.3591	0.039	-389.1
PBE0	0.7972	0.396	-787.5
M06	0.9599	1.654	-1495.6
BHHLYP	1.1402	1.322	-1139.4
B3LYP	1.1496	1.264	-1037.8
PBE	0.7574	0.455	-744.1
M06L	1.0864	2.626	-1400.8
BLYP	1.1493	1.438	-978.0
HF	1.0245	2.230	-1355.7

Table B.18: Dipole moment on the TS all components, activation energy

Functional	D_X	D_Y	D_Z	D_{TS}(Debye)	Δ E (kcal/mol)
M062X	0.3566	0.0416	-0.0000	0.3591	0.039
PBE	0.1369	0.7450	0.0000	0.7574	0.455
PBE0	-0.7938	-0.0738	0.0001	0.7972	0.396
Cam-B3LYP	-0.9098	-0.0801	0.0001	0.9134	0.587
M06	-0.9550	-0.0965	0.0001	0.9599	1.654
DSDPBE	-1.0421	-0.1177	0.0002	1.0487	1.467
M06L	-1.0757	-0.1521	0.0002	1.0864	2.626
wB97XD	-1.1127	-0.1146	0.0002	1.1186	0.970
BHHLYP	-1.1354	-0.1049	0.0002	1.1402	1.322
B2PLYP	-1.1373	-0.1291	0.0002	1.1446	1.649
BLYP	1.1370	-0.1678	0.0001	1.1493	1.438
B3LYP	1.1423	0.1286	-0.0021	1.1496	1.264
CCSD(T)	0.0	0.0	0.0	1.161	0.6
MP2	0.0	0.0	0.0	0.789	2.999
HF	0.0	0.0	0.0	1.0245	2.230

Table B.19: Evolution of the ESP charge distribution from the diketo form to the ts $\Delta ESP = ESP_{ts} - ESP_3$

Atoms	m06	B3LYP	BH&HLYP	PBE0	M062x
22 H	0.010832	0.035958	-0.358951	-0.336496	-0.06328
18 N	-0.029569	-0.264384	-0.253827	-0.218787	0.108305
20 O	-0.001821	0.107724	0.143030	0.12255	0.016678
4 C	-0.001569	-0.193671	-0.228678	-0.18106	-0.014229
1 C	-0.008946	0.221574	-0.094359	-0.059204	-0.075902
2 C	-0.001268	-0.118886	-0.111678	-0.083306	0.014766
3 C	-0.004834	0.121342	0.131754	0.095842	0.031005
5 C	-0.024481	0.178560	0.217665	0.161357	-0.015968
6 H	-0.015476	-0.057859	-0.054313	-0.050429	-0.005484
7 H	-0.004686	0.011467	0.008881	0.005498	-0.014653
8 H	0.000438	-0.003533	-0.00881	-0.002693	-0.017115
21 H	0.007758	-0.315225	-0.000293	0.014050	-0.068952
17 N	-0.028544	-0.284749	-0.218997	-0.239007	0.13002
19 O	0.021602	0.079830	0.095050	0.089114	0.002509
10 C	-0.049003	-0.152120	-0.149738	-0.151465	0.027504
9 C	0.062574	0.118339	0.063977	0.101471	-0.068252
11 C	0.013882	0.105095	0.108863	0.108685	-0.001854
12 C	0.024440	-0.08461	0.211315	0.209803	-0.036207
13 C	-0.020538	-0.090313	-0.099608	-0.099355	0.034698
14 H	0.005793	-0.013975	-0.013227	-0.012349	-0.015483
15 H	-0.004384	-0.070947	-0.069043	-0.067563	-0.006383
16 H	0.004586	-0.001077	0.001456	0.002796	-0.017509

Table B.20: ESP charge distribution in the keto-eno intermediate for GGA functionals

Atom	M06L$_{int}$	BLYP$_{int}$	Δ ESP
22 H	0.366971	0.340927	-0.026044
18 N	-0.353819	-0.320495	0.033324
20 O	-0.624350	-0.619464	0.004886
4 C	0.398760	0.388541	-0.010219
1 C	0.061296	0.037109	-0.024187
2 C	-0.192720	-0.185012	0.007708
3 C	-0.165016	-0.161768	0.003248
5 C	0.131331	0.129510	-0.001821
6 H	0.080215	0.091154	0.010939
7 H	0.131736	0.132914	0.001178
8 H	0.130396	0.134142	0.003746
9 C	-0.136415	-0.131336	0.005079
10 C	0.481158	0.475984	-0.005174
11 C	-0.226578	-0.230250	-0.003672
12 C	-0.145745	-0.140757	0.004988
13 C	-0.117542	-0.114282	0.003260
14 H	0.162972	0.166261	0.003289
15 H	0.158360	0.155068	-0.003292
16 H	0.139610	0.137476	-0.002134
17 N	0.004641	0.014318	0.009677
19 O	-0.566636	-0.564633	0.002003
21 H	0.281373	0.264592	-0.016781

Table B.21: Evolution of the ESP charge distribution from the diketo form to the ts $\Delta ESP = ESP_{ts} - ESP_3$

Atom	M06L	BLYP	PBE
22 H	-0.040980	-0.073733	-0.080937
18 N	0.063347	0.098051	0.104618
20 O	0.001880	0.007643	0.016299
4 C	-0.000784	-0.005312	-0.015267
5 C	-0.047726	-0.048301	-0.039067
1 C	0.019407	-0.007169	-0.003066
2 C	0.00839	0.036757	0.027762
3 C	0.034479	0.020348	0.021492
6 H	-0.026452	-0.021829	-0.01979
7 H	-0.019373	-0.026907	-0.022599
8 H	-0.022464	-0.021459	-0.020719
21 H	-0.064225	-0.073146	-0.084478
17 N	0.127226	0.127973	0.156817
19 O	0.02881	0.041274	0.046646
10 C	-0.016582	-0.006745	-0.032073
9 C	-0.024525	-0.026477	-0.032349
11 C	0.012949	0.005962	0.028769
12 C	-0.0233	-0.006941	-0.050618
13 C	0.01057	0.007105	0.030422
14 H	-0.00732	-0.007252	0.000597
15 H	-0.004257	-0.009918	-0.015923
16 H	-0.009068	-0.009924	-0.016536

Table B.22: Caption

Atom	M06L	BLYP	PBE
18 N	0.063347	0.098051	0.156817
20 O	0.00188	0.007643	0.046646
5 C	-0.047726	-0.048301	-0.032349
4 C	-0.000784	-0.005312	-0.032073
1 C	0.019407	-0.007169	-0.050618
2 C	0.00839	0.036757	0.030422
3 C	0.034479	0.020348	0.028769
6 H	-0.026452	-0.021829	0.000597
7 H	-0.019373	-0.026907	-0.016536
8 H	-0.022464	-0.021459	-0.015923
22 H	-0.04098	-0.073733	-0.084478
17 N	0.127226	0.127973	0.104618
19 O	0.02881	0.041274	0.016299
9 C	-0.024525	-0.026477	-0.039067
10 C	-0.016582	-0.006745	-0.015267
11 C	0.012949	0.005962	0.021492
12 C	-0.0233	-0.006941	-0.003066
13 C	0.01057	0.007105	0.027762
14 H	-0.00732	-0.007252	-0.01979
15 H	-0.004257	-0.009918	-0.020719
16 H	-0.009068	-0.009924	-0.022599
21 H	-0.064225	-0.073146	-0.080937

Table B.23: The double proton transfer were obtained by scanning the dihedral angle (previous slide). The structures were optimised on C_{2h} symmetry with tight criteria.The anti-symmetrical and symmetrical vibrational modes are represented by the first and second values, respectively.

XC/6-31+G(d,p)	func	ΔE (kcal/mol)	ν (cm^{-1})	
B2PLYP	ts	36.965	-1577.7	-1495.1
	di-eno	-16.069		
ωB97XD	ts	38.328	-1882.7	-1791.3
	di-eno	-12.480		
B3LYP	ts	35.043	-1758.9	-1681.5
	di-eno	-9.44		
BLYP	ts	21.274	-1238.9	-1153.9
	di-eno	-5.600		

B.1 Minimum Energy Path

Table B.24: M062X, x and y are the parameter of fit function.

	x	y	fit
0	-224	15.346140	15.342090
1	-208	15.203698	15.215522
2	-192	14.879907	14.918353
3	-176	14.975915	14.798973
4	-160	14.896223	14.980725

Table B.25: PBE, x and y are the parameter of fit function.

	x	y	fit
0	-255	5.658795	5.623316
1	-248	6.062905	6.081352
2	-240	5.801865	5.937383
3	-232	5.762333	5.646128
4	-231	5.405913	5.613254

Table B.26: wB97XD, x and y are the parameter of fit function.

	x	y	fit
0	-272	13.033175	13.016239
1	-263	11.925638	12.233581
2	-256	12.398772	12.168449
3	-255	12.711267	12.170210
4	-248	11.903675	12.177184

Table B.27: Cam-B3LYP, x and y are the parameter of fit function.

	x	y	fit
0	-260	12.974190	13.475827
1	-259	13.618005	13.461032
2	-256	13.574708	13.429598
3	-255	14.052862	13.422022
4	-252	13.072080	13.403356

Table B.28: PBE0, x and y are the parameter of fit function.

	x	y	fit
0	-256	9.615810	9.656600
1	-255	9.780215	9.676617
2	-248	9.495957	9.686357
3	-240	9.669147	9.554130
4	-232	9.585062	9.383013

Table B.29: M06L, x and y are the parameter of fit function.

	x	y	fit
0	-280	6.131930	6.135311
1	-260	6.159540	6.350041
2	-259	6.574945	6.331168
3	-240	5.758567	5.885683
4	-220	5.716525	5.615318

Table B.30: M06, x and y are the parameter of fit function.

	x	y	fit
0	-296	8.626243	8.782309
1	-289	9.567493	8.757508
2	-288	8.348260	8.732868
3	-282	8.230918	8.506031
4	-275	7.961093	8.136938

Table B.31: B3LYP, x and y are the parameter of fit function.

	x	y	fit
0	-308	9.487800	9.730186
1	-304	9.999213	9.773374
2	-300	10.004860	9.858036
3	-296	10.083298	9.950754
4	-292	10.027450	10.031188

Table B.32: BH&HLYP, x and y are the parameter of fit function.

	x	y	fit
0	-302	16.884770	16.880784
1	-285	14.792058	14.832917
2	-268	14.995368	14.834017
3	-252	14.292568	14.546530
4	-235	14.398615	14.322393

B.2 Mulliken

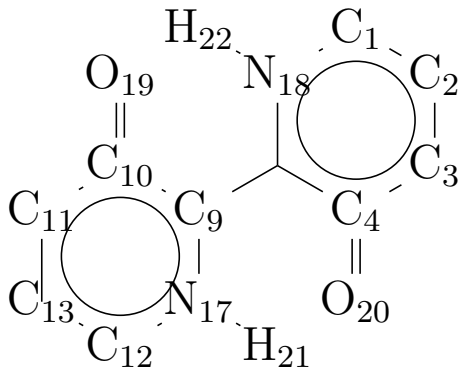

Figure B-5: Atom label as reported in the following tables

Table B.33: PBE/6-311+G(d,p), TS1=H21

Atom	diketo	ts1	dieno
1 C	-0.089197	-0.134312	-0.184067
2 C	-0.220073	-0.162037	-0.114974
3 C	0.129376	-0.171849	-0.321159
4 C	-0.431719	0.142971	0.128745
5 C	0.231393	0.060728	0.074715
6 H	0.148508	0.149052	0.137402
7 H	0.148985	0.150205	0.143005
8 H	0.148395	0.150067	0.148530
9 C	0.231393	0.030168	0.074715
10 C	-0.431719	-0.056968	0.128745
11 C	0.129376	-0.160135	-0.321159
12 C	-0.089197	-0.135199	-0.184067
13 C	-0.220073	-0.156265	-0.114974
14 H	0.148395	0.147559	0.148530
15 H	0.148508	0.143001	0.137402
16 H	0.148985	0.145820	0.143005
17 N	-0.092627	-0.151684	-0.114752
18 N	-0.092627	-0.097056	-0.114752
19 O	-0.388904	-0.400016	-0.341287
20 O	-0.388904	-0.405625	-0.341287
21 H	0.415863	0.490219	0.443842
22 H	0.415863	0.421357	0.443842

Table B.34: BLYP/6-311+G(d,p), TS1=H22

Atom	diketo	ts1	keto-eno	ts2	dieno
1 C	-0.045818	-0.065761	-0.121243	-0.126959	-0.108670
2 C	-0.179904	-0.148768	-0.120022	-0.115874	-0.116657
3 C	0.106882	-0.061672	-0.117175	-0.123374	-0.169143
4 C	-0.292078	-0.158525	-0.093431	-0.053593	0.047975
5 C	0.156232	0.003400	-0.011673	-0.018044	0.060803
6 H	0.134672	0.121359	0.118154	0.118379	0.122470
7 H	0.132595	0.124797	0.122919	0.123181	0.126441
8 H	0.133645	0.128383	0.128459	0.128599	0.132733
9 C	0.156232	0.061016	0.128208	0.118866	0.060803
10 C	-0.292078	0.167630	0.091989	0.077418	0.047975
11 C	0.106882	-0.058013	-0.085629	-0.091354	-0.169143
12 C	-0.045818	-0.058479	-0.025075	-0.025594	-0.108670
13 C	-0.179904	-0.165745	-0.165682	-0.160059	-0.116657
14 H	0.133645	0.134369	0.137748	0.137316	0.132733
15 H	0.134672	0.135046	0.136869	0.135505	0.122470
16 H	0.132595	0.134067	0.135895	0.135117	0.126441
17 N	-0.114488	-0.109445	-0.158737	-0.179491	-0.163928
18 N	-0.114488	-0.225603	-0.173419	-0.170052	-0.163928
19 O	-0.403037	-0.395340	-0.337010	-0.334686	-0.337741
20 O	-0.403037	-0.412557	-0.414557	-0.417193	-0.337741
21 H	0.371300	0.365982	0.412707	0.435606	0.405717
22 H	0.371300	0.483856	0.410704	0.406285	0.405717

Table B.35: M06L/6-311+G(d,p), TS1=H22

Atom	diketo	ts1	keto-eno	ts2	dieno
1 C	0.013149	-0.004495	-0.082254	-0.102295	-0.084295
2 C	-0.385568	-0.317118	-0.267506	-0.251838	-0.276688
3 C	0.114857	-0.084484	-0.130744	-0.135774	-0.155631
4 C	-0.281131	-0.070957	-0.064077	0.024952	-0.006005
5 C	0.264033	0.148105	0.177162	0.156818	0.271954
6 H	0.155613	0.144776	0.125108	0.125606	0.130011
7 H	0.154074	0.149661	0.140749	0.142006	0.147101
8 H	0.157478	0.156010	0.150005	0.150768	0.156202
9 C	0.264033	0.133767	0.261131	0.256154	0.271954
10 C	-0.281131	0.133107	0.052146	0.001700	-0.006005
11 C	0.114857	-0.072614	-0.087140	-0.099229	-0.155631
12 C	0.013149	-0.044516	-0.014679	-0.000426	-0.084295
13 C	-0.385568	-0.322962	-0.350077	-0.333419	-0.276688
14 H	0.157478	0.160998	0.164669	0.163383	0.156202
15 H	0.155613	0.156818	0.158044	0.151783	0.130011
16 H	0.154074	0.157401	0.161143	0.158395	0.147101
17 N	-0.126993	-0.124341	-0.152398	-0.237794	-0.239983
18 N	-0.126993	-0.256315	-0.255586	-0.249140	-0.239983
19 O	-0.448789	-0.473041	-0.368809	-0.363164	-0.373285
20 O	-0.448789	-0.459498	-0.461176	-0.476661	-0.373285
21 H	0.383276	0.379717	0.406073	0.492283	0.430619
22 H	0.383276	0.509980	0.438214	0.425891	0.430619

Table B.36: M06/6-311+G(d,p), TS1=H22

Atom	diketo	ts1	keto-eno	ts2	dieno
1 C	-0.057124	-0.034470	-0.132726	-0.146682	-0.119499
2 C	-0.248736	-0.236596	-0.185774	-0.173966	-0.177423
3 C	-0.129544	-0.128323	-0.195712	-0.211257	-0.241514
4 C	0.030796	-0.034657	-0.027585	0.037988	0.060043
5 C	0.007930	0.000075	-0.016881	-0.035452	0.043943
6 H	0.171201	0.164299	0.145768	0.146218	0.151410
7 H	0.177354	0.174107	0.165390	0.165779	0.170237
8 H	0.180333	0.177787	0.172421	0.172828	0.178823
9 C	0.007930	-0.014875	0.111028	0.103645	0.043943
10 C	0.030796	0.138671	0.081851	0.050828	0.060043
11 C	-0.129544	-0.143264	-0.162525	-0.167453	-0.241514
12 C	-0.057124	-0.071070	-0.027740	-0.015910	-0.119499
13 C	-0.248736	-0.236331	-0.250236	-0.240615	-0.177423
14 H	0.180333	0.181524	0.185856	0.185042	0.178823
15 H	0.171201	0.172468	0.175203	0.172150	0.151410
16 H	0.177354	0.178953	0.181991	0.180703	0.170237
17 N	-0.060042	-0.061798	-0.092213	-0.150003	-0.129636
18 N	-0.060042	-0.174079	-0.153837	-0.146613	-0.129636
19 O	-0.451025	-0.460246	-0.336610	-0.331782	-0.340417
20 O	-0.451025	-0.452794	-0.452841	-0.462261	-0.340417
21 H	0.378858	0.374551	0.402447	0.463278	0.404031
22 H	0.378858	0.486067	0.412727	0.403534	0.404031

Table B.37: B3LYP/6-311+G(d,p), TS1=H21

Atom	diketo	ts1	dieno
1 C	-0.038665	-0.061917	-0.110788
2 C	-0.217278	-0.184829	-0.146368
3 C	0.087677	-0.097243	-0.220847
4 C	-0.265897	0.151125	0.084099
5 C	0.197748	0.092168	0.120782
6 H	0.143336	0.144507	0.128251
7 H	0.141644	0.143562	0.135040
8 H	0.143301	0.145413	0.142485
9 C	0.197748	0.057120	0.120782
10 C	-0.265897	-0.072701	0.084099
11 C	0.087677	-0.101283	-0.220847
12 C	-0.038665	-0.050935	-0.110788
13 C	-0.217278	-0.178884	-0.146368
14 H	0.143301	0.141428	0.142485
15 H	0.143336	0.135515	0.128251
16 H	0.141644	0.137660	0.135040
17 N	-0.143940	-0.231416	-0.182144
18 N	-0.143940	-0.145172	-0.182144
19 O	-0.450043	-0.461344	-0.373884
20 O	-0.450043	-0.466683	-0.373884
21 H	0.402116	0.501609	0.423373
22 H	0.402116	0.402302	0.423373

Table B.38: BH&HLYP/6-311+G(d,p), TS1=H22

Atom	diketo	ts1	dieno
1 C	-0.031336	-0.027130	-0.094121
2 C	-0.228689	-0.214003	-0.183577
3 C	-0.120639	-0.132565	-0.262436
4 C	0.065427	-0.013605	0.116494
5 C	0.144676	0.101974	0.209381
6 H	0.149146	0.141423	0.130630
7 H	0.147376	0.143541	0.140251
8 H	0.151731	0.148699	0.149633
9 C	0.144676	0.152033	0.209381
10 C	0.065427	0.204435	0.116494
11 C	-0.120639	-0.124092	-0.262436
12 C	-0.031336	-0.043894	-0.094121
13 C	-0.228689	-0.216588	-0.183577
14 H	0.151731	0.152703	0.149633
15 H	0.149146	0.150657	0.130630
16 H	0.147376	0.149263	0.140251
17 N	-0.186770	-0.195311	-0.222767
18 N	-0.186770	-0.281234	-0.222767
19 O	-0.528338	-0.540771	-0.423426
20 O	-0.528338	-0.528849	-0.423426
21 H	0.437416	0.430655	0.439939
22 H	0.437416	0.542660	0.439939

Table B.39: PBE0/6-311+G(d,p), TS1=H22

Atom	diketo	ts1	dieno
1 C	-0.118515	-0.123989	-0.179972
2 C	-0.212722	-0.197432	-0.153308
3 C	-0.173129	-0.185290	-0.363481
4 C	0.068612	0.000240	0.171230
5 C	0.095505	0.068108	0.141300
6 H	0.156963	0.151604	0.142699
7 H	0.157851	0.154955	0.151359
8 H	0.159468	0.157351	0.158386
9 C	0.095505	0.104151	0.141300
10 C	0.068612	0.196274	0.171230
11 C	-0.173129	-0.194622	-0.363481
12 C	-0.118515	-0.129020	-0.179972
13 C	-0.212722	-0.199590	-0.153308
14 H	0.159468	0.159964	0.158386
15 H	0.156963	0.157899	0.142699
16 H	0.157851	0.159208	0.151359
17 N	-0.125830	-0.136479	-0.142112
18 N	-0.125830	-0.190818	-0.142112
19 O	-0.461135	-0.471853	-0.387928
20 O	-0.461135	-0.462564	-0.387928
21 H	0.452932	0.453276	0.461827
22 H	0.452932	0.528628	0.461827

Table B.40: M11/6-311+G(d,p), TS1=H22

Atom	diketo	ts1	dieno
1 C	-0.214492	-0.229164	-0.281110
2 C	-0.199367	-0.173295	-0.127269
3 C	-0.217707	-0.233144	-0.355842
4 C	-0.048868	-0.080303	0.026813
5 C	-0.108008	-0.137761	-0.079134
6 H	0.194517	0.188824	0.179116
7 H	0.214055	0.211137	0.207324
8 H	0.214905	0.212709	0.212852
9 C	-0.108008	-0.094611	-0.079134
10 C	-0.048868	0.036179	0.026813
11 C	-0.217707	-0.231878	-0.355842
12 C	-0.214492	-0.216461	-0.281110
13 C	-0.199367	-0.187045	-0.127269
14 H	0.214905	0.215610	0.212852
15 H	0.194517	0.195751	0.179116
16 H	0.214055	0.215486	0.207324
17 N	0.044879	0.031677	0.067984
18 N	0.044879	-0.009098	0.067984
19 O	-0.345344	-0.355410	-0.276033
20 O	-0.345344	-0.350696	-0.276033
21 H	0.465429	0.471559	0.425299
22 H	0.465429	0.519935	0.425299

Table B.41: M062X/6-311+G(d,p), TS1=H21

Atom	diketo	ts1	dieno
1 C	-0.135131	-0.138829	-0.195470
2 C	-0.163801	-0.157973	-0.106606
3 C	-0.175814	-0.182610	-0.319816
4 C	0.045756	0.091490	0.107305
5 C	0.026832	0.030275	0.053549
6 H	0.165013	0.165479	0.150327
7 H	0.173759	0.174250	0.167812
8 H	0.173998	0.174387	0.173991
9 C	0.026832	0.011501	0.053549
10 C	0.045756	0.021574	0.107305
11 C	-0.175814	-0.179378	-0.319816
12 C	-0.135131	-0.137692	-0.195470
13 C	-0.163801	-0.157711	-0.106606
14 H	0.173998	0.173203	0.173991
15 H	0.165013	0.162988	0.150327
16 H	0.173759	0.172616	0.167812
17 N	-0.106588	-0.130751	-0.097378
18 N	-0.106588	-0.111414	-0.097378
19 O	-0.461826	-0.462962	-0.355275
20 O	-0.461826	-0.463257	-0.355275
21 H	0.457800	0.485429	0.421562
22 H	0.457800	0.459385	0.421562

Table B.42: Cam-B3LYP/6-311+G(d,p), TS1=H22

Atom	diketo	ts1	dieno
1 C	-0.052287	-0.053120	-0.113740
2 C	-0.190959	-0.176417	-0.145640
3 C	-0.100077	-0.111575	-0.216558
4 C	0.020697	-0.029872	0.090354
5 C	0.061166	0.025954	0.082466
6 H	0.150535	0.144566	0.135271
7 H	0.151079	0.147977	0.144521
8 H	0.154537	0.152108	0.152881
9 C	0.061166	0.061117	0.082466
10 C	0.020697	0.124182	0.090354
11 C	-0.100077	-0.100992	-0.216558
12 C	-0.052287	-0.059415	-0.113740
13 C	-0.190959	-0.183992	-0.145640
14 H	0.154537	0.155490	0.152881
15 H	0.150535	0.151958	0.135271
16 H	0.151079	0.152564	0.144521
17 N	-0.137038	-0.143097	-0.175367
18 N	-0.137038	-0.210755	-0.175367
19 O	-0.476780	-0.479720	-0.374707
20 O	-0.476780	-0.478525	-0.374707
21 H	0.419126	0.418312	0.420520
22 H	0.419126	0.493251	0.420520

Table B.43: wB97XD/6-311+G(d,p), TS1=H22

Atom	diketo	ts1	dieno
1 C	-0.095055	-0.091528	-0.151481
2 C	-0.231999	-0.214422	-0.174253
3 C	-0.153084	-0.165082	-0.293201
4 C	0.071233	0.003241	0.127089
5 C	0.080772	0.046994	0.131382
6 H	0.167376	0.159720	0.149972
7 H	0.166525	0.162521	0.159504
8 H	0.169866	0.166798	0.168451
9 C	0.080772	0.090347	0.131382
10 C	0.071233	0.196872	0.127089
11 C	-0.153084	-0.165047	-0.293201
12 C	-0.095055	-0.106181	-0.151481
13 C	-0.231999	-0.219636	-0.174253
14 H	0.169866	0.171051	0.168451
15 H	0.167376	0.168942	0.149972
16 H	0.166525	0.168490	0.159504
17 N	-0.128883	-0.137337	-0.175608
18 N	-0.128883	-0.222543	-0.175608
19 O	-0.473350	-0.479923	-0.373650
20 O	-0.473350	-0.475604	-0.373650
21 H	0.426600	0.424083	0.431793
22 H	0.426600	0.518245	0.431793

Table B.44: DSDPBEP86/6-311+G(d,p), TS1=H22

Atom	diketo	ts1	dieno
1 C	-0.024536	-0.062467	-0.122368
2 C	-0.279635	-0.219450	-0.189718
3 C	0.043217	-0.193780	-0.342166
4 C	-0.228191	0.044592	0.162446
5 C	0.310235	0.139625	0.261664
6 H	0.161723	0.153753	0.142271
7 H	0.159106	0.155148	0.151961
8 H	0.164253	0.162314	0.163272
9 C	0.310313	0.192784	0.261664
10 C	-0.228222	0.245481	0.162447
11 C	0.043220	-0.186079	-0.342166
12 C	-0.024517	-0.063874	-0.122369
13 C	-0.279655	-0.229040	-0.189717
14 H	0.164253	0.166217	0.163272
15 H	0.161723	0.162817	0.142271
16 H	0.159105	0.160556	0.151961
17 N	-0.232817	-0.242468	-0.243646
18 N	-0.232819	-0.310063	-0.243646
19 O	-0.554601	-0.578467	-0.467827
20 O	-0.554602	-0.568200	-0.467827
21 H	0.481225	0.485764	0.484111
22 H	0.481222	0.584837	0.484111

THIS PAGE INTENTIONALLY LEFT BLANK

Appendix C

Supporting data for Chapter 3

C.1 Materials

AMCPs were prepared by precipitation from aqueous solution, according to a method taken from the literature (cite24). 10 mL of solution A (from A1 to A15, Table C.1) were mixed with 10 mL of solution B (150 mM Na2HPO4·12H2O + 50 mM NaH2PO4 · H2O), at 37 °C. Immediately after mixing, the pH was adjusted at 7.40 by means of 1 M NaOH. It was observed that the higher the concentration of the reactants used, the higher the turbidity of the reacting medium. After 15 min of reaction, the particles were collected by means of filtration, using a Millipore vacuum filtration system equipped with mixed cellulose esters filters (Millipore, pore size 0.45 μm). Immediately after filtration, the filters were placed in plastic test tubes and frozen in liquid nitrogen. The powders were then freeze-dried for 24 h, at -55 °C and $\sim$ 30 mTorr (VirTis BenchTop freeze-dryer, NY, USA) and stored in the freezer (-18 °C), tightly closed to prevent any influence from environmental humidity.

Calcium chloride (CaCl2, $\geq$ 93%), Magnesium chloride hexahydrate (MgCl2 6H2O, $\geq$ 99%), Sodium chloride (NaCl, $\geq$ 99%) and NaOH pellets ($\geq$ 99%) were purchased from Sigma-Aldrich (Milan, Italy). Sodium phosphate monobasic (NaH2PO4 H2O, $\geq$ 99%), and sodium phosphate dibasic (Na2HPO4 12H2O, $\geq$ 99%) were obtained from Carlo Erba Reagents (Milan, Italy). Milli-Q grade water (Millipore, resistivity 18.2 $M\Omega\ddot{c}m$ at 25 °C) was used during all the experiments.

Table C.1: Composition of the solutions used for the syntheses. The concentration of NaCl is 135 mM

Ca/Mg	$CaCl_2$ [nM]	$MgCl_2$ [mM]	Ca/P	Mg/P	Sample
0.4	4	10	0.02	0.05	A1
	20	50	0.1	0.25	A2
	40	100	0.2	0.5	A3
0.7	7	10	0.035	0.05	A4
	35	50	0.175	0.25	A5
	70	100	0.35	0.5	A6
1	10	10	0.05	0.05	A7
	50	50	0.25	0.25	A8
	100	100	0.5	0.5	A9
2	20	10	0.1	0.05	A10
	100	50	0.5	0.25	A11
	200	100	1	0.5	A12
3	30	10	0.15	0.05	A13
	150	50	0.75	0.25	A14
	300	100	1.5	0.5	A15

C.2 Methods

C.2.1 X-ray diffraction (XRD)

XRD patterns were collected using a D8 Advance with DAVINCI design (Bruker, Milan, Italy), using as X-ray source the Cu K α radiation (wavelength $\lambda = 1.54$ Å), at 40 kV and 40 mA, a 2 Σ range of °10-°50, a step size of °0.03, and a time/step of 0.3 s. Samples were grinded with agate mortar and pestle and flattened onto a Si zero-background sample holder. Peaks were assigned using the Powder Diffraction Files (PDF) of the ICDD database (International Centre for Diffraction Data).

$$k = 1 \tag{C.1}$$

Scherrer equation (C.1) was used to calculate the crystalline domain size (D, nm): where **k** is the Scherrer constant, typically considered 0.9, λ is the X-Ray wavelength (nm), β is the FWHM (Full Width at Half Maximum) in radians and σ is the diffraction angle in radians. The FWHM were obtained from the Multi-Peak Fitting routine of the software IgorPro, considering a logcubic function as baseline.

C.2.2 Attenuated total reflectance – fourier transform infrared spectroscopy (ATR-FTIR)

ATR-FTIR spectra on the freeze-dried samples were acquired by means of a Nexus Thermo-Nicolet 870 FTIR spectrophotometer (Madison, WI, USA) equipped with a MCT detector and a Golden Gate. The spectra were collected in the 4000-650 cm^{-1} range, with 128 scans and resolution 2 cm^{-1}.

C.2.3 Field emission-scanning electron microscopy (FE-SEM)

FE-SEM micrographs were collected by means of a Zeiss ZIGMA FE-SEM (Carl Zeiss Microscopy GmbH, Jena, Germany). The powders were placed over aluminum stubs by means of conductive tape. The use of a Field Emission source, together with a low accelerating voltage (2 kV), a reduced sample-detector distance (∼2 mm) and the In-Lens detector allowed for the imaging of non-conductive samples at high magnification. The size distribution curves were obtained with the software ImageJ by measuring about 200 particles per sample.

C.2.4 Inductively coupled plasma-atomic emission spectrometry (ICP-OES)

The amount of phosphorous in the samples was determined in triplicate by means of an Agilent 720-ES Inductively Coupled Plasma Atomic Emission Spectrometer (ICP-OES) equipped with a pneumatic nebulizer and a cyclonic spray chamber. Before the analyses, about 1.0 mg of each sample was dissolved in 10 μL of HCl, brought to 10 mL with ultrapure water and added with 1.0 ppm of Ge, used as an internal standard to correct any matrix effect. The calibration lines were obtained by preparing the standard solutions starting from commercial standards certified at 1000 ppm. Ge line used for the correction was at 209.426 nm. After each measurement, the system was washed with a 2% HNO3 solution.

C.2.5 Ionic chromatography

The amount of calcium, magnesium and sodium was determined by means of ionic chromatography using a Thermo Dionex ICS-1000 ion chromatograph with a CG-12A guard column and a CS-12A analytical column. The same solutions prepared for ICP-OES measurements were analyzed. An electrochemical suppression of the background conductivity with a current of 160 mA was used, together with an injection loop of 25 μL with a conductivity detector. The element used for the separation was H2SO4 23 mM. The calibration lines of the individual ions were constructed for subsequent dilutions starting from standard certified solutions at 1000 ppm.

For both ICP-OES and ionic chromatography, to evaluate the reproducibility of the results, on selected samples the measurements were conducted on 3 specimens prepared by repeating the same synthesis three times. In all cases, the standard deviation of the three measurements lead to atomic ratios uncertainties < 0.1.

C.2.6 Simultaneous thermogravimetry/differential scanning calorimetry (SDT)

Thermal analysis was conducted with a SDT Q600 from TA Instruments (New Castle, DE, USA), which allows for the simultaneous monitoring of the weight loss signal (TGA curve) and the heat flow profile (DSC curve). Samples were placed in an alumina pan and measured in N2 atmosphere (flow rate 100 mL/min) from room temperature to 1000 °C, at 10 °C/min. The crystallization T is expressed as average ± standard deviation of 3 measurements conducted on 3 replicas of each synthesis.

THE JOURNAL OF PHYSICAL CHEMISTRY A
A JOURNAL OF THE AMERICAN CHEMICAL SOCIETY

pubs.acs.org/JPCA Article

"Cyclopropylidene Effect" in the 1,3-Dipolar Cycloaddition of Nitrones to Alkylidene Cyclopropanes: A Computational Rationalization

Lorenzo Briccolani-Bandini, Marco Pagliai,* Franca M. Cordero,* Alberto Brandi,* and Gianni Cardini*

Cite This: J. Phys. Chem. A 2021, 125, 3892−3899 Read Online

ACCESS | Metrics & More | Article Recommendations | Supporting Information

ABSTRACT: The regioselectivity in the 1,3-dipolar cycloaddition (1,3-DC) between five-membered cyclic nitrone and methylenecyclopropane (MCP) has been studied through density functional theory (DFT) calculations. The computational study of 1,3-DC with different 1-alkyl- (or 1,1-dialkyl)-substituted alkenes and the comparison with MCP have evidenced that the electrostatic interaction has a central role in the regioselectivity of the reactions. It has been observed that the electronic effect of the substituent (donor or attractor groups) determines the polarization of the alkene double bond and the reaction mechanism, consequently determining the interaction with nitrones and favoring an orientation between this moiety and the dipolarophile.

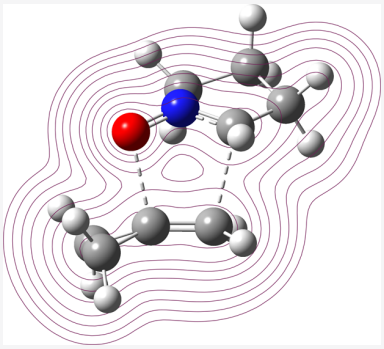

INTRODUCTION

The value of thermal rearrangement of 5-spirocyclopropane isoxazolidines **3** (Brandi-Guarna rearrangement, see Scheme 1)[1,2] for the synthesis of monocyclic and polycyclic heterocycles containing a tetrahydropyridinone ring **4** has been largely proved in recent years.[3,4] The rearrangement is made possible by the presence in the molecule of a strained oxyspirocyclopropane moiety, where the oxygen is linked to a nitrogen with a bond that is easily cleaved under thermal activation.[5,6] Another important synthetic application of 5-spirocyclopropane isoxazolidines **3** is the synthesis of β-lactams **5** by thermal fragmentation under acidic conditions.[7−9] Isoxazolidines **3** find their origin in a 1,3-dipolar cycloaddition (1,3-DC) of nitrones **1** with methylenecyclopropane (MCP, **2**).[10−12]

Scheme 1. Synthesis and Transformations of 5-Spirocyclopropane Isoxazolidines 3

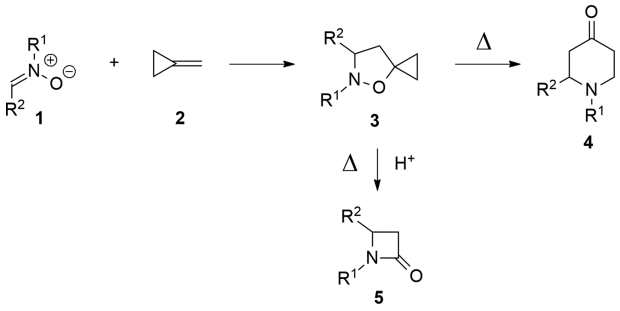

MCP is a rather volatile alkene, commercially available, that, despite its strained nature, results rather sluggish in its reactivity with nitrones. The cycloaddition process requires heating above 60 °C. The same occurs in the cycloaddition of nitrones with 1-alkyl- or 1,1-dialkyl-substituted alkenes that is even more slow.[13] This fact is not surprising knowing the nature of nitrones as electron neutral dipoles (Sustmann's classification)[14] and of dipolarophiles missing any activating electron-withdrawing group. However, the similarities of MCP with these alkenes end at this point, because regarding regioselectivity, the behavior of MCP is rather different from a normal 1-alkyl- or 1,1-dialkyl-substituted alkene. Indeed, although a dipolarophile like isobutene (**7**), which is the alkene with the highest similarity to MCP, reacts with nitrone **6** to give exclusively one adduct, i.e., the 5,5-disubstituted isoxazolidine **8** (Scheme 2),[15] MCP generally affords a mixture of regioisomers, where the 5-spirocyclopropane isoxazolidine is the major, but not the exclusive cycloadduct, as shown in the examples of Scheme 3.[16,17]

Received: March 11, 2021
Revised: April 20, 2021
Published: April 30, 2021

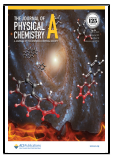

https://doi.org/10.1021/acs.jpca.1c02204
J. Phys. Chem. A 2021, 125, 3892−3899

The Journal of Physical Chemistry A pubs.acs.org/JPCA Article

Scheme 2. 1,3-DC of Nitrone 6 with Isobutene (7)

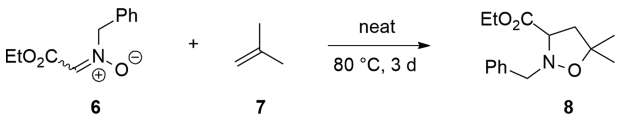

The awkwardness of this result with regard to the application of this process as a function of the successive thermal rearrangement or β-lactam synthesis is rather evident. In fact, regioisomeric 4-spirocyclopropane isoxazolidines, like **10** and **13** (Scheme 3), lacking the oxyspirocyclopropane moiety, are not able to undergo any useful rearrangement. However, the unexpected lack of regioselectivity in 1,3-DC of MCP raises several questions about the nature of its double bond and its resemblance with a simple alkene. More concerns are added if we consider the cycloaddition to another similar alkene, methylenecyclobutane (MCB, **14**) (Scheme 4), where a cyclobutane replaces the cyclopropane ring.[18]

If we assume that the strain energy of the ring has a role in the regioselectivity of the cycloaddition, a similar result for MCP and MCB should be expected. Indeed, the cycloaddition of **11** with MCB affords exclusively regioisomer **15**, analogously to the regioselectivity obtained with isobutene (7). These data make clear that there must be a "cyclopropylidene effect" in the 1,3-DC with nitrones to justify the observed lack of high regioselectivity. The 1,3-DC reaction mechanism has been computationally investigated with density functional theory (DFT) and post-HF methods: it consists of a concerted, often asynchronous, pericyclic cycloaddition mechanism.[19] To elucidate this possible cyclopropylidene effect on the regioselectivity of the 1,3-DC of MCP with nitrones, DFT calculations have been carried out on the systems summarized in Scheme 5. The choice of a five-membered cyclic nitrone like **16** for the study is justified by the copious literature available for the cycloadditions of cyclopropylidene dipolarophiles with this class of nitrones.[17,20] In addition, nitrone **16** featuring a defined configuration eliminates the *E,Z*-configuration variable that should be considered in the case of acyclic nitrones. Seven substituted dipolarophiles have been analyzed to investigate the electronic effect of the substituents: isobutene (7), methylenecyclopropane (MCP, **2**), methylenecyclobutane (MCB, **14**), isopropylidenecyclopropane (ICP, **17**), isopropylidenecyclobutane (ICB, **18**), and cyclobutylidenecyclopropane (CPCB, **19**) (Scheme 5).

COMPUTATIONAL DETAILS

The reaction mechanisms have been characterized by performing DFT calculations at the PBE0/6-311++G(d,p)[21−24] level of theory including Grimme's empirical dispersion (GD3) with

Scheme 4. 1,3-DC of Nitrone 11 with MCB (14)

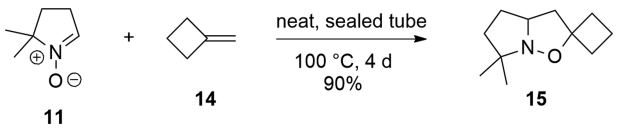

Scheme 5. Reactions Studied Through DFT Calculations at the PBE0/6-311G(d,p)-GD3 Level of Theory

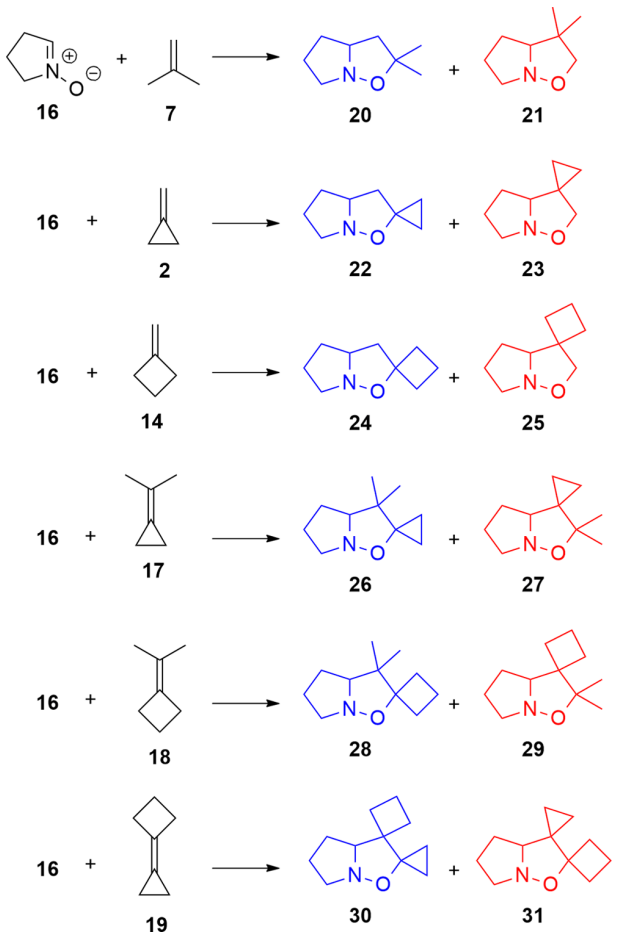

the Gaussian suite of programs.[25,26] Transition states (TS), prereactive minima, and products have been located through geometry optimization calculations with very tight convergence criteria. The QST2[27] or QST3[28] algorithms have been adopted to determine the transition states. All of the Hessian eigenvalues are positive for the prereactive minima and

Scheme 3. 1,3-DC of Nitrones 6 and 11 with MCP (2)

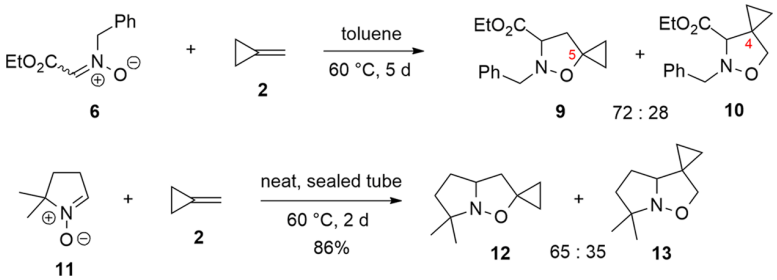

https://doi.org/10.1021/acs.jpca.1c02204
J. Phys. Chem. A 2021, 125, 3892−3899

The Journal of Physical Chemistry A pubs.acs.org/JPCA Article

products, while only one negative eigenvalue has been obtained for the TS. The eigenvector, corresponding to the negative eigenvalue, describes the displacements along the formed C−C and C−O bonds, providing insights into the concerted reaction mechanism. Different analyses have been carried out to describe the behavior of alkenes with nitrone **16** and to understand the cyclopropylidene effect. The characterization of the stationary points allows us to determine the energy gaps between the TS and reagents or products, to assess any possible kinetic control of the reaction and the balance between the products. The electronic effects of the alkyl substituent on the alkenes have been investigated by the value and the orientation of the dipole moment on the reagents and through the determination of the electrostatic potential (ESP) atomic charges.[29] To further support the electronic structure analysis, comparisons between the ESP atomic charges and those obtained through the CMS[30] and NPA[31,32] methods have been reported in Tables S1−S7 in the Supporting Information. The kinetic constants of the reactions have been calculated using the Eyring transition state theory.[33−35] The results allowed a comparison of the kinetic parameters for the two different orientations of the alkenes for each reaction in Scheme 5 and to explain the different experimental yields. For the studied systems, the expression of the kinetic constant $k(T)$ in the Eyring approximation is simplified, treating the reagents in the prereactive minimum as a single molecular complex, and results

$$k(t) = \frac{k_B T}{h} \frac{Q_{TS}^{\neq}}{Q_{GS}} e^{-\Delta E/k_B T} \quad (1)$$

where k_B is the Boltzmann constant, T is the temperature, h is the Planck's constant, and ΔE is the energy gap (zero-point energy included). The two functions are the product of vibrational and rotational partition functions for the transition state $Q_{TS}^{\neq}$ and ground state Q_{GS}. The kinetic constants have been calculated for the experimental reaction temperature range between 300 and 400 K.

RESULTS AND DISCUSSION

The 1,3-DC between nitrones and alkenes is a well-known transformation leading to isoxazolidines. The reaction mechanism is affected by the electrostatic interaction between the nitrone and the alkenes. Alkyl substituents are electron-donating groups (EDG) and increase the electron density of the double bond through an inductive donating effect. To gain a further insight, we have also considered an electron-attractor group (EWG) as a substituent: an ester group. This effect is to increase the negative charge on carbon C_α depleting the electron density over the double bond. Another possible effect is the polarization of the alkene double bond given by the high dipole moment on the nitrone.

The regioselectivity of the 1,3-DCs, i.e., the relative orientation of the substituted alkene to the nitrone in the TS, is influenced by the effect of the substituents on the dipolarophile. For this reason, we have considered two alkene orientations to explain the different selectivities for the studied reactions: the orientation labeled **a** leads to the product with the cyclopropane (or the cycloalkane) in position 5; label **b** refers to the orientation of the alkenes leading to the regioisomer spiro-fused in 4 (Scheme 6).

Cycloaddition with Isobutene (7). The 1,3-DC of a nitrone with isobutene (7) experimentally gives one single

Scheme 6. Transition States Originated from Different Paths a and b Leading to Regioisomeric Cycloadducts

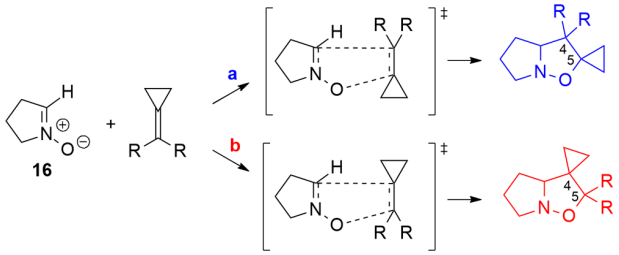

regioisomer, **9**, i.e., the 5,5-dimethyl-substituted isoxazolidine (see structure 8 in 2).

The reaction paths obtained by the computational analysis on regioisomers **20** and **21** (Scheme 7) suggest an explanation

Scheme 7. 1,3-DC between Isobutene 7 and Nitrone 16; Orientation a Leads to the 5,5-Dimethylisoxazolidine 20, and Orientation b Leads to the 4,4-Dimethylisoxazolidine 21; the Dipole Moment on 7 is Oriented toward the Dimethyl Group

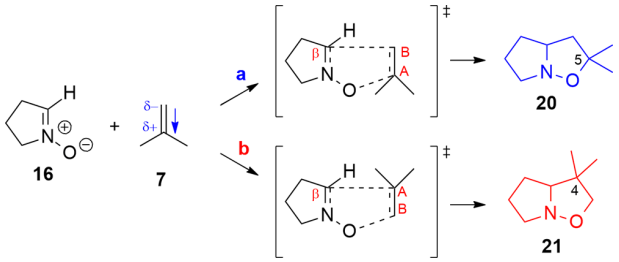

for such regioselectivity. The path **a** of the 1,3-DC with the isobutene 7 leads to the formation of isoxazolidine **20** substituted with two methyl groups on position 5. This arrangement of the reagents has a lower activation energy (ΔE_{TS}(**a** − **b**) = −18.0 kJ/mol), and the product **20** is more stable than isoxazolidine **21** (path **b**) (Table S8 in the Supporting Information).

The analysis of ESP charges has evidenced that the two methyl groups determine a positive charge on the C_A carbon (0.469) and a charge transfer toward the C_B (−0.737) of the isobutene (Scheme 7, Table S9 in the Supporting Information). This charge distribution on the isobutene corresponds to the dipole moment of 0.59 D, which lies on the C_A−C_B bond and is oriented toward the EDG groups. In the prereactive minimum, the nitrone dipole further increases the polarization of isobutene, as evidenced by the charges of the carbons C_A and C_B reported in Table S16 in the Supporting Information. The reaction mechanism is favored by the **a**-arrangement of the reactants because the carbon C_A involved in the attack of the nitrone oxygen is positive (0.506). The polarization effect given by the nitrone in the **b** orientation determines instead a negative charge on C_B (−0.748) that makes the attack of nitrone oxygen less favored (Scheme 7). Therefore, the charge distribution and orientation of the alkene's dipole moment justify the kinetic ratio calculated at the experimental temperature with Eyring's equation ($k_{a/b}$ = 114.4 at 350 K) and indicate the 5,5-disubstituted isoxazolidine **20** as the favorite product of the 1,3-DC.

https://doi.org/10.1021/acs.jpca.1c02204
J. Phys. Chem. A 2021, 125, 3892−3899

The Journal of Physical Chemistry A pubs.acs.org/JPCA Article

Cycloadditions with Methylenecyclopropane (MCP, 2) and Methylenecyclobutane (MCB, 14). The comparison of cycloaddition of nitrone 11 with methylenecyclopropane (**2**, MCP) and methylenecyclobutane (**14**, MCB) is rather interesting as the former leads experimentally to the formation of an approximately 65:35 mixture of regioisomers, where the majority is the 5-spiro-fused isoxazolidine **12**, whereas MCB affords exclusively the 5-spiro-fused isoxazolidine **15** (Schemes 3 and 4). At a first glance, this difference is surprising since it contrasts with the apparent similarity of the two dipolarophiles. The computational analysis, indeed, infers an explanation for this different reactivity. The difference in activation energy between the TS of the two chosen orientations (**a**, **b**) of the MCP is moderate (ΔE_{TS}(**a** − **b**) = −7.7 kJ/mol, Table S10 in the Supporting Information). Orientation **a** (Scheme 8) is

Scheme 8. 1,3-DC between MCP (2) and Nitrone 16; Orientation a Leads to Isoxazolidine 22, and Orientation b Leads to Isoxazolidine 23; the Dipole Moment on 2 is Oriented toward the Cyclopropane

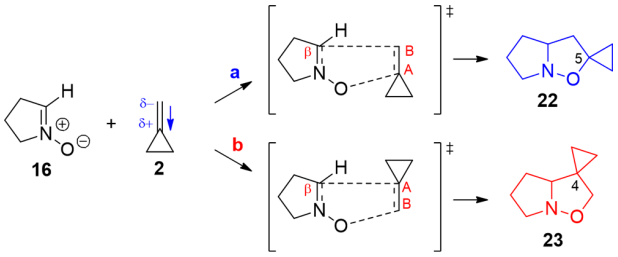

favored and leads to 5-spirocyclopropane isoxazolidine **22**, which is also more stable than the isomeric 4-spirocyclopropane **23** obtained with the **b**-oriented MCP (ΔE(**a** − **b**) = −10.4 kJ/mol).

The difference in activation energy for the two chosen orientations of MCB is higher than in the previous case (ΔE_{TS}(**a** − **b**) = −15.7 kJ/mol, Table S10 in the Supporting Information). Indeed, orientation **a** is favorable and leads to the more stable product with the spirocyclobutane in position 5 (**24**) (ΔE(**a** − **b**) = −23.6 kJ/mol) (Scheme 9). The

Scheme 9. 1,3-DC between MCB 14 and Nitrone 16; Orientation a Leads to Isoxazolidine 24, and Orientation b Leads to Isoxazolidine 25; the Dipole Moment on the Alkene is Oriented toward the Cyclobutane

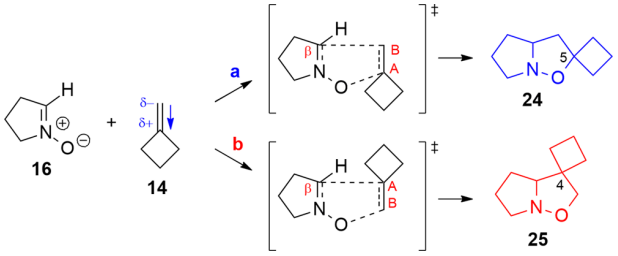

inductive effect on the cyclopropane determines a carbon with a positive charge (C_A) and one with a negative charge (C_B, Table S11 in the Supporting Information). As a proof of this charge distribution on the double bond, the dipole moment on the MCP (0.455 D) is oriented toward the cyclopropane.

In the prereactive minima, the polarization of the MCP is increased by the nitrone dipole according to the orientation (Table S11 in the Supporting Information). The two sp2 carbons (C_A, C_β), as acceptors of electron density, are involved in the bonding at the transition state (Scheme 8). Therefore, the positive charge on C_A (0.147) and the less negative charge on C_β (−0.101) in the **a** arrangement favor the reaction outcome (Table S11 in the Supporting Information).

The inductive effect of the cyclobutane on the double bond of the MCB (Table S11 in the Supporting Information) is greater if compared to the cyclopropane one. Indeed, the dipole moment of the double bond in MCB (0.612 D) lies on the double bond axis and is oriented toward the cyclobutane substituent. The dipole moment of the nitrone increases the polarization of the dipolarophile. The arrangement of the reagents in orientation **a** determines a positive charge on alkene carbon C_A (0.237) and a less negative charge on the nitrone carbon C_β (−0.143), favoring the cycloaddition mechanism (Table S11 in the Supporting Information; see also Scheme 9). Therefore, the computational results for the 1,3-DC of MCP explain the experimental regioselectivity, i.e., the obtainment of two regioisomers with a prevalence of the product deriving from orientation **a**. Indeed, the two orientations do not differ greatly in terms of activation energy, neither on product stability. The ratio between rate constants obtained for the two orientations ($k_{a/b}$ = 5) (Table S12 in the Supporting Information) suggests a reduction of the kinetic control of the regioselectivity in this cycloaddition. However, orientation **a** provides a relatively minor activation energy (ΔE_{TS}(**a** − **b**) = −7.7 kJ/mol) and the most stable isoxazolidine (ΔE(**a** − **b**) = −10.4 kJ/mol). Also, the charge distribution on the alkene **2** in the **a** arrangement suggests that the isoxazolidine **22** with the spirocyclopropane substituent in position 5 is the favored product (Table S11 in the Supporting Information). In the reaction with MCB instead, the ratio between rate constants obtained for the two orientations ($k_{a/b}$= 117) and the different stabilities of the two isoxazolidines indicate a kinetic control of the reaction. The analysis of the charge distribution on the double bond of the MCB confirms that the 5-spirocyclobutane isoxazolidine **24**, obtained with **a** arrangement, is the highly favored product (Table S12 in the Supporting Information). The different reactivities of MCP and MCB can be therefore explained by the kinetic and electrostatic behaviors in the two reactions. In the 1,3-DC with MCP, the lack of regioselectivity is due to a lower EDG effect of the substituent that leads to the formation of both **22** and **23** products according to the experimental ratio (**a** > **b**).[16,17] Instead, the electronic effect of the cyclobutane determines a charge distribution over the alkene that is conducive to the formation of the isoxazolidine **24** substituted with the spirocyclobutane on position 5.

Cycloadditions with Isopropylidenecyclopropane (ICP, 17) and Isopropylidenecyclobutane (ICB, 18). The 1,3-DC between ICP and nitrones experimentally gives one single regioisomer featuring the methyl groups on C-5 of the isoxazolidine ring.

This complete regioselectivity can be explained by the different reactivity of the ICP (**17**) in the two studied orientations. Indeed, the computed cycloaddition between the ICP and nitrone **16** shows two reaction paths that are rather different, according to the orientation chosen: the proposed orientation **a** (Scheme 10) leads to the isoxazolidine **26** spiro-fused at C-5, and orientation **b** leads to the isomer **27**.

https://doi.org/10.1021/acs.jpca.1c02204
J. Phys. Chem. A 2021, 125, 3892−3899

The Journal of Physical Chemistry A pubs.acs.org/JPCA Article

Scheme 10. 1,3-DC between ICP and Nitrone 16; Orientation a Leads to Isomer 26, and Orientation b Leads to Isomer 27; the Dipole Moment on the Alkene is Oriented toward the Dimethyl Group

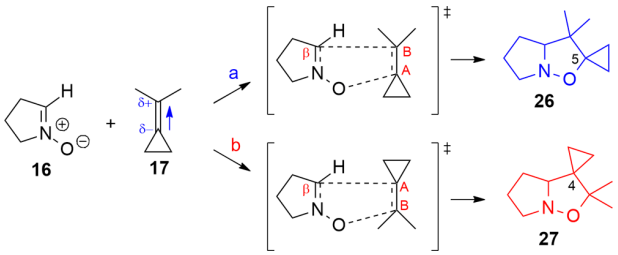

The arrangement of ICP proposed in orientation **a** has the highest activation energy of the studied reactions (99 vs 40−50 kJ/mol). The arrangement of the **b**-oriented ICP determines a sensibly lower activation energy (ΔE_{TS}(**a** − **b**) = 61.5 kJ/mol) and leads to the more stable isoxazolidine **27**, 12.540 kJ/mol (Table S13 in the Supporting Information). This difference in activation energy and the kinetic ratio ($k_{a/b}$ = 4.6 × 10^{-11}) indicates a kinetic control of the reaction leading to the formation of one product, i.e., isomer 27 (Table S15 in the Supporting Information). All substituents of ICP are EDG groups, the dipole moment of the molecule is quite small (0.167 D) compared to the values of the other alkenes. The dipole lies on the double-bond axis and is oriented toward the dimethyl group, which means that the dimethyl provides the bigger EDG contribution to the alkene favoring the formation of **27**. Indeed, in orientation **b**, the ICP carbon involved in the intermolecular O−C bond formation, has a small positive charge (0.009), whereas, in the other orientation **a**, the carbon belonging to the cyclopropane ring (C_A) experiences a negative charge (−0.020) (Table S14 in the Supporting Information).

From these data, it can be concluded that the cycloaddition between nitrone **16** and ICP **17** proceeds through the **b**-oriented TS, which is favored from a kinetic point of view and leads to the formation of the more stable product **27**. The ratio of kinetic constants between the orientations **a** and **b** ($k_{a/b}$ = 10^{-10}) (Table S15 in the Supporting Information) is much lower than 1, confirming that orientation **b** is kinetically much more favored. These results therefore explain the formation of isoxazolidine **27** as the exclusive product. Experimental data for the reaction of nitrones with the ICB (**18**) are not available, but this dipolarophile has been studied to evaluate the electronic effect of the two different cycloalkanes in the presence of the dimethyl group.

The reaction shows lower differences according to the chosen orientation of the alkene. The difference in activation energy for the two orientations of ICB with nitrone 16 is much lower (ΔE_{TS}(**a** − **b**) = 3.8 kJ/mol) than the previous case: orientation **a** (Scheme 11) leads to the 5-spirocyclobutane-4,4-dimethylisoxazolidine 28, while orientation **b** leads to the more stable 5,5-dimethyl-4-spirocyclobutane isoxazolidine **29** (ΔE(**a** − **b**) = 15.8 kJ/mol) (Table S13 in the Supporting Information). As seen in the previous case, all substituents of the alkene are EDG groups: the value of the dipole moment (0.011 D) is close to the accuracy of the method, so no consideration can be made about the dipole orientation. However, the polarization induced by nitrone dipole and the EDG effect of the substituents promotes a positive charge on

Scheme 11. 1,3-DC between ICB and Nitrone 16; Orientation a Leads to Isoxazolidine 28, and Orientation b Leads to Isomer 29; the Dipole Moment of 18 is Close to Zero

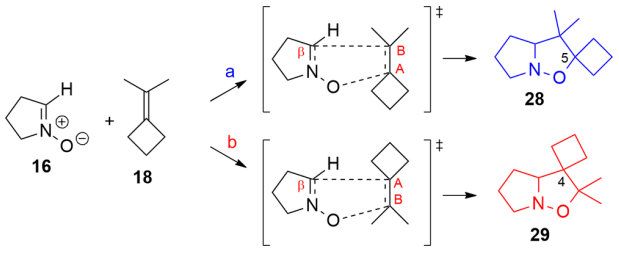

carbon C_B promoting the formation of isomer **29** (Table S14 in the Supporting Information). Indeed, the kinetic ratio of the reaction ($k_{a/b}$ = 6 × 10^{-2}) suggests that path **b** is slightly kinetically favored due to a better charge distribution over the reagents. Altogether, these data indicate that isoxazolidine **29** is only slightly favored (Table S15 in the Supporting Information). The compared assessment of reactions of ICP and ICB with nitrone **16** and their full computational analysis has brought about a sharp difference of behavior of a cyclopropylidene compared to a cyclobutylidene group. Indeed, for the ICB, the electronic effects of the dimethyl and cyclobutane are similar, as shown by the dipole moment value. Instead, the charges on the sp2 carbons (C_A, C_B) on the alkene **17** are determined by the stronger EDG effect of the two methyl groups compared to the cyclopropane; therefore, path **b** results in a more favorable charge distribution leading to isoxazolidine **27** ($k_{a/b}$ = 6 × 10^{-10}). Indeed, the cycloaddition of nitrone **11** with **32**, a dipolarophile analogous to ICB, experimentally gives only regioisomer **33**, originating from **b** orientation like **27**, in excellent yield (Scheme 12).[36]

Scheme 12. 1,3-DC of Nitrone 11 with 32

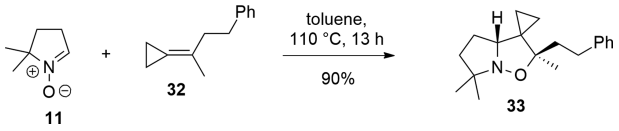

Cycloaddition with Cyclobutylidenecyclopropane (CBCP, 19). The computational study of the reaction of nitrone **16** with CBCP gives a further confirmation of the existence of this cyclopropylidene effect experimentally observed.

Experimentally, 1,3-DC of nitrone **34** with CBCP gave exclusively isoxazolidine **35** featuring the cyclopropane ring on position 4 of the isoxazolidine ring (**13**).[37]

The difference in activation energy (ΔE_{TS}(**a** − **b**) = −6.9 kJ/mol) is in favor of the **b**-oriented alkene, which leads to the isoxazolidine substituted with the cyclobutane on position 5 (isomer **31**) that is also thermodynamically more stable (−9.0 kJ/mol) than the other possible product (isomer **30**) deriving from orientation **a** (Table S16 in the Supporting Information).

The alkene dipole moment is quite small (0.168 D), since all substituents are EDG groups, and is oriented toward the cyclobutane, due to its greater inductive effect on the molecule. In the **a** arrangement, the carbon C_A is involved in the formation of C−O bond, while in orientation **b**, the carbon involved is C_B. As in the previous cases, the nitrone dipole

https://doi.org/10.1021/acs.jpca.1c02204
J. Phys. Chem. A 2021, 125, 3892−3899

The Journal of Physical Chemistry A pubs.acs.org/JPCA Article

polarizes the alkene double bond, increasing the partial charges on the sp2 carbon atoms. The reaction mechanism is therefore favored in orientation **b** by the positive charge on carbon C_B (0.125, Table S17 in the Supporting Information). These results and the kinetic ratio of the reaction ($k_{a/b}$ = 0.1) indicate that isoxazolidine **31** is the favored product in complete agreement with the experimental data (Scheme 13 and Scheme 14).

Scheme 13. 1,3-DC of Nitrone 34 with CBCP (19)

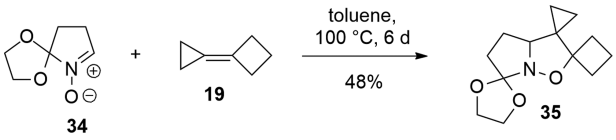

Scheme 14. 1,3-DC of 19 with Nitrone 16; Orientation a Leads to Isoxazolidine 30, and Orientation b Leads to Isomer 31; the Dipole Moment on the Alkene is Oriented toward the Cyclobutane

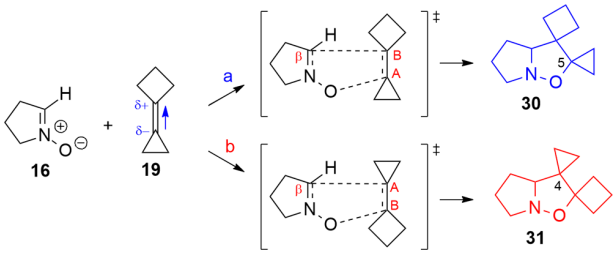

Cycloaddition with Cyclopropylideneacetate 36. We have also investigated the effect of an electron-attractor group (EWG), i.e., an ester group, combined with the cyclopropane.

1,3-DC of nitrones with **36** gives experimentally only isoxazolidines substituted with the spirocyclopropane on position 5, as shown in the example of Scheme 15. The outcome of the cycloaddition is therefore inverted with respect to the results shown previously. This depends on the electron-withdrawing character of the CO_2Me substituent.

Scheme 15. 1,3-DC of Cyclopropylideneacetate 36 with Nitrone 11

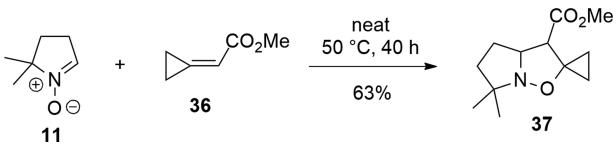

The alkene is substituted on C_A with the cyclopropane, and on C_B with the carboxymethyl group; therefore, the carbon C_A is the β carbon compared to the carbonyl acetate (**16**). Both the ester and alkyl groups contribute to polarize the double bond, increasing the negative charge on C_B (−0.807) and consequently the positive charge on C_A (0.447, Table S19 in the Supporting Information). Indeed, the resulting dipole moment (3.064 D) is oriented toward the cyclopropane group and this value is higher compared to the previous cases due to the methyl carboxylate effect. In orientation **a**, the positive charge on carbon C_A enhances the attack on the nitrone oxygen (Scheme 16). Indeed, this arrangement of the reagents determines the lowest activation energy ($\Delta E(\mathbf{a} - \mathbf{b})$ = −14.1 kJ/mol, Table S18 in the Supporting Information) and leads to the formation of 5-spirocyclopropane isoxazolidine **38**. The polarization of the double bond and the resultant negative charge on carbon C_B make **b** orientation less favored. Also, the nitrone dipole moment increases the polarization of the alkene double bond, favoring the charge distribution adopted in orientation **a**. Indeed, the kinetic constant rates ($k_{a/b}$ = 123) obtained with the Eyring equation show that the isoxazolidine **38** is the kinetic product of the 1,3-DC, in agreement with the experimental data.

Scheme 16. 1,3-DC between Cyclopropylideneacetate 36 and Nitrone 16; Orientation a Leads to Isoxazolidine 38, and Orientation b Leads to Isoxazolidine 39; the Dipole Moment on the Alkene is Oriented toward the Cyclopropane

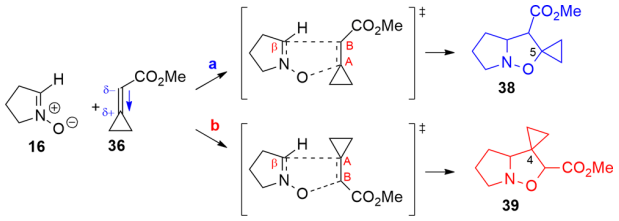

CONCLUSIONS

The lack of regioselectivity in 1,3-DC of methylenecyclopropane (MCP, **2**), compared to the high regioselectivity of other 1,1-disubstituted alkenes, has been computationally investigated through DFT calculations, to rationalize the experimental finding. The computational analysis has been extended to tetrasubstituted alkenes and to cyclopropylideneacetate to substantiate the results. It has been observed that the electrostatic interactions play a fundamental role in the regioselectivity of these 1,3-DC reactions. In fact, the electronic structure of the substituents (EDG and EWG) causes polarization of the alkene double bond, which in turn favors a proper structural arrangement between the reactants and consequently controls the regioselectivity. The comparison of the reactions between nitrone **16** and 1,1-disubstituted alkenes isobutene (**7**) and MCB (**14**) shows that for similar substituents (dimethyl, cyclobutyl), the reaction outcome is essentially due to the electrostatic interaction (atomic charges and dipole moment), with a preferential formation of the 5,5-disubstituted isoxazolidine. In the case of MCP, where the electrostatic interaction is less marked, the difference in 5- and 4-spiro-fused isoxazolidine formation is lower, and consequently the kinetic constants of the two paths are similar (the kinetic constant ratio is only $k_{a/b}$ = 5). The electronic structure analysis of 1,3-DC with the tetrasubstituted alkenes ICP (**17**), ICB (**18**), and CPCB (**19**) reveals a smaller value of the dipole moment because all of the substituents are alkyl groups, and the partial charges on the double bond are given by the subtraction of the substituent EDG effects. The alkenes ICP and CPCB feature both a cyclopropyl group on one end of the double bond, and on the other end, a geminal dimethyl group and a cyclobutyl ring, respectively. The comparison of these two dipolarophiles allows us to understand how the cycloaddition reaction is influenced by the alkene substituents with the largest EDG effect. In ICP, the EDG effect of the geminal dimethyl is stronger than the one of cyclopropyl: the $k_{a/b}$ ratio shows that the reaction is completely shifted toward the

https://doi.org/10.1021/acs.jpca.1c02204
J. Phys. Chem. A 2021, 125, 3892−3899

The Journal of Physical Chemistry A pubs.acs.org/JPCA Article

formation of isomer **27** with methyl groups on C-5 ($k_{a/b} = 6 \times 10^{-10}$). A similar behavior, although with a lower weight, occurs in CPCB. In the case of 1,3-DC with ICB, the electrostatic contributions of the substituents are similar; thus, the polarization of the double bond is small but still enough to favor the formation of the isoxazolidine with methyl groups on C-5 ($k_{a/b} = 6 \times 10^{-2}$). The cyclopropylideneacetate **36** is the only example studied featuring a cyclopropyl ring and an EWG. In this case, the two electronic effects sum, as shown by the value and orientation of the alkene dipole moment. The contribution of the EWG is dominant and leads exclusively to the formation of product **39** ($k_{a/b} = 123$). Summing up, the electronic effect of the alkene substituents measured in this study determines a polarization of the alkene double bond favoring the relative orientation between the reactants leading to the observed regioselectivity of the cycloadditions. This study has allowed us to explain the role of a cyclopropylidene group (the cyclopropylidene effect) in inducing regioselectivity in nitrone 1,3-dipolar cycloadditions.

■ ASSOCIATED CONTENT

Supporting Information

The Supporting Information is available free of charge at https://pubs.acs.org/doi/10.1021/acs.jpca.1c02204.

Comparison between ESP, CM5, and NPA population analysis (Tables S1−S7); energy variations and ESP charges for the reaction involving isobutene, respectively (Tables S8 and S9); energy variations, ESP charges, and transmission coefficients for the reaction involving methylenecyclopropane and methylenecyclobutane, respectively (Tables S10−S12); energy variations, ESP charges, and transmission coefficients for the reaction involving isopropylidenecyclopropane and isopropylidenecyclobutane, respectively (Tables S13−S15); energy variations and ESP charges for the reaction involving cyclobutylidenecyclopropane, respectively (Tables S16 and S17); and energy variations and ESP charges for the reaction involving cyclopropylideneacetate, respectively (Tables S18 and S19) (PDF)

■ AUTHOR INFORMATION

Corresponding Authors

Marco Pagliai − *Dipartimento di Chimica "Ugo Schiff", Università degli Studi di Firenze, 50019 Sesto Fiorentino, Firenze, Italy;* orcid.org/0000-0003-0240-161X; Email: marco.pagliai@unifi.it

Franca M. Cordero − *Dipartimento di Chimica "Ugo Schiff", Università degli Studi di Firenze, 50019 Sesto Fiorentino, Firenze, Italy;* orcid.org/0000-0001-6005-5941; Email: franca.cordero@unifi.it

Alberto Brandi − *Dipartimento di Chimica "Ugo Schiff", Università degli Studi di Firenze, 50019 Sesto Fiorentino, Firenze, Italy;* orcid.org/0000-0001-8273-6369; Email: alberto.brandi@unifi.it

Gianni Cardini − *Dipartimento di Chimica "Ugo Schiff", Università degli Studi di Firenze, 50019 Sesto Fiorentino, Firenze, Italy;* orcid.org/0000-0002-7292-3555; Email: gianni.cardini@unifi.it

Author

Lorenzo Briccolani-Bandini − *Dipartimento di Chimica "Ugo Schiff", Università degli Studi di Firenze, 50019 Sesto Fiorentino, Firenze, Italy;* orcid.org/0000-0002-9243-8522

Complete contact information is available at: https://pubs.acs.org/10.1021/acs.jpca.1c02204

Notes

The authors declare no competing financial interest.

■ ACKNOWLEDGMENTS

The authors thank MIUR-Italy ("Progetto Dipartimenti di Eccellenza 2018-2022" allocated to Department of Chemistry "Ugo Schiff").

■ REFERENCES

(1) Hassner, A.; Namboothiri, I. *Organic Syntheses Based on Name Reactions: a Practical Guide to 750 Transformations*; Elsevier, 2012.

(2) Wang, H. *Comprehensive Organic Name Reactions*; Wiley, 2010.

(3) Brandi, A.; Cordero, F. M.; de Sarlo, F.; Goti, A.; Guarna, A. New Synthesis of Azaheterocycles by Rearrangement of isoxazoline-5-spirocycloalkane Compounds. *Synlett* **1993**, *1993*, 1−8.

(4) Cordero, F. M.; de Sarlo, F.; Brandi, A. 5-Spirocyclopropane isoxazolidines as Versatile Intermediates in Organic Synthesis. *Monatsh. Chem.* **2004**, *135*, 649−669.

(5) Ochoa, E.; Mann, M.; Sperling, D.; Fabian, J. A Combined Density Functional and ab initio Quantum Chemical Study of the Brandi reaction. *Eur. J. Org. Chem.* **2001**, *2001*, 4223−4231.

(6) Briccolani-Bandini, L.; Brandi, A.; Cardini, G.; Chelli, R.; Cordero, F. M.; Gellini, C.; Pagliai, M. Computational Investigation of the Selective Cleavage of Diastereotopic Cyclopropane Bonds in 5-Spirocyclopropane Isoxazolidines Rearrangement. *J. Org. Chem.* **2019**, *84*, 6757−6764.

(7) Cordero, F. M.; Pisaneschi, F.; Goti, A.; Ollivier, J.; Salaün, J.; Brandi, A. New Synthesis of β-Lactams by Ethylene Extrusion from Spirocyclopropane Isoxazolidines. *J. Am. Chem. Soc.* **2000**, *122*, 8075−8076.

(8) Cordero, F. M.; Brandi, A. Synthesis of β-Lactams and β-Homoprolines by Fragmentative Rearrangement of 5-Spirocyclopropaneisoxazolidines Mediated by Acids. *Chem. Rec.* **2020**, *21*, 284−294.

(9) Diethelm, S.; Carreira, E. M. Total Synthesis of (±)-gelsemoxonine. *J. Am. Chem. Soc.* **2013**, *135*, 8500−8503.

(10) Brandi, A.; Cicchi, S.; Cordero, F. M.; Goti, A. Progress in the Synthesis and Transformations of Alkylidenecyclopropanes and Alkylidenecyclobutanes. *Chem. Rev.* **2014**, *114*, 7317−7420.

(11) Goti, A.; Cordero, F. M.; Brandi, A. Cycloadditions onto Methylene and Alkylidenecyclopropane Derivatives. In *Small Ring Compounds in Organic Synthesis V*; Springer, 1996; pp 1−97.

(12) Brandi, A.; Cicchi, S.; Cordero, F. M.; Goti, A. Heterocycles from Alkylidenecyclopropanes. *Chem. Rev.* **2003**, *103*, 1213−1270.

(13) Brandi, A.; Durust, Y.; Cordero, F. M.; de Sarlo, F. Rearrangement of isoxazoline-5-spiro derivatives. 8. Selective Formation of Tetrahydropyridones from C, C-disubstituted nitrones. *J. Org. Chem.* **1992**, *57*, 5666−5670.

(14) Sustmann, R. A Simple Model for Substituent Effects in Cycloaddition Reactions. I. 1, 3-dipolar cycloadditions. *Tetrahedron Lett.* **1971**, *12*, 2717−2720.

(15) Inouye, Y.; Watanabe, Y.; Takahashi, S.; Kakisawa, H. The Preparation of N-benzyl-. ALPHA.-ethoxycarbonylnitrone and its Reactions with some Olefins. *Bull. Chem. Soc. Jpn.* **1979**, *52*, 3763−3764.

(16) Cordero, F. M.; Salvati, M.; Pisaneschi, F.; Brandi, A. Novel Prospects of the Acidic Thermal Rearrangement of Spiro [cyclopropane-1,5′-isoxazolidines] to β-Lactams. *Eur. J. Org. Chem.* **2004**, *2004*, 2205−2213.

(17) Brandi, A.; Guarna, A.; Goti, A.; de Sarlo, F. Rearrangement of Nitrone Cycloadducts to Methylene Cyclopropane. Synthesis of Indolizidine and Quinolizidine Derivatives. *Tetrahedron Lett.* **1986**, *27*, 1727−1730.

(18) Goti, A.; Brandi, A.; de Sarlo, F.; Guarna, A. New Synthesis of Azepin-4-ones by flash vacuum Thermolysis of Dihydro and Tetrahydroisoxazole-5-spirocyclobutane Derivatives. *Tetrahedron Lett.* **1986**, *27*, 5271−5274.
(19) di Valentin, C.; Freccero, M.; Gandolfi, R.; Rastelli, A. Concerted vs stepwise Mechanism in 1, 3-Dipolar Cycloaddition of Nitrone to Ethene, Cyclobutadiene, and Benzocyclobutadiene. A Computational Study. *J. Org. Chem.* **2000**, *65*, 6112−6120.
(20) Brandi, A.; Cardona, F.; Cicchi, S.; Cordero, F. M.; Goti, A. [3+2] Dipolar Cycloadditions of Cyclic Nitrones with Alkenes. *Org. React.* **2004**, 1−321.
(21) Adamo, C.; Barone, V. Toward reliable Density Functional Methods without Adjustable parameters: The PBE0 model. *J. Chem. Phys.* **1999**, *110*, 6158−6170.
(22) Ernzerhof, M.; Scuseria, G. E. Assessment of the Perdew-Burke-Ernzerhof exchange-correlation Functional. *J. Chem. Phys.* **1999**, *110*, 5029−5036.
(23) McLean, A.; Chandler, G. Contracted Gaussian Basis Sets for Molecular Calculations. I. Second Row atoms, Z= 11-18. *J. Chem. Phys.* **1980**, *72*, 5639−5648.
(24) Krishnan, R.; Binkley, J. S.; Seeger, R.; Pople, J. A. Self-consistent Molecular Orbital Methods. XX. A basis Set for Correlated Wave Functions. *J. Chem. Phys.* **1980**, *72*, 650−654.
(25) Grimme, S. Semiempirical GGA-type Density Functional Constructed with a long-range Dispersion Correction. *J. Comput. Chem.* **2006**, *27*, 1787−1799.
(26) Frisch, M. J.; Trucks, G. W.; Schlegel, H. B.; Scuseria, G. E.; Robb, M. A.; Cheeseman, J. R.; Scalmani, G.; Barone, V.; Petersson, G. A.; Nakatsuji, H.et al. *Gaussian 16*, revision C.01; Gaussian Inc.: Wallingford, CT, 2016.
(27) Peng, C.; Bernhard Schlegel, H. Combining Synchronous Transit and quasi-newton methods to find Transition States. *Isr. J. Chem.* **1993**, *33*, 449−454.
(28) Peng, C.; Ayala, P. Y.; Schlegel, H. B.; Frisch, M. J. Using redundant Internal coordinates to Optimize Equilibrium Geometries and Transition States. *J. Comput. Chem.* **1996**, *17*, 49−56.
(29) Besler, B. H.; Merz, K. M., Jr.; Kollman, P. A. Atomic Charges Derived from Semiempirical Methods. *J. Comput. Chem.* **1990**, *11*, 431−439.
(30) Marenich, A. V.; Jerome, S. V.; Cramer, C. J.; Truhlar, D. G. Charge model 5: An Extension of Hirshfeld Population Analysis for the accurate Description of Molecular Interactions in gaseous and ondensed Phases. *J. Chem. Theory Comput.* **2012**, *8*, 527−541.
(31) Foster, J. P.; Weinhold, F. Natural Hybrid Orbitals. *J. Am. Chem. Soc.* **1980**, *102*, 7211−7218.
(32) Reed, A. E.; Weinstock, R. B.; Weinhold, F. Natural Population Analysis. *J. Chem. Phys.* **1985**, *83*, 735−746.
(33) Glasstone, S.; Laidler, K. J.; Eyring, H. *The Theory of Rate Processes; the Kinetics of Chemical Reactions, Viscosity, Diffusion and Electrochemical Phenomena*; McGraw-Hill Book Company, 1941.
(34) Anslyn, E. V.; Dougherty, D. A. *Modern Physical Organic Chemistry*; University Science Books, 2006.
(35) Hill, T. *An Introduction to Statistical Thermodynamics*, Dover Publications: 1987.
(36) Goti, A.; Brandi, A.; de Sarlo, F.; Guarna, A. Rearrangement of Isoxazoline-5-spiro derivatives. Part 7. Thermal Rearrangement of 4, 5-dihydro and tetrahydroisoxazole-5-spirocyclobutanes to azepin-4-one derivatives. *Tetrahedron* **1992**, *48*, 5283−5300.
(37) de Meijere, A.; von Seebach, M.; Kozhushkov, S. I.; Boese, R.; Blaser, D.; Cicchi, S.; Dimoulas, T.; Brandi, A. Cyclopropyl building blocks for Organic Synthesis, 72. Cyclobutylidenecyclopropane: new Synthesis and use in 1, 3-Dipolar Cycloadditions-a direct route to Spirocyclopropane-annulated Azepinone derivatives. *Eur. J. Org. Chem.* **2001**, 3789−3795.

https://doi.org/10.1021/acs.jpca.1c02204
J. Phys. Chem. A 2021, 125, 3892−3899

JOC The Journal of Organic Chemistry Article
Cite This: J. Org. Chem. 2019, 84, 6757−6764 pubs.acs.org/joc

Computational Investigation of the Selective Cleavage of Diastereotopic Cyclopropane Bonds in 5-Spirocyclopropane Isoxazolidines Rearrangement

Lorenzo Briccolani-Bandini, Alberto Brandi, Gianni Cardini,* Riccardo Chelli, Franca M. Cordero,* Cristina Gellini, and Marco Pagliai

Dipartimento di Chimica "Ugo Schiff", Università di Firenze, Via della Lastruccia 3, Sesto Fiorentino, 50019 Firenze, Italy

Supporting Information

ABSTRACT: The complete path of the Brandi−Guarna rearrangement of 5-spirocyclopropane isoxazolidines has been investigated by means of density functional theory calculations to rationalize the competing formation of tetrahydropyridones and enaminones by the determination of the minimum energy reaction paths. Our calculations confirm that the rearrangement is triggered by the homolysis of the isoxazolidine N−O bond followed by cleavage of one of the two C−CH_2 cyclopropane bonds as previously proposed by the Fabian group [*Eur. J. Org. Chem.* **2001**, *2001*, 4223]. In addition, the results of this work suggest that in the presence of a stereogenic center at isoxazolidine C-4′, the formation of a piperidinone or an enaminone as the final product depends on which of the two diastereotopic C−CH_2 bonds of cyclopropane is cleaved in the second step of the process. The result can be of great interest for the understanding of other processes involving the opening of a cyclopropane ring.

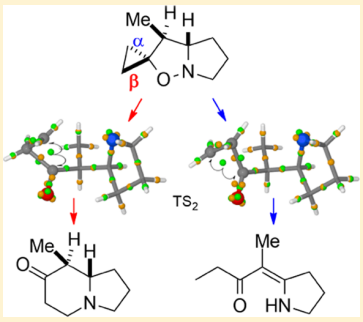

1. INTRODUCTION

The Brandi−Guarna rearrangement[1,2] of 5-spirocyclopropane isoxazolidines **1** has been widely applied in the synthesis of polycyclic heterocycles and natural products (Scheme 1).[3−12]

Scheme 1. Thermal Rearrangement of Spirocyclopropane Isoxazolidines 1 Leading to Tetrahydropyridones 2 and Enaminones 3

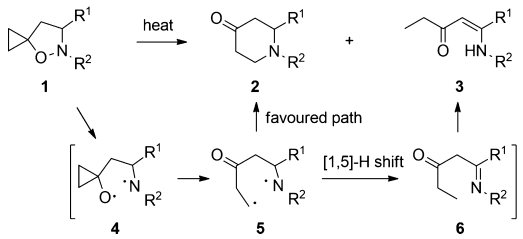

It consists of a thermal-induced ring opening of isoxazolidines **1**, leading to the formation of tetrahydropyridones **2** (Scheme 1). This type of skeleton, that is, a piperidine ring-containing framework, is widely diffused in alkaloids and bioactive molecules.[13−18]

Despite the Brandi−Guarna rearrangement being quite selective, in a few cases, the main product **2** is accompanied by a side product, that is, the open-chain isomer **3** (Scheme 1) featuring an enaminone moiety. The process is believed to occur through a homolytic cleavage of the N−O bond of isoxazolidines **1** followed by the cleavage of one of the cyclopropane vicinal bonds and intramolecular coupling of diradical intermediate **5** (Scheme 1). Furthermore, the formation of **3** is generally explained by a [1,5]-H shift from the CHR^1 carbon to the terminal C radical in intermediate **5** leading to imine **6** (Scheme 1) that in turn tautomerizes to enamine **3**.[19]

Recent experimental results have shown that the thermal rearrangement of two epimeric 5-spirocyclopropane isoxazolidine derivatives affords the piperidinone and enaminone products in different ratios.[9] How the diastereomeric environment influences the competitive formation of the cyclic and the open-chain product is not easy to be rationalized. In fact, the open-chain diradical intermediate **5** has lost most of the stereochemical constraint, and, as a consequence, the stereochemical memory is expected to be reduced at this level. To obtain useful information and provide a correct interpretation of the apparent remote influence of the stereochemical environment on favoring the different pathways, a computational study of both the competitive paths of the rearrangement mechanism has been carried out.

The rate determining step of the Brandi−Guarna reaction was thoroughly analyzed, a few years ago by Ochoa et al.,[20] using unrestricted density functional theory (UDFT) on a series of model spirofused isoxazolidines. They analyzed three alternative reaction paths for the cleavage of the N−O and C−C bonds, one concerted and two stepwise. The most energetically favorable was the stepwise mechanism consisting in the homolytic cleavage of two bonds: first, isoxazolidine N−

Received: February 20, 2019
Published: May 1, 2019

DOI: 10.1021/acs.joc.9b00499
J. Org. Chem. 2019, 84, 6757−6764

The Journal of Organic Chemistry Article

O followed by cyclopropane C−CH_2. Both intermediates and transition states are radicals; therefore, the computational approach which has to be applied in studying these systems is a critical aspect.[21−25] Performing a comparison with correlated wavefunction-based methods such as QCISD and CCSD(T) on the stationary points, Ochoa et al.[20] showed that UDFT is an adequate computational method to analyze the Brandi−Guarna rearrangement. This computational method has been applied with success in computational studies of organic systems containing radicals and in particular of ring-opening reactions.[26,27] Several authors[28−33] have shown that UDFT allows to qualitatively describe chemical reaction mechanisms involving intermediate radical systems, in agreement with both experimental data and calculations at a higher level of theory. This allows us to confidently use the same approach of Ochoa et al.[20] in the present study, aimed at the identification of the different reaction paths leading to tetrahydropyridone and enaminone.

2. RESULTS AND DISCUSSION

In the course of the studies by some of us on the synthesis of bioactive 1,2-dihydroxiindolizidines, the thermal rearrangement of diastereomeric 5-spirocyclopropane isoxazolidines **7a** and **7b** was carried out as an entry to the corresponding indolizidinones **8a** and **8b** (Scheme 2).[9] The thermal

Scheme 2. Rearrangement of Isoxazolidines 7a and 7b to Indolizidinones 8a and 8b and Enaminone 9

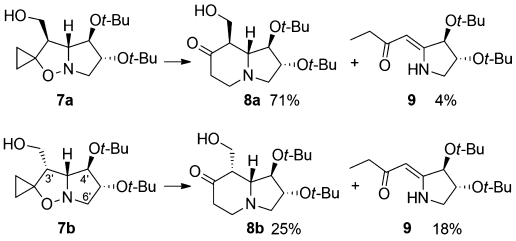

Reaction conditions: toluene, 170 °C (MW), 30-45 min

rearrangement of the two optically pure epimeric isoxazolidines **7a** and **7b** was carried out under the same reaction conditions (toluene, 170 °C, sealed vial, in a microwave apparatus; therefore, the reaction occurs at constant volume) and led to the expected indolizidinones **8a** and **8b**, in 71 and 25% yields, respectively, along with minor amounts of enaminone **9** (Scheme 2) in 4 and 18% yields, respectively.[34] A similar trend is observed for analogous isoxazolidines featuring a 3′-ethoxycarbonyl in place of the 3′-hydroxymethyl group. However, in these cases, the thermal isomerization of several stereocentres does not allow a clear-cut analysis. It is worth noting that enaminones are compounds much more fragile than the corresponding indolizidinones, and hence their yields could be affected by major loss either during the thermal process or during the chromatographic purification. The results show that the substituent at C-3′ on the concave face in **7b** hampers the formation of indolizidinone **8b** compared with **7a**, which features the 3′-hydroxymethyl group on the convex face of the molecule and is converted into indolizidinone **8a** in better yield (71 vs 25%). The other way around happens for the formation of enaminone **9**. In fact, the enaminone is more abundant when formation of the indolizidinone is disadvantaged. Interestingly, when a substituent is lacking on the isoxazolidine C-3′ carbon as in **10**, the formation of an almost 1:1 mixture of the two isomeric rearrangement products, indolizidinone **11** and enaminone **12**, is observed (Scheme 3).[35]

Scheme 3. Thermal Rearrangement of Isoxazolidine 10 to Indolizidinone 11 and Enaminone 12

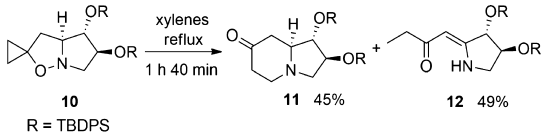

On the other hand, when C-3′ is a quaternary carbon, such as in **13** (Scheme 4), the exclusive formation of indolizidinone

Scheme 4. Thermal Rearrangement of Isoxazolidine 13 to Indolizidinone 16

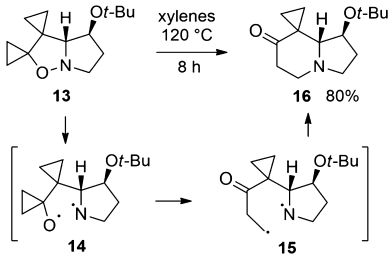

16 is observed.[36] It cannot be excluded that this result is due to the buttressing effect of the two C-3′ substituents that coerces the intramolecular radical coupling in intermediate **15** (Scheme 4).

The different behaviors of the two diastereomers **7a** and **7b** suggest a computational study to be performed to verify the origin of this different reactivity to answer the following question: is the stereochemical arrangement of the substituent on the isoxazolidine ring of **7a** and **7b** able to drive the rearrangement outcome? The thermal rearrangement of 5-spirocyclopropane isoxazolidines has been then computationally investigated through the study of model compounds to elucidate the different paths leading to cyclized products and enaminones. Starting from the results of ref 20, it was chosen to extend the calculations to other model molecules, trying to characterize the reaction path from the reactant to the first transition state and, in many cases, till the final products that can be formed. All the calculations have been performed with the Gaussian 09 suite of programs[37] using the unrestricted B3LYP exchange-correlation functional[38,39] along with 6-31G(d,p) or 6-311++G(d,p) basis sets. All optimizations have been performed with the following options: "verytight" convergence criteria,[40] the grid for numerical integration was chosen "ultrafine" and the "guess = (INDO,mix,always)", and all stationary points have been verified by performing frequency calculations. All minima are featured by real normal modes, whereas the transition states have only one imaginary normal mode frequency. The transition states have been adopted as starting points for a series of intrinsic reaction coordinate (IRC) calculations[41] using either the Hessian based predictor−corrector integrator[42,43] or the local quadratic approximation.[44,45] The solvent effect has been taken into account computing its contribution to the energy of the stationary points by polarizable continuum model calcula-

DOI: 10.1021/acs.joc.9b00499
J. Org. Chem. 2019, 84, 6757−6764

The Journal of Organic Chemistry Article

tions[46] adopting toluene as solvent. These calculations have been performed as a single point on the structures computed at the UB3LYP/6-311++G(d,p) level of theory. To characterize the electronic structure rearrangement during the reaction mechanism, the electron localization has been computed using the electron localization scheme proposed by Boys[47] at the B3LYP/sdall level of theory. A series of model compounds that differ for the substituent on the isoxazolidine ring have been analyzed (Chart 1).

Chart 1. Molecular Structures of the Studied Models

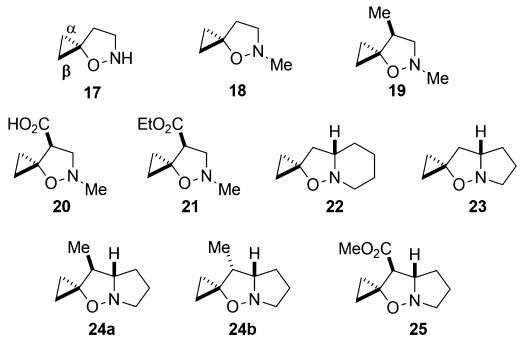

Our results, reported in the Supporting Information, confirmed those obtained by Ochoa et al.[20] Indeed, the Brandi−Guarna reaction is thermally activated and proceeds, in the first step, via a homolytic cleavage of the N−O bond that is followed by the homolytic cleavage of a C−CH_2 bond of the spirofused cyclopropane ring. These two C−CH_2 bonds seem to be equivalent because, on one side, their cleavage energies result of the same order of magnitude,[48] and on the other side, they have a similar spatial environment. However, their cleavage can give rise, at least, to two different minimum energy reaction paths. That is, by labeling as α and β the two cyclopropane C−CH_2 bonds oriented, respectively, below and above the plane of the molecule, as shown in Chart 1,[49] the cleavage of the α and β bonds triggers two different reaction paths. It is interesting to note, on the basis of the reactions reported on the Supporting Information, that the cleavage of the β bond triggers more easily to the formation of a cyclic compound independently from the kind of substituents on the adjacent C atom (C-4 in monocyclic derivatives **17**−**21**, C-3′ in bicyclic isoxazolidines **22**−**25**, see Chart 1, R = H, Me, CO_2H, CO_2Et, and CO_2Me), and this made us confident on the choice of the model systems reported in Scheme 5.

Scheme 5. Rearrangement Products of Model Isoxazolidines 24a and 24b

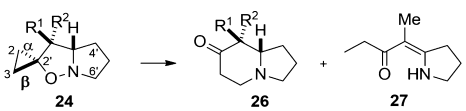

In more details, diastereomers **24a** and **24b** were used as model systems of compounds **7a** and **7b**, respectively, and the two minimum energy reaction paths arising from the cleavage of the two diastereotopic cyclopropane bonds α and β were examined. The stationary points have been initially determined at the UB3LYP/6-31G(d,p) level of theory, and their energies are reported in Table S10 of the Supporting Information. These stationary points have been reoptimized also with the basis set 6-311++G(d,p) as reported in Table S11 of the Supporting Information. As observed by Ochoa et al.,[20] all the intermediates and transition states are characterized by spin contamination, and the eigenvalues of $\langle S^2 \rangle$ are as large as 1 (Tables S12 and S15), suggesting a strong mixture with the triplet state. After purification, the value is reduced by an order of magnitude. The calculations here reported are therefore of a broken symmetry type,[50−52] and this allows us to partially take into account static correlation other than the dynamical one. Moreover, the adequacy of this approach for a qualitative, if not semiquantitative, description has been shown for this kind of reaction by Ochoa et al.[20] who have compared the DFT results with post HF methods.

The Cartesian coordinates of the optimized structures of both **24a** and **24b** at the UB3LYP/6-311++G(d,p) level of theory are reported in Tables S19 and S20 of the Supporting Information. The difference in energy between the two diastereomers is only 7.3 kJ/mol with **24a** being slightly more stable than **24b**. The results of an electronic structure analysis have been collected in Figure 1, where HOMO,

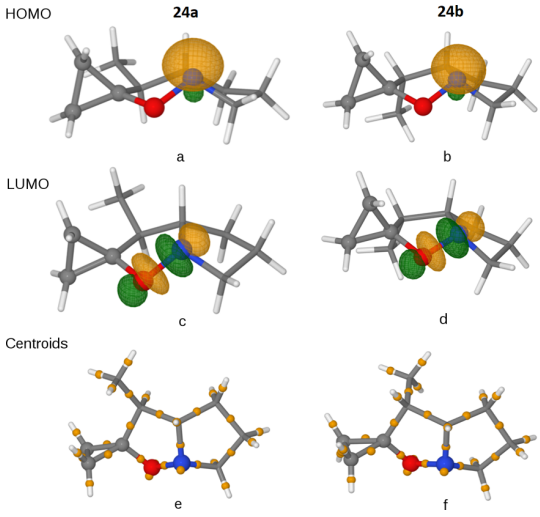

Figure 1. (a,b) HOMO, and (c,d) LUMO of **24a** and **24b**, respectively; (e,f) centroids of the Boys orbitals with small spheres.

LUMO, and centroids of the Boys orbitals are reported. While the HOMO is essentially localized on the nitrogen atom, the LUMO is characterized by a high density on the oxygen and nitrogen atoms, and practically, no probability at the center of the N−O bond is observed, suggesting a dissociative state. This information, along with the Boys centroids, provides a first insight into the chemical reactivity of the two molecules.

The effects of dispersion interactions on the stationary points for the reaction path of both **24a** and **24b** have been studied performing geometry optimization calculations at the UB3LYP/6-311++G(d,p) level of theory adding the D3 dispersion corrections proposed by Grimme et al.[53] using the Gaussian 16 suite of programs.[54]

2.1. Reaction Mechanism: Formation of Indolizidinones 26. The reaction mechanism of the rearrangement is characterized by a first step, common to all reagents, which involves the homolytic cleavage of the N−O bond and the formation of TS_1 and TS_2. The electronic structure of TS_1 is

DOI: 10.1021/acs.joc.9b00499
J. Org. Chem. 2019, 84, 6757−6764

The Journal of Organic Chemistry Article

characterized by the noncoincidence of the centroids related to α e β electrons along the N−O bond and on the cyclopropane moiety, as shown in Figure 2. This result is consistent with an

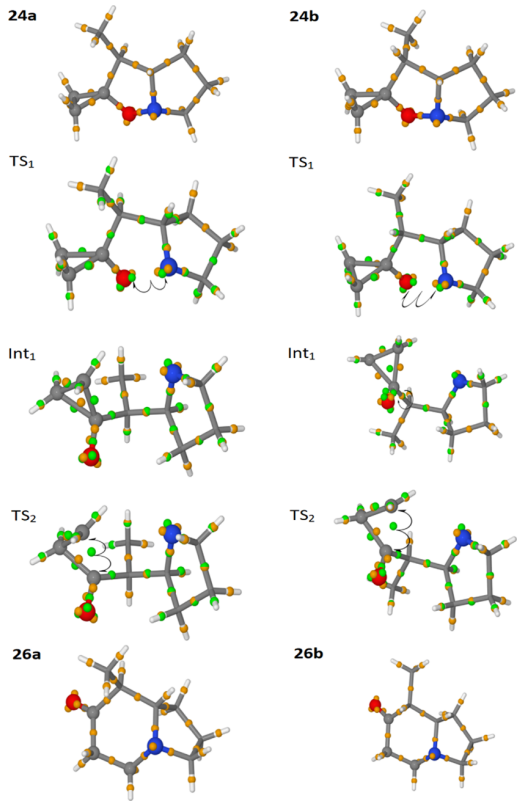

Figure 2. Minima and transition states of **24a** and **24b** reactions leading to the formation of indolizidinones **26a** and **26b**, respectively. Green and orange centroids refer to β and α spins.

initial homolytic cleavage of the N−O bond.[20] This is particularly evident in Figure 2, where the electronic rearrangement for the intermediate Int_1 is depicted. Moreover, while the other electrons on the molecule form pairs on the β bond of the cyclopropane, the two centroids are separated by ~0.4 Å along the bond, one inside the cycle and the other outside. A strong separation is also observed on the α bond, where only one electron lies on the line connecting the two carbon atoms and the other is moved very close to C-2′. The electronic structure characterization of Int_1 is important because the reaction path can now proceed along two different paths with the opening of the cyclopropane ring. Two different minimum reaction paths can be obtained, depending on the cleavage of the β or α bond for both **24a** and **24b**. The mechanism of formation of the tetrahydropyridones **2** is the same for both spirofused bicyclic isoxazolidines **24**. This result is confirmed by the electronic structure and vibrational properties of the equilibrium geometries and transition states obtained from the calculations and summarized in Figure 3. Starting from the molecular structure of the transition state, it has been verified that the nearest minima on the reaction path are reached by an IRC calculation. Although both the energy and the imaginary frequencies of the first transition state are slightly different in the reactions involving compounds **24a** and **24b**, as shown in Table 1, the electronic distribution is almost the same as confirmed by the Boys centroids analysis.

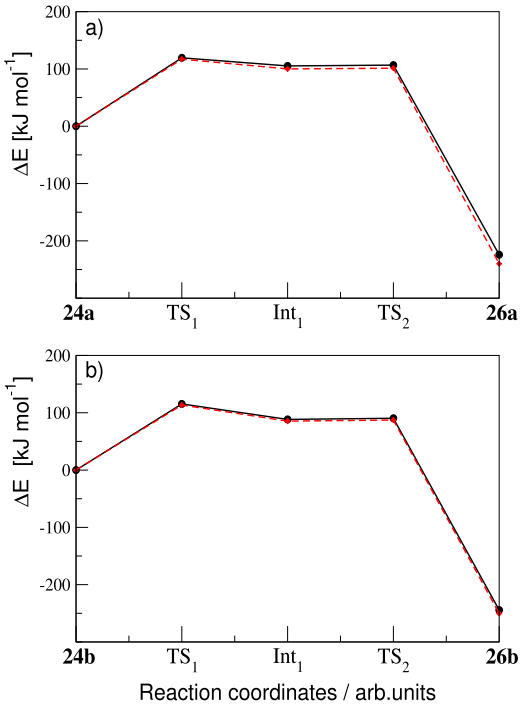

Figure 3. Reaction energy profiles related to the indolizidinone formation, at the UB3LYP/6-311++G(d,p) level of theory, from (a) **24a** and (b) **24b**, with a dashed red line are connected the relative energies of the stationary points computed with the dispersion correction.[53] The lines are guides for the eyes. Reaction mechanism: formation of enaminone **27**.

Table 1. Difference in Energy in kJ mol^{-1} with (ΔE_{PCM}) and without the Solvent Effect (ΔE) of the Stationary Points along the Reaction Paths from 24 to 26[a]

	stationary points	ΔE_{PCM}	ΔE	ΔE_{disp}	freq	$freq_{disp}$
24a	24a	0.0	0.0	0.0		
	TS_1	117.4	119.5	117.1	−209.2	−233.9
	Int_1	102.8	105.2	100.0		
	TS_2	104.2	106.7	101.3	−338.2	−331.0
	26a	−236.0	−224.1	−239.4		
24b	**24b**	0.0	0.0	0.0		
	TS_1	113.2	115.4	113.5	−266.4	−280.3
	Int_1	85.7	88.4	85.4		
	TS_2	87.6	90.4	87.2	−343.0	−337.9
	26b	−247.0	−244.3	−250.1		

[a]For comparison is reported the difference in energy computed with dispersion corrections[53] (ΔE_{disp}). The imaginary frequencies of the transition states are reported in cm^{-1}, computed with ($freq_{disp}$) and without (freq) the dispersion corrections. All the calculations have been performed at the UB3LYP/6-311++G(d,p) level of theory.

The stationary point TS_2 is reached from Int_1. It can be noted from Figure 2 that the CO bond is oriented on the opposite side with respect to the nitrogen, while the three centroids on nitrogen are very similar to those of Int_1. More interesting is the electronic rearrangement occurring in the cyclopropane and CO moieties. Only one centroid, closer to C-2 (~0.7 Å), is present along the β bond. The other centroid is moved on the CO bond that now has three centroids: a pair and an isolated one that is slightly closer to C-2′. A pair and

DOI: 10.1021/acs.joc.9b00499
J. Org. Chem. 2019, 84, 6757−6764

The Journal of Organic Chemistry Article

three centroids on the opposite side equispaced are located on the oxygen. The system evolves along the minimum reaction path toward the final product, which is characterized by all paired electrons, as shown in Figure 2. The reaction of **24b** follows the same mechanism as confirmed by the electronic structure rearrangement in Figure 2. As reported in Table 1, the effect of the solvent, computed by PCM, on the stationary points is less than 3 kJ mol^{-1} except for the final product **26a** that shows a difference of ∼12 kJ mol^{-1}. Therefore, the qualitative description of the formation mechanism of the indolizidones is not affected by the presence of toluene as solvent. Selected calculations have been performed to evaluate the contribution of the dispersion interactions on the optimized structure at the UB3LYP/6-311++G(d,p) level of theory. These results are reported in the Supporting Information (Tables S14 and S16), showing that their effect is similar, as an order of magnitude, to the solvent contribution computed with the PCM method.

To analyze in more detail the effect of the dispersion interactions all the stationary points have been optimized adding the dispersion corrections,[53] obtaining the same reaction profile. A lowering of the energy variation between the reactants (**24a** and **24b**) and the transition states (TS_1 and TS_2) and the intermediate (Int_1) and a stronger stabilization (∼15 kJ mol^{-1}) of the products (**26a** and **26b**) are observed, as expected because of the compact shape of the indolizidinones.

The reaction path involving the α bond cleavage in Int_1 and leading to the formation of the enaminone requires a different description for the **24a** and **24b** reactants as reported in Figure 4 and Table 2. In fact, while the first two steps of the reactions are similar, the TS_3 energy is different due to a different reaction path. The shift of a proton occurs in the third step (TS_3) of the rearrangement of isomer **24a** and in the fourth step (TS_4) in the case of **24b** as shown in Figures 5 and 6.

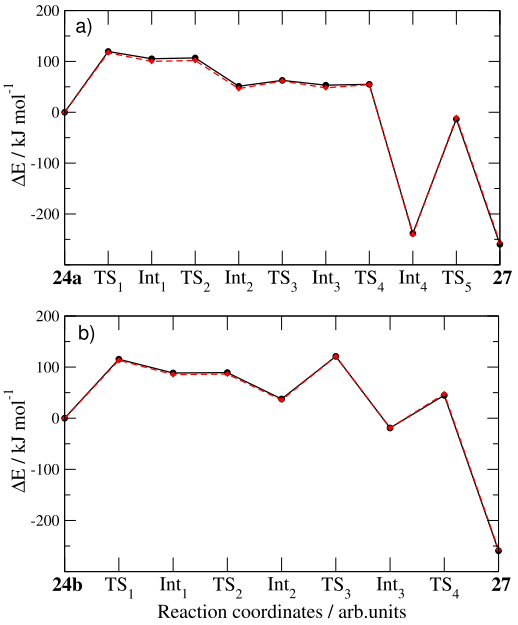

Figure 4. Reaction energy profiles related to the indolizidinone formation, at the UB3LYP/6-311++G(d,p) level of theory, from (a) **24a** and (b) **24b**, with a dashed red line are connected the relative energies of the stationary points computed with the dispersion correction.[53] The lines are guides for the eyes.

Table 2. Difference in Energy in kJ mol^{-1} with (ΔE_{PCM}) and without the Solvent Effect (ΔE) of the Stationary Points along the Reaction Paths from 24 to 27[a]

	stationary points	ΔE_{PCM}	ΔE	ΔE_{disp}	freq	freq$_{disp}$
24a	**24a**	0.0	0.0	0.0		
	TS_1	117.4	119.5	117.1	−209.2	−233.9
	Int_1	102.8	105.2	100.0		
	TS_2	103.6	106.8	101.8	−344.1	−352.9
	Int_2	48.9	51.1	46.5		
	TS_3	59.1	62.7	61.4	−54.0	−56.5
	Int_3	48.4	53.2	48.0		
	TS_4	51.1	54.9	54.5	−167.7	−127.4
	Int_4	−241.7	−238.9	−240.2		
	TS_5	−22.2	−13.3	−10.4	−1781.5	−1777.5
	27	−265.7	−259.7	−256.3		
24b	**24b**	0.0	0.0	0.0		
	TS_1	113.2	115.4	113.5	−266.4	−280.3
	Int_1	85.7	88.4	85.4		
	TS_2	86.0	89.3	86.4	−316.7	−321.8
	Int_2	35.6	37.7	35.6		
	TS_3	118.7	121.0	121.0	−1739.8	−1800.1
	Int_3	−24.2	−19.1	−19.1		
	TS_4	38.4	44.8	47.7	−1642.0	−1634.1
	27	−266.3	−259.3	−257.0		

[a]For comparison is reported the difference in energy computed with dispersion corrections[53] (ΔE_{disp}). The imaginary frequencies of the transition states are reported in cm^{-1}, computed with (freq$_{disp}$) and without (freq) the dispersion corrections. All the calculations have been performed at the UB3LYP/6-311++G(d,p) level of theory.

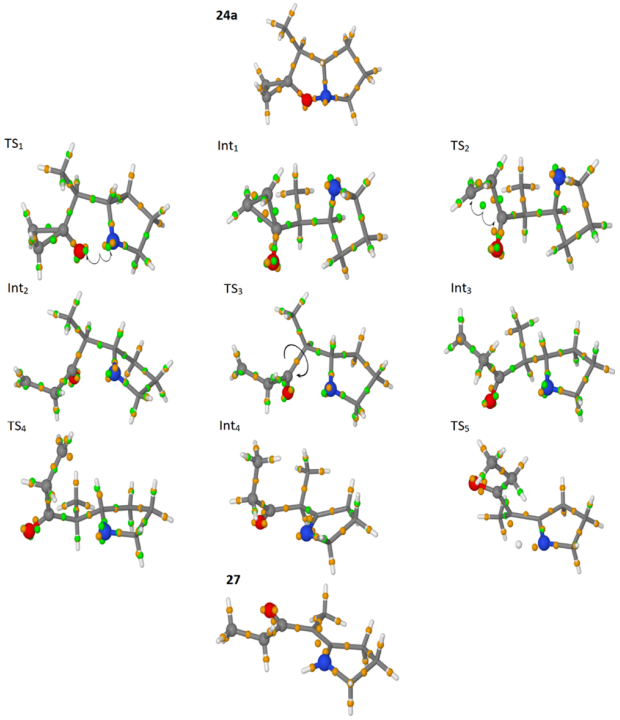

Figure 5. Minima and transition states of the reaction of **24a** leading to the formation of enaminone **27**.

Regarding the reaction of **24a** leading to enaminone **27**, the second step is characterized by the homolytic cleavage of the α

DOI: 10.1021/acs.joc.9b00499
J. Org. Chem. 2019, 84, 6757−6764

The Journal of Organic Chemistry Article

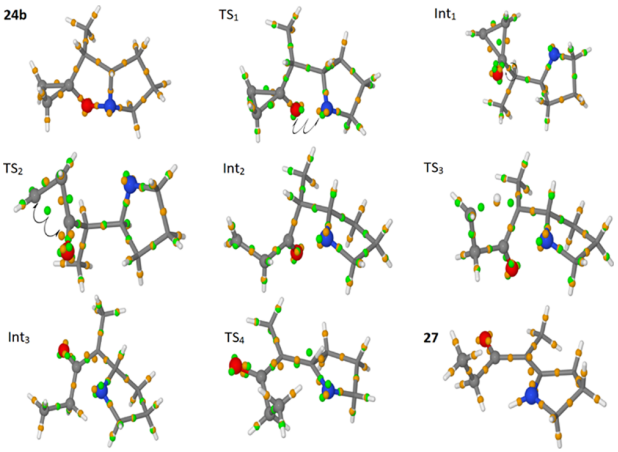

Figure 6. Minima and transition states of the reaction of **24b** leading to the formation of enaminone **27**.

bond in the cyclopropane moiety. The reaction evolves toward Int_2 through a structural rearrangement with the nitrogen and oxygen atoms at longer distance and subsequently through a rotation in TS_3, as shown in Figure 5. The terminal CH_2 group obtained by the cleavage of the α bond interacts with the hydrogen atom initially bonded to C-3a′ to obtain a terminal methyl group. Finally, the enaminone is obtained through isomerization of the imine to enamine. As in the case of **24a**, the epimeric **24b** is converted into enamine **27** through the homolysis of the cyclopropane α bond. However, the reaction occurs through a different sequence with respect to those discussed in the previous section as shown in Figure 5. As observed in the case of the reaction of **24a**, the second transition state and third stationary point (TS_2 and Int_2) are, in sequence, the α bond breaking and a structural rearrangement of the $CH_2-CH^{\bullet}$ moiety, as shown in Figures 5 and 6. The main difference with the rearrangement of **24a** stems in the transition state TS_3 (see Figure 6), which is characterized by a hydrogen atom shift, leading to the formation of the CH_2-CH_3 group. The nitrogen atom interacts with the hydrogen atom of C-**3a′** giving rise to the formation of an imine intermediate (Int_3) that isomerizes to enaminone **27**. It is to be noted that for **24a**, TS_1 is not the highest barrier along the reaction path. At this level of theory, the highest barrier is TS_3 as reported in Table 2. Considering toluene as implicit solvent, also in the case of enaminone formation, the overall energy profile is not modified appreciably, as shown in Table 2. However, the role of the solvent can be relevant on the dynamics of the reaction in the experimental conditions. In fact, the transformation is characterized by many stationary points and involves a much more complex structural rearrangement to reach the elongated enaminone structure than to obtain the pyridone.

Also for these reaction paths, the effects of the dispersion correction have been investigated, and the energy of the stationary points is reported in Table 2. In this case, the effect of the dispersion is to slightly increase the energy of the product **27** relative to the reactants (**24a** and **24b**). As shown in Figure 4, the energy profiles with and without the dispersion correction are almost indistinguishable.

3. CONCLUSIONS

The stationary points for the Brandi−Guarna rearrangement of the spirofused bicyclic isoxazolidines **24** into indolizidinones **26** and enaminone **27** have been characterized at the UB3LYP/6-311++G(d,p) level of theory. The rearrangement occurs through an initial homolysis of the isoxazolidine N−O bond followed by the cleavage of a cyclopropane $C-CH_2$ bond. The main result of the present study is that two different pathways branch off from the first intermediate Int_1 in both **24a** and **24b**. One path involves the cleavage of the a cyclopropane bond and leads to enaminone **27**, while the other that features the cleavage of the β bond ends up with indolizidinone **26** formation. This finding proves that the outcome of the rearrangement does not depend on a late step, such as higher or lower propensity to close the six-membered ring, but on the second step, that is, on the competitive cleavage of the diastereotopic α and β bonds of the cyclopropane ring. It is interesting to note that the pathways leading to enaminones require a larger number of steps with an increase of the spanned space. This can be important in the condensed phase at the experimental conditions. We can therefore hypothesize that at constant volume conditions and in the presence of the solvent, the yield of enaminones is lower than that of indolizidinones because of more complex reaction paths involving large rearrangements that can be made less probable by the presence of the solvent molecules. It is to be noted that the calculations predict a strong decrease in energy from the last transition state to the product for all the reaction paths reported. This energy can be dissipated by interaction with the solvent, but it can be also accumulated initially in the vibrational degrees of freedom, and this can reduce the percentage of enaminone that can be obtained experimentally because it is a more fragile compound. We can also notice that the curvature of the energy profile at the transition state involving the H-shift is very high, and nuclear quantum effects can be important in this reaction step.[55] Despite the differences among the energy barriers of the four calculated pathways being negligible, the study gives a clear description of the reaction mechanism. The sterical effect exerted by the substituent is involved in the selective cleavage of one of the two cyclopropane bonds with the cleavage of the β bond leading to the formation of the pyridone product.

■ ASSOCIATED CONTENT

Supporting Information

The Supporting Information is available free of charge on the ACS Publications website at DOI: 10.1021/acs.joc.9b00499.

Additional information on **17**, **18**, **19**, **20**, **21**, **22**, **23**, **24a**, **24b**, and **25** (PDF)

■ AUTHOR INFORMATION

Corresponding Authors

*E-mail: gianni.cardini@uni.it (G.C.).
*E-mail: franca.cordero@uni.it (F.M.C.).

ORCID

Alberto Brandi: 0000-0001-8273-6369
Gianni Cardini: 0000-0002-7292-3555
Riccardo Chelli: 0000-0003-3492-5709
Franca M. Cordero: 0000-0001-6005-5941
Cristina Gellini: 0000-0002-3112-6680
Marco Pagliai: 0000-0003-0240-161X

DOI: 10.1021/acs.joc.9b00499
J. Org. Chem. 2019, 84, 6757−6764

The Journal of Organic Chemistry Article

Notes

The authors declare no competing financial interest.

■ ACKNOWLEDGMENTS

The authors like to thank Prof. Roberto Cammi (University of Parma) for helpful discussion and suggestions. We thank MIUR-Italy ("Progetto Dipartimenti di Eccellenza 2018-2022" allocated to Department of Chemistry "Ugo Schiff").

■ DEDICATION

Dedicated to Professor Francesco De Sarlo on the occasion of his 80th birthday.

■ REFERENCES

(1) Hassner, A.; Namboothiri, I. *Organic Syntheses Based on Name Reactions: A Practical Guide to 750 Transformations*; Elsevier, 2012; p 60.

(2) Wang, H. *Comprehensive Organic Name Reactions*; Wiley, 2010; pp 515−520.

(3) Brandi, A.; Cicchi, S.; Cordero, F. M.; Goti, A. Heterocycles from Alkylidenecyclopropanes. *Chem. Rev.* **2003**, *103*, 1213−1270.

(4) Cordero, F. M.; De Sarlo, F.; Brandi, A. 5-Spirocyclopropane Isoxazolidines as Versatile Intermediates in Organic Synthesis. *Monatsh. Chem.* **2004**, *135*, 649−669.

(5) Cordero, F.; Machetti, F.; Giomi, D. In *Comprehensive Heterocyclic Chemistry III*; Katritzky, A., Ramsden, C., Scriven, E., Taylor, R., Eds.; Elsevier Oxford: U.K., 2008; Vol. *6*, pp 365−486.

(6) Brandi, A.; Cicchi, S.; Cordero, F. M.; Goti, A. Progress in the Synthesis and Transformations of Alkylidenecyclopropanes and Alkylidenecyclobutanes. *Chem. Rev.* **2014**, *114*, 7317−7420.

(7) Malinina, J.; Tran, T. Q.; Stepakov, A. V.; Gurzhiy, V. V.; Starova, G. L.; Kostikov, R. R.; Molchanov, A. P. [3+2] Cycloaddition reactions of arylallenes with C-(N-arylcarbamoyl)- and C,C-bis-(methoxycarbonyl)nitrones and subsequent rearrangements. *Tetrahedron Lett.* **2014**, *55*, 3663−3666.

(8) Molchanov, A. P.; Tran, T. Q.; Stepakov, A. V.; Starova, G. L.; Kostikov, R. R. Regioselective cycloaddition of C-carbamoylnitrones to methyl (E)-2-(2-phenylcyclopropylidene)acetate and methyl (E)-2-methylidene-3-phenylcyclopropane-1-carboxylate. *Russ. J. Org. Chem.* **2014**, *50*, 78−82.

(9) Cordero, F. M.; Vurchio, C.; Faggi, C.; Brandi, A. Configuration-guided Reactions: the Case of Highly Decorated Spiro[cyclopropane-1,2′(3′*H*)-pyrrolo[1,2-b]isoxazole] Derivatives en Route to Polyhydroxyindolizidines. *Org. Chem. Front.* **2016**, *3*, 1651−1660.

(10) Ma, X.-P.; Zhu, J.-F.; Wu, S.-Y.; Chen, C.-H.; Zou, N.; Liang, C.; Su, G.-F.; Mo, D.-L. Cycloaddition of Fluorenone N-Aryl Nitrones with Methylenecyclopropanes and Sequential 1,3-Rearrangement: An Entry to Synthesis of Spirofluorenylpiperidin-4-ones. *J. Org. Chem.* **2017**, *82*, 502−511.

(11) Vurchio, C.; Cordero, F. M.; Brandi, A. Domino Thermal Rearrangement/[4+2] Addition Reactions of an exo-Methylene Spirocyclopropane Isoxazolidine. *Eur. J. Org. Chem.* **2018**, *2018*, 2548−2553.

(12) Wu, S.-Y.; Chen, W.-L.; Ma, X.-P.; Liang, C.; Su, G.-F.; Mo, D.-L. Copper-Catalyzed [3+2] Cycloaddition and Interrupted Fischer Indolization to Prepare Polycyclic Furo[2,3-b]indolines from N-Aryl Isatin Nitrones and Methylenecyclopropanes. *Adv. Synth. Catal.* **2019**, *361*, 965−970.

(13) A substructure search of the piperidine ring using the Reaxys chemistry search engine revealed over 949 000 piperidine derivatives associated with any pharmacological data. In the list were included discrete monocyclic piperidines (>59 800), In Bicyclic Indolizidines (>2000) and Quinolizidines (>1300).

(14) Hesse, M. *Alkaloids: Nature's Curse or Blessing?*; John Wiley & Sons, 2002.

(15) Prichard, K.; Campkin, D.; O'Brien, N.; Kato, A.; Fleet, G. W.; Simone, M. I. Biological Activities of 3, 4, 5-trihydroxypiperidines and their N-and O-derivatives. *Chem. Biol. Drug Des.* **2018**, *92*, 1171−1197.

(16) Källström, S.; Leino, R. Synthesis of Pharmaceutically Active Compounds Containing a Disubstituted Piperidine Framework. *Bioorg. Med. Chem.* **2008**, *16*, 601−635.

(17) Crossley, S. W. M.; Shenvi, R. A. A Longitudinal Study of Alkaloid Synthesis Reveals Functional Group Interconversions as Bad Actors. *Chem. Rev.* **2015**, *115*, 9465−9531.

(18) Kandepedu, N.; Abrunhosa-Thomas, I.; Troin, Y. Stereoselective Strategies for the Construction of Polysubstituted Piperidinic Compounds and Their Applications in Natural Products Synthesis. *Org. Chem. Front.* **2017**, *4*, 1655−1704.

(19) In One Case, Likely Because of Steric Hindrance, the H Extraction Occurred from the Methylene α to Ketone Moiety Leading to an α,β-unsaturated Ketone (see ref 9).

(20) Ochoa, E.; Mann, M.; Sperling, D.; Fabian, J. A Combined Density Functional and Ab Initio Quantum Chemical Study of the Brandi Reaction. *Eur. J. Org. Chem.* **2001**, *2001*, 4223−4231.

(21) Cramer, C. J.; Squires, R. R. Prediction of Singlet-Triplet Splittings for Aryne Biradicals from 1H Hyperfine Interactions in Aryl Radicals. *J. Phys. Chem. A* **1997**, *101*, 9191−9194.

(22) Bally, T.; Borden, W. T. In *Calculations on Open-shell Molecules: A Beginner's Guide*; Lipkowitz, K. B., Boyd, D. B., Eds.; Reviews in Computational Chemistry; Wiley-VCH, John Wiley and Sons, INC: New York, 1999; Vol. *13*, Chapter 1, pp 1−97.

(23) Debbert, S. L.; Cramer, C. J. Systematic comparison of the benzynes, pyridynes, and pyridynium cations and characterization of the Bergman cyclization of Z-but-1-en-3-yn-1-yl isonitrile to the meta diradical 2,4-pyridyne. *Int. J. Mass Spectrom.* **2000**, *201*, 1−15.

(24) Cramer, C. J. *Essentials of Computational Chemistry: Theories and Models*; John Wiley & Sons Inc., 2004.

(25) Ghosh, S.; Verma, P.; Cramer, C. J.; Gagliardi, L.; Truhlar, D. G. Combining Wave Function Methods with Density Functional Theory for Excited States. *Chem. Rev.* **2018**, *118*, 7249−7292.

(26) Goddard, J. D.; Orlova, G. Density Functional Theory with Fractionally Occupied Frontier Orbitals and the Instabilities of the Kohn-Sham Solutions for Defining Diradical Transition States: Ring-opening Reactions. *J. Chem. Phys.* **1999**, *111*, 7705−7712.

(27) Orlova, G.; Goddard, J. D. Singularities in the Behavior of Density Functionals in Predictions of Singlet Biradicals: The 1,2-dichalcogenins. *J. Chem. Phys.* **2000**, *112*, 10085−10094.

(28) Kishi, R.; Murata, Y.; Saito, M.; Morita, K.; Abe, M.; Nakano, M. Theoretical Study on Diradical Characters and Nonlinear Optical Properties of 1,3-Diradical Compounds. *J. Phys. Chem. A* **2014**, *118*, 10837−10848.

(29) Marell, D. J.; Furan, L. R.; Woods, B. P.; Lei, X.; Bendelsmith, A. J.; Cramer, C. J.; Hoye, T. R.; Kuwata, K. T. Mechanism of the Intramolecular Hexadehydro-DielsAlder Reaction. *J. Org. Chem.* **2015**, *80*, 11744−11754.

(30) Zhang, H.; Wu, G.; Yi, H.; Sun, T.; Wang, B.; Zhang, Y.; Dong, G.; Wang, J. Copper(I)-Catalyzed Chemoselective Coupling of Cyclopropanols with Diazoesters: Ring-Opening CC Bond Formations. *Angew. Chem.* **2017**, *129*, 4003−4008.

(31) Wan, W.; Jenness, G. R.; Xiong, K.; Vlachos, D. G.; Chen, J. G. Ring-Opening Reaction of Furfural and Tetrahydrofurfuryl Alcohol on Hydrogen-Predosed Iridium(111) and Cobalt/Iridium(111) Surfaces. *ChemCatChem* **2017**, *9*, 1701−1707.

(32) Huo, R.-P.; Guo, L.-h.; Zhang, F.-q.; Zhang, X. Multiple Electronic State Mechanism for Carboryne Reaction with Benzene: A DFT Study. *Int. J. Quantum Chem.* **2017**, *117*, No. e25372.

(33) Alves, M.; Méreau, R.; Grignard, B.; Detrembleur, C.; Jérôme, C.; Tassaing, T. DFT Investigation of the Reaction Mechanism for the Guanidine Catalysed Ring-opening of Cyclic Carbonates by Aromatic and Alkyl-amines. *RSC Adv.* **2017**, *7*, 18993−19001.

(34) The enaminone product, in this particular case, derives from the primary enaminone by CH_2O moiety extrusion (see ref 14).

(35) Brandi, A.; Cicchi, S.; Cordero, F. M.; Frignoli, R.; Goti, A.; Picasso, S.; Vogel, P. Assignment of the Absolute Configuration of

DOI: 10.1021/acs.joc.9b00499
J. Org. Chem. 2019, 84, 6757−6764

Natural Lentiginosine by Synthesis and Enzymic Assays of Optically Pure (+) and (-)-enantiomers. *J. Org. Chem.* **1995**, *60*, 6806−6812.
(36) Zorn, C.; Anichini, B.; Goti, A.; Brandi, A.; Kozhushkov, S. I.; de Meijere, A.; Citti, L. Studies on the Synthesis of Aza Analogues of Illudins by Cycloadditions to Highly Strained Methylenecyclopropanes. *J. Org. Chem.* **1999**, *64*, 7846−7855.
(37) Frisch, M. J.; Trucks, G. W.; Schlegel, H. B.; Scuseria, G. E.; Robb, M. A.; Cheeseman, J. R.; Scalmani, G.; Barone, V.; Mennucci, B.; Petersson, G. A. ; et al. *Gaussian 09*, Revision C.01; Gaussian Inc.: Wallingford CT, 2010.
(38) Becke, A. D. Density Functional Thermochemistry. III: The Role of Exact Exchange. *J. Chem. Phys.* **1992**, *97*, 9173−9177.
(39) Lee, C.; Yang, W.; Parr, R. G. LYP Gradient-Corrected Functional. *Phys. Rev. B: Condens. Matter Mater. Phys.* **1988**, *37*, 785−789.
(40) threshold in atomic units: maximum force = 2×10^{-6}, rms force = 1×10^{-6}, maximum displacement = 6×10^{-6} and rms displacement = 4×10^{-6}.
(41) Page, M.; Doubleday, C.; McIver, J. W., Jr Following Steepest Descent Reaction Paths. The Use of Higher Energy Derivatives with Ab Initio Electronic Structure Methods. *J. Chem. Phys.* **1990**, *93*, 5634−5642.
(42) Hratchian, H. P.; Schlegel, H. B. Using Hessian Updating to Increase the Efficiency of a Hessian Based Predictor-Corrector Reaction Path Following Method. *J. Chem. Theory Comput.* **2005**, *1*, 61−69.
(43) Hratchian, H. P.; Schlegel, H. B. Accurate Reaction Paths Using a Hessian Based Predictor−Corrector Integrator. *J. Chem. Phys.* **2004**, *120*, 9918−9924.
(44) Page, M.; McIver, J. W., Jr On Evaluating the Reaction Path Hamiltonian. *J. Chem. Phys.* **1988**, *88*, 922−935.
(45) Page, M.; Doubleday, C.; McIver, J. W., Jr Following Steepest Descent Reaction Paths. The Use of Higher Energy Derivatives with Ab Initio Electronic Structure Methods. *J. Chem. Phys.* **1990**, *93*, 5634−5642.
(46) Tomasi, J.; Mennucci, B.; Cammi, R. Quantum Mechanical Continuum Solvation Models. *Chem. Rev.* **2005**, *105*, 2999−3094.
(47) Boys, S. F. Construction of Some Molecular Orbitals to Be Approximately Invariant for Changes from One Molecule to Another. *Rev. Mod. Phys.* **1960**, *32*, 296.
(48) Briccolani-Bandini, L. Brandi Reaction, a Computational Study, M. Sc. thesis, Università di Firenze (IT), 2016.
(49) In bicyclic isoxazolidines **22**−**25** the cyclopropane bond is on the same side as the bridgehead C−H bond.
(50) Perdew, J.; Savin, A.; Burke, K. Escaping the Symmetry Dilemma through a Pair-Density Interpretation of Spin-Density Functional Theory. *Physical Review A: Atomic, Molecular, and Optical Physics* **1995**, *51*, 4531−4541.
(51) Jacob, C. R.; Reiher, M. Spin in Density-Functional Theory. *Int. J. Quantum Chem.* **2012**, *112*, 3661−3684.
(52) Kraka, E.; Cremer, D. Enediynes, Enyne-allenes, their Reactions, and Beyond. *Wiley Interdiscip. Rev.: Comput. Mol. Sci.* **2014**, *4*, 285−324.
(53) Grimme, S.; Antony, J.; Ehrlich, S.; Krieg, H. A Consistent and Accurate Ab Initio Parametrization of Density Functional Dispersion Correction (DFT-D) for the 94 Elements H-Pu. *J. Chem. Phys.* **2010**, *132*, 154104.
(54) Frisch, M. J.; Trucks, G. W.; Schlegel, H. B.; Scuseria, G. E.; Robb, M. A.; Cheeseman, J. R.; Scalmani, G.; Barone, V.; Petersson, G. A.; Nakatsuji, H.; et al. *Gaussian 16*, Revision B.01., 2016; Gaussian Inc: Wallingford CT.
(55) Wigner, E. Über das Überschreiten von Potentialschwellen Bei Chemischen Reaktionen. *Z. Phys. Chem.* **1932**, *19*, 203−216.

DOI: 10.1021/acs.joc.9b00499
J. Org. Chem. 2019, 84, 6757−6764

Journal of Colloid and Interface Science 606 (2022) 444–453

Contents lists available at ScienceDirect

Journal of Colloid and Interface Science

journal homepage: www.elsevier.com/locate/jcis

Exploring the effect of Mg^{2+} substitution on amorphous calcium phosphate nanoparticles

Rita Gelli [a,b], Lorenzo Briccolani-Bandini [a], Marco Pagliai [a], Gianni Cardini [a], Francesca Ridi [a,b,*], Piero Baglioni [a,b]

[a] Department of Chemistry "Ugo Schiff", University of Florence, via della Lastruccia 3, 50019 Sesto Fiorentino, Florence, Italy
[b] CSGI, Center for Colloid and Surface Science, via della Lastruccia 3, 50019 Sesto Fiorentino, Florence, Italy

GRAPHICAL ABSTRACT

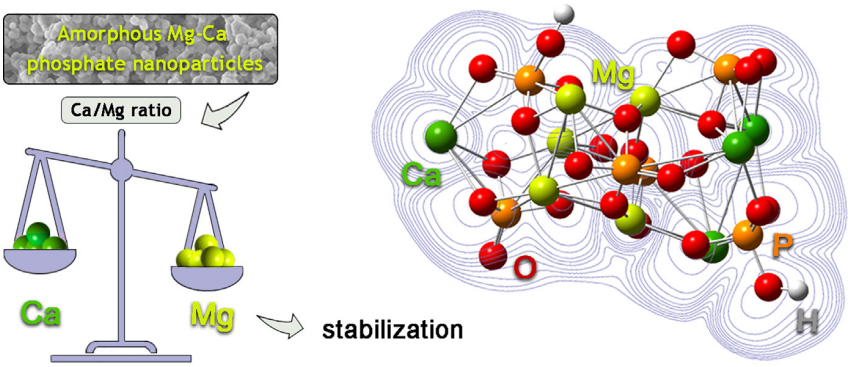

ARTICLE INFO

Article history:
Received 15 July 2021
Revised 5 August 2021
Accepted 6 August 2021
Available online 9 August 2021

Keywords:
Amorphous calcium phosphates
Magnesium
Posner's cluster
Nanoparticles
Nanostructure
Morphology
Stability
Thermal analysis
Simulations

ABSTRACT

Hypothesis: The study of Amorphous Calcium Phosphate (ACP) has become a hot topic due to its relevance in living organisms and as a material for biomedical applications. The preparation and characterization of Mg-substituted ACP nanoparticles (AMCP) with tunable Ca/Mg ratio is reported in the present study to address the effect of Mg^{2+} on their structure and stability.
Experiments: AMCPs particles were synthesized by precipitation of the precursors from aqueous solutions. The particles were analyzed in terms of morphology, crystallinity, and thermal stability, to get a complete overview of their physico-chemical characteristics. Computational methods were also employed to simulate the structure of ACP clusters at different levels of Mg^{2+} substitution.
Findings: Our results demonstrate that AMCP particles with tunable composition and crystallinity can be obtained. The analysis of the heat-induced crystallization of AMCP shows that particles' stability depends on the degree of Mg^{2+} substitution in the cluster, as confirmed by computational analyses. The presented results shed light on the effect of Mg^{2+} on ACP features at different structural levels and may be useful guidelines for the preparation and design of AMCP particles with a specific Ca/Mg ratio.

1. Introduction

Amorphous Calcium Phosphate (ACP) is particularly relevant among the different forms of Calcium Phosphate (CaP) present in

* Corresponding author at: Department of Chemistry "Ugo Schiff" & CSGI, University of Florence, via della Lastruccia 3, 50019 Sesto Fiorentino, Florence, Italy.
E-mail address: francesca.ridi@unifi.it (F. Ridi).

https://doi.org/10.1016/j.jcis.2021.08.033
0021-9797/

nature and in living organisms [1]. Given its chemical and structural versatility, ACP has a dramatic biological importance as a transient intermediate in the formation of the apatitic inorganic matrix of bones and teeth and in the formation of other types of functional structures such as casein micelles, calciprotein particles and amorphous nanoparticles in the small intestine [2]. Despite its amorphous nature, ACP displays a short-range order corresponding to the so-called "Posner's Cluster" $Ca_9(PO_4)_6$ [3], which is thermodynamically unstable and spontaneously converts into a crystalline form of CaP, such as hydroxyapatite (HA, $Ca_{10}(PO_4)_6(OH)_2$), brushite ($CaHPO_4{\cdot}2H_2O$) or octacalcium phosphate ($Ca_8(HPO_4)_2(PO_4)_4{\cdot}5H_2O$) [4]. The intrinsically metastable and dynamic nature of ACP and, in general, of amorphous materials, makes them very versatile and attractive for several applications in the biomedical field, including drug delivery [5–7], dentistry [8,9] and bone regeneration [10,11].

Notwithstanding the importance of pure ACP, the role that Mg^{2+} exerts on ACP features and stability is receiving considerable attention from the scientific community, due to the key functions exerted in biological organisms. On the average, an adult human body contains about 24 g of Mg^{2+}, about half stored in bone tissue [12]. Magnesium levels in our organism are tightly controlled, in order to prevent the multiple pathologic situations caused by its deficiency, such as low bone mass, reduced bone growth, osteoporosis and increased skeletal fragility [13–15]. Besides Mg^{2+} role in cellular metabolism [16] and bone formation [17], it has recently emerged that *in vivo* its interaction with ACP results in the formation of AMCP (Amorphous Magnesium Calcium Phosphate) particles both in the small intestine [18] and in enamel [19,20].

Long before the full recognition of the biological importance of Mg^{2+} interplay with ACP, its effect on the formation and crystallization of CaP was thoroughly investigated starting from the sixties [21–29]. In a seminal study from Boskey and Posner, the conversion kinetic of ACP to HA in the presence of Mg^{2+} was investigated, revealing that an increase in Mg/Ca ratio from 0 to 0.04 extends the amorphous phase's lifetime, from 4 to 9 times depending on the temperature [21]. The stabilizing effect of Mg^{2+} was ascribed to a decrease in the solubility of ACP, while other authors suggest that the formation of Mg-phosphate complexes is responsible for the enhancement of the amorphous' lifetime [22]. As an alternative mechanism for the stabilization, Abbona and Baronnet hypothesize that the initial Mg^{2+} substitution for Ca^{2+} in Posner's clusters induces mechanical strains and hinders HA nucleation, in addition to the effect due to Mg^{2+} adsorption onto the surfaces of ACP and of apatite crystallites [26]. Despite the large number of studies carried out from the sixties, the role that Mg^{2+} exerts on ACP is still an open issue [30–37]. Yang *et al.* suggested that the formation of Mg-phosphate ion pairs reduces the thermodynamic driving force for ACP nucleation and the subsequent crystallization to HA [30], while others proposed that Mg^{2+} might also have an effect in increasing HA's solubility [33]. A study by Ding *et al.* addressed the effect of Mg^{2+} ions on the different stages of HA precipitation from ACP, which can either be adsorbed or incorporated into the ACP precursor particles [31]. Other investigations took advantage of combined experimental-computational approaches to tackle this issue [32]. However, the studies conducted so far are not able to shed light on the role of Mg^{2+} in the stabilization of the amorphous phase, likely resulting from multiple simultaneous mechanisms with implications in the *in vivo* biomineralization processes.

It is important to point out that Mg^{2+} role is meaningful not only for the crystallization pathway of ACP, but also for the structural features of the amorphous phase itself, as Mg^{2+} can be incorporated in the amorphous cluster to form AMCP particles. Few reports describe the preparation of AMCPs with different Ca/Mg ratio [24,38], sometimes coupled with the study of their evolution in simulated body fluids [39,40]. However, little attention is devoted to the characterization of the features of the different amorphous phases, and to the understanding of the Ca^{2+} ions substitution in the amorphous cluster. The control of AMCP particles with tailored Ca/Mg ratio and the knowledge of their structural features is of fundamental importance to prepare particles with predetermined stability, to be used in several applications as the treatment of dentin hypersensitivity [41,42], as well as to reproduce the endogenous nanoparticles present in the small intestine [43].

The aim of this study is the investigation of the variation of the Ca/Mg ratio and the total cations concentration on the properties of the precipitated amorphous phases. A systematic analysis was conducted by performing 15 different syntheses in which the concentrations of the reacting solutions were varied to test 5 different Ca/Mg ratios (0.4, 0.7, 1, 2 and 3), each at 3 different Mg^{2+} concentrations (10, 50 and 100 mM). The obtained particles were analyzed in terms of crystallinity, morphology, elemental composition, and thermal stability, while computational approaches were used to gain insights into the structure of these particles at the atomic level, disclosing new insights into the role of Mg^{2+} substitution in ACP.

2. Materials and methods

2.1. Materials

Calcium chloride ($CaCl_2$, ≥93%), Magnesium chloride hexahydrate ($MgCl_2{\cdot}6H_2O$, ≥99%), Sodium chloride (NaCl, ≥99%) and NaOH pellets (≥99%) were purchased from Sigma-Aldrich (Milan, Italy). Sodium phosphate monobasic ($NaH_2PO_4{\cdot}H_2O$, ≥99%), and sodium phosphate dibasic ($Na_2HPO_4{\cdot}12H_2O$, ≥99%) were obtained from Carlo Erba Reagents (Milan, Italy). Milli-Q grade water (Millipore, resistivity 18.2 MΩ·cm at 25 °C) was used during all the experiments.

2.2. Preparation of AMCP

AMCPs were prepared by precipitation from aqueous solution, according to a method readapted from the literature [24]. 10 mL of solution A (from A1 to A15, see Table 1) were mixed with 10 mL of solution B (150 mM $Na_2HPO_4{\cdot}12H_2O$ + 50 mM $NaH_2PO_4{\cdot}H_2O$), at 37 °C. Immediately after mixing, the pH was adjusted at 7.40 by means of 1 M NaOH. It was observed that the higher the concentration of the reactants used, the higher the turbidity of the reacting medium. After 15 min of reaction, the particles were collected by means of filtration, using a Millipore vacuum filtration system equipped with mixed cellulose esters filters (Millipore, pore size 0.45 μm). Immediately after filtration, the filters were placed in plastic test tubes and frozen in liquid nitrogen. The powders were then freeze-dried for 24 h, at −55 °C and ~30 mTorr (VirTis BenchTop freeze-dryer, NY, USA) and stored in the freezer (−18 °C), tightly closed to prevent any influence from environmental humidity [11].

2.3. Characterization techniques

2.3.1. X-ray diffraction (XRD)

XRD patterns were collected using a D8 Advance with DAVINCI design (Bruker, Milan, Italy), using as X-ray source the Cu Kα radiation (wavelength λ = 1.54 Å), at 40 kV and 40 mA, a 2θ range of 10°–50°, a step size of 0.03°, and a time/step of 0.3 s. Samples were grinded with agate mortar and pestle and flattened onto a Si zero-background sample holder. Peaks were assigned using the Powder Diffraction Files (PDF) of the ICDD database (International Centre for Diffraction Data).

R. Gelli, L. Briccolani-Bandini, M. Pagliai et al. Journal of Colloid and Interface Science 606 (2022) 444–453

Table 1
Composition of the solutions used for the syntheses.

Sample	$CaCl_2$ [mM]	$MgCl_2$ [mM]	NaCl [mM]	Ca/P	Mg/P	Ca/Mg
A1	4	10	135	0.02	0.05	0.4
A2	20	50	135	0.1	0.25	0.4
A3	40	100	135	0.2	0.5	0.4
A4	7	10	135	0.035	0.05	0.7
A5	35	50	135	0.175	0.25	0.7
A6	70	100	135	0.35	0.5	0.7
A7	10	10	135	0.05	0.05	1
A8	50	50	135	0.25	0.25	1
A9	100	100	135	0.5	0.5	1
A10	20	10	135	0.1	0.05	2
A11	100	50	135	0.5	0.25	2
A12	200	100	135	1	0.5	2
A13	30	10	135	0.15	0.05	3
A14	150	50	135	0.75	0.25	3
A15	300	100	135	1.5	0.5	3

Scherrer equation (Eq. (1)) was used to calculate the crystalline domain size (D, nm):

$$D = \frac{\kappa\lambda}{\beta\cos(\theta)} \quad \text{(Eq.1)}$$

where κ is the Scherrer constant, typically considered 0.9, λ is the X-Ray wavelength (nm), β is the FWHM (Full Width at Half Maximum) in radians and θ is the diffraction angle in radians [44]. The FWHM were obtained from the Multi-Peak Fitting routine of the software IgorPro, considering a logcubic function as baseline.

2.3.2. Attenuated total reflectance – fourier transform infrared spectroscopy (ATR-FTIR)

ATR-FTIR spectra on the freeze-dried samples were acquired by means of a Nexus Thermo-Nicolet 870 FT-IR spectrophotometer (Madison, WI, USA) equipped with a MCT detector and a Golden Gate. The spectra were collected in the 4000–650 cm^{-1} range, with 128 scans and resolution 2 cm^{-1}

2.3.3. Field emission-scanning electron microscopy (FE-SEM)

FE-SEM micrographs were collected by means of a Zeiss ΣIGMA FE-SEM (Carl Zeiss Microscopy GmbH, Jena, Germany). The powders were placed over aluminum stubs by means of conductive tape. The use of a Field Emission source, together with a low accelerating voltage (2 kV), a reduced sample-detector distance (~2 mm) and the In-Lens detector allowed for the imaging of non-conductive samples at high magnification. The size distribution curves were obtained with the software ImageJ by measuring about 200 particles *per* sample.

2.3.4. Inductively coupled plasma-atomic emission spectrometry (ICP-OES)

The amount of phosphorous in the samples was determined in triplicate by means of an Agilent 720-ES Inductively Coupled Plasma Atomic Emission Spectrometer (ICP-OES) equipped with a pneumatic nebulizer and a cyclonic spray chamber. Before the analyses, about 1.0 mg of each sample was dissolved in 10 μL of HCl, brought to 10 mL with ultrapure water and added with 1.0 ppm of Ge, used as an internal standard to correct any matrix effect. The calibration lines were obtained by preparing the standard solutions starting from commercial standards certified at 1000 ppm. Ge line used for the correction was at 209.426 nm. After each measurement, the system was washed with a 2% HNO_3 solution.

2.3.5. Ionic chromatography

The amount of calcium, magnesium and sodium was determined by means of ionic chromatography using a Thermo Dionex ICS-1000 ion chromatograph with a CG-12A guard column and a CS-12A analytical column. The same solutions prepared for ICP-OES measurements were analyzed. An electrochemical suppression of the background conductivity with a current of 160 mA was used, together with an injection loop of 25 μL with a conductivity detector. The element used for the separation was H_2SO_4 23 mM. The calibration lines of the individual ions were constructed for subsequent dilutions starting from standard certified solutions at 1000 ppm.

For both ICP-OES and ionic chromatography, to evaluate the reproducibility of the results, on selected samples the measurements were conducted on 3 specimens prepared by repeating the same synthesis three times. In all cases, the standard deviation of the three measurements lead to atomic ratios uncertainties <0.1.

2.3.6. Simultaneous thermogravimetry/differential scanning calorimetry (SDT)

Thermal analysis was conducted with a SDT Q600 from TA Instruments (New Castle, DE, USA), which allows for the simultaneous monitoring of the weight loss signal (TGA curve) and the heat flow profile (DSC curve). Samples were placed in an alumina pan and measured in N_2 atmosphere (flow rate 100 mL/min) from room temperature to 1000 °C, at 10 °C/min. The crystallization T is expressed as average ± standard deviation of 3 measurements conducted on 3 replicas of each synthesis.

2.3.7. Computational details

To investigate the structural properties of selected magnesium and calcium phosphate clusters, DFT calculations have been performed at the B3LYP/6-31G(d) level of theory with the Gaussian suite of programs [45] using tight criteria. The initial molecular structure has been obtained by optimizing the atomic positions of a brushite crystal (Fig. S1) with the CP2K suite of programs [46]. The crystal structure calculations have been performed with the Quick Step module employing the LDA exchange and correlation functional within the Padé approximation [47]. The wave functions for each atomic species have been described through a DZVP-MOLOPT basis set [48], whereas the electron density has been represented with a plane wave expansion with a 340 Ry cutoff. The supercell is made up by 3 × 1 × 3 unit cells. The calculations show a complete agreement between the computed and experimental structure [49]. Moreover, two phosphate ions have been hydrogenated according to the experimental results (see the characterization of the obtained particles in the Results section) and some calcium ions have been progressively replaced by magnesium ions, as summarized in Table 2, where the chemical compositions of the studied clusters are collected. In the Table, the simulated clusters are identified as An', where the presence

Table 2
Different Ca/Mg, Ca/P and Mg/P ratios for the analyzed Posner's clusters. Four different arrangements have been chosen for each sample.

Simulated cluster[†]	Ca/Mg	Ca/P	Mg/P	N_Ca[††]	N_Mg[†††]
Ca_0	0	0	1.5	0	9
A0′	0.12	0.16	1.33	1	8
A3′	0.5	0.5	1	3	6
A6′	0.8	0.66	0.83	4	5
A1′	2	1	0.5	6	3
A7′	3.5	1.16	0.33	7	2
Mg_0	0	1.5	0	9	0

[†] Simulated clusters are identified with the An' label, which indicates an elemental composition close to the synthesized An samples. The simulated clusters Ca_0 and Mg_0 refer to clusters containing only Mg or Ca atoms, respectively.
[††] Number of Ca atoms in the simulated cluster.
[†††] Number of Mg atoms in the simulated cluster.

of the apex indicates a chemical composition of the cluster close to that obtained in the synthesized samples An (Table 3 in the Results and Discussion section). The "N_Ca" or "N_Mg" label indicates the number of Ca or Mg ions present in the simulated cluster, respectively.

The optimized structures have been subsequently analyzed to obtain information on the distances between the oxygen atoms and metal ions. The interaction energy between one selected Mg^{2+} ion and the remaining cluster has been calculated with the counterpoise correction method [50,51].

3. Results and discussion

3.1. Crystallinity

The synthesized particles were analyzed by means of X-Ray Diffraction, in order to assess their amorphous nature. The diffractograms, reported in Fig. 1, reveal that in almost all cases the formation of completely amorphous particles is achieved, as confirmed by the hump at ~30° that is the fingerprint of amorphous calcium phosphates [52,53]. On the other hand, samples A12, A14 and A15 also display sharp diffraction peaks which reveal the presence of brushite ($CaHPO_4{\cdot}2H_2O$, dicalcium phosphate dihydrate); this is particularly evident for the A15 sample, prepared with the highest Ca^{2+} concentration. The average crystallite size for brushite crystals, calculated using the Scherrer equation (Eq. (1)), is (61 ± 11) nm for A12, (60 ± 16) nm for A14 and (65 ± 15) nm for A15: these results suggest that no modifications in the crystallite size of brushite occur due to the different synthetic conditions. It is worth noting that despite the 7.40 pH used for the synthesis, the relatively acidic phase brushite is formed, due to the presence of Mg^{2+} ions in solution, which strongly hinder the formation of hydroxyapatite [4]. The small peaks at 31.7° and 45.5° in samples A11, A14, A6, A9, A12 and A15 are compatible with residual NaCl from the synthetic medium (average crystallite size of NaCl: 41 ± 15 nm).

The findings from XRD analysis were corroborated by ATR-FTIR analysis: the spectra for all samples are reported in Fig. S2 in the Supplementary Material. The spectra for A1, representative of amorphous samples, and A15, representative of brushite, are shown in Fig. 2. All spectra, except A15, display vibrational peaks characteristic of amorphous phosphates, namely: *i.* broad band at 3400–2600 cm^{-1} due to water's O—H stretching; *ii.* peak at 1653 cm^{-1} due to water bending; *iii.* intense peak at about 1000 cm^{-1} due to phosphate stretching and *iv.* peak at 877 cm^{-1} due to H—O(P) stretching in HPO_4^{2-} ions [11,23,52]. The A15 spectrum presents the characteristic sharp and defined peaks typical of brushite [54,55].

XRD and FTIR analyses show that the final product can be pure amorphous particles or a mix of amorphous particles and brushite crystals, depending on the initial concentration and Ca^{2+} and Mg^{2+} ratio used in the synthesis.

3.2. Morphology

The morphology of the synthesized particles was investigated by means of scanning electron microscopy: the micrographs of A1 and A15 are reported as an example in Fig. 3A and B, respectively, whereas a complete overview of all the samples can be found in Figs. S3 and S4. The nano-sized amorphous particles present spherically shaped particle units that aggregate. The size distribution curves (see the insets in Fig. S3) show that the single unit constituting the aggregate is polydisperse with an average diameter from about 40 nm to 80 nm. Despite the large polydispersity,

Table 3
Elemental ratios of the particles as obtained by means of ICP-OES and ionic chromatography. The error associated to each ratio is < 0.1 (see Section 2.3.5).

	Ca/Mg	Ca/P	Mg/P	(Ca + Mg)/P	Na/P
A1	2.13	0.82	0.38	1.20	0.24
A2	0.97	0.60	0.62	1.23	0.29
A3	0.63	0.45	0.71	1.17	0.29
A4	2.62	0.87	0.33	1.21	0.23
A5	1.39	0.65	0.47	1.12	0.27
A6	0.95	0.58	0.62	1.20	0.30
A7	3.11	0.92	0.30	1.21	0.25
A8	1.68	0.75	0.44	1.19	0.29
A9	1.38	0.74	0.54	1.27	0.30
A10	4.07	0.97	0.24	1.21	0.23
A11	2.46	0.87	0.35	1.22	0.27
A12*	2.48	0.96	0.39	1.35	0.26
A13	5.42	1.02	0.19	1.21	0.26
A14*	3.65	0.93	0.26	1.19	0.25
A15*	7.81	1.16	0.15	1.31	0.20

* Samples also containing brushite.

R. Gelli, L. Briccolani-Bandini, M. Pagliai et al. Journal of Colloid and Interface Science 606 (2022) 444–453

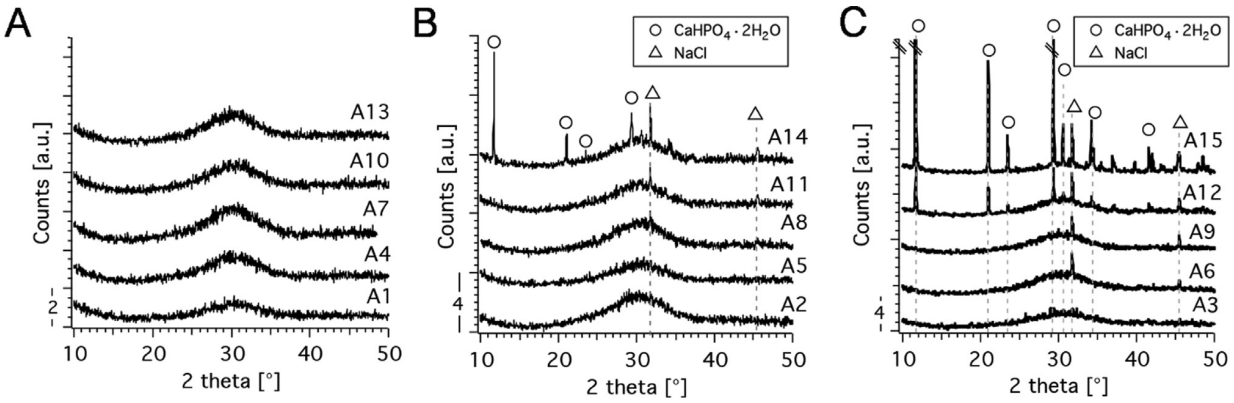

Fig. 1. XRD patterns of the synthesized particles. (A) [Mg^{2+}] = 10 mM series, (B) [Mg^{2+}] = 50 mM series, (C) [Mg^{2+}] = 100 mM series. All diffractograms correspond to AMCP, except for A12, A14 and A15 which also contain $CaHPO_4{\cdot}2H_2O$ (brushite, PDF: 09-0077, circle markers). The triangular markers correspond to NaCl crystals (halite, PDF: 01-0993). Diffractograms are offset for display purposes.

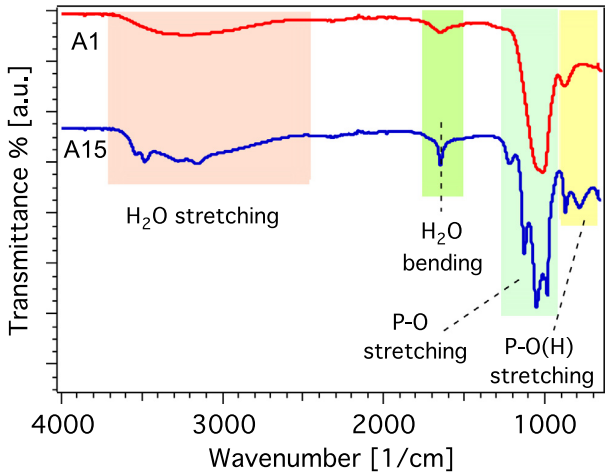

Fig. 2. ATR-FTIR spectra of A1 (top, red curve) and A15 (bottom, blue curve).

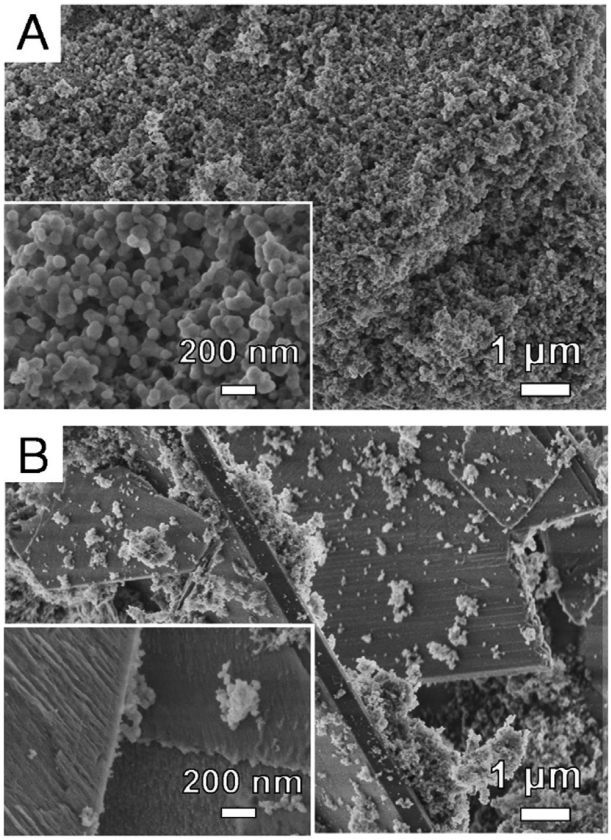

Fig. 3. (A) FE-SEM micrograph of sample A1, showing AMCP particles; (B) FE-SEM micrograph of sample A15, which shows the presence of AMCP together with brushite platelets. In the insets, high magnification micrographs are shown.

the data reported in Fig. S3 show that the dimension of the single units decreases when the total concentration of Ca^{2+} and Mg^{2+} is increased with respect to phosphate at a given Ca/Mg ratio, in agreement to the nucleation and growth theory [56].

In addition to amorphous aggregates, samples A12, A14 and A15 display well-defined platelets typical of well-crystalline brushite (see Figs. S4 and Fig. 3B), in agreement with XRD findings.

3.3. Elemental composition

The elemental composition of the particles was investigated by means of ICP-OES (for the quantification of P) and ionic chromatography (for the quantification of Ca, Mg and Na). The atomic ratios are reported in Table 3 and Fig. S5, while the Ca/Mg ratio as a function of the Ca/Mg ratio used in the synthesis of the particles is shown in Fig. 4.

The Ca/Mg in the precipitated particles is always higher than that of the solutions used to prepare them, suggesting the preferential incorporation of Ca^{2+} with respect to Mg^{2+}, which is related to the lower solubility of CaPs with respect to MgPs [57]. In any case, we observe that an increase in the Ca/Mg ratio of the synthetic solutions always corresponds to an increase in the Ca/Mg ratio of the precipitated particles. Moreover, for a given Ca/Mg ratio the amount of Ca^{2+} incorporated in the particles is higher in the more diluted regimes. The Ca/Mg ratio of samples containing brushite is not a reliable guess of the composition of the amorphous particles, as the presence of brushite crystalline phase (containing only Ca^{2+}) induces an overestimate of the Ca/Mg ratio (samples A12, A14 and A15, marked with a * in Fig. 4) especially

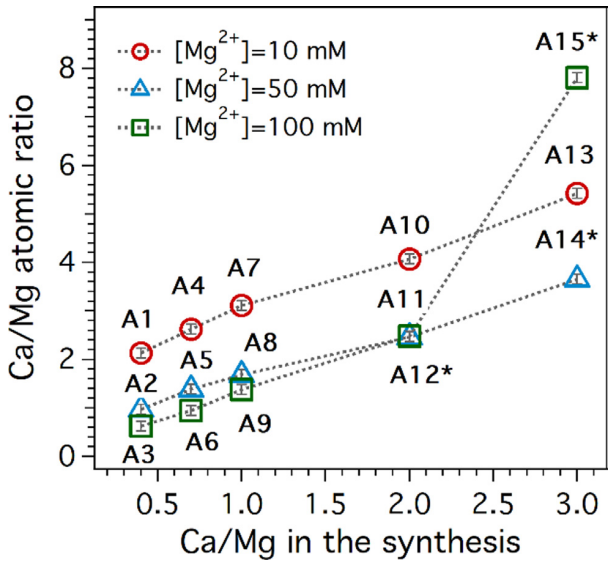

Fig. 4. Plot of the Ca/Mg atomic ratio obtained with ICP-OES/ionic chromatography vs the Ca/Mg molar ratio used in the synthesis. Samples marked with * also contain brushite, thus their Ca/Mg ratio may include not only the contribution of AMCP.

for A15, which is the most crystalline sample (see Fig. 1C). It is interesting that above a certain Ca/Mg threshold ($[Mg^{2+}]$ = 50 mM) an increase in the total cations amount does not reflect on a different Ca/Mg ratio in the particles. These results suggest that, despite almost all particles display an amorphous nature, a different amount of Ca^{2+} and Mg^{2+} is incorporated within their structure, disclosing a simple guideline to prepare amorphous particles with a tunable composition. A small and almost constant amount of Na is also present in the particles, likely due to residual traces of NaCl from the synthetic medium in the samples (as already observed in the XRD patterns of some samples in Fig. 1). Finally, the (Ca + Mg)/P ratio always smaller than 1.5 suggests that some hydrogenphosphate ions are present in the lattice, consistently with FTIR findings (see Fig. 2).

3.4. Thermal behavior

Some peculiar structural information can be obtained by analyzing the thermal degradation of the particles and the simultaneous heat flow profile by means of SDT. The derivative thermograms, reported in Fig. 5, show that the degradation of the amorphous particles occurs in three different stages: *i.* the loss of loosely bound water (yellow region in the figure, step I), *ii.* the loss of strongly bound internal water (green region, step II) and *iii.* weight loss occurring in correspondence of the crystallization process (blue region; step III) [58,59]. Samples A12, A14 and A15 also display a very sharp weight loss centered at 187 °C, due to the loss of brushite's two molecules of crystallization water ($CaHPO_4{\cdot}2H_2O \rightarrow CaHPO_4 + 2H_2O$, orange area in Fig. 5) [60].

The heat flow profiles reported in Fig. 6 show that amorphous particles undergo a crystallization process at a T ranging from 540 °C to 630 °C. The observation of crystallization events in amorphous materials is an interesting tool to gain insights into their features [61–64]. Here, the fact that samples display a different number and location of peaks suggests that structural differences among amorphous calcium-magnesium phosphate samples are present. Samples A2 and A3 display one sharp peak above 600 °C, whereas A5, A9 and A6 samples display a single but broadened peak at lower temperatures; all other samples crystallize into two distinct steps. Samples A12, A14 and A15, containing brushite, were not considered for the analysis of the amorphous crystallization. Samples A2, A7, A8 and A10 were analyzed as case studies to identify the crystalline phase at a temperature above the crystallization peaks. The XRD patterns, reported in Fig. S6, show that sample A2 converts to crystalline sodium calcium magnesium phosphate with a whitlockite-like structure ($Ca_9MgNa(PO_4)_7$, PDF n° 88-0797) and small amounts of $Ca_9Mg_7Na_2(PO_4)_6$ (PDF n° 47-1763). The pattern of samples A7, A8 and A10 recovered after the first crystallization peak matches the pattern of $Ca_9MgNa(PO_4)_7$, whereas the small peaks which appear after the second peak are compatible with the conversion of residual amorphous material to pyrophosphates ($Mg_2P_2O_7$, PDF 01-0866 and $Na_2MgP_2O_7$, PDF 48-0574). According to literature reports, pure amorphous calcium phosphate converts to α-TCP or β-TCP above 600 °C, depending on the preparation conditions [58,61,65–67]. When Mg^{2+} ions are

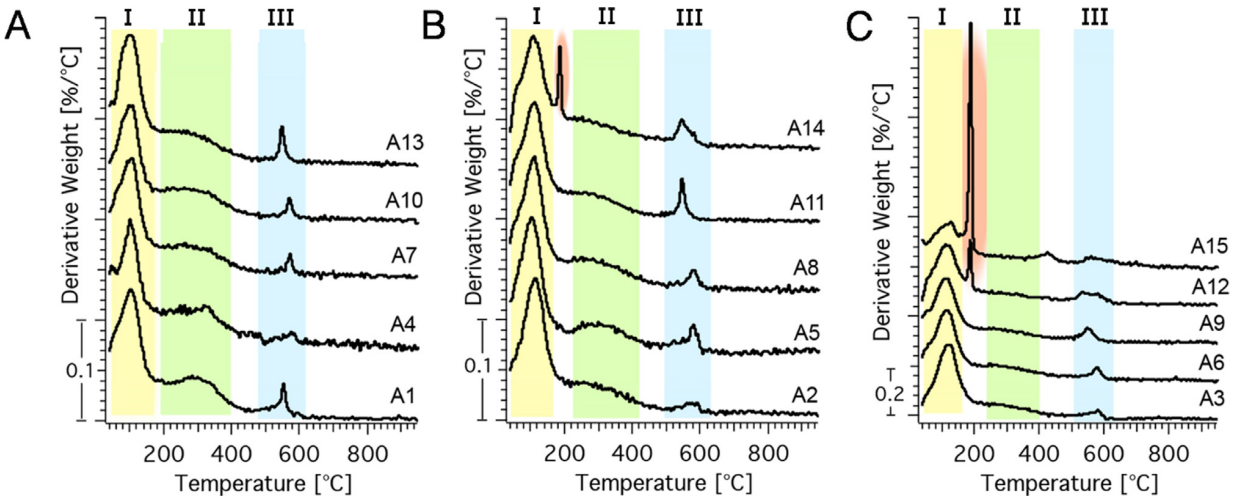

Fig. 5. Derivative thermogravimetric curves of the samples under investigation; (A) $[Mg^{2+}]$ = 10 mM series, (B) $[Mg^{2+}]$ = 50 mM series, C) $[Mg^{2+}]$ = 100 mM series. The yellow (I), green (II) and blue (III) regions respectively indicate the weight losses of: (I) loosely bound water, (II) strongly bound water and (III) weight loss occurring during crystallization. The orange circles indicate the weight loss diagnostic of brushite. All the thermograms are offset for display purposes.

R. Gelli, L. Briccolani-Bandini, M. Pagliai et al. Journal of Colloid and Interface Science 606 (2022) 444–453

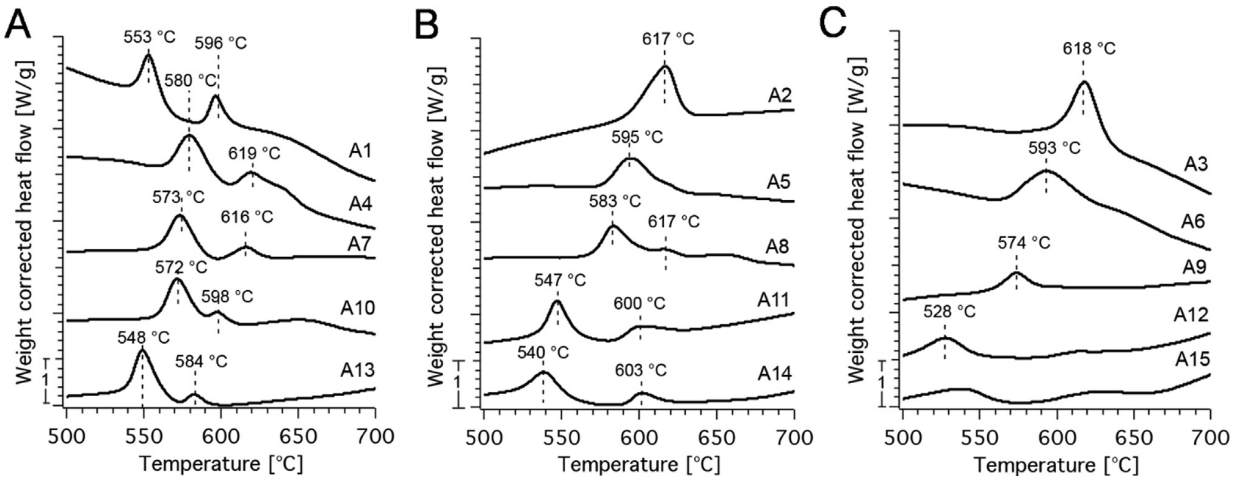

Fig. 6. Weight corrected heat flow profiles (exo up) of (A) [Mg^{2+}] = 10 mM series, (B) [Mg^{2+}] = 50 mM series, (C) [Mg^{2+}] = 100 mM series. The curves are offset for display purposes.

present in the lattice, the formation of β -TMCP (Mg-substituted TCP), which has a diffraction pattern similar to the detected phase, was observed [38]. The substitution of divalent cations on ACP is analyzed in a recent work [68], in which it is shown that Mg^{2+} content in ACP affects the thermal behavior, promoting the formation of β-TCP over α-TCP at lower temperatures.

This work shows that the different crystallization temperatures observed in the AMCP samples do not correspond to the conversion towards different phases. A very interesting outcome arises from the observation of the plot of the crystallization temperature (maximum of the first peak) vs the particles' Ca/Mg ratio, reported in Fig. 7 (left y axis), which reveals that the lower the Ca/Mg ratio of the particles, the higher the crystallization temperature. This assumption holds up to a Ca/Mg ratio of about 2. Therefore Mg^{2+}, in addition to its known stabilizing action in the conversion of amorphous to crystalline calcium/magnesium phosphates in solution [21,36], promotes the stabilization of the amorphous phase against heating when incorporated in the lattice of the particles.

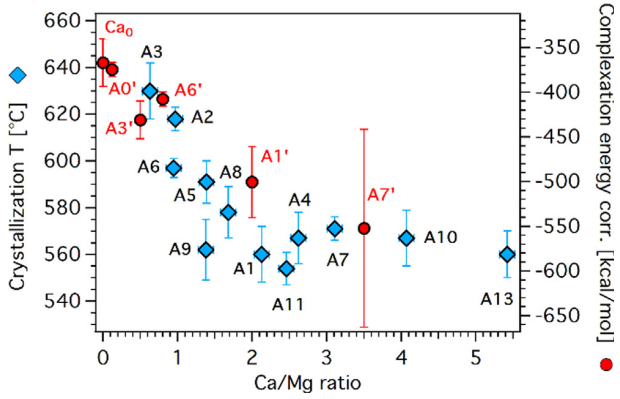

Fig. 7. Plot of the crystallization T (1st peak maximum) vs the Ca/Mg ratio (left y axis). The blue diamond markers represent the average values ± standard deviations (see the materials and methods section). The plot also shows the counterpoise correction energy (red dots) as a function of Ca/Mg ratio. The error bars in calculations progressively enlarge due to the limit in configuration sampling.

3.5. DFT calculations

These conclusions are further corroborated by the computational analyses. The interaction energies between the inner site of Mg^{2+} ion and the remaining Posner's cluster for different Ca/Mg ratio were calculated and are reported in Fig. 7 (right y axis). For the homogeneous system Ca_0 (only magnesium cations) the interaction energy of the inner site with the cluster is approximately of −357 kcal/mol. Instead, in the case of the cluster with two Mg^{2+} and seven Ca^{2+} (A7′, see Table 2), the counterpoise correction energy is −552 kcal/mol. The obtained trend confirms the stabilizing contribute of the Mg^{2+} cation with the increasing of calcium concentration. In fact, the binding energy in Posner's cluster increases (in absolute value) with calcium content. Qualitatively, this trend can be rationalized considering the greater coordination effect due to the higher hardness for magnesium than calcium. This determines a reduction of intermolecular distances, also considering those involving Mg^{2+} ions. In this respect, the electrostatic repulsion is greater in clusters with higher magnesium content and consequently the binding energy is lower.

These conclusions are supported by the analysis of the Mg-O distances of the clusters where the Ca^{2+} ions are replaced by Mg^{2+} ions (see computational details in 2.3.7). An increase of the magnesium content in the cluster determines a progressive stabilization of the interactions at Mg-O distances greater than 4.0 Å as it can be observed in Fig. 8A. On the contrary, starting from a fully magnesium-substituted Posner cluster and increasing the number of Ca^{2+}, a loss of the structure for Ca-O distances greater than 4.0 Å occurs (see Fig. 8B). This behavior can be rationalized considering the higher hardness of Mg^{2+} ion than Ca^{2+} ion, as expected. To further ascertain the stabilizing character of magnesium, the structure of the crystalline phase which AMCP particles tend to convert to (brushite, see XRD, FTIR and SEM results previously discussed) was considered, and it was re-optimized upon substitution of all calcium atoms with magnesium atoms (Brushite-Mg). Keeping fix the cell parameters, the comparison between the atomic positions in the two optimized crystals confirms these findings, as can be appreciated in Table 4 and in Fig. 8C. All the intermolecular distances involving the Mg^{2+} ion and the first neighbors are shorter than those corresponding in the calcium crystal, as it can be observed in Table 4. The shortening

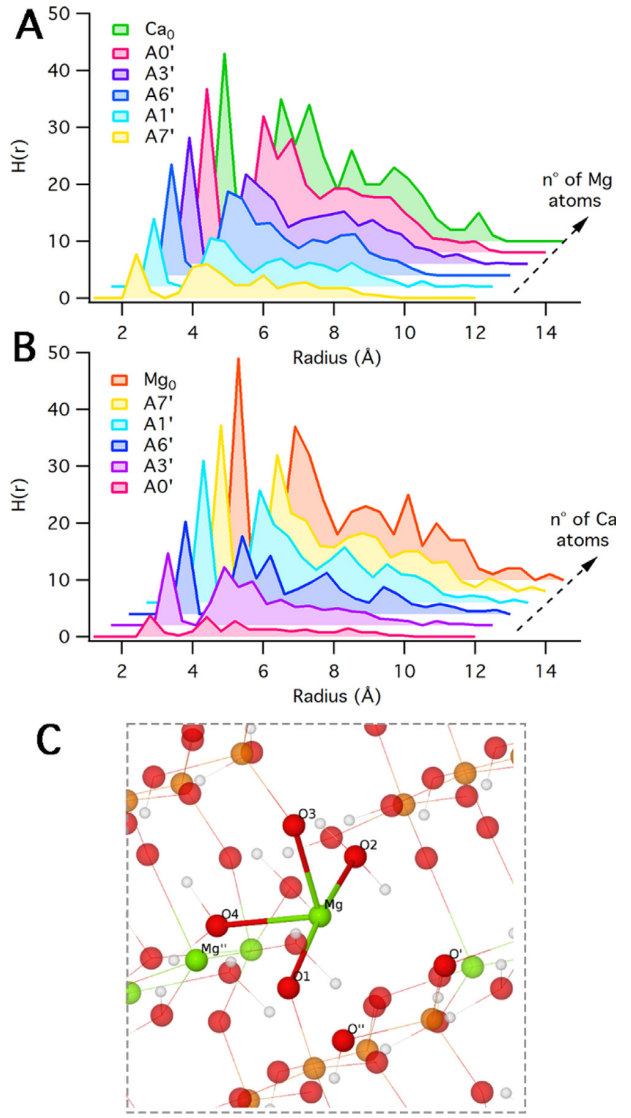

Fig. 8. Distribution of the Mg-O interactions (A) and Ca-O interactions (B) by increasing the number of Mg atoms (A) or Ca atoms (B). (C) Identification of atoms in Brushite-Mg structure as in Table 4.

Table 4
Distances between metal cation and first neighbors in optimized Brushite-Mg and Brushite crystal structures. The identification of the atoms refers to Fig. 8C.

	Distance (Å) – Brushite-Mg	Distance (Å) – Brushite
M^{2+}—O_1 (O)	2.03	2.37
M^{2+}—O_2 (OH)	2.08	2.38
M^{2+}—O_3 (O)	2.04	2.51
M^{2+}—O_4 (OH)	2.14	2.51
M^{2+}—O′ (O)	2.36	2.45
M^{2+}—O″ (OH)	2.57	2.67
M^{2+}—$M^{2+\prime\prime}$	3.91	4.04

in the distances is in agreement with the optimization calculations on the Posner's clusters.

In conclusion, the simulations well agree with the experimental results, as the comparison of the crystallization temperature and the interaction energies in Fig. 7 both indicate a stabilizing effect of Mg^{2+} when it is included in the structure of ACP.

4. Conclusions

In this work, the effect of Mg-substitution on the features of ACP nanoparticles is discussed. In biological organisms, Mg-substituted ACP nanoparticles are present in different regions and fulfill some important functions [2]. For this reason, understanding the role of Mg^{2+} in ACP structure and stability is important both to gain insights into the biological mechanisms as well as to prepare nanoparticles with defined composition to reproduce and study *in vitro* biological processes. In this context, some reports in the literature describe the preparation of AMCPs with different Ca/Mg ratio [24,38] and their stability in simulated body fluids [39,40]. Nevertheless, the features of the amorphous phases and the effect of Mg^{2+} in the amorphous cluster are poorly investigated.

In this paper a systematic analysis on this topic was conducted by performing 15 different syntheses in which the concentrations of the reacting solutions were varied to test 5 different Ca/Mg ratios (0.4, 0.7, 1, 2 and 3), each at 3 different Mg^{2+} concentrations (10, 50 and 100 mM). The precipitated AMCP nanoparticles were characterized with a multi-technique approach which allowed for the assessment of the structural features. We succeeded in identifying the best synthetic conditions to obtain pure amorphous nanoparticles and to prevent the formation of crystalline brushite. Despite XRD, FT-IR and SEM analyses did not show significant differences among the prepared particles, the analysis of their elemental composition revealed a variable Ca/Mg ratio in the particles, which was correlated to the synthetic conditions. Most importantly, calorimetric analyses demonstrated that the amount of Mg^{2+} in the particles has a key importance in delaying the thermal crystallization of AMCP, suggesting a stabilizing effect of this ion when included in ACP structure. These results are strengthened by computational analyses in which different Posner's-like clusters containing an increasing amount of Mg were modelled. The computed Mg-O and Ca-O distances in the clusters, as well as the interaction energies, confirm a stabilization of the cluster with the increase of Mg atoms.

The presented results could be useful for researchers working on inorganic colloids and in particular on amorphous phosphates, as they provide a simple but effective strategy to tune the composition and thermal stability of AMCP nanoparticles; furthermore, from a fundamental perspective, they contribute to shed light on the effect of Mg^{2+} substitution in ACP-based systems. These nanoparticles could be of interest for biomedical applications, for instance in the treatment of dentin hypersensitivity [41,42], or to reproduce and study the endogenous nanoparticles present in the small intestine [43].

CRediT authorship contribution statement

Rita Gelli: Conceptualization, Methodology, Formal analysis, Investigation, Writing – original draft, Writing – review & editing, Visualization. **Lorenzo Briccolani-Bandini:** Conceptualization, Methodology, Formal analysis, Investigation, Writing – original draft, Writing – review & editing, Visualization. **Marco Pagliai:** Conceptualization, Methodology, Formal analysis, Resources, Writing – review & editing, Visualization, Supervision, Funding acquisition. **Gianni Cardini:** Conceptualization, Methodology, Formal analysis, Resources, Writing – review & editing, Visualization, Supervision, Funding acquisition. **Francesca Ridi:** Conceptualization, Methodology, Formal analysis, Resources, Writing – review & editing, Visualization, Supervision, Funding acquisition. **Piero Baglioni:** Conceptualization, Methodology, Formal analysis, Resources, Writing – review & editing, Visualization, Supervision, Funding acquisition.

Declaration of Competing Interest

The authors declare that they have no known competing financial interests or personal relationships that could have appeared to influence the work reported in this paper.

Acknowledgements

Fondazione CR Firenze (project 2017.0720), CSGI consortium, MUR PRIN- 2017249YEF, MIUR-Italy (“Progetto Dipartimenti di Eccellenza 2018-2022” allocated to Department of Chemistry “Ugo Schiff”) are acknowledged for financial support. We thank Prof. Mirko Severi for ICP-OES and ionic chromatography measurements.

Appendix A. Supplementary material

Supplementary data to this article can be found online at https://doi.org/10.1016/j.jcis.2021.08.033.

References

[1] S.V. Dorozhkin, Calcium orthophosphates (CaPO4): occurrence and properties, Prog. Biomater. 5 (2016) 9–70, https://doi.org/10.1007/s40204-015-0045-z.
[2] R. Gelli, F. Ridi, P. Baglioni, The importance of being amorphous: calcium and magnesium phosphates in the human body, Adv. Colloid Interface Sci. 269 (2019) 219–235, https://doi.org/10.1016/j.cis.2019.04.011.
[3] F. Betts, A.S. Posner, An X-ray radial distribution study of amorphous calcium phosphate, Mater. Res. Bull. 9 (1974) 353–360, https://doi.org/10.1016/0025-5408(74)90087-7.
[4] M.-S.-A. Johnsson, G.H. Nancollas, The role of brushite and octacalcium phosphate in apatite formation, Crit. Rev. Oral Biol. Med. 3 (1992) 61–82, https://doi.org/10.1177/10454411920030010601.
[5] R. Sun, M. Åhlén, C.-W. Tai, É.G. Bajnóczi, F. de Kleijne, N. Ferraz, I. Persson, M. Strømme, O. Cheung, Highly porous amorphous calcium phosphate for drug delivery and bio-medical applications, Nanomaterials. 10 (2020) 20, https://doi.org/10.3390/nano10010020.
[6] G.-J. Ding, Y.-J. Zhu, C. Qi, B.-Q. Lu, F. Chen, J. Wu, Porous hollow microspheres of amorphous calcium phosphate: soybean lecithin templated microwave-assisted hydrothermal synthesis and application in drug delivery, J. Mater. Chem. B 3 (2015) 1823–1830, https://doi.org/10.1039/C4TB01862A.
[7] W. Yu, T.-W. Sun, C. Qi, Z. Ding, H. Zhao, F. Chen, D. Chen, Y.-J. Zhu, Z. Shi, Y. He, Strontium-doped amorphous calcium phosphate porous microspheres synthesized through a microwave-hydrothermal method using fructose 1,6-Bisphosphate as an organic phosphorus source: application in drug delivery and enhanced bone regeneration, ACS Appl. Mater. Interfaces 9 (2017) 3306–3317, https://doi.org/10.1021/acsami.6b12325.
[8] J. Zhao, Y. Liu, W. Sun, H. Zhang, Amorphous calcium phosphate and its application in dentistry, Chem. Cent. J. 5 (2011) 40, https://doi.org/10.1186/1752-153X-5-40.
[9] M. Iafisco, L. Degli Esposti, G.B. Ramírez-Rodríguez, F. Carella, J. Gómez-Morales, A.C. Ionescu, E. Brambilla, A. Tampieri, J.M. Delgado-López, Fluoride-doped amorphous calcium phosphate nanoparticles as a promising biomimetic material for dental remineralization, Sci. Rep. 8 (2018) 17016, https://doi.org/10.1038/s41598-018-35258-x.
[10] M. Luginina, R. Orru, G. Cao, D. Grossin, F. Brouillet, G. Chevallier, C. Thouron, C. Drouet, First successful stabilization of consolidated amorphous calcium phosphate (ACP) by cold sintering: toward highly-resorbable reactive bioceramics, J. Mater. Chem. B 8 (2020) 629–635, https://doi.org/10.1039/C9TB02121C.
[11] C. Combes, C. Rey, Amorphous calcium phosphates: synthesis, properties and uses in biomaterials, Acta Biomater. 6 (2010) 3362–3378, https://doi.org/10.1016/j.actbio.2010.02.017.
[12] M. Nabiyouni, T. Brückner, H. Zhou, U. Gbureck, S.B. Bhaduri, Magnesium-based bioceramics in orthopedic applications, Acta Biomater. 66 (2018) 23–43, https://doi.org/10.1016/j.actbio.2017.11.033.
[13] R.K. Rude, H.E. Gruber, L.Y. Wei, A. Frausto, B.G. Mills, Magnesium deficiency: effect on bone and mineral metabolism in the mouse, Calcif. Tissue Int. 72 (2003) 32–41, https://doi.org/10.1007/s00223-001-1091-1.
[14] R.K. Rude, H.E. Gruber, Magnesium deficiency and osteoporosis: animal and human observations, J. Nutr. Biochem. 15 (2004) 710–716, https://doi.org/10.1016/j.jnutbio.2004.08.001.
[15] S. Castiglioni, A. Cazzaniga, W. Albisetti, J.A.M. Maier, Magnesium and osteoporosis: current state of knowledge and future research directions, Nutrients 5 (2013) 3022–3033, https://doi.org/10.3390/nu5083022.
[16] M.E. Maguire, J.A. Cowan, Magnesium chemistry and biochemistry, Biometals 15 (2002) 203–210, https://doi.org/10.1023/A:1016058229972.
[17] J. Tao, D. Zhou, Z. Zhang, X. Xu, R. Tang, Magnesium-aspartate-based crystallization switch inspired from shell molt of crustacean, Proc. Natl. Acad. Sci. 106 (2009) 22096–22101, https://doi.org/10.1073/pnas.0909040106.
[18] J.J. Powell, E. Thomas-McKay, V. Thoree, J. Robertson, R.E. Hewitt, J.N. Skepper, A. Brown, J.C. Hernandez-Garrido, P.A. Midgley, I. Gomez-Morilla, G.W. Grime, K.J. Kirkby, N.A. Mabbott, D.S. Donaldson, I.R. Williams, D. Rios, S.E. Girardin, C. T. Haas, S.F.A. Bruggraber, J.D. Laman, Y. Tanriver, G. Lombardi, R. Lechler, R.P. H. Thompson, L.C. Pele, An endogenous nanomineral chaperones luminal antigen and peptidoglycan to intestinal immune cells, Nat. Nanotechnol. 10 (2015) 361–369, https://doi.org/10.1038/nnano.2015.19.
[19] L.M. Gordon, M.J. Cohen, K.W. MacRenaris, J.D. Pasteris, T. Seda, D. Joester, Amorphous intergranular phases control the properties of rodent tooth enamel, Science 347 (2015) 746–750, https://doi.org/10.1126/science.1258950.
[20] A.L. Fontaine, A. Zavgorodniy, H. Liu, R. Zheng, M. Swain, J. Cairney, Atomic-scale compositional mapping reveals Mg-rich amorphous calcium phosphate in human dental enamel, Sci. Adv. 2 (2016) e1601145, https://doi.org/10.1126/sciadv.1601145.
[21] A.L. Boskey, A.S. Posner, Magnesium stabilization of amorphous calcium phosphate: a kinetic study, Mater. Res. Bull. 9 (1974) 907–916, https://doi.org/10.1016/0025-5408(74)90169-X.
[22] B.N. Bachra, H.R.A. Fischer, The effect of some inhibitors on the nucleation and crystal growth of apatite, Calcif. Tissue Res. 3 (1969) 348–357, https://doi.org/10.1007/BF02058677.
[23] C. Holt, M.J.J.M. Van Kemenade, L.S. Nelson, D.W.L. Hukins, R.T. Bailey, J.E. Harries, S.S. Hasnain, P.L. De Bruyn, Amorphous calcium phosphates prepared at pH 6.5 and 6.0, Mater. Res. Bull. 24 (1989) 55–62, https://doi.org/10.1016/0025-5408(89)90008-1.
[24] C. Holt, M. Van Kemenade, J.E. Harries, L.S. Nelson, R.T. Bailey, D.W.L. Hukins, S. S. Hasnain, P.L. De Bruyn, Preparation of amorphous calcium-magnesium phosphates at pH 7 and characterization by x-ray absorption and fourier transform infrared spectroscopy, J. Cryst. Growth 92 (1988) 239–252, https://doi.org/10.1016/0022-0248(88)90455-1.
[25] N.C. Blumenthal, F. Betts, A.S. Posner, Stabilization of amorphous calcium phosphate by Mg and ATP, Calcif. Tissue Res. 23 (1977) 245–250, https://doi.org/10.1007/BF02012793.
[26] F. Abbona, A. Baronnet, A XRD and TEM study on the transformation of amorphous calcium phosphate in the presence of magnesium, J. Cryst. Growth 165 (1996) 98–105, https://doi.org/10.1016/0022-0248(96)00156-X.
[27] J. Christoffersen, M.R. Christoffersen, W. Kibalczyc, F.A. Andersen, A contribution to the understanding of the formation of calcium phosphates, J. Cryst. Growth 94 (1989) 767–777, https://doi.org/10.1016/0022-0248(89)90102-4.
[28] W. Kibalczyc, J. Christoffersen, M.R. Christoffersen, A. Zielenkiewicz, W. Zielenkiewicz, The effect of magnesium ions on the precipitation of calcium phosphates, J. Cryst. Growth 106 (1990) 355–366, https://doi.org/10.1016/0022-0248(90)90080-5.
[29] A.S. Posner, F. Betts, N.C. Blumenthal, Role of ATP and Mg in the stabilization of biological and synthetic amorphous calcium phosphates, Calcif. Tissue Res. 22 (1976) 208–212, https://doi.org/10.1007/BF02064066.
[30] X. Yang, B. Xie, L. Wang, Y. Qin, Z.J. Henneman, G.H. Nancollas, Influence of magnesium ions and amino acids on the nucleation and growth of hydroxyapatite, CrystEngComm 13 (2011) 1153–1158, https://doi.org/10.1039/C0CE00470G.
[31] H. Ding, H. Pan, X. Xu, R. Tang, Toward a detailed understanding of magnesium ions on hydroxyapatite crystallization inhibition, Cryst. Growth Des. 14 (2014) 763–769, https://doi.org/10.1021/cg401619s.
[32] O. Bertran, L.J. del Valle, G. Revilla-López, M. Rivas, G. Chaves, M.T. Casas, J. Casanovas, P. Turon, J. Puiggalí, C. Alemán, Synergistic approach to elucidate the incorporation of magnesium ions into hydroxyapatite, Chem. - Eur. J. 21 (2015) 2537–2546, https://doi.org/10.1002/chem.201405428.
[33] Q. Liu, Z. Chen, H. Pan, B.W. Darvell, J.P. Matinlinna, Effect of magnesium on the solubility of hydroxyapatite, Eur. J. Inorg. Chem. 2016 (2016) 5623–5629, https://doi.org/10.1002/ejic.201601056.
[34] I. Buljan Meić, J. Kontrec, D. Domazet Jurašin, B. Njegić Džakula, L. Štajner, D.M. Lyons, M. Dutour Sikirić, D. Kralj, Comparative study of calcium carbonates and calcium phosphates precipitation in model systems mimicking the inorganic environment for biomineralization, Cryst. Growth Des. 17 (2017) 1103–1117, https://doi.org/10.1021/acs.cgd.6b01501.
[35] W. Jin, Z. Liu, Y. Wu, B. Jin, C. Shao, X. Xu, R. Tang, H. Pan, Synergic effect of Sr^{2+} and Mg^{2+} on the stabilization of amorphous calcium phosphate, Cryst. Growth Des. 18 (2018) 6054–6060, https://doi.org/10.1021/acs.cgd.8b00908.
[36] R. Gelli, M. Scudero, L. Gigli, M. Severi, M. Bonini, F. Ridi, P. Baglioni, Effect of pH and Mg^{2+} on amorphous magnesium-calcium phosphate (AMCP) stability, J. Colloid Interface Sci. 531 (2018) 681–692, https://doi.org/10.1016/j.jcis.2018.07.102.
[37] E. Colaço, D. Brouri, C. Méthivier, L. Valentin, F. Oudet, K. El Kirat, C. Guibert, J. Landoulsi, Calcium phosphate mineralization through homogenous enzymatic catalysis: investigation of the early stages, J. Colloid Interface Sci. 565 (2020) 43–54, https://doi.org/10.1016/j.jcis.2019.12.097.
[38] D. Lee, P.N. Kumta, Chemical synthesis and characterization of magnesium substituted amorphous calcium phosphate (MG-ACP), Mater. Sci. Eng., C 30 (2010) 1313–1317, https://doi.org/10.1016/j.msec.2010.05.009.
[39] M. Shahrezaee, M. Raz, S. Shishehbor, F. Moztarzadeh, F. Baghbani, A. Sadeghi, K. Bajelani, F. Tondnevis, Synthesis of magnesium doped amorphous calcium phosphate as a bioceramic for biomedical application: in vitro study, Silicon 10 (2018) 1171–1179, https://doi.org/10.1007/s12633-017-9589-y.

[40] E. Babaie, H. Zhou, B. Lin, S.B. Bhaduri, Influence of ethanol content in the precipitation medium on the composition, structure and reactivity of magnesium–calcium phosphate, Mater. Sci. Eng., C 53 (2015) 204–211, https://doi.org/10.1016/j.msec.2015.04.011.
[41] C. Berg, E. Unosson, H. Engqvist, W. Xia, Amorphous calcium magnesium phosphate particles for treatment of dentin hypersensitivity: a mode of action study, ACS Biomater. Sci. Eng. 6 (2020) 3599–3607, https://doi.org/10.1021/acsbiomaterials.0c00262.
[42] C. Berg, E. Unosson, L. Riekehr, W. Xia, H. Engqvist, Electron microscopy evaluation of mineralization on peritubular dentin with amorphous calcium magnesium phosphate microspheres, Ceram. Int. 46 (2020) 19469–19475, https://doi.org/10.1016/j.ceramint.2020.04.295.
[43] L.C. Pele, C.T. Haas, R.E. Hewitt, J. Robertson, J. Skepper, A. Brown, J.C. Hernandez-Garrido, P.A. Midgley, N. Faria, H. Chappell, J.J. Powell, Synthetic mimetics of the endogenous gastrointestinal nanomineral: Silent constructs that trap macromolecules for intracellular delivery, Nanomed. Nanotechnol. Biol. Med. 13 (2017) 619–630, https://doi.org/10.1016/j.nano.2016.07.008.
[44] C.F. Holder, R.E. Schaak, Tutorial on powder X-ray diffraction for characterizing nanoscale materials, ACS Nano 13 (2019) 7359–7365, https://doi.org/10.1021/acsnano.9b05157.
[45] M.J. Frisch, G.W. Trucks, H.B. Schlegel, G.E. Scuseria, M.A. Robb, J.R. Cheeseman, G. Scalmani, V. Barone, G.A. Petersson, H. Nakatsuji, X. Li, M. Caricato, A.V. Marenich, J. Bloino, B.G. Janesko, R. Gomperts, B. Mennucci, H.P. Hratchian, J.V. Ortiz, A.F. Izmaylov, J.L. Sonnenberg, Williams, F. Ding, F. Lipparini, F. Egidi, J. Goings, B. Peng, A. Petrone, T. Henderson, D. Ranasinghe, V.G. Zakrzewski, J. Gao, N. Rega, G. Zheng, W. Liang, M. Hada, M. Ehara, K. Toyota, R. Fukuda, J. Hasegawa, M. Ishida, T. Nakajima, Y. Honda, O. Kitao, H. Nakai, T. Vreven, K. Throssell, J.A. Montgomery Jr., J.E. Peralta, F. Ogliaro, M.J. Bearpark, J.J. Heyd, E.N. Brothers, K.N. Kudin, V.N. Staroverov, T.A. Keith, R. Kobayashi, J. Normand, K. Raghavachari, A. P. Rendell, J.C. Burant, S.S. Iyengar, J. Tomasi, M. Cossi, J.M. Millam, M. Klene, C. Adamo, R. Cammi, J.W. Ochterski, R.L. Martin, K. Morokuma, O. Farkas, J.B. Foresman, D.J. Fox, Gaussian 16 Rev. C.01, Wallingford, CT, 2016.
[46] T.D. Kühne, M. Iannuzzi, M. Del Ben, V.V. Rybkin, P. Seewald, F. Stein, T. Laino, R.Z. Khaliullin, O. Schütt, F. Schiffmann, D. Golze, J. Wilhelm, S. Chulkov, M.H. Bani-Hashemian, V. Weber, U. Borštnik, M. Taillefumier, A.S. Jakobovits, A. Lazzaro, H. Pabst, T. Müller, R. Schade, M. Guidon, S. Andermatt, N. Holmberg, G.K. Schenter, A. Hehn, A. Bussy, F. Belleflamme, G. Tabacchi, A. Glöß, M. Lass, I. Bethune, C.J. Mundy, C. Plessl, M. Watkins, J. VandeVondele, M. Krack, J. Hutter, CP2K: An electronic structure and molecular dynamics software package - quickstep: efficient and accurate electronic structure calculations, J. Chem. Phys. 152 (2020) 194103, https://doi.org/10.1063/5.0007045.
[47] S. Goedecker, M. Teter, J. Hutter, Separable dual-space Gaussian pseudopotentials, Phys. Rev. B. 54 (1996) 1703–1710, https://doi.org/10.1103/PhysRevB.54.1703.
[48] J. VandeVondele, J. Hutter, An efficient orbital transformation method for electronic structure calculations, J. Chem. Phys. 118 (2003) 4365–4369, https://doi.org/10.1063/1.1543154.
[49] P.F. Schofield, K.S. Knight, J.A.M. van der Houwen, E. Valsami-Jones, The role of hydrogen bonding in the thermal expansion and dehydration of brushite, di-calcium phosphate dihydrate, Phys. Chem. Miner. 31 (2004) 606–624, https://doi.org/10.1007/s00269-004-0419-6.
[50] S.F. Boys, F. Bernardi, The calculation of small molecular interactions by the differences of separate total energies. Some procedures with reduced errors, Mol. Phys. 19 (1970) 553–566, https://doi.org/10.1080/00268977000101561.
[51] S. Simon, M. Duran, J.J. Dannenberg, How does basis set superposition error change the potential surfaces for hydrogen-bonded dimers?, J Chem. Phys. 105 (1996) 11024–11031, https://doi.org/10.1063/1.472902.
[52] A.C. Tas, X-ray-amorphous calcium phosphate (ACP) synthesis in a simple biomineralization medium, J. Mater. Chem. B 1 (2013) 4511, https://doi.org/10.1039/c3tb20854k.
[53] S.V. Dorozhkin, Amorphous calcium (ortho)phosphates, Acta Biomater. 6 (2010) 4457–4475, https://doi.org/10.1016/j.actbio.2010.06.031.
[54] L. Tortet, J.R. Gavarri, G. Nihoul, A.J. Dianoux, Study of protonic mobility in CaHPO4·2H2O (Brushite) and CaHPO4(Monetite) by infrared spectroscopy and neutron scattering, J. Solid State Chem. 132 (1997) 6–16, https://doi.org/10.1006/jssc.1997.7383.
[55] M.P. Gashti, M. Bourquin, M. Stir, J. Hulliger, Glutamic acid inducing kidney stone biomimicry by a brushite/gelatin composite, J. Mater. Chem. B 1 (2013) 1501–1508, https://doi.org/10.1039/C3TB00088E.
[56] N.T.K. Thanh, N. Maclean, S. Mahiddine, Mechanisms of nucleation and growth of nanoparticles in solution, Chem. Rev. 114 (2014) 7610–7630, https://doi.org/10.1021/cr400544s.
[57] E. Königsberger, L. Königsberger, (Eds.), Biomineralization: medical aspects of solubility, J. Wiley, Chichester, England ; Hoboken, NJ, 2006.
[58] S.V. Dorozhkin, Amorphous calcium orthophosphates: nature, chemistry and biomedical applications, Int. J. Mater. Chem. 2 (2012) 19–46, https://doi.org/10.5923/j.ijmc.20120201.04.
[59] Y. Kojima, K. Sakama, T. Toyama, T. Yasue, Y. Arai, Dehydration of water molecule in amorphous calcium phosphate, Phosphorus Res. Bull. 4 (1994) 47–52, https://doi.org/10.3363/prb1992.4.0_47.
[60] A. Betke, G. Kickelbick, Bottom-up, wet chemical technique for the continuous synthesis of inorganic nanoparticles, Inorganics 2 (2014) 1–15, https://doi.org/10.3390/inorganics2010001.
[61] J. Vecstaudza, M. Gasik, J. Locs, Amorphous calcium phosphate materials: formation, structure and thermal behaviour, J. Eur. Ceram. Soc. 39 (2019) 1642–1649, https://doi.org/10.1016/j.jeurceramsoc.2018.11.003.
[62] V. Uskoković, S. Marković, L. Veselinović, S. Škapin, N. Ignjatović, D.P. Uskoković, Insights into the kinetics of thermally induced crystallization of amorphous calcium phosphate, PCCP 20 (2018) 29221–29235, https://doi.org/10.1039/C8CP06460A.
[63] L.D. Esposti, S. Markovic, N. Ignjatovic, S. Panseri, M. Montesi, A. Adamiano, M. Fosca, J.V. Rau, V. Uskoković, M. Iafisco, Thermal crystallization of amorphous calcium phosphate combined with citrate and fluoride doping: a novel route to produce hydroxyapatite bioceramics, J. Mater. Chem. B (2021), https://doi.org/10.1039/D1TB00601K.
[64] D. Griesiute, L. Sinusaite, A. Kizalaite, A. Antuzevics, K. Mazeika, D. Baltrunas, T. Goto, T. Sekino, A. Kareiva, A. Zarkov, The influence of Fe3+ doping on thermally induced crystallization and phase evolution of amorphous calcium phosphate, CrystEngComm 23 (2021) 4627–4637, https://doi.org/10.1039/D1CE00371B.
[65] S. Somrani, C. Rey, M. Jemal, Thermal evolution of amorphous tricalcium phosphate, J. Mater. Chem. 13 (2003) 888–892, https://doi.org/10.1039/B210900J.
[66] T. Kanazawa, T. Umegaki, N. Uchiyama, Thermal crystallisation of amorphous calcium phosphate to α-tricalcium phosphate, J. Chem. Technol. Biotechnol. 32 (1982) 399–406, https://doi.org/10.1002/jctb.5030320206.
[67] V.M. Wu, S. Tang, V. Uskoković, Calcium phosphate nanoparticles as intrinsic inorganic antimicrobials: the antibacterial effect, ACS Appl. Mater. Interfaces 10 (2018) 34013–34028, https://doi.org/10.1021/acsami.8b12784.
[68] L. Sinusaite, A. Kareiva, A. Zarkov, Thermally induced crystallization and phase evolution of amorphous calcium phosphate substituted with divalent cations having different sizes, Cryst. Growth Des. 21 (2021) 1242–1248, https://doi.org/10.1021/acs.cgd.0c01534.